FuturUM
1974 2024

MAŠINSKI
FAKULTET
PODGORICA

ThermaEComp

ThermaEComp2024

Sixth International Conference on

COMPUTATIONAL METHODS FOR THERMAL AND ENERGY PROBLEMS

Edited by

Nicola Massarotti
Perumal Nithiarasu
Igor Vusanovic

SEPTEMBER
9-11, 2024
BUDVA,
MONTENEGRO

THERMAECOMP2024

SIXTH INTERNATIONAL CONFERENCE ON COMPUTATIONAL METHODS FOR THERMAL AND ENERGY PROBLEMS

SEPTEMBER 9-11, 2024, BUDVA, MONTENEGRO

EDITED BY:

IGOR VUŠANOVIĆ
FACULTY OF MECHANICAL ENGINEERING
UNIVERSITY OF MONTENEGRO
PODGORICA, MONTENEGRO

NICOLA MASSAROTTI
DIPARTIMENTO DI INGEGNERIA
UNIVERSITÀ DEGLI STUDI DI NAPOLI "PARTHENOPE"
NAPOLI, ITALY

PERUMAL NITHIARASU
ZIENKIEWICZ INSTITUTE FOR MODELLING, DATA AND AI
FACULTY OF SCIENCE AND ENGINEERING
SWANSEA UNIVERSITY
SWANSEA, UNITED KINGDOM

WITH THE SUPPORT FROM:
ALESSANDRO MAURO AND ARMANDO DI MEGLIO
UNIVERSITÀ DEGLI STUDI DI NAPOLI "PARTHENOPE"

6th International Conference on Computational Methods for Thermal and Energy Problems,
2024, Budva, Montenegro

Sixth Edition, August 2024

ISSN 3006-9874 (Online)
ISSN 3006-9866 (Print)

PREFACE

It is our pleasure to welcome all participants of the *Sixth International Conference on Computational Methods for Thermal and Energy Problems* (THERMAECOMP2024) to Budva, Montenegro. Computational and mathematical methods have a profound impact on the understanding and advancement of engineering science and technology. When the series of Conferences was started in 2009, the idea was to have a focused conference in the area of computational methods for thermal problems, and since then energy problem has become even more pressing after COVID-19. Therefore, the Conference now aims to convene a diverse scientific audience of mathematicians, physicists and computational scientists that have a communal interest in modelling thermal and energy problems. We hope that the interaction between scientists during the conference leads to new topics of research, new collaborations, and possibly new friendships.

THERMAECOMP2024 consists of three plenary lectures, six keynote lectures, three organized mini-symposia and four parallel sessions. We are grateful to all invited speakers for accepting our invitation.

We would also like to take this opportunity to thank THERMAECOMP2024 sponsors, mini-symposium organizers, executive and advisory committee members, as well as everyone who has been involved in the organization for their support.

Igor Vušanović	Nicola Massarotti	Perumal Nithiarasu
University of Montenegro	*Università di Napoli Parthenope*	*Swansea University*
Montenegro	Italy	United Kingdom

Sponsors

University of Montenegro

Università degli Studi di Napoli "Parthenope"

Swansea University

Supporting Organizations

Dipartimento di Ingegneria
Università di Napoli Parthenope

Consorzio di Ricerca per l'Ambiente, l'Energia i Veicoli e i Biocombustibili

COMMITTEES

CO-CHAIRS

N. Massarotti, University of Naples “Parthenope”, Italy
P. Nithiarasu, Swansea University, UK
I. Vušanović, University of Montenegro, Montenegro

INTERNATIONAL EXECUTIVE COMMITTEE

P. Cheng, Shanghai Jiao Tong University, China
Pradip Dutta, Indian Institute of Science, India
Y. Jaluria, Rutgers, The State University of New Jersey, USA
Y. Joshi, Georgia Institute of Technology, USA
Xikui Li, Dalian University of Technology, China
J. Murthy, Oregon State University, USA
V. Naso, Università di Napoli Federico II, Italy
C. Ranganayakulu, Birla Institute of Technology & Science, Pilani, India
B. Šarler, University of Ljubljana, Slovenia
B. Sunden, Lund University, Sweden
W. Q. Tao, Xi'an Jiao Tong University, China
K. Vafai, University of California, Riverside, USA

INTERNATIONAL ADVISORY COMMITTEE

F. Arpino, Università di Cassino e del Lazio Meridionale, Italy
B. Rabi Baliga, McGill University, Canada
A. C. Benim, University of Applied Sciences Düsseldorf, Germany
G. Biswas, Indian Institute of Technology Kanpur, India
A. Carotenuto, Università di Napoli “Parthenope”, Italy
A. J. Chamkha, Prince Mohammad Bin Fahd University, Kuwait
S. Chang, National University of Singapore, Singapore
F. Chinesta, ENSAM ParisTech, France
R. Codina, Universitat Politècnica de Catalunya, Spain
H. Combeau, Ecole des Mines de Nancy, France
R. M. Cotta, Universidade Federal do Rio de Janeiro, Brazil
D. Drikakis, University of Nicosia, Cyprus
G. Dulikravich, Florida International University, U.S.A
D. Givoli, Technion - Israel Institute of Technology, Israel
D. Gobin, CNRS, France
S. Idelsohn CIMNE - International Center for Numerical Methods in Engineering, Spain
A. Kassab, University of Central Florida, USA
R. Lohner, George Mason University, USA
J.C. Mandal, Indian Institute of Technology Bombay, India
O. Manca, Università degli Studi della Campania “Luigi Vanvitelli”, Italy
P. Nikrityuk, University of Alberta, Canada
A. Mauro, Università degli Studi della Campania “Luigi Vanvitelli”, Italy
C. Nonino, Università di Udine, Italy
A. J. Nowak, Silesian Polytechnic University, Poland
I. Pop, Babeş-Bolyai University, Romania
A. Sciacovelli, University of Birmingham, UK
L. Vanoli, Università di Napoli "Parthenope", Italy
V.R. Voller, University of Minnesota, USA
L. Xiaobing, Huazong University of Science and Technology, China
G. Xie, Northwestern Polytechnical University, China

ORGANISING COMMITTEE

Esad Tombarević, University of Montenegro
Milan Šekularac, University of Montenegro
Rade Grujičić, University of Montenegro
B. Hrnčić, University of Montenegro
S. Di Fraia, Università di Napoli “Parthenope”, Italy
A. Di Meglio, Università di Napoli “Parthenope”, Italy

CONTENTS

PLENARY LECTURES

KEYNOTE LECTURES

PARALLEL SESSIONS

MINI-SYMPOSIA

THERMOACOUSTICS FOR ENERGY CONVERSION SYSTEMS

MINI-SYMPOSIUM ORGANISED BY A. DI MEGLIO, N. MASSAROTTI, E. DI GIULIO, R.A. ROMANO, R. DRAGONETTI, R. BACCOLI, A. PICCOLO

Porous media correlations for thermoacoustic stacks
Di Meglio Armando, Massarotti Nicola

Analysis of Thermoacoustic Instability through a Macroscopic Modeling of the Stack
Di Giulio Elio, Dragonetti Raffaele, Romano Rosario Aniello

Compact thermoacoustic cooler (TACOT): design and experimental qualification
Baillet Hélène, Ramadan Islam, Fontbonne Martin, Poignad Gaelle.

Compact thermoacoustic cooler (TACOT): numerical approach
Baltean Carles Diana, Weisman Catherine. Fraigneau Yann

GEOTHERMAL ENERGY, A SUSTAINABLE FUTURE FOR HEATING AND COOLING

MINI-SYMPOSIUM ORGANISED BY F. AHMED, L. ARESTI, N. MAKASIS

Comparison of analytical models for Ground Heat Exchangers
Christodoulides Paul, Skaliontas Andreas, Aresti Lazaros, Florides Georgios

Foundation Slabs as an Energy Geo-Structure in a Moderate Climate
Aresti Lazaros, Florides Georgios, Christodoulides Paul

Design optimization and performance advancement of ground coupled heat exchanger
Mohamed A. Samaha, Muhannad T. Ali, Ghalib Y. Kahwaji

Exploring a novel geo-exchange system on Ischia island, southern Italy: an experimental study
Carotenuto Alberto, Guida Vincenzo, Massarotti Nicola, Mauro Alessandro

Modeling temperature distribution in in different grouting materials for ground source heat pumps
Ahmed Fawad, Massarotti Nicola

DIGITAL TWINNING OF THERMAL AND ENERGY SYSTEMS

MINI-SYMPOSIUM ORGANISED BY A. DI MEGLIO, N. MASSAROTTI, W. BIELAJEWA, N. K. CHAKSHU, P. NITHIARASU

Digital Twinning of a container house HVAC system for controlling and optimizing energy consumption
Di Meglio Armando, Laudiero Davide, Mauro Alessandro, Massarotti Nicola, Nithiarasu Perumal

Digital twinning using novel nonlinear finite-element approach for sparse-data solution reconstruction
Bielajewa Wiera, Tindall Michelle, Nithiarasu Perumal

Geogrid Viewer for sustainable exploitation of geothermal digital twins
Iorio Marina, Donnarumma Gianpaolo, Mercadante Antonio, Massarotti Nicola, Fawad Ahmed

Solution reconstruction of Hive sample using Physis-Informed Neural Networks
Sharma Prakhar, Tindall Michelle, Nithiarasu Perumal

Thermal management system of railway power electronics through a digital twin optimized via the new refine algorithm
De Rosa Raffaele, Senatore Adolfo, Romagnuolo Luca, Frosina Emma

PHASE CHANGE PROBLEMS

Cylindrical battery thermal management with different phase change material solutions
Piccirillo Francesco, Iasiello Marcello, Bianco Nicola, Chiu Wilson K. S.

Efficient explicit time stepping enthalpy methods for phase change problems
Vušanović Igor, Vaughan R Voller

High fidelity and simplified modelling of hydrophobic surfaces performances for anti-icing applications.
Croce Giulio, Suzzi Nicola

Numerical analysis of passive cooling of PV panels using PCM
Hrnčić Boris, Vušanović Igor

Sensitivity study in simulation of melting in a cylindrical geometry
Anthony G. Straatman, Maryam Hemmat, Kyle Teather

HEAT EXCHANGERS AND MICRO HEAT TRANSPORT

Optimization of Colburn and Fanning friction factors in an offset strip plate-fin heat exchanger using genetic algorithm
Negi Vinay Pratap Singh, Khandelwal Sarvesh, Ranganayakulu

A porous-medium approach for the thermal analysis of microchannel heat sinks
Nonino Carlo, Savino Stefano.

ENERGY RELATED PROBLEMS

CFD investigation of heat and mass transport in solid oxide fuel cells
Grossi Giorgio, Arpino Fausto, Canale Christian, Cortellessa Gino, Ficco Giorgio, Hamidi Jahromi Reza, Pumiglia Davide

Energy retrofit impact in European container houses: a simulation study
Bianco Vincenzo, Carotenuto Alberto, Cascetta Furio, Laudiero Davide Maria, Mauro Alessandro

Harnessing waste heat and solar thermal integration for sustainable brewery cooling: a case study approach
Shah Musannif, Palomba Valeria, Frazzica Andrea, Arenas-Larrañaga Mikel, Carbonell Daniel

Investigation of multiple ORC plant configurations for waste heat stream recovery
Morrone Biagio, Serag Saif, Ageorges Hélène

Life cycle based comparison of different solutions for urban passengers' transportation
Massarotti Nicola, Santagata Remo, Vanoli Laura

Prediction of CO2 emissions inside a building with machine learning based on experimental data
Rossi di Schio Eugenia, Vallerini Vincenzo, Sentimenti Christian, Valdiserri Paolo

NUMERICAL METHODS

All Mach number two-phase Riemann solver for compressible flows
Bharate Ghanshyam, Mandal J. C.

An electroneutrality-preserving approach for multi-ionic transport using finite element methods applied to the electrolytic neutral pickling of stainless steel
Bossio Alvaro, Blommaert Maarten, Vaelmans Martine, Fransaer Jan, Gielen Ruben

CVFEM solution for the vorticity-stream function formulation: MATLAB implementation for lid driven cavity flow
Tombarevič Esad, Šekularac Milan, Vušanović Igor, Karadžić Uroš

Experimental and numerical analysis of a side-mirror model through PTV and CFD technique
Canale Christian, Arpino Fausto, Cortellessa Gino, Grossi Giorgio, Schiaccitano Andrea

Heat conduction simulation via the meshless fragile points method (FPM) and various explicit/implicit ode numerical solvers
Grujičić Rade, Vilotijevic Vidosava, Vušanović Igor, Komatina Mirko

Modelling of thermal comfort conditions in a train cabin
Hamidi Jahromi Reza, Mauro Alessandro, Di Fraia Simona, Massarotti Nicola, Grossi Giorgio

On the numerical approach for thermal effects in tunnel fires
Šekularac Milan, Tombarevič Esad

CONDUCTION, CONVECTION AND RADIATION

Designing a commercial cooking oven using gas fuels by adaptive combustion approach
Remzi Timur, Kahraman Zafer, Haci Murat, Serhad Soyhan Hakan

Numerical simulation of change of “diffusion-convection” modes in isothermal ternary mixtures based on lattice Boltzmann equations.
Kossov Vladimir, Zhumali Ainur, Fedorenko Olga

PLENARY LECTURES

Sixth International Conference on Computational Methods for Energy and Thermal Problems
THERMAECOMP2024, Sept. 9-11, 2024, Budva, Montenegro
N. Massarotti, P. Nithiarasu, and I. Vušanović (Eds.)

HYBRID ARTIFICIAL INTELLIGENCE FOR OPTIMAL PLANNING AND DECISION MAKING IN URBAN SYSTEMS

Francisco Chinesta

PIMM, UMR CNRS, Arts et Métiers Institute of Technology, Paris, France

CNRS@CREATE, CREATE Campus for Research Excellence and Technological Enterprise, Singapore

Dominique Baillargeat

CNRS@CREATE, CREATE Campus for Research Excellence and Technological Enterprise, Singapore

XLIM, UMR CNRS, Limoges, France

ABSTRACT

Intelligent modelling technologies such as digital twins, applied to urban infrastructures and systems, can enhance community-centric planning by simulating urban environments and developing predictive scenarios in response to critical and uncertain situations, allowing both optimal planning and aided or even automated real-time decision-making. This paper revisits the main methodologies and some proofs of concept developed within the DesCartes programme leaded by CNRS@CREATE.

Key Words: *Hybrid AI, Hybrid Twin, Critical urban systems, Smart cities*

1. INTRODUCTION

Concerning the virtual representation, for design and operation of a given asset (component, system and/or complex system of systems), two levels of digitalization (two classes of digital twins) can be distinguished:

- The first level, leading to the so-called *digital twin prototype*, concerns the virtual representation of the asset, equipped with its physics-based behaviour, enabling the emulation of the asset operation. The digital twin prototype is composed by a state-of-the-art physics-based model, that from the assumed inputs (actions) predicts the asset (component or system) responses, to evaluate if the requested performances and robustness are ensured. This digital twin, purely virtual, precedes the existence of the asset, and precisely, it is used for optimal design purposes.
- The main protagonist of the second level of digitalisation is the so-called *digital twin instance*, that comes into the scene as soon as the asset exist and operates, enabling real-time diagnosis, prognosis and decision making. It includes also data, sent from the asset to the virtual computational model (to ensure monitoring) and from the virtual model to the asset for control purposes.

In both cases, an accurate and agile model is needed, providing the asset response to any input. Here, the main question concerns the nature of that model. Two main possibilities exist:

- Physics-based models use the existing knowledge expressed mathematically from a system of coupled partial differential equations, reflecting the coupled nonlinear multi-scale and multi-physics behaviours, with a series of constraints and domain knowledge. The main limitation of such an approach is the loss of accuracy in long-time predictions because of the limitations of models to exactly represent the observed reality.
- Data-driven models learn from the available data, however, in engineering, data is constrained by the cost of sensors, the difficulty of its massive deployment, the data transmission, storage and treatment, … Thus, the construction of fields from the, usually scarce, collected data, needs some approximations with their intrinsic loss of accuracy. Increasing the amount of measurements becomes unreasonable, and sometimes impossible because of the existing regulations.

A gateway consists of combining both paradigms into an hybrid one, in which data is not used to learn the model itself, but to learn the gap between the physics-based model predictions and the measures. If the available physics-based model is accurate enough, the gap is expected being small enough to facilitate its approximation from few data points, enabling not only to explain the resulting hybrid model, at least its physic-abased component, but also reducing significantly the amount of required data to reach high accuracy in the predictions.

Moreover, the physics knowledge enables to drive the data collection, within the so-called active learning paradigm, that is, determining the data to be collected, and the location and time at which performing the measures.

The hybrid modelling [1-3] proceeds as follows:

- Using machine learning to construct the physics-based model surrogate, able to proceed in real-time while ensuring high levels of accuracy. The surrogate construction procedure involves five main steps:

    1. The model (M) and the parameters that it involves, grouped in vector P and defined in the parametric domain (W), are set.
    2. A DoE (design of experiments) is defined, composed on different parameter choices P1, P2, … to cover at the best the domain W, or to ensure maximum accuracy in the region of interest (active learning).
    3. Model M is discretized and solved for the different DoE points, whose discrete solutions are referred by S1, S2, …
    4. Data-reduction, linear (e.g. PCA) or nonlinear (e.g. autoencoder), can be applied for expressing those solutions in a reduced latent space, where they read: s1, s2, … that represents the solutions embedding. Thus, the linear and nonlinear encoding s(S) and decoding S(s) are established.
    5. Now, with each reduced solution (s1, s2, …) associated with a parameters choice (P1, P2, …), that is, s1 related to P1, s2 related to P2, and so on … a linear (e.g. regularized polynomial) or nonlinear (e.g. neural network) regression can be constructed to obtain: s(P). From it, inference proceeds from an arbitrary parameters choice P, that using the just referred regression leads to the reduced solution s(P), and the full solution S(P) by decoding S(P)=S(s(P)).

- For the different available states of the asset, related to P1, P2, …, data is extracted (measurements performed at different locations and times) and grouped into vectors D1, D2, … These measures are compared with the predictions provided by the model, contained in vectors S1, S2, … The difference (gap) at the measurement points between D and S, for the different parameters P1, P2, … are noted by g1, g2, … Now, by using an adequate approximation basis (the PCA modes extracted from S1, S2, … constitutes an appealing choice), the gap, only known at the measurement points, is extended everywhere in the physical domain (data completion), leading to the extended vectors G1, G2, …

Now, the rationale described before applies again, but now on the gap-field (G1, G2, …), to finally obtain de gap model: G(P).

- The hybridation performs as soon as the surrogate of the physics-based model S(P) and the model of the gap G(P) are available. From both, one is tempted to improve predictions by adding to the physics-based prediction S(P) the enrichment (or correction) G(P), to obtain the so-called hybrid solution $S^H(P)$ that writes: $S^H(P)=S(P)+G(P)$.

Thus, we can conclude that AI (machine learning) has been employed with a triple objective: (i) *making faster* thanks to the physics-based surrogate S(P); (ii) *making better* by adding a data-driven enrichment (correction) G(P) to the physics-based surrogate S(P); and (iii) making cheaper, taking into account that modelling the gap requires much less data than the one required for learning the model itself. Moreover, the resulting hybrid model is explainable, at least its main component, the physics-based, and that the existing knowledge (physics-based model) makes also possible an optimal data acquisition (active learning).

This new knowledge/data alliance enables real-time diagnosis, prognosis and decision-making, using less data (frugality) with better accuracy in predictions, it remains almost explainable, and minimizes the ecological footprint (sustainability). By enabling human-driven updating of knowledge and security certifications, it also enables a human centric approach where the privacy of citizens is ensured.

Through Hybrid Artificial Intelligence (HAI), different technological functionalities can be elaborated and, subsequently, closely combined for constituting the complex system of systems emulating the city functioning within its environment.

This new paradigm is applied to several case-based solutions for critical urban systems, where environmental maps (wind, pollution, temperature etc.), digital energy, and smart sensing of large critical civil and industrial infrastructures, are assimilated to perform predictive maintenance, optimize energy production and distribution, and enhance crisis and emergency management, ton in essence contribute to the life quality, pleasure and safety of citizens.

2. TOWARDS A CITY HYBRID TWIN

The integration workflow is sketched in Fig. 1 where the fundamental research gives rise to implementable algorithms, that integrate the so-called hybrid-twin combining surrogates of physics-based model (able to operate under the stringent real-time constraints) with data-driven models of the prediction to measurement biases (the gap or physics-based model ignorance), most of time consisting of informed learning.

These hybrid twins are then applied to model the different system components, that at their turn are integrated in the so-called “control tower”, the system of system hybrid twin, that could and should be advantageously employed for taking decisions, and eventually informing people, governmental services and authorities, able to proceed with optimal operation or with mitigation procedures in case of emergencies.

FIGURE 1. Workflow: from research to decision making

A proof of concept is being developed within the DesCartes research programme, that the French CNRS is developing in its hub in Singapore, into CREATE, a NRF campus of excellence.

Descartes considers different demonstrators: (i) the city environment hybrid twin; (ii) the digital energy; (iii) remote sensing of large civil, urban or industrial infrastructures; (iv) drones trajectory planning, as the ones employed for monitoring, gods' delivery, or mobility; and (v) management of emergency crises, as illustrated in Fig. 2, where the same rationale applies for the different addressed cases.

FIGURE 2. Descartes demonstrators developed in collaboration with industry and agencies

Concerning the city hybrid twin, applied to Marina Bay district (in Singapore) and La Defense district in Paris (France), the main protagonist was the wind, intimately coupled with many other physical phenomena (temperature, noise, air quality, plume dispersion, drone trajectory planning, …) as illustrated in Fig. 3.

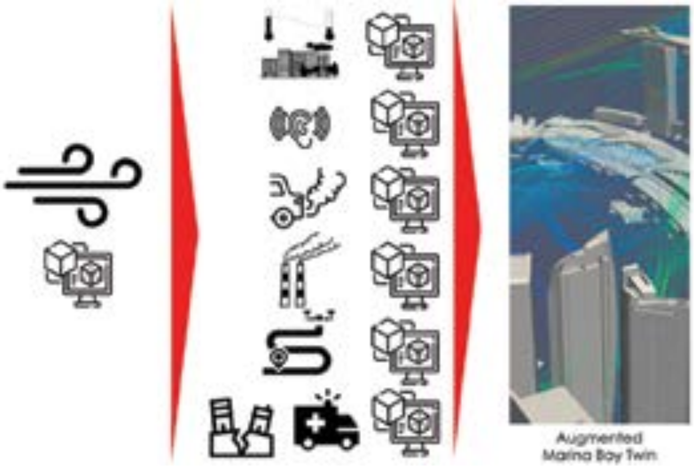

FIGURE 3. Towards the urban digital twins

3. WIND MAP

When focusing in a geographical area, at large scale, statistical data exists, grouped into the so-called wind-rose chart, representing the histogram of wind intensity and direction along a long period (years) to consider it representative (Fig 4).

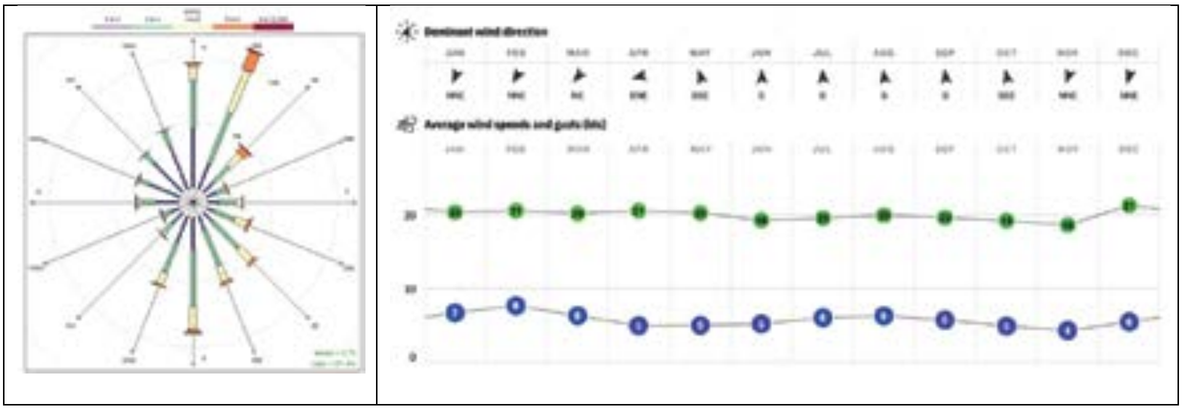

FIGURE 4. Wind rose charts

For nearby time predictions, weather forecast provides an estimation of the wind intensity and direction in a particular geographical area, as depicted in Fig. 5 for Singapore.

FIGURE 5. Wind estimation

However, the scale concerned by the weather forecast (Fig. 5) remains too far from the one involved in the everyday life of citizens, the meter resolution at the street level, illustrated in Fig. 6.

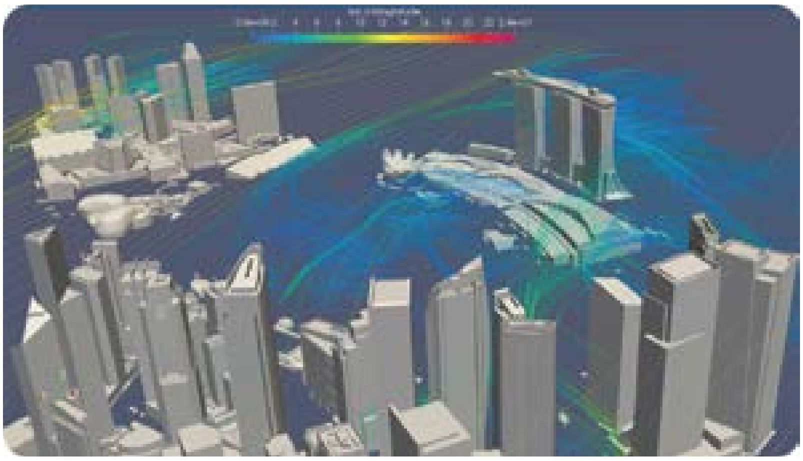

FIGURE 6. Simulated wind in Marina Bay district (Singapore)

Thus, the question is how moving from coarse to fine scales in the wind representation, that is, how to obtain the wind field illustrated in Fig. 6 from the knowledge provided at larger scales (Fig. 5).

Following the rationale described above, the wind at large-scale is parametrized by its intensity and direction, considered as boundary conditions in the computational fluid dynamics model and its simulation. The DoE is defined by considering different wind intensities and directions, from which, the OpenFOAM CFD opensource software computes the different wind fields in the considered urban area. These solutions are then reduced by invoking a linear dimensionality reduction, the principal component analysis (PCA), on which, a regularized polynomial regression applies. To account the expected nonlinear solutions, rich polynomial nonlinear approximations are considered. However, to keep as reduced as possible (despite the approximation richness) the CFD computations, providing the data feeding the regressions, regularization becomes compulsory. Our simulations proceed with the velocity vectors to guarantee the incompressibility constraint of the regressed solutions, and an “elastic-net” regularization, that combines “ridge” regularization that prevents overfitting and “lasso” regularization that promotes sparsity, is used [4].

Even if in the present the model only involves two parameters (wind intensity and direction), to ensure the scale-up and then the possibility of operating in highly multi-dimensional parametric settings, separated representations for expressing the unknown fields are considered, with a greedy constructor that continues enriching the solution (adding modes) until reaching a small enough residual [4]. Fig. 7 sketches the DoE (left) and the real-time wind-map inference in the right.

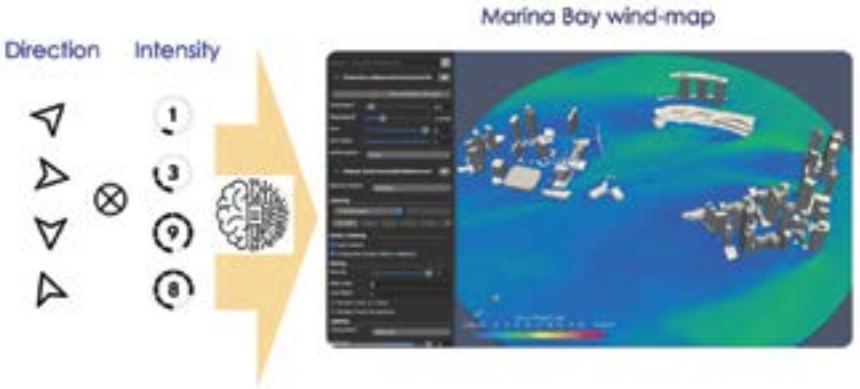

FIGURE 7. DoE (left) and resulting Marina Bay parametric wind-map (right)

When solutions exhibit parameter-dependent localization, usual approximations produce spurious effects, as a direct consequence of the so-called Kolmogorov n-width issue. To overcome this issue, nonlinear transformations enabling further reduction, or parametric optimal transport [5] can be applied.

The wind model could be enriched by adding to the wind intensity and direction and their fluctuations (amplitude and frequency) to compute the transient responses and their time statistics.

4. DERIVED REAL-TIME MAPS

With the wind map available, different physics depending on it can be addressed. Air quality depends on the wind in each street, the density of traffic and the cars velocity distribution. By using state-of-the art models, the air quality can be estimated. The more expensive model input remains the wind field, but having the wind-map, enabling real-time particularization, the evaluation of the air quality performs almost instantaneously (Fig. 8).

FIGURE 8. Air quality prediction for a given wind and traffic conditions

Emissions dispersion can be also easily evaluated from the wind map. As the wind-map can be particularized in almost real-time as just commented, now a passive-scalar representing the pollution concentration, can be dispersed by using a particles representation, by moving each particle because of the wind-induced convection and the stochastic motion representing turbulent diffusion. Thus, many scenarios can be simulated in almost real-time to take certified decisions (Fig. 9).

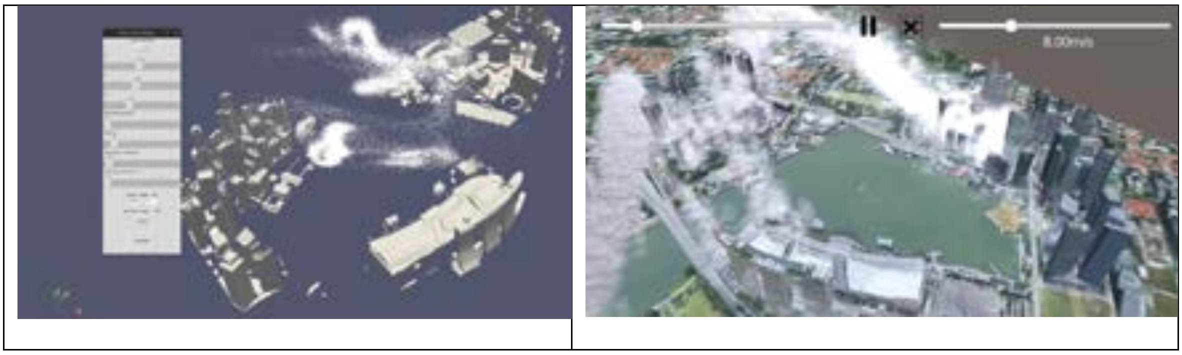

FIGURE 9. Dispersion scenario computed from a parametric model that consider the emission location, the emission rate, the emission surface area and the far-field wind conditions, intensity and orientation, both eventually evolving in time (left) and plume dispersion from a vessel leak (right).

A temperature map can be elaborated by using the same rationale employed for computing the wind map, to infer, depending on the solar intensity and the wind conditions, the temperature at the ground and on the building's walls, as well as the effects induced by temperature on the wind velocity field (thermo-convective flows).

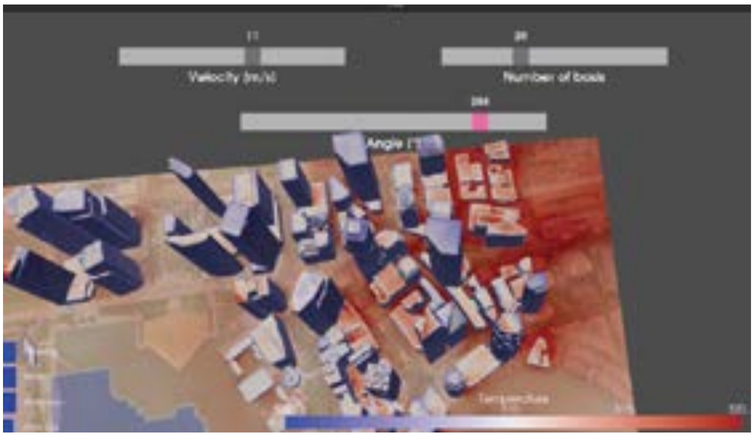

FIGURE 10. Ground temperature for a given solar heating and wind conditions.

6. IMMERSIVE EXPERIENCE

All these maps can be use in augmented reality, in our case the Marina Bay reduced model, or in immersive virtual reality platforms, as shown in Figs. 11, 12 and 13.

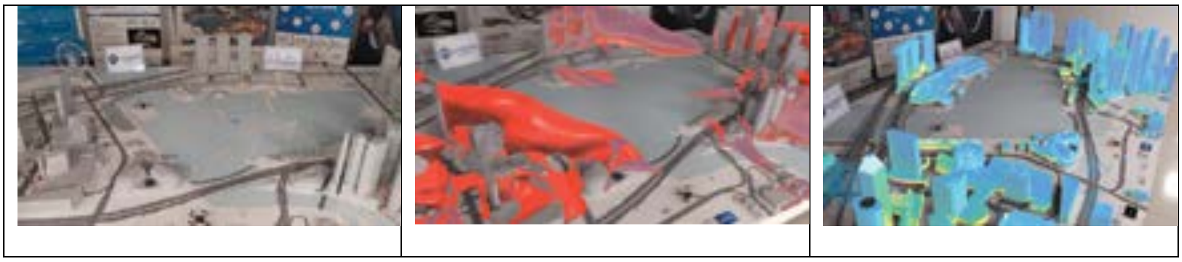

FIGURE 11. Augmented reality application: wind field and drone following its optimal trajectory for minimizing the energy consumption (left), turbulence map defining the nonflying zones in red (center) and temperature map (right).

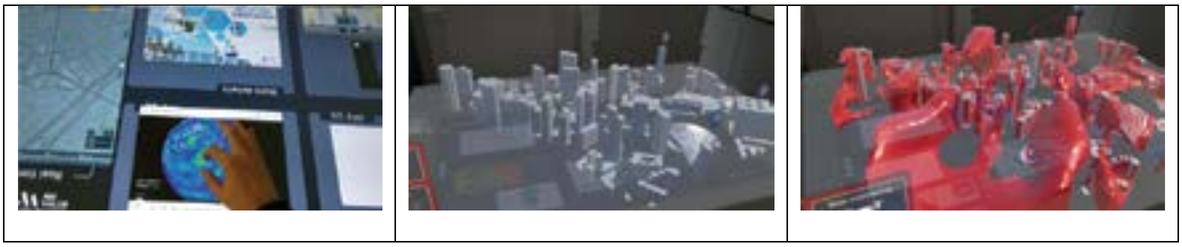

FIGURE 12. Collaborative engineering (left), 3D VR model (center) and wind and turbulence envelopes (right)

FIGURE 13. Immersive VR: model (left), temperature (center) and wind velocity (right)

CONCLUSIONS

Hybrid twins, consisting of physics-based surrogates enriched from data-driven models describing the prediction to measurement gap, constitute an opportunity for modelling complex systems of systems, where usual paradigms (fully knowledge-based or fully data-driven) fail to provide fast and accurate predictions, compulsory in optimal design and optimal operation.

This paper describes the main methodological concepts and computational procedures for advanced and efficient modelling. It also illustrates and discusses some proofs of concept addressed within the DesCartes programme, leaded by CNRS@CREATE (Singapore), where hybrid modelling contributes to the real-time decision making in critical urban systems.

Now, large experimental campaigns are being defined to validate the physic-based predictions, and when needed, enriching them by associating the data-driven model of the noticed gap (deviation or ignorance), in close collaboration with different Singaporean agencies.

ACKNOWLEDGEMENT

Authors thanks the essential contribution of many colleagues: V. Champaney, D. Di Lorenzo, A. Pasquale, B. Boris Huljak, A. Ammar, Kyaw Zin Htun, … our industrial partners IMMERSION and ESI GROUP, as well as SLA (Singapore Land Authority) for providing the Marina Bay district geometry model.

This research is part of the DesCartes programme, supported by the National Research Foundation, Prime Minister's Office, Singapore under its Campus for Research Excellence and Technological Enterprise (CREATE) programme.

REFERENCES

[1] Chinesta, F., Cueto, E., Abisset, E., Duval, J.L. and El Khaldi, F (2020) Virtual, Digital and Hybrid Twins. A new paradigm in data-based engineering and engineered data. Archives of Computational Methods in Engineering, 27, 105-134.

[2] Chinesta, F. and Cueto, E. (2022) Empowering Engineering with Data, Machine Learning and Artificial Intelligence: A Short Introductive Review. Adv. Model. and Simul. in Eng. Sci. 9, 21.

[3] Chinesta, F. and Cueto, E. (2023) Conciliating accuracy and efficiency to empower engineering based on performance: a short journey. CRAS, 1-13.

[4] Sancarlos, A., Champaney, V., Cueto, E. and Chinesta, F. (2023) Regularized regressions for parametric models based on separated representations. Advanced Modeling and Simulation in Engineering Sciences 10:4

[5] Torregrosa, S., Champaney, V., Ammar, A., Herbert, V. and Chinesta, F. (2022) Surrogate parametric metamodel based on Optimal Transport. Mathematics and Computers in Simulation, 194, 36-63.

Sixth International Conference on Computational Methods for Energy and Thermal Problems
THERMAECOMP2024, Sept. 9-11, 2024, Budva, Montenegro
N. Massarotti, P. Nithiarasu, and I. Vušanović (Eds.)

UNDERGROUND COAL GASIFICATION

Hywel R Thomas

Swansea University, Bay Campus, Swansea, thomashr@cardiff.ac.uk

Sivachidambaram Sadasivam, Maram Almolliyeh, Wu Gao, and Shakil Masum

Cardiff University, School of Engineering, sadasivams@cardiff.ac.uk, and m.almolliyeh@gmail.com

ABSTRACT

This paper investigates the topic of "underground coal gasification" (UCG), with a particular emphasis on a modelling approach developed by the team to describe the process. Geoenvironmental considerations serve as the driving force behind the research, allowing any environmental concerns to be addressed more thoroughly. The lecture will begin with an overview of the subject so that the necessary background information can be presented. The new modelling approach will then be described in detail, followed by a discussion of the results within the context of a European Union project that funded the research. Finally, conclusions drawn from the work will be highlighted.

Key Words: *Underground Coal Gasification (UCG), Modelling Approach, Geoenvironmental Considerations.*

1. INTRODUCTION

Undoubtedly, coal is a significant fossil fuel. Coal is estimated to account for approximately 25% of global energy consumption, with an estimated 18 trillion tonnes of coal in existence [1]. Regrettably, it is estimated that less than one-sixth of coal is economically accessible. Furthermore, the conventional utilisation of coal has resulted in an insufficient amount of environmental damage. For instance, coal and gas-fired power plants generate over 2.3 billion metric tonnes of carbon pollution annually, which constitutes approximately 40% of the total energy-related carbon pollution in the United States [2]. Coal has been associated with pollution. The coal plants generate millions of tonnes of coal ash pollution annually, which is a toxic byproduct that remains after the coal is burned. Burning coal releases toxic mercury that is deposited into rivers and streams. Nevertheless, the abundance of unexploited coal is undoubtedly a significant temptation. Is there a sustainable method of utilising coal?

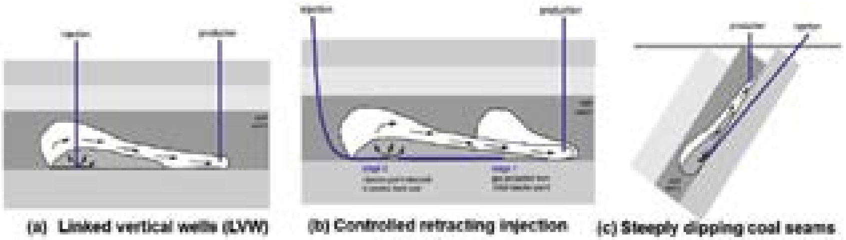

(a) Linked vertical wells (LVW) (b) Controlled retracting injection point (CRIP) (c) Steeply dipping coal seams (Perkins, 2018)

Step 1: Well drilling and link establishment Step 2: Coal seam ignition and commencement of gasification Step 3: Site clean-up by flushing with steam and water to remove potential contaminants

FIGURE 1. Various techniques of UCG.

Underground coal gasification (UCG) might be part of the answer. Compared to conventional mining, the advantages of UCG are self-evident. Without the need of mining, the solid coal can be turned into a mixture of gases in-situ [3]. Various types of UCG techniques are shown in Figure 1. Various methods were suggested to conduct UCG in a variety of strata conditions and coal quality; a) In coals that are relatively shallow and of low rank, linked vertical wells were determined to be a dependable method, b) The controlled retracting injection point method enables operators to relocate the injection location at the surface, thereby enabling a staged access to the coal seam, and c) The third method is appropriate for coal seams that dip at significant angles, and it has been demonstrated that the gas quality is exceptional [4].

Research into this solution has been carried out worldwide. One example, on which this talk is based, is a project funded by the European Fund for Coall and Steel, named: "Unconventional MEthane Production from Deep European Coal Seams through combined Coal Bed Methane (CBM) and Underground Coal GAsification (UCG) technologies" with the code name MEGA +.

2. DESCRIPTION OF PHYSICO/CHEMICAL PROCESS.

UCG is a complex multiphysics coupling problem (Figure 2a & b). Five processes are involved, including flow transfer, deformation, and a series of chemical reactions. Geochemical reactions in coal are at the heart of UCG because they provide the driving force for the entire process and influence flow transfer and deformation. Flow transfer and deformation, in turn, have an effect on chemical kinetics. The other processes are also connected. These will be discussed in detail during the talk.

The geological and hydrogeologic environment in which an in-situ gasification plant operates has a significant impact on its performance. UCG operations can have an impact on the air, surface soil, surface waters, underground rocks, and groundwater. In general, UCG poses environmental risks such as underground water pollution, gas emissions, and surface subsidence. The research was motivated by a desire to improve understanding of these aspects.

The work describes coal gasification using a three-stage model: In the first stage, wet coal is dried at around 100 °C, transforming it into dry coal and evaporating moisture. When the temperature rises to around 400 °C, dry coal is decomposed into char, tar, and volatiles: the 'pyrolysis of coal'. In the third stage, a series of reactions occur between the char and various gases. The main gases we considered were O_2, CO, CH_4, H_2, H_2O, and CO_2. Flow transfer and mass change occur simultaneously. Under the high temperature and intense chemical reactions in a UCG reactor, coal undergoes distinct structural changes (Figure 2C).

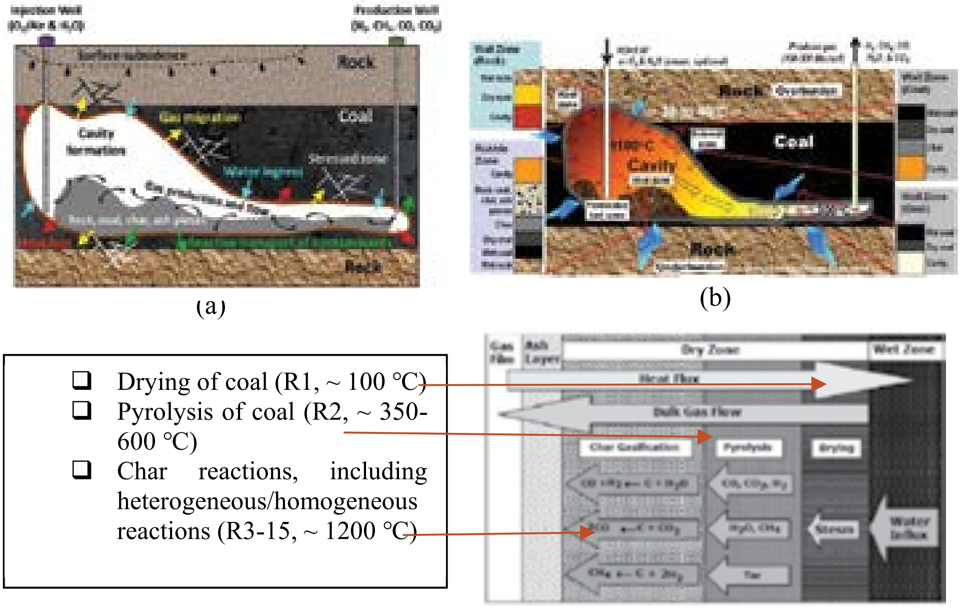

(a)

(b)

- ☐ Drying of coal (R1, ~ 100 °C)
- ☐ Pyrolysis of coal (R2, ~ 350-600 °C)
- ☐ Char reactions, including heterogeneous/homogeneous reactions (R3-15, ~ 1200 °C)

(c)

FIGURE 2. Physico-chemical process of UCG [5].

3.MODELLING APPROACH EMPLOYED.

A model for "Simulation of UCG based on a coupled thermal-hydraulic-chemical model" is developed in detail. Explaining cavity growth, temperature transfer, and syngas production is the main goal. See Figure 3 for a model development overview. Heat transfer, multi-component gas/mass transfer, and chemical reactions govern. Properties like porosity, permeability, thermal conductivity, and heat capacity are accommodated.

The in-house simulation software (COMPASS) analyses flow and deformation "step by step." Temperature (T), moisture (TH), air (THA), and mechanical (TMM) theoretical formulations were developed simultaneously. THM includes biological and microbiological processes like THCBM and chemical processes like HC, THC, and THCM.

COMPASS discretises governing equations spatially using finite elements and temporally using implicit mid-interval finite differences. COMPASS finds the transport equations converged primary variables. CANTERA calculates sink/source terms to update converged primary variables. A sequential non-iterative approach updates the converged primary variables using sink/source terms calculated by CANTERA.

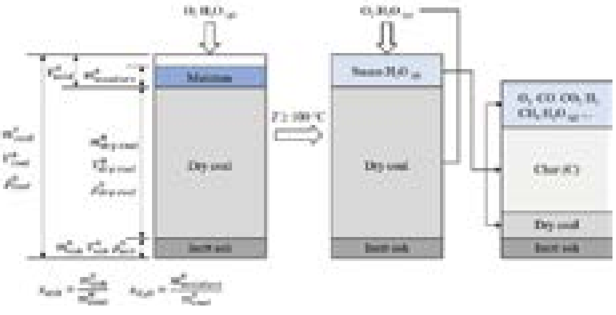

FIGURE 3. Schematic of domain structure, component and phase change of UCG (Gao et al., 2021[6]).

3.RESULTS

The experiments conducted by Prabu and Jayanti [2, 7-9] and Stańczyk et al. (2011) were in the THC model to simulate results. The experiment's two-dimensional geometry and mesh were divided into two porous zones: coal blocks and the gasification channel. The boundary and initial conditions were determined using experimental information and literature data. The temperature, dry coal, and char concentration distributions at the end of the simulation showed a teardrop-shaped temperature contour with a high-temperature core. The char distribution can be used to determine fierce heterogeneous reactions that occurred near the high-temperature core, which corresponds to temperature distributions.

The porosity distribution at the end of the simulation was estimated using porosity values, and an L-shaped cavity was created by treating the porosity of at least 0.6 as a cavity. The weight loss data showed that coal lost 30% of its original weight when the temperature reached 1578 K, specifically in the third hour, and the remaining 70% was consumed in 8 hours at a temperature no lower than 1320 K. As expected, the porosity and permeability of coal increased significantly during the UCG process.

A coupled flow-geomechanical model was used to investigate ground deformation during UCG using the stress-strain relationship for isotropic and homogeneous geologic materials, such as coal seams and surrounding strata. The stress-strain relationship for isotropic and homogeneous geologic materials is given by the equation below, while thermal expansion and contraction are also assumed to be isotropic. Heat conduction is assumed to be the primary mechanism for heat transfer in geologic materials, while pore gas and pore water flow are not considered.
After 20 days of simulation, the figure depicts the base case distributions of temperature, dry coal centration, char centration, and the corresponding cavity when porosity is at least 0.6. The highest temperature was around 1690 K near the injection well, and a temperature front of up to 1200 K reached the production well due to the rapid transport of heat along the horizontal gasification channel. The generated syngas was primarily composed of CO_2, CO, and CH_4, but the concentrations of H_2 and O_2 were extremely low. The positive vertical displacement, or heave, in the range of 1.8-2.95 cm at the top of the

caprock can be seen by varying the initial thermal expansion coefficient. Few exemplary results obtained from the work are presented in Figure 4 and 5.

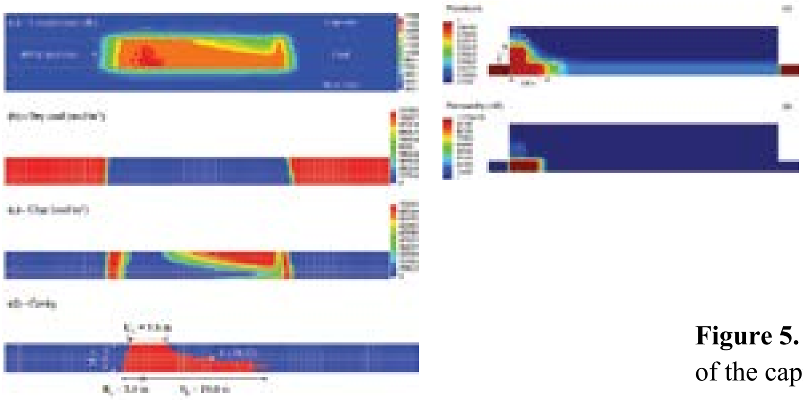

Figure 4. Distributions of (a) temperature, (b) dry coal concentration, (c) char concentration, (d) porosity, and (e) permeability at the end of simulation.

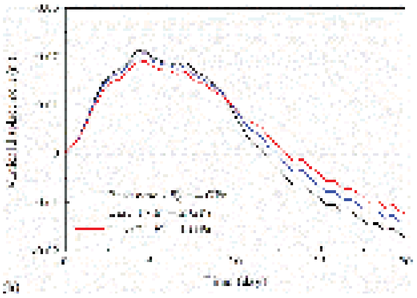

Figure 5. Vertical displacement at the top of the caprock after 20 days of simulation.

4. CONCLUSIONS

The laboratory and modeling studies conducted provide valuable insights into the underground coal gasification (UCG) process and its associated thermal and mechanical effects. The experimental borehole combustion by Prabu and Jayanti demonstrated the formation of a cavity and temperature distribution, which were crucial for understanding the pyrolysis and gasification reactions within the coal block. The simulation studies based on this experiment successfully captured the temperature and cavity formation, showing good agreement with the experimental data, particularly in the vertical direction. The modeling also highlighted the relationship between temperature, porosity, and permeability changes during UCG, revealing significant increases in both porosity and permeability, which are key to effective gasification. The coupled flow-geomechanical model further explored ground deformation, showing that thermal expansion and cavity evolution can cause vertical displacement in the caprock, with variations depending on material properties. These findings collectively advance our understanding of UCG dynamics.

REFERENCES

1. Couch, G.R. and I.C.R.C.C. Centre, *Underground Coal Gasification*. 2009: IEA Clean Coal Centre.
2. Amoco, B., *Statistical Review of World Energy*. 2002: BP Amoco.
3. Bhutto, A.W., A.A. Bazmi, and G. Zahedi, *Underground coal gasification: From fundamentals to applications.* Progress in Energy and Combustion Science, 2013. **39**(1): p. 189-214.
4. Perkins, G., *Underground coal gasification – Part I: Field demonstrations and process performance.* Progress in Energy and Combustion Science, 2018. **67**: p. 158-187.
5. Perkins, G., *Underground coal gasification – Part II: Fundamental phenomena and modeling.* Progress in Energy and Combustion Science, 2018. **67**: p. 234-274.
6. Gao, W., R. Zagorščak, and H.R. Thomas, *Insights into solid-gas conversion and cavity growth during Underground Coal Gasification (UCG) through Thermo-Hydraulic-Chemical (THC) modelling.* International Journal of Coal Geology, 2021. **237**: p. 103711.
7. Prabu, V. and S. Jayanti, *Heat-affected zone analysis of high ash coals during ex situ experimental simulation of underground coal gasification.* Fuel, 2014. **123**: p. 167-174.
8. Prabu, V. and S. Jayanti, *Laboratory scale studies on simulated underground coal gasification of high ash coals for carbon-neutral power generation.* Energy, 2012. **46**(1): p. 351-358.
9. Prabu, V. and S. Jayanti, *Simulation of cavity formation in underground coal gasification using bore hole combustion experiments.* Energy, 2011. **36**(10): p. 5854-5864.

Sixth International Conference on Computational Methods for Energy and Thermal Problems
THERMAECOMP2024, Sept. 9-11, 2024, Budva, Montenegro
N. Massarotti, P. Nithiarasu, and I. Vušanović (Eds.)

NONLINEAR TRANSPORT PHENOMENA ANALYSIS WITH INTEGRAL TRANSFORMS AND IMPLICIT FILTERING: APPLICATION TO MEMBRANE MEDIATED PROCESSES

Renato M. Cotta[1,2], Kleber M. Lisboa[3], João N.N. Quaresma[4],
Carolina P. Naveira-Cotta[1], Simone A. Cardoso[4], Emanuel N. Macedo[4],
[1]LabMEMS, Mech. Eng. Dept., POLI/COPPE, Federal University of Rio de Janeiro, RJ, Brazil
[2]Navy Research Institute, IPqM-CTMRJ, DGDNTM, Brazilian Navy, Rio de Janeiro, RJ, Brazil
[3]LATERMO, Mechanical Eng. Dept., TEM/PGMEC, Fluminense Federal University, RJ, Brazil
[4]Chemical Eng. Department, Institute of Technology, Federal University of Pará, Belém, PA, Brazil
cotta@mecanica.coppe.ufrj.br

ABSTRACT

Computational heat and fluid flow deals with nonlinearities in various forms, such as in nonlinear physical properties, nonlinear convective terms, including boundary layer and Navier-Stokes formulations, phase change moving boundaries, reaction or dissipation terms, and nonlinear source terms. Despite the vast accumulated knowledge on the traditional discrete simulation tools, they tend to be costly and eventually prohibitive when accuracy and its control is at a premium and intensive computations are required, such as in inverse problem analysis, design optimization, machine learning, simulation under uncertainty, and other highly demanding CPU processes. The present lecture reviews a well-established hybrid numerical-analytical approach known as the Generalized Integral Transform Technique (GITT), for all such classes of nonlinearity in transport phenomena formulations. Emphasis is given to the description of an implicit filtering solution strategy, which results in significant convergence enhancement and precision gain in dealing with nonlinear convection-diffusion problems. Two applications dealing with heat and mass transfer processes through membranes are more closely considered, associated with water desalination through vacuum-enhanced air gap membrane distillation and metals extraction with supported liquid membranes.

Key Words: *Nonlinear Problem, Hybrid Methods, Integral Transforms, Implicit Filtering, Water Desalination, Membrane Distillation, Metals Extraction, Supported Liquid Membranes.*

1. INTRODUCTION

Phenomenological computer simulation in engineering and physical sciences has been a continuously growing research front since the advent of the digital computer, further stimulated in recent years by the increase in computational power availability and the revived interest in artificial intelligence applications, combining simulation and real-world data. The well-balanced combination of data-based and physics-informed prediction tools have been offering new avenues for modern engineering analysis. While traditional numerical methods are very mature in different fields, including transport phenomena, there is always the drive to seek more robust, precise, and cost-effective algorithms especially in computationally intensive computations. In this context, alternative hybrid numerical-analytical approaches have been proposed along the last few decades and adopted either as benchmark tools or simulation algorithm alternatives. The present lecture is aimed at reviewing one such hybrid numerical-analytical methodology in transport phenomena simulation, known as the Generalized Integral Transform Technique (GITT).

The Classical Integral Transform Method has been consolidated in the treatise of Mikhailov and Ozisik [1] for the solution of linear transformable diffusion problems and it is a valuable tool in obtaining exact solutions to different classes of problems. The generalization to non-transformable problems was originally dealt with in [2,3], first in the context of approximate analytical solutions, and later on extended to a complete hybrid numerical-analytical treatment [4,5], numerically handling the associated coupled ordinary differential system of transformed potentials. The extension of this integral transformation concept to nonlinear problems was proposed in [6] and in the following years it was rapidly disseminated in the treatment of different classes of nonlinear problems, including nonlinear physical properties, convective terms, nonlinear boundary conditions, moving boundary problems, boundary layer, and Navier-Stokes formulations. Such developments were then systematically presented in different review and reference works [7-10]. In a natural development sequence, efforts were then directed to the computational enhancement of the hybrid methodology, including convergence improvement approaches such as analytical filtering, non-classical eigenvalue problems, and *a priori* and *a posteriori* eigenfunction expansion modification. More recent reviews have consolidated these developments on the computational aspects of the methodology [11-15].

Among recent advancements in hybrid integral transforms for nonlinear problems, two approaches should be pointed out, which can be invoked independently or jointly. First, the adoption of nonlinear eigenvalue problems [16-18], in particular for nonlinear boundary conditions, has been shown to be quite beneficial in terms of convergence enhancement, though the solution complexity might increase significantly when considering nonlinearities in the eigenvalue problem equation itself, requiring the simultaneous numerical solution of a nonlinear algebraic eigenvalue problem and of the nonlinear transformed ODE system. Second, and most important in the present context, nonlinear implicit filters can effectively eliminate boundary and, partially, equation nonlinear source terms. Though this feature has been used in different applications before [19-22], a unified formalism for the proposition of implicit filtering to nonlinear problems had not yet been presented. The main goal of filtering is reducing the importance of source terms, which have a direct impact on convergence rates. For nonlinear problems, traditional filtering implies the proposition of filter formulations that require some sort of linearization of the source terms, which may have a limited filtering effect in a certain time range. For this reason, implicit filtering appears as an interesting alternative, by fully accounting for the nonlinear source terms in either or both the boundary conditions and original equation and yields a more effective filtering enhancement. However, the filter itself also needs to be solved simultaneously with the transformed potentials of the original problem, as discussed in what follows.

In addition, the present review provides examples of filtering strategies in heat and mass transfer applications mediated by membranes, more specifically in the analysis of water desalination via vacuum-enhanced air gap membrane distillation and in the analysis of metals extraction through supported liquid membranes. The selected examples offer a clear demonstration of the relative merits of employing the hybrid integral transform methodology and the filtering strategy.

2. ANALYSIS

2.1. Formal Solution

Consider a nonlinear convection-diffusion problem for M coupled potentials, $T_k(\mathbf{x},t)$, k=1,2,...M, eventually including nonlinear convective terms already incorporated into the nonlinear coupling source terms, $P_k(\mathbf{x},t,\mathbf{T})$:

$$w_k(\mathbf{x},t,T_k)\frac{\partial T_k(\mathbf{x},t)}{\partial t} = \nabla.K_k(\mathbf{x},t,T_k)\nabla T_k - d_k(\mathbf{x},t,T_k)T_k + P_k(\mathbf{x},t,\mathbf{T}), \text{ in } \mathbf{x}\in V,\ t>0,\ k=1,2,...M \quad (1a)$$

with initial and boundary conditions written as

$$T_k(\mathbf{x},0) = f_k(\mathbf{x}), \qquad \mathbf{x}\in V \quad (1b)$$

$$\alpha_k(\mathbf{x},t,T_k)\ T_k(\mathbf{x},t)+\beta_k(\mathbf{x},t,T_k)\ K_k(\mathbf{x},t,T_k)\ \frac{\partial T_k}{\partial \mathbf{n}}=\phi_k(\mathbf{x},t,\mathbf{T})\ , \quad \mathbf{x}\in S\ ,\ \mathrm{t}>0 \tag{1c}$$

where w, K, and d are nonlinear equation coefficients, while α and β are nonlinear boundary condition coefficients, $\mathbf{n}$ is the outward drawn normal vector to surface S, and $\phi_k(\mathbf{x},t,\mathbf{T})$ are the nonlinear coupling boundary source terms. The nonlinear equation and boundary condition coefficients were here written as functions of the single potential $T_k(\mathbf{x},t)$ only, while the equation and boundary source terms are written in terms of the whole vector of potentials, $\mathbf{T}$, thus coupling the various balance equations and potentials. In spite of that, this formulation is fairly general, once any missing term can be incorporated into the equation and boundary source terms, $P_k(\mathbf{x},t,\mathbf{T})$ and $\phi_k(\mathbf{x},t,\mathbf{T})$.

The formal solution of the nonlinear problem (1) through the GITT involves the selection of a linear eigenvalue problem, which offers the basis for the eigenfunction expansion that represents the potential, as first proposed in [6]. This is in fact equivalent to rewriting problem (1) with characteristic linear coefficients that have only $\mathbf{x}$ dependence, i.e., $w^*(\mathbf{x})$, $K^*(\mathbf{x})$, $d^*(\mathbf{x})$, $\alpha^*(\mathbf{x})$, and $\beta^*(\mathbf{x})$, while the modified nonlinear source terms then incorporate the remaining nonlinear portions of the equation and boundary conditions operators, already including nonlinear convection terms, in the form:

$$w_k^*(\mathbf{x})\frac{\partial T_k(\mathbf{x},t)}{\partial t}=\nabla.K_k^*(\mathbf{x})\nabla T_k-d_k^*(\mathbf{x})T_k+P_k^*(\mathbf{x},t,\mathbf{T})\ , \quad \text{in } \mathbf{x}\in V,\ t>0,\ k=1,2,...M \tag{2a}$$

with initial and boundary conditions given by

$$T_k(\mathbf{x},0)=f_k(\mathbf{x})\ , \quad \mathbf{x}\in V \tag{2b}$$

$$\alpha_k^*(\mathbf{x})\ T_k(\mathbf{x},t)+\beta_k^*(\mathbf{x})\ K_k^*(\mathbf{x})\ \frac{\partial T_k}{\partial \mathbf{n}}=\phi_k^*(\mathbf{x},t,\mathbf{T})\ , \quad \mathbf{x}\in S\ ,\ \mathrm{t}>0 \tag{2c}$$

where the nonlinear source terms are now given by

$$\begin{aligned}P_k^*(\mathbf{x},t,\mathbf{T})=P_k(\mathbf{x},t,\mathbf{T})\ &-[w_k(\mathbf{x},t,T_k)-w_k^*(\mathbf{x})]\frac{\partial T_k(\mathbf{x},t)}{\partial t}+\\ &+\nabla.[K_k(\mathbf{x},t,T_k)-K_k^*(\mathbf{x})]\nabla T_k-[d_k(\mathbf{x},t,T_k)-d_k^*(\mathbf{x})]T_k\end{aligned} \tag{2d}$$

$$\phi_k^*(\mathbf{x},t,\mathbf{T})=\phi_k(\mathbf{x},t,\mathbf{T})-[\alpha_k(\mathbf{x},t,T_k)-\alpha_k^*(\mathbf{x})]\ T_k(\mathbf{x},t)-[\beta_k(\mathbf{x},t,T_k)K_k(\mathbf{x},t,T_k)-\beta_k^*(\mathbf{x})\ K_k^*(\mathbf{x})\ ]\ \frac{\partial T_k}{\partial \mathbf{n}} \tag{2e}$$

The following formal GITT solution is documented in previous works [6-15], and therefore is just briefly described here. The chosen characteristic $\mathbf{x}$-dependent coefficients that appear in eqs. (2) already represent the linear eigenvalue problem to be chosen, written as:

$$\nabla.K_k^*(\mathbf{x})\nabla\psi_{k,i}(\mathbf{x})+\left[\mu_{k,i}^2 w_k^*(\mathbf{x})-\ d_k^*(\mathbf{x})\right]\psi_{k,i}(\mathbf{x})=0\ ,\ \mathbf{x}\in V \tag{3a}$$

with boundary conditions

$$\alpha_k^*(\mathbf{x})\psi_{k,i}(\mathbf{x})+\beta_k^*(\mathbf{x})K_k^*(\mathbf{x})\frac{\partial\psi_{k,i}(\mathbf{x})}{\partial\mathbf{n}}=0,\ \mathbf{x}\in S \tag{3b}$$

The integral transform pair is then defined from problem (3):

$$\bar{T}_{k,i}(t)=\int_V w_k^*(\mathbf{x})\psi_{k,i}(\mathbf{x})T_k(\mathbf{x},t)\,dv\ , \qquad \text{transform} \tag{4a}$$

$$T_k(\mathbf{x},t)=\sum_{i=1}^{\infty}\frac{1}{N_{k,i}}\psi_{k,i}(\mathbf{x})\bar{T}_{k,i}(t)\ , \qquad \text{inverse} \tag{4b}$$

with the normalization integrals

$$N_{k,i}=\int_V w_k^*(\mathbf{x})\psi_{k,i}^2(\mathbf{x})\ dv \tag{4c}$$

Application of the integral transformation procedure over eq. (3a) through the operator $\int_V(-)\psi_{k,i}(\mathbf{x})\ dv$, leads to the ordinary differential system for the transformed potentials, $\bar{T}_{k,i}(t)$, written as:

$$\frac{d\bar{T}_{k,i}(t)}{dt}+\mu_{k,i}^2\bar{T}_{k,i}(t)=\bar{g}_{k,i}(t,\bar{\mathbf{T}}),\ \ t>0,\ k=1,2,...M,\ i=1,2... \tag{5a}$$

with initial conditions

$$\bar{T}_{k,i}(0)=\bar{f}_{k,i} \tag{5b}$$

where,

$$\bar{g}_{k,i}(t,\bar{\mathbf{T}})=\int_V\psi_{k,i}(\mathbf{x})P_k^*(\mathbf{x},t,\mathbf{T})\ dv+\int_S\phi_k^*(\mathbf{x},t,\mathbf{T})\left(\frac{\psi_{k,i}(\mathbf{x})\ -K_k^*(\mathbf{x})\dfrac{\partial\psi_{k,i}}{\partial\mathbf{n}}}{\alpha_k^*(\mathbf{x})+\beta_k^*(\mathbf{x})}\right)ds \tag{5c}$$

$$\bar{f}_{k,i}=\int_V w_k^*(\mathbf{x})\ \psi_{k,i}(\mathbf{x})f_k(\mathbf{x})\ dv \tag{5d}$$

The nonlinear initial value problem (5) is then numerically solved with automatic accuracy control through available routines in either public domain or scientific subroutines libraries, as well as in symbolic-numerical computation packages. After numerically computing the transformed potentials along the *t*-variable, the inverse formula recovers the original potentials.

2.2. Nonlinear Eigenvalue Problem

A new formalism was proposed in [16] based on a nonlinear eigenvalue problem choice, by carrying along to the eigenfunction expansion base, the nonlinear original problem coefficients and operators. Thus, considering the original formulation here under analysis, Eqs. (1), the following general nonlinear eigenvalue problem can be adopted:

$$\nabla.K_k(\mathbf{x},t,T_k)\nabla\psi_{k,i}(\mathbf{x};t)+\left[\mu_{k,i}^2(t)w_k(\mathbf{x},t,T_k)-d_k(\mathbf{x},t,T_k)\right]\psi_{k,i}(\mathbf{x};t)=0,\mathbf{x}\in V \tag{6a}$$

with boundary conditions

$$\alpha_k(\mathbf{x},t,T_k)\psi_{k,i}(\mathbf{x};t)+\beta_k(\mathbf{x},t,T_k)K_k(\mathbf{x},t,T_k)\frac{\partial\psi_{k,i}(\mathbf{x};t)}{\partial\mathbf{n}}=0,\ \ \mathbf{x}\in S \tag{6b}$$

Thus, the following integral transform pair is defined from problem (6):

$$\bar{T}_{k,i}(t)=\int_V w_k(\mathbf{x},t,T)\ \psi_{k,i}(\mathbf{x};t)T_k(\mathbf{x},t)\ dv, \qquad \text{transform} \tag{7a}$$

$$T_k(\mathbf{x},t)=\sum_{i=1}^{\infty}\frac{1}{N_{k,i}(t)}\psi_{k,i}(\mathbf{x};t)\bar{T}_{k,i}(t), \qquad \text{inverse} \tag{7b}$$

with the normalization integral

$$N_{k,i}(t) = \int_V w_k(\mathbf{x},t,T_k)\psi_{k,i}^2(\mathbf{x};t)\, dv \tag{7c}$$

After application of the integral transformation procedure through the operator $\int_V (-)\psi_{k,i}(\mathbf{x};t)dv$, the resulting ODE system for the transformed potentials, $\bar{T}_{k,i}(t)$, is written as:

$$\frac{d\bar{T}_{k,i}(t)}{dt} + \sum_{j=1}^{\infty} E_{k,i,j}(t,\bar{\mathbf{T}})\bar{T}_{k,j}(t) = \bar{g}_{k,i}(t,\bar{\mathbf{T}}),\ t>0,\ k=1,2,...,M,\ i=1,2,\dots \tag{8a}$$

with initial conditions

$$\bar{T}_{k,i}(0) = \bar{f}_{k,i} \tag{8b}$$

where,

$$E_{k,i,j}(t,\bar{\mathbf{T}}) = \delta_{ij}\mu_{k,i}^2(t) - \frac{1}{N_{k,j}(t)}\int_V \frac{\partial}{\partial t}[w_k(\mathbf{x},t,T_k)\psi_{k,i}(\mathbf{x};t)]\psi_{k,j}(\mathbf{x};t)dv \tag{8c}$$

$$\bar{g}_{k,i}(t,\bar{\mathbf{T}}) = \int_V \psi_{k,i}(\mathbf{x};t)P_k(\mathbf{x},t,\mathbf{T})\, dv + \int_S \phi_k(\mathbf{x},t,\mathbf{T}) \left(\frac{\psi_{k,i}(\mathbf{x};t) - K_k(\mathbf{x},t,T_k)\dfrac{\partial \psi_{k,i}}{\partial \mathbf{n}}}{\alpha_k(\mathbf{x},t,T_k) + \beta_k(\mathbf{x},t,T_k)} \right) ds \tag{8d}$$

$$\bar{f}_{k,i} = \int_V w_k[\mathbf{x},0,T_k(\mathbf{x},0)]\psi_{k,i}(\mathbf{x};0)f_k(\mathbf{x})dv \tag{8e}$$

This more involved approach has been shown to result in improved convergence rates [16-18]. On the other hand, it has the drawback of requiring that the eigenvalue problem be solved simultaneously with the transformed ODE system, yielding coupled time-dependent transformed potentials, eigenvalues, and eigenfunctions. The GITT solution of the nonlinear eigenvalue problem (6) has also been discussed in [16] by considering an auxiliary linear eigenvalue problem of known solution, leading to a nonlinear algebraic eigenvalue problem that needs to be solved simultaneously with the ODE system.

2.3. Nonlinear Implicit Filtering

The formal solutions shown above are the basic working expressions for the integral transform approach, either adopting a linear or a nonlinear eigenvalue problem. In either case, for an improved computational performance, it is suggested to reduce the importance of the equation and boundary source terms, thus improving the eigenfunction expansions convergence rates. For instance, one may propose analytical filtering solutions, which partially remove information from the original nonlinear source terms, while retaining a desirably simple analytical expression. Any filter, either explicit or implicit, is proposed in general form as [19]:

$$T_k(\mathbf{x},t) = T_k^*(\mathbf{x},t) + T_{k,f}(\mathbf{x};t) \tag{9}$$

where the filter solution proposition, $T_{k,f}(\mathbf{x};t)$, is usually obtained as an explicit analytical filter that satisfies representative linearized versions of the original boundary and/or equation source terms. In addition, multi-pass filters can be implemented by re-filtering the filtered potential, generating a sequence towards improved convergence [20].

Eventually, a nonlinear implicit filter proposal is required, for instance, to make the boundary conditions (1c) homogeneous, even in the presence of nonlinear boundary source terms [19-21]. The simplest implicit filter formulation would then just satisfy the original nonlinear boundary conditions, while a more complete filtering strategy, and thus more involved, would also partially filter the original nonlinear equation source term. In this more general sense, the implicit filter problem could be formulated as:

$$\nabla.K_k^*(\mathbf{x})\nabla T_{k,f} - d_k^*(\mathbf{x})T_{k,f} + P_k^*(\mathbf{x},t,\mathbf{T}) = 0, \quad \text{in } \mathbf{x}\in V,\ t>0,\ k\text{=}1,2,...M \tag{10a}$$

with boundary conditions given by

$$\alpha_k^*(\mathbf{x})\ T_{k,f} + \beta_k^*(\mathbf{x})\ K_k^*(\mathbf{x})\ \frac{\partial T_{k,f}}{\partial \mathbf{n}} = \phi_k^*(\mathbf{x},t,\mathbf{T})\ , \quad \mathbf{x}\in S\ ,\ \mathrm{t}>0 \tag{10b}$$

In both source terms, the coupling potentials vector is present, which also couples the solution of the filter with the filtered potential itself, and for this reason is called an implicit filter. Then, the filtered problem is written as:

$$w_k^*(\mathbf{x})\frac{\partial T_k^*(\mathbf{x},t)}{\partial t} = \nabla.K_k^*(\mathbf{x})\nabla T_k^* - d_k^*(\mathbf{x})T_k^* + P_k^{**}(\mathbf{x},t,\mathbf{T})\ , \quad \text{in } \mathbf{x}\in V,\ t>0, k\text{=}1,2,...M \tag{11a}$$

with initial and boundary conditions given by

$$T_k^*(\mathbf{x},0) = f_k^*(\mathbf{x}) \equiv f_k(\mathbf{x}) - T_{k,f}(\mathbf{x};0), \quad \mathbf{x}\in V \tag{11b}$$

$$\alpha_k^*(\mathbf{x})\ T_k^*(\mathbf{x},t) + \beta_k^*(\mathbf{x})\ K_k^*(\mathbf{x})\ \frac{\partial T_k^*}{\partial \mathbf{n}} = 0\ , \quad \mathbf{x}\in S\ ,\ \mathrm{t}>0 \tag{11c}$$

where the nonlinear source terms of the filtered problem are now given by

$$P_k^{**}(\mathbf{x},t,\mathbf{T}) = -w_k^*(\mathbf{x})\frac{\partial T_{k,f}(\mathbf{x};t)}{\partial t} \tag{11d}$$

It can be noticed that the implicit filter defined with the original source terms makes the boundary conditions homogeneous and eliminates the original equation source term, but incorporates a new equation source term that is related to the transient behavior of the filter itself. It should also be pointed out that solving eqs.(10) with the full coupling equation source terms might not be so straightforward and it might be sufficient to choose a decoupling linearization of this source term, $P_{k,f}^*(\mathbf{x},t,T_{k,f})$ in the following form:

$$\nabla.K_k^*(\mathbf{x})\nabla T_{k,f} - d_k^*(\mathbf{x})T_{k,f} + P_{k,f}^*(\mathbf{x},t,T_{k,f}) = 0, \quad \text{in } \mathbf{x}\in V,\ t>0,\ k\text{=}1,2,...M \tag{12a}$$

Then, the filtered problem source term becomes:

$$P_k^{**}(\mathbf{x},t,\mathbf{T}) = P_k^*(\mathbf{x},t,\mathbf{T}) - P_{k,f}^*(\mathbf{x},t,T_{k,f}) - w_k^*(\mathbf{x})\frac{\partial T_{k,f}(\mathbf{x};t)}{\partial t} \tag{12b}$$

while the filter problem boundary conditions still account for the full nonlinear source term, eq.(10b), and the filtered problem boundary source terms would still be eliminated. The filter problem eq.(10a) can be further simplified or even disregarded so that the filter becomes only an algebraic expression to satisfy the nonlinear boundary conditions [21,22]. In this case, the general form of the filtered problem source term can be recalled, given by:

$$P_k^{**}(\mathbf{x},t,\mathbf{T}) = P_k^*(\mathbf{x},t,\mathbf{T}) + \nabla.[K_k^*(\mathbf{x})]\nabla T_{k,f} - d_k^*(\mathbf{x})T_{k,f} - w_k^*(\mathbf{x})\frac{\partial T_{k,f}(\mathbf{x};t)}{\partial t} \tag{12c}$$

In multidimensional problems, the concept of a progressive filtering scheme [22] may be recalled, by transforming in each spatial direction successively until all spatial directions have been transformed.

3. TEST CASES

Two applications are now considered that illustrate the use of filtering strategies to enhance the convergence behavior of the eigenfunction expansions in the GITT solution of nonlinear heat and mass transfer problems. The first test case deals with water desalination using membrane distillation, a hybrid thermal-membrane process that is becoming more popular in recent years, in association with the reutilization of recovered waste heat in other processes. Here, the configuration analyzed involves an air gap (vacuum enhanced) and a condensing cold plate (V-AGMD – Vacuum-enhanced Air Gap Membrane Distillation). The second test case refers to the extraction of metals through supported liquid membranes (SLMs), in which the immobilized liquid is the actual membrane phase and a microporous polymeric film provides support for the membrane. A limited physical discussion of the two phenomena will be carried out in this review, since the focus is on the methodological improvement description and illustration, but the readers may find further information in the cited references.

3.1. Water Desalination by Vacuum-Enhanced Air Gap Membrane Distillation

Developed in the 1960s but only gaining traction with the development of new membranes in the 21st century, membrane distillation (MD) has been consolidating in the last two decades as an alternative to reverse osmosis (RO), multi-stage flash (MSF), and multi-effect distillation (MED) [23]. Its operating principle is based on the separation of two free surfaces formed by liquid water, kept apart by at least one hydrophobic membrane. By imposing a temperature difference between the two free surfaces, a vapor pressure gradient is formed and induces the migration of water vapor molecules from the hot surface to the cold one, where the vapor condenses. Its main advantages are the higher quality of the distilled water compared to that treated with RO, the ability to operate at relatively low pressures and temperatures [23], making it particularly suitable to be powered by renewable energy sources and waste heat recovery [24], besides the possibility of treating hypersaline waters, including RO reject [25].

The most studied MD configuration is direct contact membrane distillation (DCMD) [23], in which a permeate flow passes through the cold side of the membrane, where, in its pores, it forms a free surface where water condenses. Despite having simple construction and operation, the heat loss by conduction through the membrane is excessive, which significantly reduces its energy efficiency. On the other hand, air-gap membrane distillation (AGMD) interposes a humid air compartment and a cooling wall between the cold side of the membrane and a cold stream [26]. The water vapor contained in the compartment condenses on the wall when cooled by the cold stream, forming the free surface with which the one on the hot side of the membrane will carry out the water mass transfer. The air gap thermally insulates the hot stream, reducing conductive losses. Furthermore, if the hot stream is redirected after leaving the module to the cold-water channel, latent heat recovery can be performed within the module itself, without the need for dedicated equipment for this purpose. As a result, the energy efficiency of AGMD is typically higher than that of DCMD, although it has the side effect of reducing water productivity due to the additional resistance to vapor transport imposed by the presence of air [27]. However, this last disadvantage can be addressed with a variant of AGMD called vacuum-assisted air-gap membrane distillation (V-AGMD), in which a Venturi tube and the suction of the cooling pump are used to impose a pressure below atmospheric inside the air gap, intensifying water productivity [25].

In this context, this work solves, using GITT and implicit filters, the heat and mass transfer in a single envelope of a spiral-wound V-AGMD water desalination module. The analysis is carried out in a 2D parallel plates channel measuring $2a^*$ in height and L^* in length and bounded by hydrophobic membranes. Hot saline water enters this channel and undergoes heat and mass transfer across the membranes. Vapor transport is driven by a pressure difference between the saline feed and permeate. Given the minor influence of 3D and curvature effects in spiral-wound modules, a 2D model is considered sufficient.

3.1.1. Fluid flow

The dimensionless form of the flow equations in the laminar regime, assuming constant thermophysical properties, can be written as:

$$\frac{\partial u}{\partial x}+\frac{\partial v}{\partial y}=0 \tag{13a}$$

$$u\frac{\partial u}{\partial x}+v\frac{\partial u}{\partial y}=-\frac{\partial p}{\partial x}+\frac{\partial^2 u}{\partial y^2} \tag{13b}$$

$$u\frac{\partial v}{\partial x}+v\frac{\partial v}{\partial y}=-\mathrm{Re}_{a^*}^2\frac{\partial p}{\partial y}+\frac{\partial^2 v}{\partial y^2} \tag{13c}$$

with boundary conditions given by

$$u(0,y)=u_0(y)=\frac{3}{2}(1-y^2) \tag{13d}$$

$$\left.\frac{\partial u}{\partial y}\right|_{y=0}=0 \tag{13e}$$

$$v(x,0)=0 \tag{13f}$$

$$u(x,1)=0;\;\; v(x,1)=f(x) \tag{13g, h}$$

where u_0 is the dimensionless fully developed velocity profile for impermeable wall parallel plates channels and Re_{a^*} is the Reynolds number based on half the channel height.

A perturbation series built around a small parameter ε and the fully developed impermeable wall channel flow is developed in the form

$$u\cong u_0(y)+u_1(x,y)\varepsilon \tag{14a}$$

$$v\cong v_1(x,y)\varepsilon \tag{14b}$$

$$p\cong p_{in}-3x+p_1(x,y)\varepsilon \tag{14c}$$

where terms of order ε^2 or higher were neglected and p_{in} is the dimensionless pressure at the fluid inlet. Defining a perturbation streamfunction, ψ_1, as

$$u_1=\frac{\partial\psi_1}{\partial y} \tag{15a}$$

$$v_1=-\frac{\partial\psi_1}{\partial x} \tag{15b}$$

we then have

$$u_0\frac{\partial^3\psi_1}{\partial x\,\partial y^2}-\frac{\partial\psi_1}{\partial x}\frac{d^2u_0}{dy^2}=\frac{\partial^4\psi_1}{\partial y^4} \tag{16a}$$

with boundary conditions given by

$$\psi_1(0,y)=0 \tag{16b}$$

$$\psi_1(x,0)=0 \tag{16c}$$

$$\left.\frac{\partial^2 \psi_1}{\partial y^2}\right|_{y=0} = 0 \tag{16d}$$

$$\psi_1(x,1) = g(x) = -\frac{1}{\varepsilon}\int_0^x f(\xi)d\xi \tag{16e}$$

$$\left.\frac{\partial \psi_1}{\partial y}\right|_{y=1} = 0 \tag{16f}$$

3.1.2. Heat and Mass Transfer

The heat transfer model, in dimensionless form, can be written as

$$u\frac{\partial T}{\partial x} + v\frac{\partial T}{\partial y} = \frac{1}{\mathrm{Pr}}\frac{\partial^2 T}{\partial y^2} \tag{17a}$$

with boundary conditions given by

$$T(0,y) = 1 \tag{17b}$$

$$\left.\frac{\partial T}{\partial y}\right|_{y=0} = 0 \tag{17c}$$

$$-\left.\frac{\partial T}{\partial y}\right|_{y=1} = f(x)\frac{\mathrm{Pr}}{\mathrm{Ste}} + \sigma T(x,1) \tag{17d}$$

where Pr and Ste are respectively the Prandtl and Stefan numbers, and σ is the dimensionless thermal conductance of the membrane and air gap.

Finally, the dimensionless form of the mass transfer model is

$$u\frac{\partial w}{\partial x} + v\frac{\partial w}{\partial y} = \frac{1}{\mathrm{Sc}}\frac{\partial^2 w}{\partial y^2} \tag{18a}$$

with boundary conditions given by

$$w(0,y) = 1 \tag{18b}$$

$$\left.\frac{\partial w}{\partial y}\right|_{y=0} = 0 \tag{18c}$$

$$f(x)w(x,1) - \frac{1}{\mathrm{Sc}}\left.\frac{\partial w}{\partial y}\right|_{y=1} = 0 \tag{18d}$$

where w is the dimensionless mass fraction and Sc is the Schmidt number.

For air gap membrane distillation, the dimensionless form of the mass flux, f, is given by

$$f = B_{eq}(p_{mf} - p_c) \tag{19}$$

where B_{eq} is the dimensionless equivalent permeability of the membrane and air gap, and p_{mf} and p_c are the partial pressures of water at the hot side of the membrane and at the permeate free surface, respectively. The partial pressures may be determined using Antoine´s equation and the modified Raoult’s law [28].

3.1.3. Implicit filter

The perturbation streamfunction, temperature, and mass fraction can be decomposed into filter and filtered solutions in the following form:

$$\psi_1(x,y) = \psi_f(x,y) + \hat{\psi}(x,y) \tag{20a}$$

$$T(x,y) = T_f(x) + \hat{T}(x,y) \tag{20b}$$

$$w(x,y) = w_f(x,y) + \hat{w}(x,y) \tag{20c}$$

where the subscript f indicates the filter solution.

The filter solutions for the streamfunction, temperature, and mass fraction are determined as

$$\psi_f(x,y) = g(x)\left(\frac{3}{2}y - \frac{1}{2}y^3\right) \tag{21a}$$

$$T_f(x) = -\frac{f(x)}{\sigma}\frac{\mathrm{Pr}}{\mathrm{Ste}} \tag{21b}$$

$$w_f(x,y) = c(x)y^2 \tag{21c}$$

where $c(x)$ is restricted by

$$c(x) = \frac{\mathrm{Sc}}{2}f(x)w(x,1) \tag{21d}$$

3.1.4. Eigenvalue problems

A biharmonic eigenvalue problem is used for the perturbation streamfunction in the form

$$\frac{d^4\varphi_i}{dy^4} = \lambda_i^4\varphi_i(y) \tag{22a}$$

with boundary conditions given by

$$\varphi_i(0) = 0;\ \ \varphi_i''(0) = 0 \tag{22b, c}$$

$$\varphi_i(1) = 0;\ \ \varphi_i''(1) = 0 \tag{22d, e}$$

whose solution satisfies the following orthogonality property

$$\int_0^1 \varphi_i(y)\varphi_j(y)dy = \delta_{ij} \tag{22f}$$

For both the temperature and the mass fraction, Helmholtz-type eigenvalue problems are proposed as follows:

Temperature eigenvalue problem:

$$\frac{d^2\Omega_m}{dy^2} + \omega_m^2\Omega_m(y) = 0 \tag{23a}$$

with boundary conditions given by

$$\Omega_m''(0) = 0;\ \sigma\Omega_m(1) + \Omega_m'(1) = 0 \tag{23b, c}$$

and the following orthogonality property

$$\int_0^1 \Omega_m(y)\Omega_n(y)dy = N_{T,m}\delta_{mn} \tag{23d}$$

and normalization

$$\tilde{\Omega}(y) = \frac{\Omega_m(y)}{\sqrt{N_m}} \tag{23e}$$

Mass fraction eigenvalue problem:

$$\frac{d^2\Gamma_r}{dy^2} + \eta_r^2\Gamma_r(y) = 0 \tag{24a}$$

with boundary conditions given by

$$\Gamma_r'(0) = 0;\ \Gamma_r'(1) = 0 \tag{24b, c}$$

the following orthogonality property

$$\int_0^1 \Gamma_r(y)\Gamma_s(y)dy = N_{w,r}\delta_{rs} \tag{24d}$$

and normalization

$$\tilde{\Gamma}_r(y) = \frac{\Gamma_r(y)}{\sqrt{N_{w,r}}} \tag{24e}$$

3.1.5. Transformed problem

The orthogonality properties of the eigenfunctions ψ_i, Ω_m, and Γ_r allow for the establishment of the following transform-inverse pairs:

For the streamfunction:

$$\text{Transform: } \overline{\psi}_i(x) = \int_0^1 \varphi_i(y)\hat{\psi}(x,y)dy \tag{25a}$$

$$\text{Inverse: } \hat{\psi}(x,y) = \sum_{i=1}^{\infty} \overline{\psi}_i(x)\varphi_i(y) \tag{25b}$$

For the temperature:

$$\text{Transform: } \overline{T}_m(x) = \int_0^1 \tilde{\Omega}_m(y)\hat{T}(x,y)dy \tag{26a}$$

$$\text{Inverse: } \hat{T}(x,y) = \sum_{m=1}^{\infty} \overline{T}_m(x)\tilde{\Omega}_m(y) \tag{26b}$$

For the mass fraction:

$$\text{Transform: } \overline{w}_r(x) = \int_0^1 \tilde{\Gamma}_r(y)\hat{w}(x,y)dy \tag{27a}$$

$$\text{Inverse: } \hat{w}(x,y) = \sum_{r=1}^{\infty} \overline{w}_r(x)\tilde{\Gamma}_r(y) \tag{27b}$$

Employing the filter decompositions of eqs. (20.a-c) into the governing equations (16.a-g), (17.a-d), and (18.a-d), integral transforming them, and finally substituting eqs. (25.b), (26.b), and (27.b), yields

$$\sum_{j=1}^{\infty} A_{ij}\frac{d\overline{\psi}_i}{dx} + \overline{\gamma}_i(x) = \lambda_i^4\overline{\psi}_i(x),\ i = 1,2,3,\ldots \tag{28a}$$

$$\sum_{n=1}^{\infty}\sum_{j=1}^{\infty}\left(B_{mjn}\bar{\psi}_j\frac{d\bar{T}_n}{dx}+C_{mjn}\frac{d\bar{\psi}_j}{dx}\bar{T}_n\right)+\sum_{n=1}^{\infty}\left(E_{mn}\frac{d\bar{T}_n}{dx}+F_{mn}\bar{T}_n\right)+$$

$$\sum_{j=1}^{\infty}G_{mj}\bar{\psi}_j+\frac{\omega_m^2}{\mathrm{Pr}}\bar{T}_m(x)=\bar{\phi}_m(x), m=1,2,3,\dots \tag{28b}$$

$$\sum_{s=1}^{\infty}\sum_{j=1}^{\infty}\left(H_{rjs}\bar{\psi}_j\frac{d\bar{w}_s}{dx}+I_{rjs}\frac{d\bar{\psi}_j}{dx}\bar{w}_s\right)+\sum_{s=1}^{\infty}\left(J_{rs}\frac{d\bar{w}_s}{dx}+K_{rs}\bar{w}_s\right)+$$

$$\sum_{j=1}^{\infty}\left(O_{rj}\frac{d\bar{\psi}_j}{dx}+S_{rj}\bar{\psi}_j\right)+\frac{\eta_r^2}{\mathrm{Sc}}\bar{w}_r(x)=\bar{\zeta}_r(x), r=1,2,3,\dots \tag{28c}$$

with boundary conditions given by

$$\bar{\psi}_i(0)=0,\ i=1,2,3,\dots \tag{28d}$$

$$\bar{T}_m(0)=\beta_m, m=1,2,3,\dots \tag{28e}$$

$$\bar{w}_r(0)=\xi_r, r=1,2,3,\dots \tag{28f}$$

and integral coefficients given by

$$A_{ij}=\int_0^1\varphi_i(y)\left[u_0(y)\frac{d^2\varphi_j}{dy^2}-\frac{d^2u_0}{dy^2}\varphi_j(y)\right]dy \tag{28g}$$

$$B_{mjn}=\varepsilon\int_0^1\tilde{\Omega}_m(y)\frac{d\varphi_j}{dy}\tilde{\Omega}_n(y)dy \tag{28h}$$

$$C_{mjn}=-\varepsilon\int_0^1\tilde{\Omega}_m(y)\varphi_j(y)\frac{d\tilde{\Omega}_n}{dy}dy \tag{28i}$$

$$E_{mn}=\int_0^1\left[u_0(y)+\varepsilon\frac{\partial\psi_f}{\partial y}\right]\tilde{\Omega}_m(y)\tilde{\Omega}_n(y)dy \tag{28j}$$

$$F_{mn}=-\varepsilon\int_0^1\frac{\partial\psi_f}{\partial x}\tilde{\Omega}_m(y)\frac{d\tilde{\Omega}_n}{dy}dy \tag{28k}$$

$$G_{mj}=\varepsilon\int_0^1\frac{dT_f}{dx}\tilde{\Omega}_m(y)\frac{d\varphi_j}{dy}dy \tag{28l}$$

$$H_{rjs}=\varepsilon\int_0^1\tilde{\Gamma}_r(y)\frac{d\varphi_j}{dy}\tilde{\Gamma}_s(y)dy \tag{28m}$$

$$I_{rjs}=-\varepsilon\int_0^1\tilde{\Gamma}_r(y)\varphi_j(y)\frac{d\tilde{\Gamma}_s}{dy}dy \tag{28n}$$

$$J_{rs}=\int_0^1\left(u_0+\varepsilon\frac{\partial\psi_f}{\partial y}\right)\tilde{\Gamma}_r(y)\tilde{\Gamma}_s(y)dy \tag{28o}$$

$$K_{rs}=-\varepsilon\int_0^1\frac{\partial\psi_f}{\partial x}\tilde{\Gamma}_r(y)\frac{d\tilde{\Gamma}_s}{dy}dy \tag{28p}$$

$$O_{rj}=-\varepsilon\int_0^1\frac{\partial w_f}{\partial y}\tilde{\Gamma}_r(y)\frac{d\varphi_j}{dy}dy \tag{28q}$$

$$S_{rj} = \varepsilon \int_0^1 \frac{\partial w_f}{\partial x} \tilde{\Gamma}_r(y) \frac{d\varphi_j}{dy} dy \tag{28r}$$

$$\bar{\gamma}_i(x) = \int_0^1 \varphi_i(y) \left[u_0(y) \frac{\partial^3 \psi_f}{\partial x\, \partial y^2} - \frac{d^2 u_0}{dy^2} \frac{\partial \psi_f}{\partial x} \right] dy \tag{28s}$$

$$\bar{\phi}_m = -\int_0^1 \left[u_0(y) + \varepsilon \frac{\partial \psi_f}{\partial y} \right] \frac{dT_f}{dx} \tilde{\Omega}_m(y) dy \tag{28t}$$

$$\beta_m = \int_0^1 [1 - T_f(0)] \tilde{\Omega}_m(y) dy \tag{28u}$$

$$\zeta_r = \int_0^1 \tilde{\Gamma}_r(y) \left\{ \frac{1}{\mathrm{Sc}} \frac{\partial^2 w_f}{\partial y^2} - u_0 \frac{\partial w_f}{\partial x} + \varepsilon \left(\frac{\partial \psi_f}{\partial x} \frac{\partial w_f}{\partial y} - \frac{\partial \psi_f}{\partial y} \frac{\partial w_f}{\partial x} \right) \right\} dy \tag{28v}$$

$$\xi_r = \int_0^1 \tilde{\Gamma}_r(y) [1 - w_f(0, y)] dy \tag{28w}$$

For the solution of the transformed problem of eqs. (28a-c) to be feasible, the summations from the inverse formulae (25b), (26b), and (27b) must be truncated to the finite orders $\mathcal{N}_\psi$, $\mathcal{N}_T$, and $\mathcal{N}_w$, respectively. The transformed problem of eqs. (28a-c) together with eqs. (19) and (21d) are solved together using the IDA method built-in the *NDSolve* function from *Wolfram Mathematica v13.3*.

3.2. Metals Extraction by Supported Liquid Membranes

Supported liquid membrane (SLM) separation is an emerging and promising unit operation to replace the traditional solvent extraction separation process. As it is a selective metal separation technique, interest in the use of SLMs has increased. Such membranes contain an extractant substance or a carrier which facilitates the selective permeation process by using facilitated transport mechanisms. This extractant substance is an element of great importance in membrane selectivity, as it is intended to facilitate extraction and be selective to the solute of interest [32-36].

In metals extraction using planar supported liquid membranes, the typical dimensionless formulation of the nonlinear mass transfer problem is written as follows:

$$\frac{\partial \theta_A(\eta,\tau)}{\partial \tau} = \frac{\partial^2 \theta_A(\eta,\tau)}{\partial \eta^2}, \quad \frac{\partial \theta_{AB}(\eta,\tau)}{\partial \tau} = \xi \frac{\partial^2 \theta_{AB}(\eta,\tau)}{\partial \eta^2}, \quad \text{in } 0 < \eta < 1, \quad \tau > 0 \tag{29a,b}$$

$$\theta_A(\eta,0) = 1, \quad \theta_{AB}(\eta,0) = 0, \quad 0 \le \eta \le 1 \tag{29c,d}$$

$$\begin{aligned} \frac{1}{\gamma_1} \frac{\partial \theta_A(0,\tau)}{\partial \eta} &= \beta_1 \theta_{B1}(\tau) [\theta_A(0,\tau)]^m - \theta_{AB}(0,\tau) = -\frac{1}{\alpha_1} \frac{d\theta_{B1}(\tau)}{d\tau} \\ \frac{\xi}{\gamma_1} \frac{\partial \theta_{AB}(0,\tau)}{\partial \eta} &= \theta_{AB}(0,\tau) - \beta_1 \theta_{B1}(\tau) [\theta_A(0,\tau)]^m = \frac{1}{\alpha_1} \frac{d\theta_{B1}(\tau)}{d\tau} \end{aligned} \tag{29e,f}$$

$$\begin{aligned} \frac{1}{\gamma_2} \frac{\partial \theta_A(1,\tau)}{\partial \eta} &= \theta_{AB}(1,\tau) - \beta_2 \theta_{B2}(\tau) [\theta_A(1,\tau)]^m = \frac{1}{\alpha_2} \frac{d\theta_{B2}(\tau)}{d\tau} \\ \frac{\xi}{\gamma_2} \frac{\partial \theta_{AB}(1,\tau)}{\partial \eta} &= \beta_2 \theta_{B2}(\tau) [\theta_A(1,\tau)]^m - \theta_{AB}(1,\tau) = -\frac{1}{\alpha_2} \frac{d\theta_{B2}(\tau)}{d\tau} \end{aligned} \tag{29g,h}$$

The kinetic equations are given by:

$$\frac{1}{\alpha_1}\frac{d\theta_{B1}(\tau)}{d\tau} = -\beta_1\theta_{B1}(\tau)\left[\theta_A(0,\tau)\right]^m + \theta_{AB}(0,\tau) \tag{29i}$$

$$\theta_{B1}(0) = 1 \tag{29j}$$

$$\frac{1}{\alpha_2}\frac{d\theta_{B2}(\tau)}{d\tau} = \theta_{AB}(1,\tau) - \beta_2\theta_{B2}(\tau)\left[\theta_A(1,\tau)\right]^m \tag{29k}$$

$$\theta_{B2}(0) = 0 \tag{29l}$$

In the formulation given by eqs. (29), $\theta_A(\eta,\tau)$, $\theta_{AB}(\eta,\tau)$, $\theta_{B1}(\tau)$, and $\theta_{B2}(\tau)$ are the dimensionless concentrations of extractant, species complex, metal concentrations at position η=0 and η=1 in membrane, respectively, and m is the reaction order. In obtaining eqs. (29), the following dimensionless groups were employed:

$$\eta = \frac{x}{\delta},\ \tau = \frac{D_A t}{\delta^2},\ \theta_A = \frac{C_A}{C_A^0},\ \theta_{AB} = \frac{C_{AB}}{C_A^0},\ \theta_{B1} = \frac{C_{B1}}{C_{B1}^0},\ \theta_{B2} = \frac{C_{B2}}{C_{B1}^0},\ \alpha_1 = \frac{K_{b1}\delta^2 C_A^0}{D_A L C_{B1}^0},\ \alpha_2 = \frac{K_{b_2}\delta^2 C_A^0}{D_A L C_{B1}^0},$$
$$\beta_1 = K_{ex_1} C_{B1}^0\left[C_A^0\right]^{m-1},\ \beta_2 = K_{ex_2} C_{B1}^0\left[C_A^0\right]^{m-1},\ \gamma_1 = \frac{K_{b_1}\delta}{D_A},\ \gamma_2 = \frac{K_{b_2}\delta}{D_A},\ \xi = \frac{D_{AB}}{D_A},\ K_{ex1} = \frac{K_{f1}}{K_{b1}}, \tag{30}$$
$$K_{ex2} = \frac{K_{f2}}{K_{b2}}$$

Solutions for the potentials $\theta_A(\eta,\tau)$ and $\theta_{AB}(\eta,\tau)$ are proposed in such a way that the original problem given by Eqs. (29) is homogenized by employing an implicit filtering scheme. Therefore:

$$\theta_A(\eta,\tau) = \theta_{A,av}(\tau) + \theta_{A,f}(\eta;\tau) + \theta_{A,h}(\eta,\tau) \tag{31a}$$

$$\theta_{AB}(\eta,\tau) = \theta_{AB,av}(\tau) + \theta_{AB,f}(\eta;\tau) + \theta_{AB,h}(\eta,\tau) \tag{31b}$$

where the average potentials $\theta_{A,av}(\tau)$ and $\theta_{AB,av}(\tau)$ are defined as:

$$\theta_{A,av}(\tau) = \int_0^1 \theta_A(\eta,\tau)d\eta,\ \ \theta_{AB,av}(\tau) = \int_0^1 \theta_{AB}(\eta,\tau)d\eta \tag{31c,d}$$

Through the definitions in eqs. (31) and the manipulation of eqs. (31a,b) and (29), we obtain the following expressions for $\theta_{A,av}(\tau)$, $\theta_{AB,av}(\tau)$ and for the filters $\theta_{A,f}(\eta;\tau)$ and $\theta_{AB,f}(\eta;\tau)$, respectively:

$$\theta_{A,av}(\tau) = 1 + \frac{\gamma_1}{\alpha_1}\left[\theta_{B1}(\tau) - 1\right] + \frac{\gamma_2}{\alpha_2}\theta_{B2}(\tau) \tag{32a}$$

$$\theta_{AB,av}(\tau) = -\frac{\gamma_1}{\alpha_1}\left[\theta_{B1}(\tau) - 1\right] - \frac{\gamma_2}{\alpha_2}\theta_{B2}(\tau) \tag{32b}$$

$$\theta_{A,f}(\eta;\tau) = \frac{\gamma_1}{\alpha_1}\frac{d\theta_{B1}(\tau)}{d\tau}\left(\frac{\eta^2}{2} - \eta + \frac{1}{3}\right) + \frac{\gamma_2}{\alpha_2}\frac{d\theta_{B2}(\tau)}{d\tau}\left(\frac{\eta^2}{2} - \frac{1}{6}\right) \tag{32c}$$

$$\theta_{AB,f}(\eta;\tau) = -\frac{\gamma_1}{\xi\alpha_1}\frac{d\theta_{B1}(\tau)}{d\tau}\left(\frac{\eta^2}{2} - \eta + \frac{1}{3}\right) - \frac{\gamma_2}{\xi\alpha_2}\frac{d\theta_{B2}(\tau)}{d\tau}\left(\frac{\eta^2}{2} - \frac{1}{6}\right) \tag{32d}$$

Now, introducing eqs. (31) and (32), we obtain the following system of partial differential equations for determination of the homogeneous potentials, $\theta_{A,h}(\eta,\tau)$ and $\theta_{AB,h}(\eta,\tau)$:

$$\frac{\partial\theta_{A,h}(\eta,\tau)}{\partial\tau} = \frac{\partial^2\theta_{A,h}(\eta,\tau)}{\partial\eta^2} - \frac{\gamma_1}{\alpha_1}\frac{d^2\theta_{B1}(\tau)}{d\tau^2}\left(\frac{\eta^2}{2} - \eta + \frac{1}{3}\right) - \frac{\gamma_2}{\alpha_2}\frac{d^2\theta_{B2}(\tau)}{d\tau^2}\left(\frac{\eta^2}{2} - \frac{1}{6}\right) \tag{33a}$$

$$\theta_{A,h}(\eta,0) = \beta_1\gamma_1\left(\frac{\eta^2}{2}-\eta+\frac{1}{3}\right) \tag{33b}$$

$$\frac{\partial\theta_{A,h}(0,\tau)}{\partial\eta}=0,\quad \frac{\partial\theta_{A,h}(1,\tau)}{\partial\eta}=0,\quad \int_0^1\theta_{A,h}(\eta,\tau)d\eta=0 \tag{33c-e}$$

$$\frac{\partial\theta_{AB,h}(\eta,\tau)}{\partial\tau}=\xi\frac{\partial^2\theta_{AB,h}(\eta,\tau)}{\partial\eta^2}+\frac{\gamma_1}{\xi\alpha_1}\frac{d^2\theta_{B1}(\tau)}{d\tau^2}\left(\frac{\eta^2}{2}-\eta+\frac{1}{3}\right)+\frac{\gamma_2}{\xi\alpha_2}\frac{d^2\theta_{B2}(\tau)}{d\tau^2}\left(\frac{\eta^2}{2}-\frac{1}{6}\right) \tag{33f}$$

$$\theta_{AB,h}(\eta,0)=-\frac{\beta_1\gamma_1}{\xi}\left(\frac{\eta^2}{2}-\eta+\frac{1}{3}\right) \tag{33g}$$

$$\frac{\partial\theta_{AB,h}(0,\tau)}{\partial\eta}=0,\quad \frac{\partial\theta_{AB,h}(1,\tau)}{\partial\eta}=0,\quad \int_0^1\theta_{AB,h}(\eta,\tau)d\eta=0 \tag{33h-j}$$

and the kinetics equations are rewritten as:

$$\begin{aligned}\frac{d\theta_{B1}(\tau)}{d\tau}&=-\alpha_1\beta_1\theta_{B1}(\tau)\left\{1+\frac{\gamma_1}{\alpha_1}\left[\theta_{B1}(\tau)-1+\frac{1}{3}\frac{d\theta_{B1}(\tau)}{d\tau}\right]+\frac{\gamma_2}{\alpha_2}\left[\theta_{B2}(\tau)-\frac{1}{6}\frac{d\theta_{B2}(\tau)}{d\tau}\right]+\theta_{A,h}(0,\tau)\right\}^m\\&+\alpha_1\left\{-\frac{\gamma_1}{\alpha_1}\left[\theta_{B1}(\tau)-1+\frac{1}{3\xi}\frac{d\theta_{B1}(\tau)}{d\tau}\right]-\frac{\gamma_2}{\alpha_2}\left[\theta_{B2}(\tau)-\frac{1}{6\xi}\frac{d\theta_{B2}(\tau)}{d\tau}\right]+\theta_{AB,h}(0,\tau)\right\}\end{aligned} \tag{33k}$$

$$\theta_{B1}(0)=1 \tag{33l}$$

$$\begin{aligned}\frac{d\theta_{B2}(\tau)}{d\tau}&=-\alpha_2\beta_2\theta_{B2}(\tau)\left\{1+\frac{\gamma_1}{\alpha_1}\left[\theta_{B1}(\tau)-1-\frac{1}{6}\frac{d\theta_{B1}(\tau)}{d\tau}\right]+\frac{\gamma_2}{\alpha_2}\left[\theta_{B2}(\tau)+\frac{1}{3}\frac{d\theta_{B2}(\tau)}{d\tau}\right]+\theta_{A,h}(1,\tau)\right\}^m\\&+\alpha_2\left\{-\frac{\gamma_1}{\alpha_1}\left[\theta_{B1}(\tau)-1-\frac{1}{6\xi}\frac{d\theta_{B1}(\tau)}{d\tau}\right]-\frac{\gamma_2}{\alpha_2}\left[\theta_{B2}(\tau)+\frac{1}{3\xi}\frac{d\theta_{B2}(\tau)}{d\tau}\right]+\theta_{AB,h}(1,\tau)\right\}\end{aligned} \tag{14m}$$

$$\theta_{B2}(0)=0 \tag{33n}$$

The integral transformation of the system of equations (33) is now performed and, for this purpose, the following auxiliary eigenvalue problems are chosen.

- For the potential $\theta_{A,h}(\eta,\tau)$:

$$\frac{d^2\Phi_i(\eta)}{d\eta^2}+\lambda_i^2\Phi_i(\eta)=0 \tag{34a}$$

$$\frac{d\Phi_i(0)}{d\eta}=0,\quad \frac{d\Phi_i(1)}{d\eta}=0 \tag{34b,c}$$

$$\Phi_i(\eta)=\cos(\lambda_i\eta),\quad \lambda_i=i\pi,\quad \text{i=1,2,3,...} \tag{34d,e}$$

$$\int_0^1\Phi_i(\eta)\Phi_j(\eta)d\eta=\begin{cases}0, & \text{for } i\neq j\\ M_i, & \text{for } i=j\end{cases},\quad M_i=\int_0^1\Phi_i^2(\eta)d\eta=\frac{1}{2},\quad \tilde{\Phi}_i(\eta)=\Phi_i(\eta)/\sqrt{M_i} \tag{34f-h}$$

where λ_i are the eigenvalues, Φ_i are the eigenfunctions, and M_i is the normalization integral.

- For the potential $\theta_{AB,h}(\eta,\tau)$:

$$\frac{d^2\psi_i(\eta)}{d\eta^2}+\mu_i^2\psi_i(\eta)=0 \tag{35a}$$

$$\frac{d\psi_i(0)}{d\eta}=0,\quad \frac{d\psi_i(1)}{d\eta}=0 \tag{35b,c}$$

$$\psi_i(\eta)=\cos(\mu_i\eta),\quad \mu_i=i\pi,\quad \text{i=1,2,3,...} \tag{35d,e}$$

$$\int_0^1\psi_i(\eta)\psi_j(\eta)d\eta=\begin{cases}0, & \text{for } i\neq j\\ N_i, & \text{for } i=j\end{cases},\quad N_i=\int_0^1\psi_i^2(\eta)d\eta=\frac{1}{2},\quad \tilde{\psi}_i(\eta)=\psi_i(\eta)/\sqrt{N_i} \tag{35f-h}$$

Similarly, μ_i are the eigenvalues, ψ_i are the eigenfunctions, and N_i is the normalization integral.

The eigenvalue problems given by eqs. (34) and (35) allow the definition of the following integral transform pairs for the potentials $\theta_{A,h}(\eta,\tau)$ and $\theta_{AB,h}(\eta,\tau)$, respectively:

$$\bar{\theta}_{A,i}(\tau)=\int_0^1\tilde{\Phi}_i(\eta)\theta_{A,h}(\eta,\tau)d\eta\,,\quad \text{transform} \tag{36a}$$

$$\theta_{A,h}(\eta,\tau)=\sum_{i=1}^{\infty}\tilde{\Phi}_i(\eta)\bar{\theta}_{A,i}(\tau)\,,\quad \text{inverse} \tag{36b}$$

$$\bar{\theta}_{AB,i}(\tau)=\int_0^1\tilde{\psi}_i(\eta)\theta_{AB,h}(\eta,\tau)d\eta\,,\quad \text{transform} \tag{37a}$$

$$\theta_{AB,h}(\eta,\tau)=\sum_{i=1}^{\infty}\tilde{\psi}_i(\eta)\bar{\theta}_{AB,i}(\tau)\,,\quad \text{inverse} \tag{37b}$$

Equations (33) are integral transformed to obtain the system of ODEs to compute the transformed potentials $\bar{\theta}_{A,i}(\tau)$ and $\bar{\theta}_{AB,i}(\tau)$. Therefore, after the usual manipulations in this integral transform procedure, the following coupled systems of ODEs are obtained:

$$\frac{d\bar{\theta}_{A,i}(\tau)}{d\tau}+\lambda_i^2\bar{\theta}_{A,i}(\tau)\;=\bar{g}_{A,i}(\tau) \tag{38a}$$

$$\frac{d\bar{\theta}_{AB,i}(\tau)}{d\tau}+\mu_i^2\xi\bar{\theta}_{AB,i}(\tau)\;=\bar{g}_{AB,i}(\tau) \tag{38b}$$

$$\bar{\theta}_{A,i}(0)=\bar{f}_{A,i}=\frac{\beta_1\gamma_1}{\sqrt{M_i}}\int_0^1\left(\frac{\eta^2}{2}-\eta+\frac{1}{3}\right)cos(\lambda_i\eta)d\eta \tag{38c}$$

$$\bar{\theta}_{AB,i}(0)=\bar{f}_{AB,i}=-\frac{\beta_1\gamma_1}{\xi\sqrt{N_i}}\int_0^1\left(\frac{\eta^2}{2}-\eta+\frac{1}{3}\right)cos(\mu_i\eta)d\eta \tag{38d}$$

where,

$$\bar{g}_{A,i}(\tau)\;=-\frac{\gamma_1}{\alpha_1}\frac{d^2\theta_{B1}(\tau)}{d\tau^2}\int_0^1\left(\frac{\eta^2}{2}-\eta+\frac{1}{3}\right)\tilde{\Phi}_i(\eta)d\eta-\frac{\gamma_2}{\alpha_2}\frac{d^2\theta_{B2}(\tau)}{d\tau^2}\int_0^1\left(\frac{\eta^2}{2}-\frac{1}{6}\right)\tilde{\Phi}_i(\eta)d\eta \tag{38e}$$

$$\bar{g}_{AB,i}(\tau)\;=\frac{\gamma_1}{\xi\alpha_1}\frac{d^2\theta_{B1}(\tau)}{d\tau^2}\int_0^1\left(\frac{\eta^2}{2}-\eta+\frac{1}{3}\right)\tilde{\psi}_i(\eta)d\eta+\frac{\gamma_2}{\xi\alpha_2}\frac{d^2\theta_{B2}(\tau)}{d\tau^2}\int_0^1\left(\frac{\eta^2}{2}-\frac{1}{6}\right)\tilde{\psi}_i(\eta)d\eta \tag{38f}$$

After introducing the inverse formulae given by eqs. (36b) and (37b), the kinetic equations are obtained as

$$\begin{aligned}\frac{d\theta_{B1}(\tau)}{d\tau}=&-\alpha_1\beta_1\theta_{B1}(\tau)\left\{1+\frac{\gamma_1}{\alpha_1}\left[\theta_{B1}(\tau)-1+\frac{1}{3}\frac{d\theta_{B1}(\tau)}{d\tau}\right]+\frac{\gamma_2}{\alpha_2}\left[\theta_{B2}(\tau)-\frac{1}{6}\frac{d\theta_{B2}(\tau)}{d\tau}\right]+\sum_{i=1}^{\infty}\tilde{\Phi}_i(0)\bar{\theta}_{A,i}(\tau)\right\}^m\\&+\alpha_1\left\{-\frac{\gamma_1}{\alpha_1}\left[\theta_{B1}(\tau)-1+\frac{1}{3\xi}\frac{d\theta_{B1}(\tau)}{d\tau}\right]-\frac{\gamma_2}{\alpha_2}\left[\theta_{B2}(\tau)-\frac{1}{6\xi}\frac{d\theta_{B2}(\tau)}{d\tau}\right]+\sum_{i=1}^{\infty}\tilde{\psi}_i(0)\bar{\theta}_{AB,i}(\tau)\right\}\end{aligned} \tag{39a}$$

$$\theta_{B1}(0)=1 \tag{39b}$$

$$\begin{aligned}\frac{d\theta_{B2}(\tau)}{d\tau}=&-\alpha_2\beta_2\theta_{B2}(\tau)\left\{1+\frac{\gamma_1}{\alpha_1}\left[\theta_{B1}(\tau)-1-\frac{1}{6}\frac{d\theta_{B1}(\tau)}{d\tau}\right]+\frac{\gamma_2}{\alpha_2}\left[\theta_{B2}(\tau)+\frac{1}{3}\frac{d\theta_{B2}(\tau)}{d\tau}\right]+\sum_{i=1}^{\infty}\tilde{\Phi}_i(1)\bar{\theta}_{A,i}(\tau)\right\}^m\\&+\alpha_2\left\{-\frac{\gamma_1}{\alpha_1}\left[\theta_{B1}(\tau)-1-\frac{1}{6\xi}\frac{d\theta_{B1}(\tau)}{d\tau}\right]-\frac{\gamma_2}{\alpha_2}\left[\theta_{B2}(\tau)+\frac{1}{3\xi}\frac{d\theta_{B2}(\tau)}{d\tau}\right]+\sum_{i=1}^{\infty}\tilde{\psi}_i(1)\bar{\theta}_{AB,i}(\tau)\right\}\end{aligned} \tag{39c}$$

$$\theta_{B2}(0)=0 \tag{39d}$$

The system of coupled ODEs given by eqs. (38) and (39) is a nonlinear initial value problem for computation of $\overline{\theta}_{A,i}(\tau)$, $\overline{\theta}_{AB,i}(\tau)$, $\theta_{B1}(\tau)$, and $\theta_{B2}(\tau)$. It is needed to truncate the infinite series in a sufficient number of terms, *NT*, for computational purposes. Appropriate subroutines must be employed since such a system has numerical stiffness characteristics. The subroutine DIVPAG from the IMSL Library has been employed, which has the important feature of automatic controlling the relative error in the solution of the ODEs system.

4. RESULTS AND DISCUSSION

4.1. Water Desalination by Vacuum-Enhanced Air Gap Membrane Distillation

Root mean square (RMS) errors for the inverse formulae (25.b), (26.b), and (27.b) can be estimated by applying Parseval's identity, yielding

$$\epsilon_{\psi}^2 = \max_{x\in[0,L]} \int_0^1 \left(\sum_{i=\mathcal{N}_{\psi}+1}^{\infty} \overline{\psi}_i \varphi_i \right)^2 dy \cong \max_{x\in[0,L]} \sum_{i=\mathcal{N}_{\psi}-4}^{\mathcal{N}_{\psi}} \overline{\psi}_i^2 \tag{40a}$$

$$\epsilon_{T}^2 = \max_{x\in[0,L]} \int_0^1 \left(\sum_{m=\mathcal{N}_{T}+1}^{\infty} \overline{T}_m \tilde{\Omega}_m \right)^2 dy \cong \max_{x\in[0,L]} \sum_{m=\mathcal{N}_{T}-4}^{\mathcal{N}_{T}} \overline{T}_m^2 \tag{40b}$$

$$\epsilon_{w}^2 = \max_{x\in[0,L]} \int_0^1 \left(\sum_{r=\mathcal{N}_{w}+1}^{\infty} \overline{w}_m \tilde{\Gamma}_m \right)^2 dy \cong \max_{x\in[0,L]} \sum_{r=\mathcal{N}_{w}-4}^{\mathcal{N}_{w}} \overline{w}_r^2 \tag{40c}$$

where ϵ_{ψ}, ϵ_T, and ϵ_w are the root mean square errors for the streamfunction, the temperature, and the mass fraction, respectively.

Table 1 presents the root mean square errors from eqs. (40a-c) for varying truncation orders $\mathcal{N}_{\psi}$, $\mathcal{N}_T$, and $\mathcal{N}_w$. It is clear that the truncation order $\mathcal{N}_{\psi} = 20$ is more than sufficient to achieve a good convergence of the streamfunction, due to the marginal effect the membrane suction has on the velocity profile. For the temperature and mass fraction, $\mathcal{N}_T = 40$ and $\mathcal{N}_w = 80$ suffice to keep the root mean square error below 10^{-4}, which give a good balance between numerical precision and computational cost. Henceforth, the results will be obtained for these truncation orders.

Table 1. Convergence behavior of the integral transform solution of the V-AGMD model.

Streamfunction		**Temperature**		**Mass fraction**	
$\mathcal{N}_{\psi}$	ϵ_{ψ}	$\mathcal{N}_T$	ϵ_T	$\mathcal{N}_w$	ϵ_w
20	2.52×10^{-9}	20	0.000454	20	0.00191
25	7.49×10^{-10}	30	0.000176	40	0.000393
30	2.83×10^{-10}	40	0.0000932	60	0.000165
35	1.25×10^{-10}	50	0.0000576	80	0.0000902
40	6.18×10^{-10}	60	0.0000391	100	0.0000568

Figures 1a and 1b present an extensive validation effort involving both experimental results from the COPPE/UFRJ polygeneration plant [29,30] and independent experimental results reported in [31], for spiral-wound V-AGMD modules manufactured by AquaStill (Netherlands). In the horizontal axes, results from the simulation are marked, while the vertical axes represent the experimental results. The proposed model and solution methodology are capable of accurately predicting the results for the mass flux across the membrane for a wide range of module sizes and operational conditions, totaling 86 cases, 41 from the COPPE/UFRJ polygeneration plant [29,30] and 45 from [31].

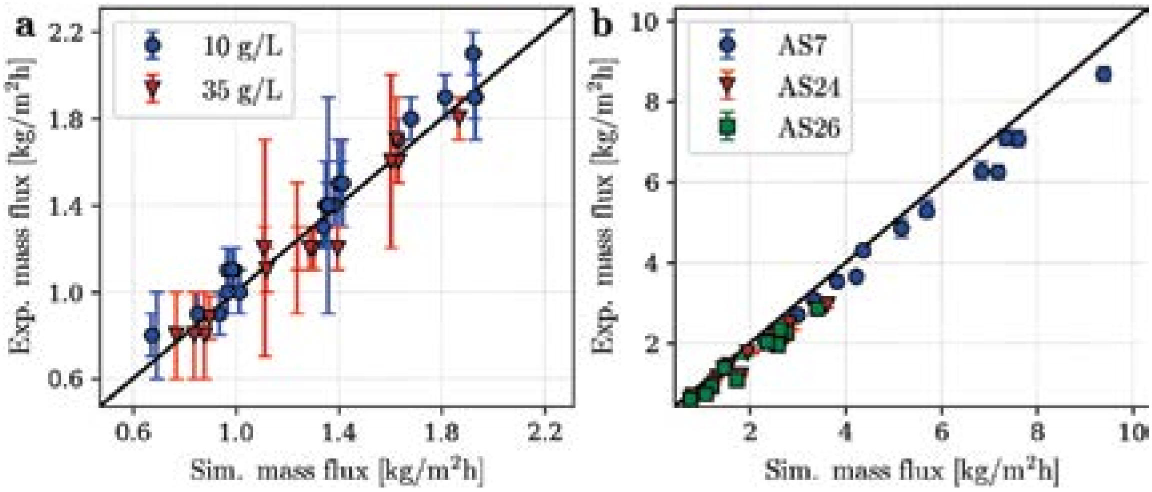

Figure 1. Validation against 86 experimental results. (a) Comparison with 41 experimental results from the COPPE/UFRJ polygeneration plant [29,30]; (b) Comparison with 45 results from Andrés-Mañas et al. 2022 [31].

4.2. Metals Extraction by Supported Liquid Membranes

To illustrate the metal extraction by supported liquid membranes, we consider as test-case a chemical reaction of order m=1 (typical case of separation of Cd(II), as raised by Wang et al. [32]). For the simulation analysis of the influence of the composition and membrane thickness, the diffusion coefficient and the kinetic parameters are those presented in Table 2. The calculation of the membrane composition was based on the experimental data of Argiropoulos et al. [33].

Table 2 - Physicochemical parameters for the computational simulation of Cd (II) extraction.

D_A (m^2/s)	D_{AB} (m^2/s)	K_{b1} (m/s)	K_{b2} (m/s)	K_{f1} (m^4/mol.s)	K_{f2} (m^4/mol.s)	δ (μm)	L (m)	C_{A0} (g/g)	C_{B0} (mg/l)
$1x10^{-13}$	$1xD_A$	$1.1x10^{-6}$	$0.1xK_{b1}$	$1.7x10^{-7}$	$1xK_{f1}$	81.7	0.1	30%	120
$9x10^{-12}$	$1xD_A$	$7x10^{-9}$	$0.1xK_{b1}$	$9.99x10^{-10}$	$0.1xK_{f1}$	279	0.1	30%	100
$8.2x10^{-13}$	$1xD_A$	$5x10^{-7}$	$10^{-4}xK_{b1}$	$2.3x10^{-7}$	$0.1xK_{f1}$	138	0.1	40%	100
$3.85x10^{-11}$	$1xD_A$	$1.5x10^{-7}$	$1xK_{b1}$	$1x10^{-8}$	$1xK_{f1}$	133	0.1	50%	100

Figure 2 shows the influence of the membrane composition on the extraction of Cd (II). It can be seen in this figure that the extraction of Cd (II) is more efficient when higher concentrations of the extractant Aliquat 336 are used. In the case of Aliquat 336 with a concentration of 50% in the membrane, an extraction of more than 50% of the amount of Cd (II) was obtained after a period of 20 hours. The simulated results obtained in the present work showed good agreement when compared with the experimental results of Wang et al. [32]. The behavior of the concentration of Aliquat 336 in the extraction process can be explained by L'Chatelier's principle. Thus, from Eq. (41) below, an increase in the concentration of Aliquat 336 promotes a shift in the equilibrium in the reaction to promote the formation of the complex species AB(me) in the membrane. Observing Table 2 above, for the case of a membrane with 50% Aliquat 336, the diffusivity was greater in relation to the membranes with 30% and 40% Aliquat 336, thus favoring the extraction of cadmium due to the increase in the diffusivity of the complex species in the membrane.

$$mA_{(me)} + B_{(aq)} \underset{K_{b1}}{\overset{K_n}{\rightleftarrows}} \left[A_m B\right]_{(me)} \tag{41}$$

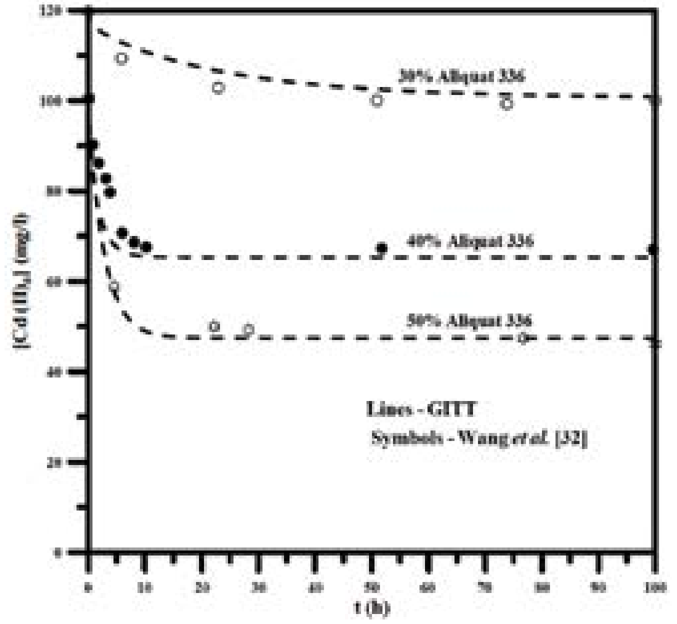

Figure 2 - Influence of Aliquat 336 concentration on the membrane during Cd (II) extraction and comparison of GITT results against experimental results of Wang et al. [32].

Figure 3 shows the behavior of cadmium extraction under the influence of variable membrane thickness. The results presented were simulated using membranes with a concentration of 30% in Aliquat 336 and thicknesses of 81.7 and 279 μm, since the thickness of the organic phase (membrane), the phase in which the diffusion of ion pairs occurs, will influence the transfer rate of the metal-complex species formed by the reversible ion exchange reaction to the depletion and enrichment phases, according to eqs. (29i) and (29k). It is evident in this figure that the extraction is more efficient for the case of a membrane with a thickness of 279 μm, and, again, the results are in good agreement with the experimental results obtained by Wang et al. [32] for the same analysis.

Figure 4 presents a comparative analysis between the GITT solution of this work and the solution for the same problem obtained with the Method of Lines (MOL) [34]. The converged results obtained by GITT were obtained with NT=400 terms, while in the solution through the MOL procedure, a spatial grid was used with M=300 nodes. It can be observed in these figures that there is an excellent agreement between the two sets of results, thus verifying the computational code developed in this work.

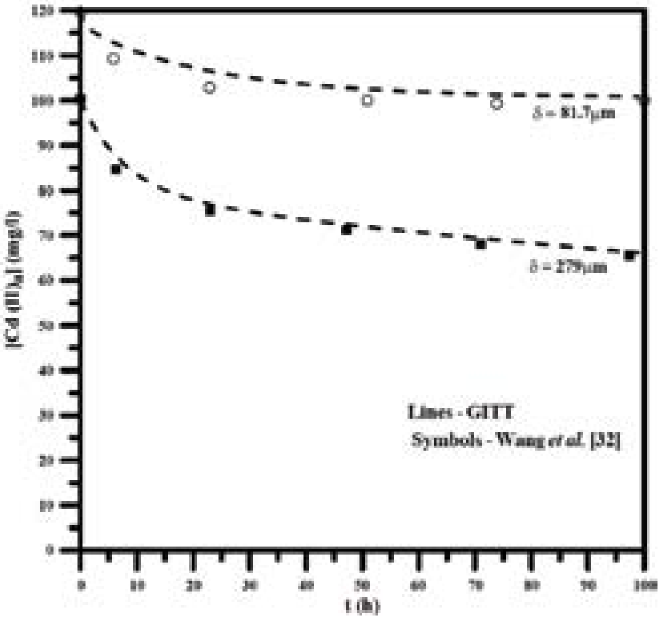

Figure 3 - Influence of the membrane thickness during the Cd (II) extraction with 30% of Aliquat 336 in the membrane and comparison of GITT results against experimental results of Wang et al. [32].

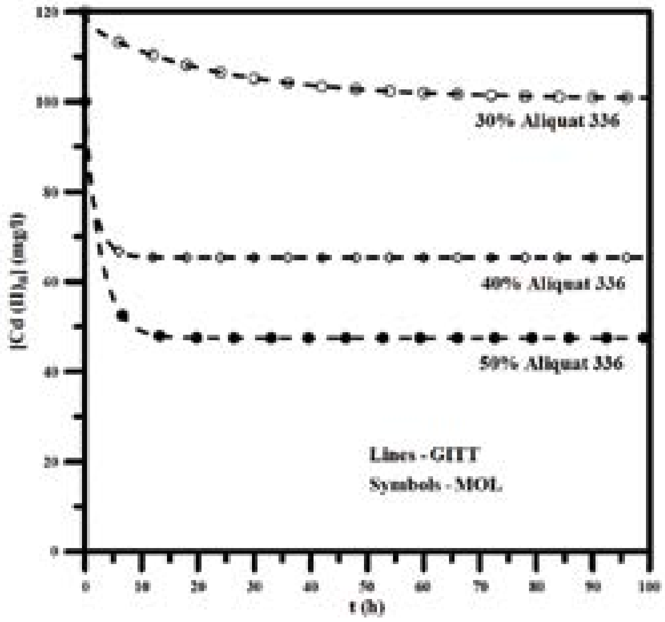

Figure 4 - Comparison of the results obtained with GITT and MOL (Method of Lines) [34] procedures for the analysis of the influence of the concentration of Aliquat 336 in the membrane during the extraction of Cd (II).

5. CONCLUSIONS

The Generalized Integral Transform Technique (GITT) is reviewed with focus on nonlinear convection-diffusion problems and in the use of filtering strategies for the eigenfunction expansions convergence enhancement. The formal solution is first revisited by adopting a linear eigenvalue problem as the basis for the eigenfunction expansion, by concentrating all the nonlinearities in the equation and boundary conditions source terms. Then, the adoption of an expansion base offered by a nonlinear eigenvalue problem is summarized, as a methodological alternative for convergence rates improvement. Finally, the employment of explicit analytical filters and an implicit nonlinear filtering strategy are detailed. The aim of filtering is to enhance convergence by extracting information from the source terms, which are responsible for slowing down convergence rates, especially the boundary conditions source terms, that impede an uniform convergence behavior. Even for nonlinear boundary source terms, the implicit filter can fully eliminate them from the filtered problem formulation and offer a significant improvement in convergence, especially at and near the boundaries. The filtering strategies are then illustrated in two test cases related to ongoing research by the authors. Both problems are applications of membrane mediated transport phenomena, one dealing with vacuum-enhanced air gap membrane distillation for water desalination and the other related with mass transfer through supported liquid membranes for selective metals extraction. Besides presenting the methodological derivations for each case, including the filtering strategy adopted, sample results illustrate and demonstrate the hybrid method with convergence analysis and validation with experimental results. There are various possibilities for extension and application of the present approach that go far beyond the transport phenomena field, but in all cases the relative merits shall be more evident for simulations with highly intensive CPU usage and high accuracy and automatic control requirements.

ACKNOWLEDGEMENTS

The authors are grateful for the financial support offered by the Brazilian Government agencies CNPq, CAPES-PROCAD Defesa, ANP/PETROGAL, and FAPERJ. RMC is also grateful to the kind hospitality of Prof. Michael Ohadi, Department of Mechanical Engineering, University of Maryland, College Park, during preparation of the manuscript in July 2024.

REFERENCES

[1] M.D. Mikhailov, and M.N. Özisik, *Unified Analysis and Solutions of Heat and Mass Diffusion*, John Wiley, New York, 1984; also, Dover Publications, 1994.

[2] M.N. Ozisik and R.L. Murray, On the solution of linear diffusion problems with variable boundary condition parameters, *J. Heat Transfer*, 96c, 48-51, 1974.

[3] M.D. Mikhailov, On the solution of the heat equation with time dependent coefficient, *Int. J. Heat & Mass Transfer*, 18, 344-345, 1975.

[4] R.M. Cotta, Diffusion in media with prescribed moving boundaries: Application to metals oxidation at high temperatures, Proc. of the *2nd Latin American Congress of Heat & Mass Transfer*, vol. 1, pp. 502-513, São Paulo, Brasil, May 1986.

[5] R.M. Cotta and M.N. Ozisik, Laminar forced convection in ducts with periodic variation of inlet temperature, *Int. J. Heat Mass & Transfer*, 29, 1495-1501, 1986.

[6] R.M. Cotta, Hybrid numerical-analytical approach to nonlinear diffusion problems, *Num. Heat Transfer, Part B*, 127, 217-226, 1990.

[7] R.M. Cotta, *Integral Transforms in Computational Heat and Fluid Flow*, CRC Press, Boca Raton, FL, 1993.

[8] R.M. Cotta, Benchmark results in computational heat and fluid flow: - The integral transform method, *Int. J. Heat Mass Transfer* (Invited Paper), 37, 381-394, 1994.

[9] R.M. Cotta, *The Integral Transform Method in Thermal and Fluids Sciences and Engineering*, Begell House, New York, 1998.

[10] R. M. Cotta and M. D. Mikhailov, Hybrid methods and symbolic computations. In: *Handbook of Numerical Heat Transfer,* 2nd edition, Chapter 16, W.J. Minkowycz; E.M. Sparrow; J.Y. Murthy (eds.), John Wiley, New York, 2006.

[11] R.M. Cotta, C.P. Naveira-Cotta, D.C. Knupp, J.L.Z. Zotin, P.C. Pontes, and A.P. Almeida, Recent advances in computational-analytical integral transforms for convection-diffusion problems, *Heat & Mass Transfer*, Invited Paper, 54, 2475–2496, 2018.

[12] R.M. Cotta, D.C. Knupp, and J.N.N. Quaresma, Analytical methods in heat transfer. In: *Handbook of Thermal Science and Engineering*, v. 1, Chapter 2, pp.61-126, In: F. Kulacki et al. (eds.), Springer, 2018.

[13] R.M. Cotta, K.M. Lisboa, M.F. Curi, S. Balabani, J.N.N. Quaresma, J.S. Pérez Guerrero, E.N. Macêdo, and N.S. Amorim, A review of hybrid integral transform solutions in fluid flow problems with heat or mass transfer and under Navier-Stokes equations formulations, *Num. Heat Transfer, Part B*, 76, 60-87, 2019.

[14] R.M. Cotta, D.C. Knupp, K.M. Lisboa, C.P. Naveira-Cotta, J.N.N. Quaresma, J.L.Z. Zotin, and H.K. Miyagawa, Integral transform benchmarks of diffusion, convection-diffusion, and conjugated problems in complex domains, *50 Years of CFD in Engineering Sciences - A Commemorative Volume in Memory of D. Brian Spalding*, Ed. A.K. Runchal, Chapter 20, p. 719-750, Springer-Verlag, 2020.

[15] R.M. Cotta, K.M. Lisboa, C.P. Naveira-Cotta, J.N.N. Quaresma, D.C. Knupp, and L.A. Sphaier, Unified integral transforms with non-classical eigenvalue problems in heat and mass transfer, *ASME J. Heat and Mass Transfer*, Review Article, 145, no.1, 1-23, 2023.

[16] R.M. Cotta, C.P. Naveira-Cotta, and D.C. Knupp, Nonlinear eigenvalue problem in the integral transforms solution of convection-diffusion with nonlinear boundary conditions, *Int. J. Num. Meth. Heat & Fluid Flow,* Invited Paper, 25th Anniversary Special Issue, 26, 767-789, 2016.

[17] P.C. Pontes, K.B. Oliveira, E.N. Macedo, J.N.N. Quaresma, C.P. Naveira-Cotta, and R.M. Cotta, Nonlinear eigenvalue problem approach for mass transfer in supported liquid membrane co-transport separation processes, *J Braz. Soc. Mech. Sci. Eng.*, 44, no.12, 1-16, 2022.

[18] I.S. Carvalho, R.M. Cotta, C.P. Naveira Cotta, and M.K. Tiwari, Hybrid integral transform analysis of supercooled droplets solidification, *Proc. Royal Society A - Mathematical, Physical and Eng. Sciences*, 477, 1-25, 2021.

[19] A.R. Almeida and R.M. Cotta, A comparison of convergence acceleration schemes for eigenfunction expansions of partial differential equations, *Int. J. Num. Meth. Heat & Fluid Flow*, 6, no.6, 85-97, 1996.

[20] J.W. Ribeiro and R.M. Cotta, On the solution of nonlinear drying problems in capillary porous media through integral transformation of Luikov equations, *Int. J. Num. Meth. Eng.*, 38, 1001-1020, 1995.

[21] C.F.T. Matt, Transient response of general one-dimensional distributed systems through eigenfunction expansion with an implicit filter scheme, *Applied Mathematical Modelling*, 39, no. 9, 2470-2488, 2015.

[22] R.M. Cotta, D.C. Knupp, C. P. Naveira-Cotta, L.A. Sphaier, and J.N.N. Quaresma, Unified integral transforms algorithm for solving multidimensional nonlinear convection-diffusion problems, *Num. Heat Transfer, part A - Applications*, 63, 1-27, 2013.

[23] E. Drioli, A. Ali, and F. Macedonio, Membrane distillation: Recent developments and perspectives, *Desalination*, 356, 56-84, 2015.

[24] A. Deshmukh, C. Boo, V. Karanikola, S. Lin, A.P. Straub, T. Tong, D.M. Warsinger, and M. Elimelech, Membrane distillation at the water-energy nexus: Limits, opportunities, and challenges, *Energy Environ. Sci.*, 11, no. 5, 1177-1196, 2018.

[25] J.A. Andrés-Mañas, I. Requena, and G. Zaragoza, Membrane distillation of high salinity feeds: Steady-state modelling and optimization of a pilot-scale module in vacuum-assisted air gap operation, *Desalination*, 553, 116449, 2023.

[26] V.T. Shahu and S.B. Thombre, Air gap membrane distillation: A review, *Journal of Renewable and Sustainable Energy*, 11, no. 4, 045901, 2019.

[27] L. Eykens, I. Hitsov, K. de Sitter, C. Dotremont, L. Pinoy, and B. van der Bruggen, Direct contact and air gap membrane distillation: Differences and similarities between lab and pilot scale, *Desalination*, 422, 91-100, 2017.

[28] Ó. Andrjesdóttir, C.L. Ong, M. Nabavi, S. Paredes, A.S.G. Khalil, B. Michel, and D. Poulikakos, An experimentally optimized model for heat and mass transfer in direct contact membrane distillation, *Int. J. Heat and Mass Transf.*, 66, 855-867, 2013.

[29] C.P. Naveira-Cotta, I.V. Curcino, B. Scaramuza dos Reis, A.O. Cárdenas Gómez, P.R.S. Costa Jr., J.D.C.G. Carvalho, L.E. Peñaranda Chenche, J.A. Lima, and R.M. Cotta, A sustainable polycogeneration prototype for decentralized production of electricity, distilled water and biodiesel, Proc. of the *8th Thermal and Fluids Engineering Conference (TFEC)*, ASTFE, Paper # TFEC-2023-47412, p.703-707, College Park, MD, USA, March 26th-29th, 2023.

[30] I.V. Curcino, B. Scaramuza dos Reis, A.O. Cárdenas Gómez, L.E. Peñaranda Chenche, J.A. Lima, C.P. Naveira-Cotta, and R.M. Cotta, "Experimental evaluation of solar desalination system with vacuum-enhanced air gap membrane distillation", Proc. of the *17th International Heat Transfer Conference – IHTC17*, Paper # IHTC17-1011, Cape Town, South Africa, August 14th-18th, pp. 1-10, 2023.

[31] J.A. Andrés-Mañas, I. Requena, and G. Zaragoza, Characterization of the use of vacuum enhancement in commercial pilot-scale air gap membrane distillation modules with different designs, *Desalination*, 528, 115490, 2022.

[32] L. Wang, R. Paimin, R.W. Cattral, W. Shen, and S.D. Kolev, The extraction of cadmium (II) and copper (II) from hydrochloric acid solutions using an Aliquat 336/PVC membrane, *J. Membr. Sci.*, 176, 105-111, 2000.

[33] G.A. Argiropoulos, R.W. Cattral, I.C. Hamilton, S.D. Kolev, and R. Paimin, The study of a membrane for extracting gold (III) from hydrochloric acid solutions, *J. Membr. Sci.*, 138, 279-285, 1998.

[34] S.A. Cardoso, E.N. Macedo, J.N.N. Quaresma, and R.M. Cotta, Computational simulation of metal extraction process using polymeric membranes, *Int. Conf. of the Brazilian Society of Mechanical Sciences, COBEM-2007*, Paper # 2076, pp.1-10, Brasilia, DF, Brazil, November 2007.

[35] A. M. Urtiaga, A. Irabien, and P. Stroeve, Effect of a variable solute distribution coefficient on mass separation in hollow fibers*, Ind. Eng. Chem. Res.*, 31, 1362-1366, 1992.

[36] A. Gherrou and H. Kerdjoudi, Removal of gold as Au (Tu)2+ complex with a supported liquid membrane containing macrocyclic polyethers ligands as carriers", *Desalination*, 144, 231-236, 2002.

KEYNOTE LECTURES

Sixth International Conference on Computational Methods for Energy and Thermal Problems
THERMAECOMP2024, Sept. 9-11, 2024, Budva, Montenegro
N. Massarotti, P. Nithiarasu, and I. Vušanović (Eds.)

MODELLING OF SORPTION BASED HEATING AND COOLING SYSTEMS

Pradip Dutta[1], Kartik Jain[2]
Department of Mechanical Engineering, Indian Institute of Science, Bangalore, INDIA
[1]pradip@iisc.ac.in; [2]kartik@iisc.ac.in

ABSTRACT

Designing the reactor in a TCES system is crucial as it involves desorption, adsorption, and heat exchange with the HTF. Effective reactor design must address bed thermal resistance, permeability for gas/vapor mass transport, and reaction kinetics, all of which are interdependent. This study presents a systematic scaling analysis to address these coupled phenomena. Using ANSYS FLUENT® (version 2021 R1), transport equations of mass, momentum, and heat coupled with reaction kinetics are numerically solved. A parametric study demonstrates the impact of water vapor transport on reaction kinetics in reactors with varying aspect ratios, particle sizes, and operating conditions. This research provides a framework for designing thermochemical energy storage systems and optimizing operating parameters for various heating and cooling applications.

Key Words: *Thermochemical energy storage, potassium carbonate salt hydrate, hydration, dehydration, scaling analysis, numerical modelling.*

1. INTRODUCTION

Building heating, including space heating and domestic hot water production, accounts for about 46% of global heat consumption [1, 2]. Prioritizing renewable energy sources can reduce fossil fuel dependence and lower greenhouse gas emissions, but solar energy's intermittent nature presents challenges. High-density thermal energy storage systems with minimal losses are needed. Sorption heat storage (SHS) systems, or sorption thermal batteries, offer alternatives to conventional heat pumps for space heating and hot water production [1, 3]. These systems use an endothermic reaction in a sorption material during charging to store surplus heat (e.g., solar energy or waste heat). The stored heat is later retrieved through a reversible exothermic reaction during discharging, making it available for heating applications. Among sorption materials, salt hydrates are suitable for low and medium-temperature applications due to their high energy storage density (>2GJ/m^3) and their cost-effectiveness [4]. In this study, potassium carbonate salt is chosen which stores energy based on reversible thermochemical reaction given by Equation 1:

$$K_2CO_3.1.5H_2O\ (s) \underset{Hydration}{\overset{Dehydration}{\rightleftarrows}} K_2CO_3(s) + 1.5\ H_2O(g) \qquad (1)$$

The proposed SHS system operates in a closed cycle. During charging, surplus heat (Q_{ch}) from solar or industrial waste heat is added to the energy storage reactor through a heat transfer fluid (HTF), causing water vapor to be released from the hydrous salt via an endothermic dehydration reaction (Figure 1a). The released water vapor is stored separately in an evaporator/condenser unit. When the stored heat is needed, water vapor is sent back to the reactor, enabling the exothermic hydration reaction (Figure 1b). The released heat (Q_{dis}) can be used for heating by circulating a suitable HTF through the reactor. Reactor design is crucial for facilitating hydration and dehydration reactions, which involve interconnected heat and mass transfer, directly affecting performance metrics such as specific power and energy storage capacity. However, reactor design is challenging due to the low thermal conductivity and low permeability of salt hydrates [5].

A recent study by the present authors established a scaling procedure for estimating critical length scales for optimal bed design, showing that critical regions in the porous reactor bed experience limited reactions due to thermal diffusion and vapor transport rates [6]. The present study demonstrates a numerical model of hydration/dehydration processes for potassium carbonate salt, incorporating vapor flow, heat transfer, and chemical reaction kinetics.

2. SCALING AND NUMERICAL MODEL

Packed bed reactors are commonly used in TCES systems due to their high energy storage density and adequate vapor flow permeability. In this configuration, granular thermochemical energy storage material is packed in a bed with heat-exchanging surfaces (such as fins or HTF tubes), while water vapor enters or exits from the top. Figure 1 (left) illustrates a domain inside such a reactor, where K_2CO_3 hydrate is packed between two heat-exchanging surfaces, with a water vapor inlet from the top. The chosen two-dimensional domain represents the area between two heat transfer surfaces, capturing effective heat diffusion and vapor flow scales through theoretical scaling analysis [6] and numerical simulations.

As shown in Figure 1 (right), the pressure boundary condition applied at the vapor inlet of the domain (i.e. top surface) corresponds to the saturation pressure of water vapor at the ambient temperature. The boundary condition on the left wall is assumed to be isothermal, corresponding to the HTF temperature. The bottom wall of the domain is assumed to be thermally insulated, while a symmetric boundary condition is applied at the right-side boundary.

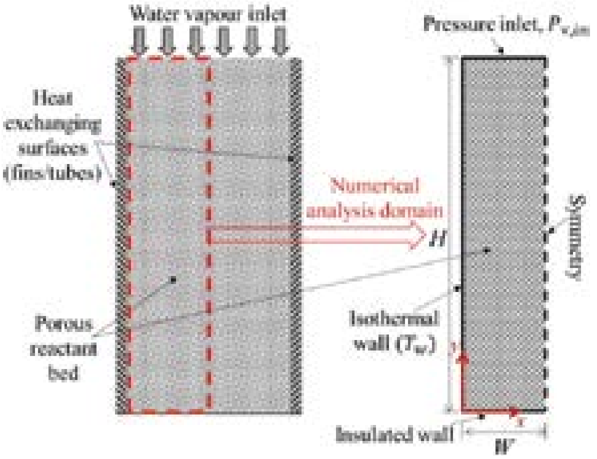

FIGURE 1. A representative domain inside a packed bed reactor configuration (left) and domain for scaling and numerical analysis (right).

The principal governing equations consist of mass, momentum, and energy conservation equations.

$$\frac{\partial(\Phi\,\rho_v)}{\partial t} + \nabla.(\rho_v\,\vec{v}) + \chi\frac{(1-\Phi)\,\rho_s}{M_s}M_v\frac{d\xi}{dt} = 0 \qquad (2)$$

The last term ($\dot{S}_m$) denotes the mass sink term for water vapor adsorption during the hydration reaction. The term ($d\xi/dt$) represents the hydration reaction rate given by Equation 3 as [7]:

$$\frac{d\xi}{dt} = A_{f,h}\exp\left(\frac{-E_{a,h}}{RT}\right).(1-\xi)^{\frac{2}{3}}.\left(\frac{P_v}{P_{eq}}\right) \qquad (3)$$

where P_{eq} is the equilibrium pressure, given by Equation 4. For hydration reaction to occur, the vapor pressure, P_v, must be greater than the equilibrium pressure, $P_{eq}(T)$, corresponding to a particular temperature T (i.e. $P_v > P_{eq}(T)$).

$$P_{eq} = 4.228 * 10^{12}\exp\left(\frac{-7337}{T}\right) \qquad (4)$$

The conservation of momentum equation for the flow of water vapor through the pores between reactant particles is written as:

$$\frac{1}{\Phi}\frac{\partial(\rho_v\overline{v})}{\partial t} + \frac{1}{\Phi^2}\nabla.(\rho_v\overline{v}\,\overline{v}) = -\nabla P_v + \frac{\mu_v}{\Phi}\nabla^2\overline{v} - \frac{\mu_v}{\lambda_p}\overline{v} \qquad (5)$$

The energy conservation equation is given as follows:

$$\Phi\rho_v C_{p,v}\frac{\partial T}{\partial t} + (1-\Phi)\rho_s C_{p,s}\frac{\partial T}{\partial t} + \nabla.(\rho_v C_{p,v} T\,\overline{v}) = \nabla.(k_{eff}\nabla T) + \chi\frac{(1-\Phi)\,\rho_s}{M_s}\frac{d\xi}{dt}\Delta h_r \qquad (6)$$

The governing partial differential equations subjected to initial and boundary conditions are simultaneously solved using ANSYS FLUENT v.2021R1 software, a commercial package based on the Finite Volume Method (FVM). User-defined functions (UDFs) are used to prescribe TCM thermophysical properties, reaction kinetics, and appropriate source terms in continuity and energy equations. The continuity and momentum equations are solved using the COUPLED [8] algorithm and second-order implicit scheme for transient formulation with time steps chosen in the range of 10^{-4}-10^{-3} s.

3. RESULTS

This section examines the impact of domain width, domain height, and inlet vapor pressure on the hydration reaction (discharging process) in a two-dimensional packed bed reactor with potassium carbonate salt hydrate.

3.1 Critical domain width

During the hydration reaction, heat release increases bed temperature and decreases the hydration reaction rate. To sustain the process, the side wall must dissipate the exothermic heat. The critical heat diffusion length derived from the scaling analysis of energy equation [6], given by Equation 7, indicates the critical domain width (X_{cr}) for the time scale (t_h), beyond which reactants do not participate in the reaction due to limited thermal diffusion.

$$X_{cr} = \left(\frac{k_{eff}(T_{max}-T_w)t_h}{\rho_{bed}\,\Delta h_h}\right)^{1/2} \qquad (7)$$

Figure 2 shows numerical simulation results validating X_{cr}, with contour plots of temperature and conversion profiles at t = 1500 s for three domain widths (5, 10, and 25 mm). Figure 2a shows that temperature increases along the x-direction as the distance from the left side wall increases. The smallest domain width has the least temperature increase due to better heat transport to the side wall. For a domain width of 25 mm, temperature beyond 10 mm from the side wall remains constant at the reaction equilibrium temperature for the corresponding vapor pressure. Vapor pressure decreases along the domain height, so the reaction equilibrium temperature is higher near the top inlet and decreases along the height. Figure 2b shows a sharp reaction front dividing the bed into hydrated (reacted) and fully dehydrated (unreacted) regions. For smaller widths (5 and 10 mm), the fully unreacted region is limited to the y-direction, but for 25 mm, it extends along the x-direction (indicated by a dotted line). Beyond this line, reaction rate and conversion are nearly zero because temperature equals the reaction equilibrium temperature, so the condition for the hydration reaction ($P_v > P_{eq}$) is not satisfied in this region. Figure 2b shows the estimated critical width from numerical simulation matches this value, confirming the derived scale.

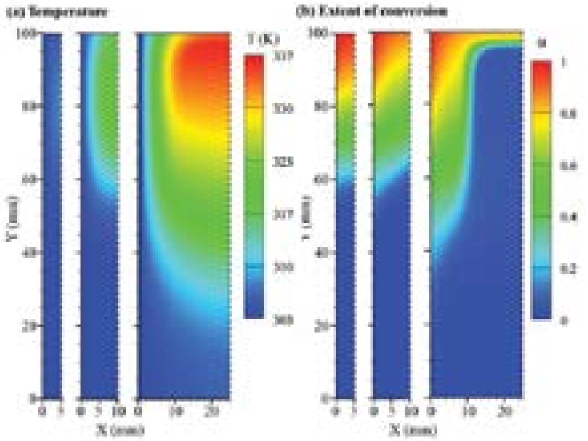

FIGURE 2: Contour plots of (a) temperature (b) extent of conversion during the discharging process at time instant *t* = 1500 s for different domain widths.

3.2 Critical vapor penetration depth

The scaling analysis of the continuity and momentum equation gives the vapor penetration depth scale (Y_{cr}), which indicates the critical depth for vapor supply during the time scale (t_h), as the reactants beyond this depth do not participate in the hydration reaction due to limited vapor supply.

$$Y_{cr} = \left[\left(P_{v,in} - P_{Y,min}\right)\left(\frac{M_s}{M_v}\frac{\rho_{in}}{\rho_{bed}}\,\frac{\lambda_p\, t_h}{\chi\, \mu_v}\right)\right]^{1/2} \qquad (8)$$

Figure 3 shows the contours of vapor pressure, conversion profile, and reaction rate for a domain with W = 10 mm and H = 250 mm at 1500 s and 15000 s. The pressure contours (Figure 3a) indicate that vapor pressure remains nearly constant and equals the reaction equilibrium pressure beyond the dotted line at both times. The conversion profiles (Figure 3b) show the reaction front dividing the region into hydrated (reacted) and fully dehydrated (unreacted) regions along the y-direction. Most material above the dotted line is reacted, while below it, the material is unreacted due to insufficient vapor pressure for the hydration reaction. Figure 3c demonstrates that, even in the unreacted zone, the reaction rate is significantly lower due to low vapor pressure.

4. CONCLUSIONS

This study developed a two-dimensional numerical model using ANSYS® FLUENT to simulate the discharging process of a thermochemical energy storage system based on potassium carbonate

(K_2CO_3) salt hydrate. The results show a region along the domain width, beyond the critical domain width (X_{cr}), where reactant conversion is nearly zero due to poor thermal diffussion. Similarly, a region along the domain height, beyond the critical vapor penetration depth (Y_{cr}), shows zero reactant conversion due to limited vapor supply.

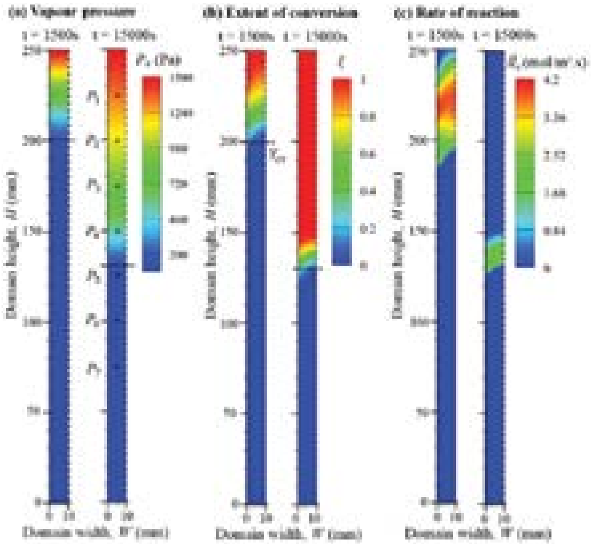

FIGURE 3: Contour plots of the (a) vapor pressure, (b) extent of conversion, and (c) rate of reaction for a domain with $W = 10$ mm and $H = 250$ mm during discharging process at time instants, $t_1 = 1500$ s and $t_2 = 15000$ s.

REFERENCES

[1] H. Lund, S. Werner, R. Wiltshire, S. Svendsen, J.E. Thorsen, F. Hvelplund, B.V. Mathiesen, 4th Generation District Heating (4GDH): Integrating smart thermal grids into future sustainable energy systems, Energy 68 (2014) 1–11.

[2] X.S. Jiang, Z.X. Jing, Y.Z. Li, Q.H. Wu, W.H. Tang, Modelling and operation optimization of an integrated energy based direct district water-heating system, Energy 64 (2014) 375–388.

[3] L. Gao, J. Zhao, Z. Tang, A Review on Borehole Seasonal Solar Thermal Energy Storage, Energy Procedia 70 (2015) 209–218.

[4] P.A.J. Donkers, L.C. Sögütoglu, H.P. Huinink, H.R. Fischer, O.C.G. Adan, A review of salt hydrates for seasonal heat storage in domestic applications, Appl Energy 199 (2017) 45–68.

[5] W. Li, J.J. Klemeš, Q. Wang, M. Zeng, Salt hydrate–based gas-solid thermochemical energy storage: Current progress, challenges, and perspectives, Renewable and Sustainable Energy Reviews 154 (2022) 111846.

[6] K. Jain, S. Dash, P. Dutta, A scaling procedure for designing thermochemical energy storage system, Int J Heat Mass Transf 220 (2024) 124981.

[7] M. Gaeini, S.A. Shaik, C.C.M. Rindt, Characterization of potassium carbonate salt hydrate for thermochemical energy storage in buildings, Energy Build 196 (2019) 178–193.

[8] ANSYS (2018) ANSYS Fluent User's Guide, Release 19.0. ANSYS, Canonsburg, PA. , (n.d.).

Sixth International Conference on Computational Methods for Energy and Thermal Problems
THERMAECOMP2024, Sept. 9-11, 2024, Budva, Montenegro
N. Massarotti, P. Nithiarasu, and I. Vušanović (Eds.)

Enhancing Heat Exchanger Performance: Integrating Computational Modeling and Experimental Studies for Optimization Approaches

Sara Rainieri
Dipartimenti di Ingegneria e Architettura- Università di Parma Parco Area delle Scienze 181/A
Parma ITALY, sara.rainieri@unipr.it

ABSTRACT

One significant challenge continually encountered by manufacturers of heat exchangers is the imperative for a design approach grounded in technological innovation aimed at producing devices that are not only more thermally efficient, but also feature reduced pressure drop, volume, manufacturing and operational costs and high-quality surface finishing to mitigate fouling phenomena [1].

A strategy that has been successfully explored in literature to achieve this goal consists in the use of emerging additive manufacturing technologies, that enable to produce surfaces with an optimized morphology [2]. This challenge requires a multidisciplinary approach that couples the advantages of numerical approaches to experimental advanced measurement and data processing procedures, mostly based on highly resolved infrared thermographic systems [3]. The possibility of obtaining detailed information about the heat transfer capability of enhanced surfaces can be suitably achieved by using numerical tools in the optimization problem that adopts experimental data as a necessary either input or validation elements [4].

The present contribution aims at presenting some applications of the two complementary approaches (numerical and experimental) with regards to heat transfer enhancement passive solutions implemented in heat exchangers.

Key Words: *Heat Transfer Enhancement, Optimization approaches, Heat Exchangers Design.*

1. INTRODUCTION

In forced convection heat transfer within internal flow configurations, the selection of passive enhancement strategies is highly dependent on the established flow regime, which is primarily influenced by the fluid's rheological properties and by the geometrical features as well.

In particular, when the laminar flow regime limiting boundaries cannot be overcome, the only possibility to passively enhance the heat transfer phenomenon is associated to solutions that force the fluid mixing, such as flow inserts or twisted tapes [5]. Another interesting strategy when dealing with the laminar flow regime is related to the curvature of the ducts' wall, implemented for instance in coils or other helical geometries: in this case the onset of the Dean vortices due to curvature effects, induces flow acceleration that positively affect the convective heat transfer mechanism [6]. These solutions are often implemented with the awareness that pressure drop penalties are also significantly augmented, as "manipulating" the thermal boundary layer requires modifications to the velocity boundary layer, and this cannot be achieved without cost.

More interesting are the flow conditions where the laminar velocity boundary layer is susceptible to destabilization, favouring the onset of turbulence, which strongly enhances the heat transfer mechanism [7]. This strategy is implemented in solutions based on turbulators, surface roughness modification, and by using nanofluids to enhance thermal conductivity [8]. In these cases, the pressure drop penalties are often significant as well, but generally, their augmentation is limited in comparison to the benefit that the early transition brings to the convective heat transfer phenomenon [7].

When the flow is in the fully turbulent flow regime, further enhancement of the convective heat transfer is of more limited interest. However, in some engineering applications, due to the peculiarities either of the fluid or of the process, it remains an important issue [4].

The understanding of these complex phenomena requires the adoption of both the numerical approach, able to reconstruct the local velocity and temperature fields and of advanced experimental methodologies. The combination of this information become necessary for approaching the strategy for topological and morphological optimization of the heat transfer sections with the ultimate aim of increasing the overall energy efficiency of industrial equipment.

Regarding the experimental approach, an interesting and effective strategy is found in the use of infrared thermography to acquire highly spatially resolved temperature maps on the external surface of heat exchanger's sections for numerically solving the inverse heat conduction problem in the solid wall for estimating the local heat transfer coefficient at the fluid-internal wall interface [9-10]. This methodology has been successfully applied to single-phase convective heat transfer problems in duct-flow with regards to different geometries. This detailed information, coupled to the numerical CFD evidence of the fluid's velocity distribution within the device, is essential for several engineering applications. For instance, in the thermal processing of fluid foods, that must accurately achieve the required microbial load reduction that is governed by the local temperature history of the fluid particles and not only on the average overall heat transfer capability of the device [11].

In the following some applicative cases are briefly described to show the potential of the advanced and integrated investigation methodology.

2. SOME APPLICATIVE CASES

2.1 Insert devices, the butterfly shape flow inserts.

Butterfly inserts have been explored in literature as a promising geometry to achieve heat transfer augmentation in single-phase tubular heat exchangers due to the additional turbulence and mixing effects introduced by wings [12]. To optimize the geometry, some interesting results have been shown by Bozzoli et al. [4] and Pagliarini et al [13]. The experimental data have been obtained by adopting the advanced methodology above mentioned, based on the solution of the Inverse Heat Conduction Problem in the tube's wall in correspondence to the location were the butterfly insert is located, by starting from Infrared temperature data. The inverse computed solution of the heat transfer problem within the wall, enables to estimate the local convective heat transfer coefficient at the internal fluid wall interface.

The experimental results have been compared with numerical outcome obtained by steady RANS simulations, performed by adopting the Realizable k-ε model with enhanced wall function. An adjoint approach has therefore been used for morphological optimization of the butterfly insert, i.e., to obtain an optimal balance between heat transfer enhancement and pressure losses mitigation in the tube by modifying the insert geometry.

The geometry tested and some representative results are shown in Figures 1-6.

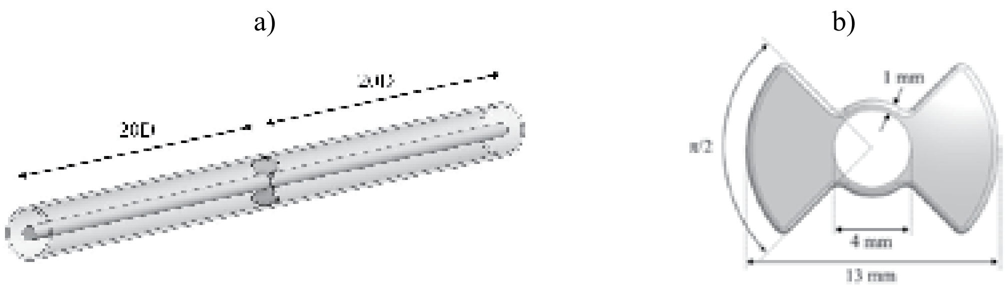
a) b)

FIGURE 1: The flow inserts configuration considered (a) and details of the butterfly insert (b).

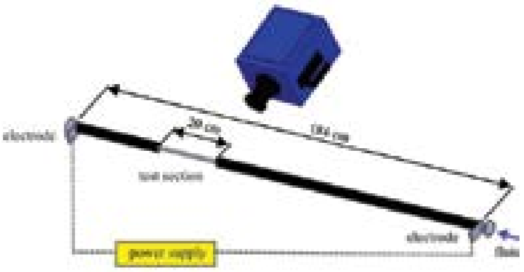

FIGURE 2: Schematic representations of the infrared thermographic measuring system adopted.

FIGURE 3: A representative infrared image: butterfly insert - Re = 5030.

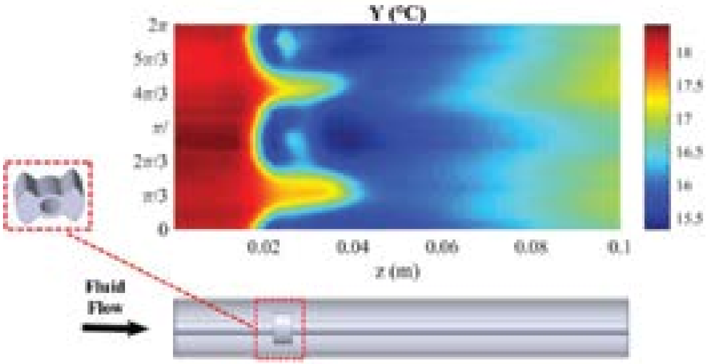

FIGURE 4: Wall temperature map: butterfly insert - Re = 5030.

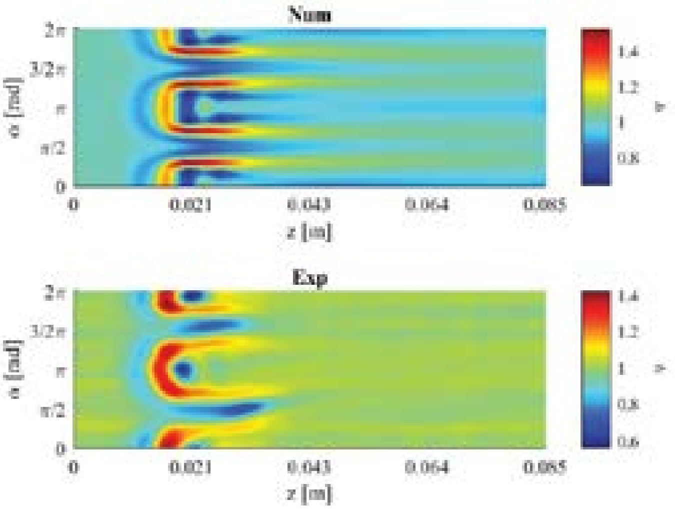

FIGURE 5: Normalized heat flux distribution at the wall-fluid interface (Re = 7110), numerically (Num) and experimentally (Exp) evaluated.

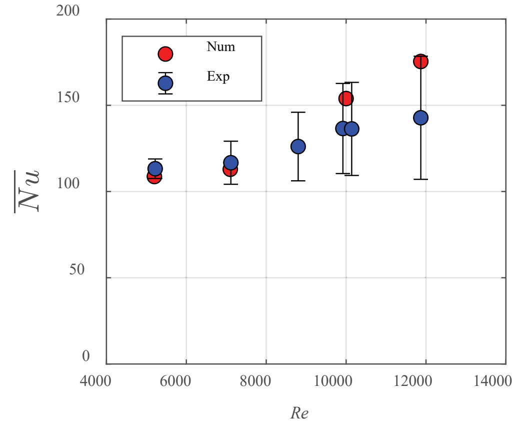

FIGURE 6: Comparison between numerically and experimentally estimated Nu as a function of Re.

Shape optimization of the insert was then explored through a discrete adjoint approach provided in Ansys Fluent© (v. 2023 R1). Input variables (design parameters, i.e., insert geometry) were iteratively varied to reach the maximization of the observable of engineering interest (ratio between Nusselt number and pressure losses). The Performance Evaluation Criterion PEC $PEC=\frac{\varepsilon_h}{\varepsilon_f^{1/3}}$ was considered as the observable of interest for the adjoint optimizer, where $\varepsilon_h=\frac{\overline{Nu}_e}{Nu_0}$ and $\varepsilon_f=\frac{f_e}{f_0}$, being f the friction factor. The subscripts e and 0 refer to the modified and reference (straight tube without insert) geometries, respectively. Some results are reported din Figure 7.

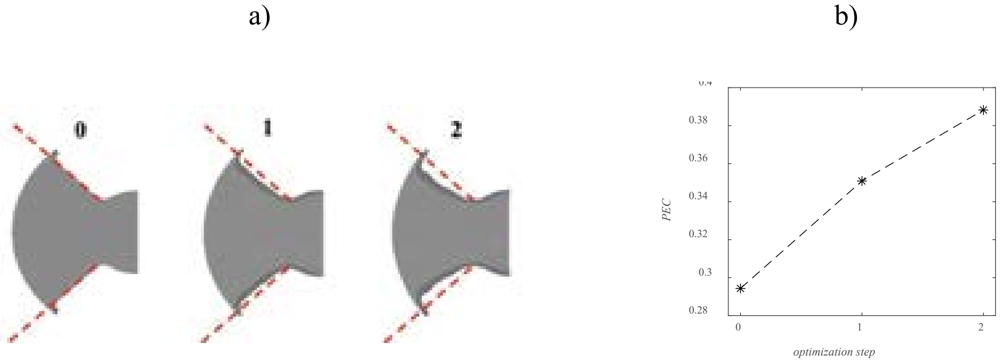

FIGURE 7: Modified geometries throughout the shape optimization process (a) and values of PEC computed at each optimization step.

2.2 Wall corrugated straight and curved tubes.

Another exemplificative and interesting example of optimization approaches applied to single-phase convective heat transfer problems in duct-flow is found in the study of wall corrugated straight and curved tubes [6]. Different corrugation morphologies have been considered in literature and both numerical and experimental results have been presented. Regarding the experimental approaches, the Infrared Thermography was adopted to capture information related to the local thermal fluid dynamics phenomena, that ultimately determines the heat flux exchanged at fluid-wall interface. A massive campaign has been developed by Rainieri and Pagliarini [14] for exploring the heat transfer enhancement, as compared to pressure drop penalties augmentation, in single and cross-helix wall corrugated tubes both in the laminar and in the turbulent flow regimes, by also considering the combined effects due to the wall curvature [6]. Some of the geometries tested with the corresponding results obtained are reported in Figures 8-10. The overall results proof that beneficial effects to heat transfer brought by wall corrugation are mainly ascribable to the onset of instabilities that anticipate the turbulence transport phenomena mechanism.

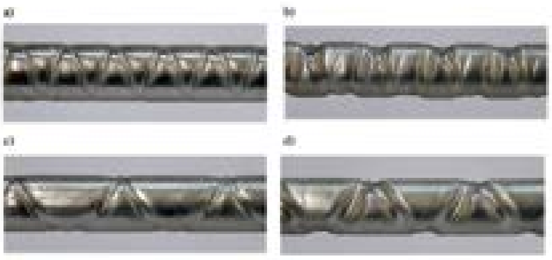

FIGURE 8: Some of the straight wall corrugated tubes tested.

FIGURE 9: A section of the coiled wall corrugated tubes tested.

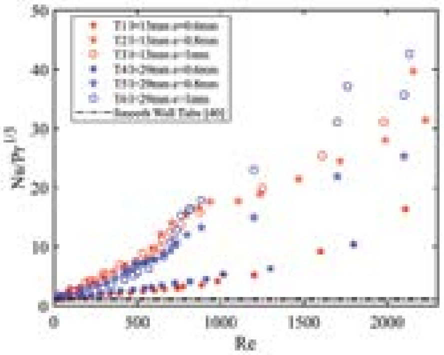

FIGURE 10: Heat transfer performance of wall corrugated straight tubes in the Reynolds umber range 50-2300.

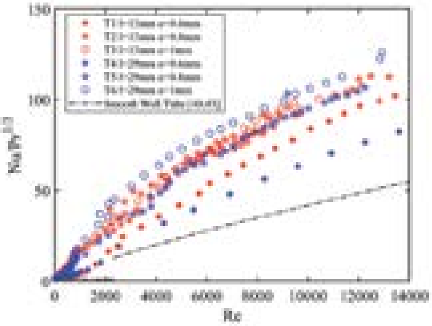

FIGURE 11: Heat transfer performance of wallcorrugated straight tubes in the Reynolds number range 50-14,000.

This experimental evidence has been confirmed by numerical DNS results [15] performed on a wall corrugated tube, with arc-shaped axial symmetrical profile, as reported in Figure 12-15: the data clearly show that the flow destabilizing is the effect responsible for the enhancement of the convective heat transfer.

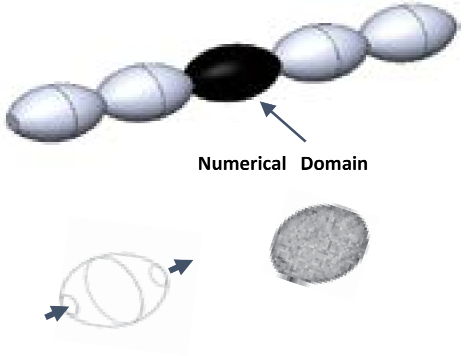

FIGURE 12: The wall corrugated tube numerically tested.

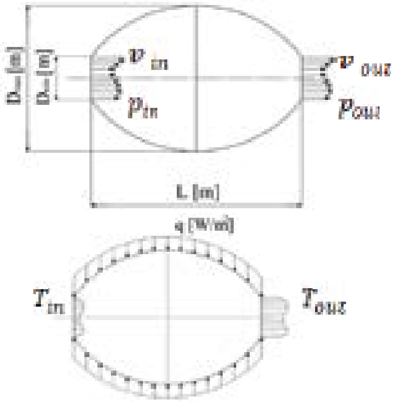

FIGURE 13: The boundary condition considered.

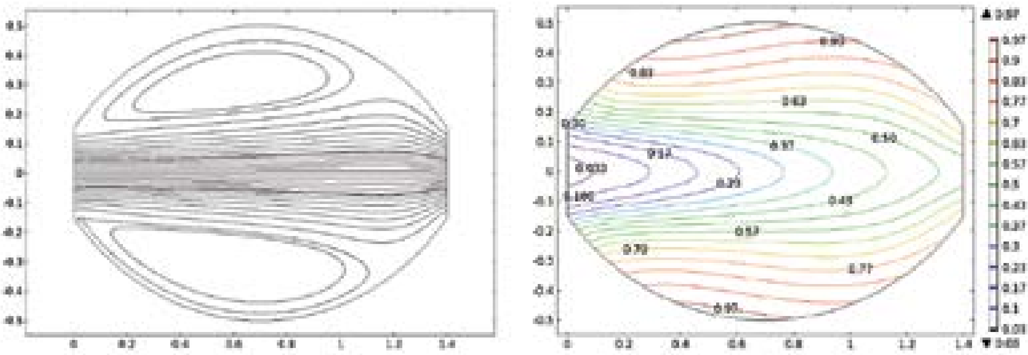

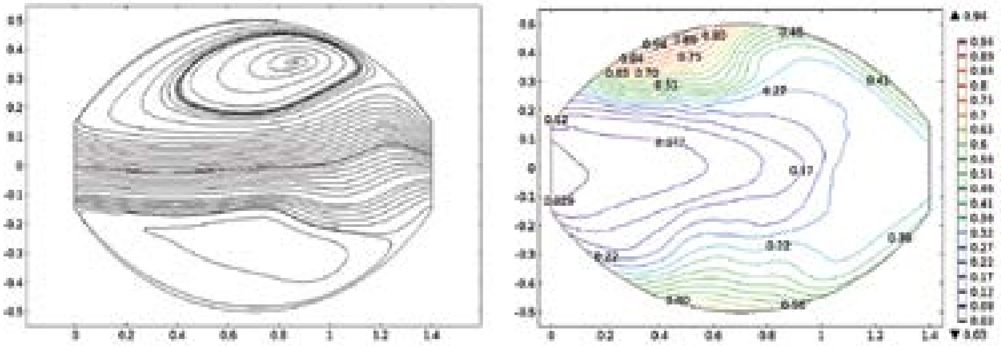

FIGURE 14: Streamlines (left) and tempertaure contours (rigth) ad the diametral cross section for Re=21 (a) and Re=75 (b)

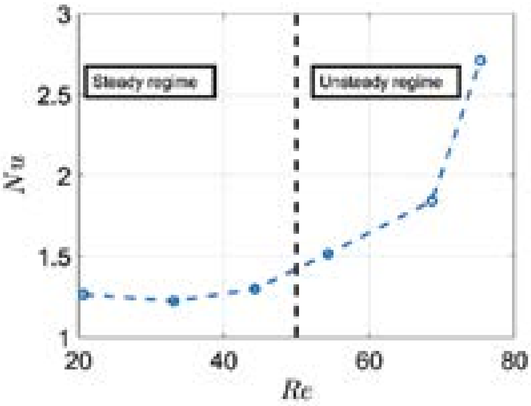

FIGURE 15: Nusselt Number versus Reynolds number.

Regarding the curvature effects again the CFD approach combined with experimental data enabled to identify the additional contribution to the augmentation mechanism. Some representative results are reported in [16].

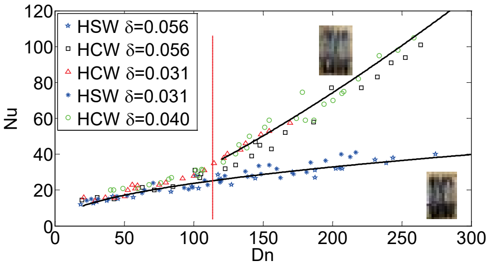

FIGURE 16: Nusselt Number versus Reynolds number for coiled smooth and corrugated tubes with evidence of the onset of instabilities.

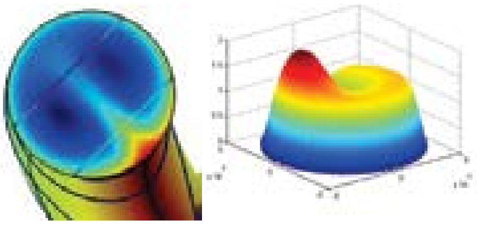

FIGURE 17: Velocity distribution in a coiled tube.

2.3 Double pipe heat exchangers with staggered fins.

Double pipe heat exchangers are often used in various industrial applications, such as in the food industry [11]. In this field, highly viscous fluids, often exhibiting non-Newtonian behavior, are treated in continuous processing equipment to achieve the required thermal pasteurization and sterilization standards. In these applications, the main challenge is to overcome the limitation associated to the low heat transfer coefficient achievable in the laminar flow regime. Consequently, significant research and technological efforts are continuously dedicated to identifying innovative and effective solutions to enhance the convective heat transfer in such conditions. In this scenario, a representative example is found in tubular heat exchangers equipped with helical fins to promote the mixing of the fluid.

A relevant application of an optimization procedure of this geometry is suggested in [17], where numerical results have been obtained with the aim of implementing the optimal geometry able to positively interrupt the thermal boundary layer by constantly remixing the fluid along the thermal path. Some representative results are summarized in Figures 18-21.

FIGURE 18: The investigated double pipe heat exchanger with staggered helical fins.

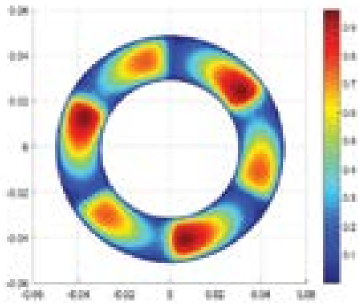

FIGURE 19: Axial velocity distribution on the cross section.

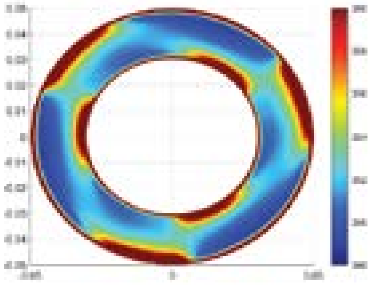

FIGURE 20: Temperature distribution on the cross -section.

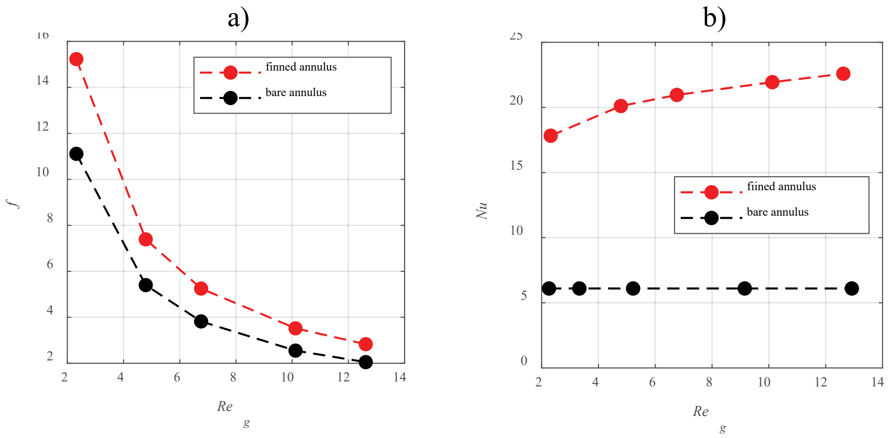

FIGURE 21: Friction factor (a) and Nusselt number (b) for the finned and bare annuli (non-Newtonian power-law fluid; m = 22.43 Pa s^n, n = 0.46).

3. CONCLUSIONS

In this contribution, several passive methodologies for enhancing convective heat transfer in heat exchangers are presented, with the aim of highlighting the potential of two complementary investigation approaches: numerical and experimental. The complexity of the thermal fluid dynamics problem involved in heat transfer enhancement necessitates diverse, flexible and highly resolved (in time and space) tools to identify the optimal geometry that can achieve the desired thermal treatment while simultaneously limiting the rise in pressure drop. The applicative cases described here pave the way for a more ambitious path towards the development of digital twin models of heat exchangers able of predicting the dynamic responses of the equipment in real industrial engineering working conditions.

4. ACKNOWLEDGMENTS

The Author would like to acknowledge financial support from PNRR-M4C2- I1.1 – MUR Call for proposals n.104 of 02-02-2022 - PRIN 2022 - ERC sector PE8- Project title: MOOD4HEX - MOrphology Optimized Design for Heat EXchangers - Project Code 2022SJP2A5 - CUP Code D53D23004040006 - Funded by the European Union – NextGenerationEU.

REFERENCES

[1] A. Patel, Heat Exchangers in Industrial Applications: Efficiency and Optimization Strategies, *International Journal of Engineering Research & Technology (IJERT)*, 12 (9), 2023.

[2] A. Seyed, N. & M. Mortazavi and Dongsheng Li, Additively manufactured heat exchangers: a review on opportunities and challenges, *The International Journal of Advanced Manufacturing Technology*, 12, 601-618, 2021.

[3] T. Astarita, G.M. Carlomagno, Infrared Thermography for Thermo-Fluid-Dynamics, Springer, 2013.

[4] F. Bozzoli, L. Cattani, A. Mocerino, S. Rainieri, I. Tougri, and M. Colaço, Characterization of the heat transfer in displaced enhancement devices by means of inverse problem approach applied to IR images. Quantitative InfraRed Thermography Journal, 18(2), 108–126, 2019.

[5] V. D. Zimparov, P. J. Bonev, J. Y. Hristov, New insight into the heat transfer and pressure drop correlations for laminar and turbulent flow in a circular tube with a twisted-tape insert: A

discriminated dimensional analysis, *International Journal of Heat and Mass Transfer,* 221, 2024.

[6] S. Rainieri, F. Bozzoli, L. Cattani and G. Pagliarini, Compound convective heat transfer enhancement in helically coiled wall corrugated tubes, International Journal of Heat and Mass Transfer, 59, 353-362, 2013.

[7] F. Bozzoli, L. Cattani and S. Rainieri, Cross-helix corrugation: The optimal geometry for effective food thermal processing, *International Journal of Heat and Mass Transfer*, 147, 2020.

[8] R.L Webb, Principles of Enhanced Heat Transfer, Wiley, New York, 1994.

[9] W.Azam, L. Cattani, M. Malavasi and Fabio Bozzoli, Experimental Study of the Corrugation Profile Effect on the Local Heat Transfer Coefficient, Muhammad, *Energies*, 16, 7181, 2023 .

[10] F. Bozzoli, L. Cattani, S. Rainieri and Giorgio Pagliarini, Estimation of local heat transfer coefficient in coiled tubes under inverse heat conduction problem approach, *Experimental Thermal and Fluid Science*, 59, 246–251, 2014.

[11] S. Srivastava, V. K. Pandey, A. Fatima, M. Sachin V, S. Pandey, R. Singh, A. H. Dar and B. Dhillon, A literature review on process intensification: An innovative and sustainable food processing method, *Applied Food Research,* 4, 2024.

[12] R. Pandey and U. Madanan, Heat transfer enhancement through pitch ratio optimization of butterfly inserts in minichannel heat sinks, Thermal Science and Engineering Progress 46, 102262, 2023.

[13] L. Pagliarini, F Bozzoli, L Cattani and S Rainieri, Morphological Optimization of Butterfly-Shaped Inserts for Heat Transfer Enhancement In Tubular Heat Exchangers: a Numerical Case Study, *European Thermal Sciences Conference - Eurotherm 2024*, 10-13 June Slovenia.

[14] S. Rainieri and G. Pagliarini, Convective heat transfer to temperature dependent property fluids in the entry region of corrugated tubes, *International Journal of Heat and Mass Transfer*, 45, (22), 4525-4536, 2002.

[15] P. Vocale, F. Bozzoli, A. Mocerino and Sara Rainieri, Direct numerical simulation applied to the analysis of the convective heat transfer enhancement in an arc-shaped wall corrugated tube, *Computational Thermal Sciences*, 11(4),315–325, 2019.

[16] S. Rainieri, F. Bozzoli, L. Schiavi and G. Pagliarini, Numerical analysis of convective heat transfer enhancement in swirl tubes, International Journal of Numerical Methods for Heat & Fluid, 21 (5), 559-571, 2011.

[17] L Pagliarini, F. Bozzoli, R. Fallahzadeh and S. Rainieri, Numerical investigation on the effects of staggered helical fins on non-Newtonian convective heat transfer in annuli, 41th UIT International Heat Transfer Conference June 19-21, 2024, Napoli, Italy

Sixth International Conference on Computational Methods for Energy and Thermal Problems
THERMAECOMP2024, Sept. 9-11, 2024, Budva, Montenegro
N. Massarotti, P. Nithiarasu, and I. Vušanović (Eds.)

Applying thermal computational methods for the modeling of carbon mineralization

Vaughan R. Voller

Department of Civil, Environmental, and Geo- Engineering, University of Minnesota, Minneapolis, MN 55455, USA, vole001@umn.edu

ABSTRACT

There are two objectives in this paper:
(1) The primary objective is to demonstrate how computational methods, developed for thermal and energy problems, can be extended and applied to large-scale environmental problems, with a particular focus on the subsurface storage of CO2 via mineralization.
(2) The secondary objective is to place the efforts presented within an historical arc, spanning the development of computational modeling of heat and mass transfer processes.

Key Words: *Mineral Carbon Storage, Applications of Thermal Computations, History of Thermal Computations*.

1. INTRODUCTION

A short historical perspective – a personal viewpoint

The universal starting point, for the computation of almost every thermal system, is the Fourier heat conduction equation, developed in the early 1800's [1]. To illustrate this, let us consider the class of problems related to modeling phase change (*e.g.*, melting) systems. Initial work on this class of problems, based directly on the Fourier equation, includes the classic analytical solution and scaling work carried out by Neumann [2] and Stefan [3, 4] in the mid to late 1800's. Computations on phase change problems arose with the advent of computational devices, both digital and mechanical, in the middle of the 1900's. Landmarks would have to include the Crank-Nicolson scheme for the Fourier equation [5] and the modeling of phase change systems presented by Eyres et al. [6], and Price and Slack [7], works that produced relatively simple models for predicting process data and advancing the understanding of heat transfer phenomena.

A critical point in the "main streaming" of computational methods would have to be the conference series on computational method for thermal problems (a forerunner of the current conference series) initiated by Profs. Roland Lewis and Ken Morgan, the inaugural 1979 conference at the University of Swansea, Wales [8] (see Fig. 1) featuring keynotes from two of the giants in the field of computational methods, O.C. Zienkiewicz and John Crank. When one reviews the proceedings of this conference, the clear focus is on developing computational techniques for solving basic problems. For example, there are 10 papers directly on solution methods for phase change problems and an additional 10 or so papers on applications of these methods in industrial settings. Again, it is reasonable to conclude that the foci of these modeling efforts were equally devoted to making predictions and gaining understanding.

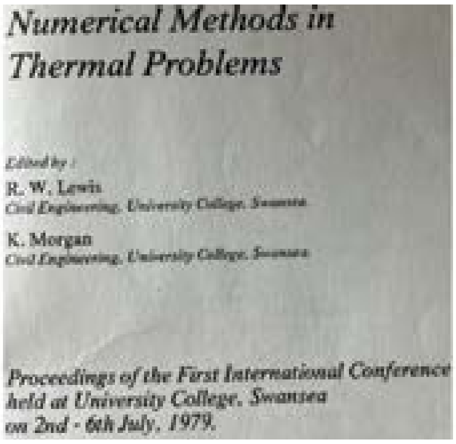

Numerical Methods in Thermal Problems

Edited by :
R. W. Lewis
Civil Engineering, University College, Swansea
K. Morgan
Civil Engineering, University College, Swansea

Proceedings of the First International Conference held at University College, Swansea on 2nd - 6th July, 1979.

FIGURE 1. Front piece of 1979 “Numerical Methods in Thermal Problems” proceedings.

Over the almost half-century following the 1979 meeting, there has been significant advances in the field of thermal computations. Now, as indicated by the scope of the current conference, the application of thermal computations is at the core of large *multi-scale, multi-physics* calculations, or more appropriately, recognizing the increasing efforts to include biological and chemical components into large-scale computations, *multi-scale, multi-science* calculations, efforts that require an accounting of behavior (*e.g.,* the automatous motion of cyanobacteria in thermally stratified lakes [9]) and the satisfaction of an additional conservation equation – the balance of amount, *i.e.,* the moles in a chemical reaction. In an even wider view, we should also recognize the increasing need for coupling computations with the social sciences, particularly true when modeling environmental systems.

To conclude this historical persecutive, while I fully see the need and benefit of increasing model complexity, afforded by the *multi-scale, multi-science* computational engines. I would like to strongly advocate that we do not lose sight or undervalue the 1979 tradition of working with and analyzing reduced complexity models, an approach that adds insights and understanding beyond just data.

Background of the Carbon Mineralization Process

The main objective of this paper is to demonstrate how computational heat transfer techniques can be applied to carbon mineralization processes. Carbon mineralization is a promising technology for the permanent storage of carbon dioxide (CO2). In this pathway, water charged with dissolved CO2 is pumped into a subsurface reservoir, where it reacts with the surrounding host rock to form mineralized carbon products within the pore spaces [10, 11]. The process is governed by transport equations closely related to those used in modeling thermal systems, *e.g.*, advection-diffusion-reaction phenomena and the solidification of metal alloys.

Thus, in the light of the opening discussion, there are clear applications for large scale thermal computational techniques in furthering the advance of CO2 mineralization. Indeed, such computations are a mandate of the DOE funded center on Geo-processes in Mineral Carbon Storage (GMCS, https://gmcs.umn.edu/). However, it is very much true to say that we do not completely understand the full nature of the process constituents of carbon mineralization, in particular interactions between transport, geochemistry, and geomechanics. As such, in this paper, I would like to return to the spirit of the 1979 conference and focus on first order models that generate a basic understanding of the processes that couple transport, geochemistry, and geomechanics phenomena during carbon mineralization. In this respect, we will consider two case studies.

2. INFILTRATION AND HYDRATION

In the first case study, I will investigate infiltration and hydration in an initially dry porous rock medium. This is a preconditioning process; host rocks that have undergone a hydration reaction are more susceptible to subsequent carbon mineralization. The infiltration component of this problem is a classic Stefan melting problem [2], in the limit case where the specific heat vanishes; the predicted value of interest is the position of the advancing infiltration front $\Lambda(\tau)$. The hydration reaction provides an additional source term. This complicates computations, because the range over which this source term operates changes with time. Initially, the entire infiltrated region is reacting but as time advances, the reaction collapses onto the infiltration front. Ongoing work [12] demonstrates that an effective computational means of solving this problem is to use a modification of the fixed grid source-based enthalpy method [13,14]. The results from an initial model reveal two limiting similarity (square root in time) solutions that bound the numerical solution for the infiltration front advance; see Fig 2. The early time bounding solution is the analytical solution for the case of an infiltration without the hydration source; at very early times transport dominates. The late time analytical solution is obtained by assuming that the hydration reaction is coincident with the infiltration front, modifying the value of the fluid deficit (the "latent heat term") that must be provided to advance the front. This result provides critical inputs into understanding how material expansion, due to hydration, will determine the mechanical fracturing behavior of the host rock [15].

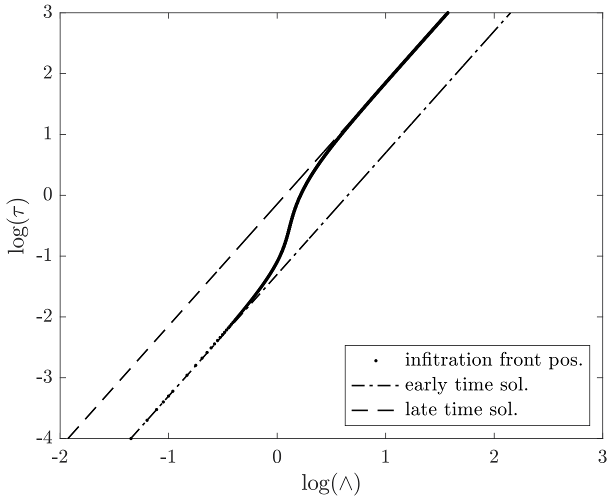

FIGURE 2. Log-Log plot of an infiltration front with time, in the presence of a hydration reaction. Note the crossover from early to late similarity solutions with square root in time behaviour.

3. CARBON STORAGE

Key questions that drive research in carbon mineralization are: What is the storage potential of a given host rock? How much CO2 can be stored within host pore spaces, fissures, and fractures? Typically, these questions are addressed by determining the volume fraction of the reactive minerals in the system. In porous rocks, however, *e.g.*, basalts ($\phi \sim 0.1$), the process might be limited by the ability to continuously flow the charge through the medium. In a process controlled by a fixed head drop, as the CO2 mineralizes in the pore space, the hydraulic conductivity reduces. This in turn leads to a slowing of the flow of the charge through the system, eventually leading to shutoff and the termination of further mineralization. This behavior can be simply modeled by coupling an advection-diffusion-reaction equation – a core ingredient of the computational heat transfer discipline – with an equation that tracks the porosity and hydraulic conductivity changes. Results from such models [16], operating in 1 and 2 dimensions, provide two critical scales: a time scale that represents the time over which an operation can continue before shutoff and a length scale that is associated with the maximum storage potential in a system. We can express this latter scale as

$$L_{max} = a\sqrt{\frac{K_i \Delta h}{k}}$$

where L_{max} [m] is the optimum distance between an input and output well, K_i [m/s] is the initial hydraulic conductivity, Δh [m] is the head drop across the system (between the wells), k [1/s] is an effective reaction rate, and a [-] is an order 1 pre-factor. This optimum value of L is the result of competition between available reactive area and charge flow rate. As L increases there is more surface available in the aquifer for reaction. However, a larger L also means a slower flow rate (the head drop between the input and output wells is fixed at Δh). Thus, as L increases, it becomes increasing difficult for the charge to access all the available reactive surface. Figure 2 shows the control volume finite element prediction for the fraction of mineral (per aquifer height) in the pore space at shutoff. The results are presented in a dimensionless square domain. The sides of the domain are no flow boundaries. A fixed dimensionless head of 1 is applied at $\xi = 0, \zeta = 0$ and fixed dimensionless head of 0 is applied at $\xi = 0.85, \zeta = 0.85$. In this configuration, the amount stored is close to the optimum, thus the optimum dimensionless distance between the input and output wells is 1.2, confirming the order 1 nature of the pre-factor a.

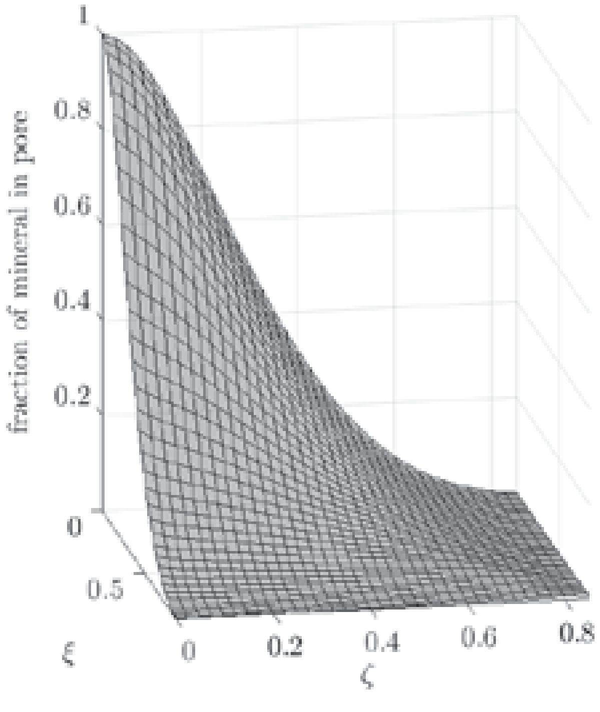

FIGURE 3. Numerical prediction of volume fraction of mineral (per reservoir height) in pore spaces at process shutoff

4. CONCLUSION

This paper demonstrates the continuing and important role of computational methods for thermal and energy systems. These methods will always take a leading role in furthering and advancing the process that are directly related to heat transfer phenomena, *e.g.*, energy storage and the production of metallic alloys. In addition, computational methods for thermal and energy systems are a key element in *multi-scale, multi-science* platforms, tools that can be readily applied to tackle the looming environmental problems faced by our society, particularly those related to energy and climate change. In this respect, the one concept I would like to reinforce is that such efforts should not be restricted to just large-scale computations. I strongly believe that there is still significant merit in complimenting such necessary large-scale endeavors with the analysis of more basic models that focus on elucidating understanding over creating data.

4. ACKNOWLEDGEMENT

Work funded by Center on Geo-processes in Mineral Carbon Storage, an Energy Frontier Research Center funded by the U.S. Department of Energy (DOE), Office of Science, Basic Energy Sciences (BES), under Award No. DE-SC0023429. The authors is also grateful for discussion and collaboration with Emmanuel Detournay, Joseph Labuz, and Peter Kang.

REFERENCES

[1] J. Fourier, Théorie Analytique de la Chaleur, Firmin Dicot Père et Fils, Paris, 1822.

[2] J. Crank, Free and Moving Boundary Problems, Clarendon Press, Oxford, UK, 1984.

[3] J. Stefan, Über die Theorie der Eisbildung. *Monatshefte für Mathematik* 1(1), 1–6, 1890.

[4] B. Šarler, Stefan's work on solid-liquid phase changes. *Eng. Anal. Boundary Elements,* 16, 83–92, 1995.

[5] J. Crank, P. Nicolson, A practical method for numerical evaluation of solutions of partial differential equations of the heat conduction type. *Proc. Camb. Phil. Soc.* .43, 50–67, 1947.

[6] N.R. Eyres *et al.*, The calculation of variable heat flow in solids. *Philosophical Transactions of the Royal Society of London. Series A, Mathematical and Physical Sciences,* 240, 1-57, 1946.

[7] P.H. Price, M.R. Slack, The effect of latent heat on numerical solutions of the heat flow equation, *British Journal of Applied. Physics*, 285–287, 1954.

[8] R.W. Lewis, K. Morgan (eds), Numeral Methods in Thermal Problems, Pineridge Press, Swansea, Wales, 1979.

[9] J. Taylor, M, Hondzo, V.R. Voller, Abiotic drivers of a deep cyanobacteria layer in a stratified and eutrophic lake. *Water Resources Research*, 57, e2020WR027987, 2021.

[10] J.M. Matter, P.B. Kelemen, Permanent storage of carbon dioxide in geological reservoirs by mineral carbonation. *Nature Geoscience,* 2, 837-841, 2009.

[11] S.Ó. Snæbjörnsdóttir *et al.*, Carbon dioxide storage through mineral carbonation. *Nature Reviews Earth & Environment,* 1, 90–102, 2020.

[12] E. Detournay, V.R. Voller, A simple model of a hydration experiment. In preparation, 2024.

[13] V.R. Voller, S. Peng, Y.F. Chen, Numerical solution of transient, free surface problems in porous media. *International Journal for Numerical Methods in Engineering*, 39, 2889–2906, 1996.

[14] V.R. Voller, C.R. Swaminathan, B.G. Thomas. Fixed grid techniques for phase change problems: A review. *International Journal for Numerical Methods in Engineering,* 30, 875–898, 1990.

[15] M. Uno *et al.*, Volatile-consuming reactions fracture rocks and self-accelerate fluid flow in the lithosphere, *Proceeding National Academy of Science*, 119, e2110776118, 2022.

[16] V.R. Voller, M. Chen, P.K. Kang, Estimating the capacity of basalts for carbon mineralization: Transport limitations and storage potential, to be presented at CouFrac2024.

Sixth International Conference on Computational Methods for Energy and Thermal Problems
THERMAECOMP2024, Sept. 9-11, 2024, Budva, Montenegro
N. Massarotti, P. Nithiarasu, and I. Vušanović (Eds.)

SOLAR PV SYSTEMS WITH ENHANCED PASSIVE COOLING AND VENTILATION

Victoria Timchenko

School of Mechanical and Manufacturing Engineering, University of New South Wales, Sydney, NSW 2052, Australia

ABSTRACT

The application of renewable energies such as solar energy in the building sector has increased notably considering the adverse impacts of climate change on human life; hence many studies have focused on the application of photovoltaic panels in buildings. A major problem with photovoltaic panels is that their electrical performance and lifespan decrease with an increase of their temperature. This work will present an overview of computational and experimental research undertaken at the UNSW Sydney on development of a passive cooling method, which enhances convection heat flux on the module's rear surface for both stand alone and rooftop PV systems. The effects of radiation and natural convection flow in a building integrated photovoltaic (BIPV) system will be also presented.

Key Words: *Heat Transfer, PV module, Passive cooling.*

1. INTRODUCTION

Reducing photovoltaic (PV) module operating temperature potentially brings system-level economic benefits and positively impacts the environment. Despite the newly adapted cell technologies a lower temperature dependency for the output power, a module would still have a loss of around 8%-9% of the electrical generation if operated 30°C above the standard test condition. A technique that could reduce the module operating temperature reduces this thermal loss and also the material degradation rate within the PV module. It was estimated that even just 1°C of temperature reduction could increase the longevity of the module by 7% [1]. With a cost-effective cooling approach, the module lifespan can be extended considerably while increasing the project profitability and reducing the need for recycling.

With these potential benefits in sight, several PV cooling technologies have been investigated in the last decade [1-3]. However, most of these are yet to demonstrate on a large scale in a cost-effective manner. Although passive air cooling using aluminium fins on the module rear surface has the potential to deliver a positive economic impact, it comes with a few drawbacks. The most crucial concern is the high electrical insulation requirement needed for such a conductive metal backsheet [4].

To alleviate the issues with the existing passive cooling methods and to enhance the convective heat flux on the rear surface of a PV module, we proposed and investigated a low coverage-ratio and low-cost approach using vortex generators (VGs) [5-6]. In this works VGs have been tested both numerically and experimentally primarily under free convection condition, indoors. We have also studied numerically a full scale BIPV system to acess performance in terms of passive ventilation of a room and passive cooling of the rooftop-mounted PV panels [7]. Different solar heat fluxes and ambient temperatures under the natural convection mechanism have been considered and the role of surface emissivity for the part of the roof beneath the PV panels has been evaluated.

2. METHODOLOGY

To study the effect of VGs on the PV module's thermal and fluid-dynamic behaviour the computational models were developed for both standalone PV module and the rooftop PV system. A cylindrical air domain was created to simulate the natural convective flow around the entire module in 3D, as shown in Figure 1 (only the rooftop PV system is presented). The module was tilted 45° to the horizontal floor and placed in the middle of the simulated cylinder, centred at 0.5 m above the ground corresponding to the experimental setup. Instead of VGs being directly attached to the heated module rear surface, we have developed a VG design that attaches to the roof surface, where the VGs have no physical contact with the PV module. This arrangement bypasses the IEC testing requirement [8] that would apply for VGs attached on the module surfaces and therefore allows a broader choice of material and a more feasible retrofitting solution. The module and the roof form a tilted channel where the airflow is driven by buoyancy force in the absence of wind. The designed VG array can interact with the free convection channel flow and produce longitudinal vortexes.

All simulations were performed using ANSYS FLUENT computational fluid dynamics (CFD) software, with the 'rectangular wing' (RW) design selected from COMSOL Multiphysics® optimisation, based on the criterion of a minimum area-average PV module surface temperature. The side and top boundaries of the cylinder were modelled as openings, via the 'pressure outlet' boundary type in ANSYS Fluent. Such setup with cylindrical domain and this boundary type has been successfully used in literature for engineering simulations of fluid flow which involve natural convection. Heat transfer within the layers of a PV module has been accounted for by using the 'shell conduction' model in ANSYS Fluent, with the module being added to the geometry as a zero-thickness surface. This model included the material names and thicknesses of the layers of the PV module, as published in our previous work [5]. The shell conduction modelling approach has also been adopted for modelling the roof, with a good agreement of numerical and experimentally measured 10°C temperature differences between the top and bottom surfaces of the roof. The heat flux of 570 W/m^2 was assumed (based on the experiment specification) to be generated in the silicon layer of the PV module.

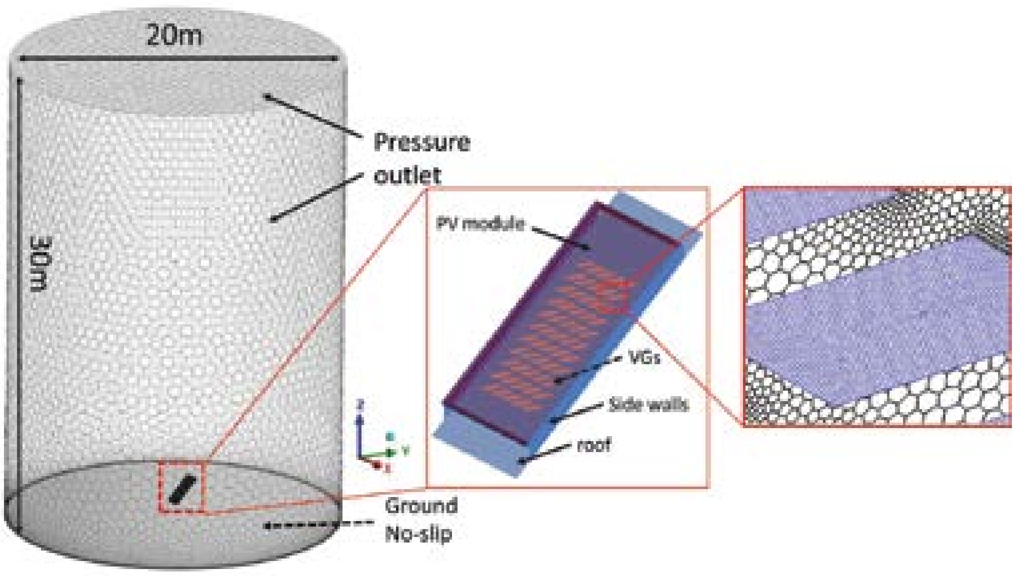

Figure 1 Diagram of the cylindrical computational domain including the PV module and roof arrangement (left); mesh on the PV module and the VGs (right).

The Shear Stress Transport (SST) model, suitable for a wide range of engineering applications, was used to represent turbulent structures generated underneath the module and in proximity to the VGs and the module frame. Air has been assumed to follow the perfect gas law. Transient simulation has been adopted as unsteady flow structures have been identified both in the experiment and in the numerical results. In addition, the surface-to-surface radiation model was enabled in ANSYS Fluent to accurately capture the radiation exchange, especially between the VGs and the module surface, as well as between the surface of the module and the surface of the roof in the case of the rooftop system.

A series of experiments were undertaken using infrared thermography and particle image velocimetry (PIV) to investigate the performance of VGs on a PV module. The VGs were 3D printed at a thickness of 1.5 mm using Polylactic acid (PLA) material. The thermography measurement quantifies the VG performance in terms of the module front surface temperature reduction. By measuring the velocity field on a plane normal to the module surface, the PIV measurement provides an insight into the interaction between free convection boundary layer and a selected VG design. The algorithm first performs a Particle Image Velocity (PIV) pass on the image sequence to obtain a velocity field estimate and then tracks individual particles using PTV algorithm. The experiments were conducted in a large, enclosed laboratory with an area of ~400 m^2 and a ceiling height of approximately 10 m, which allowed us to reproduce near free convection conditions in a laboratory setting. All details for the experimental set-up can be found in our works [5-6].

3. RESULTS

The numerical models developed in this work were validated with the experimental setup by comparing velocity contours obtained from the CFD simulation to that of the PTV measurement at matched conditions on a vertical slice of the flow field for the baseline case and the VG case. One of the examples of validation is shown in Figure 2.

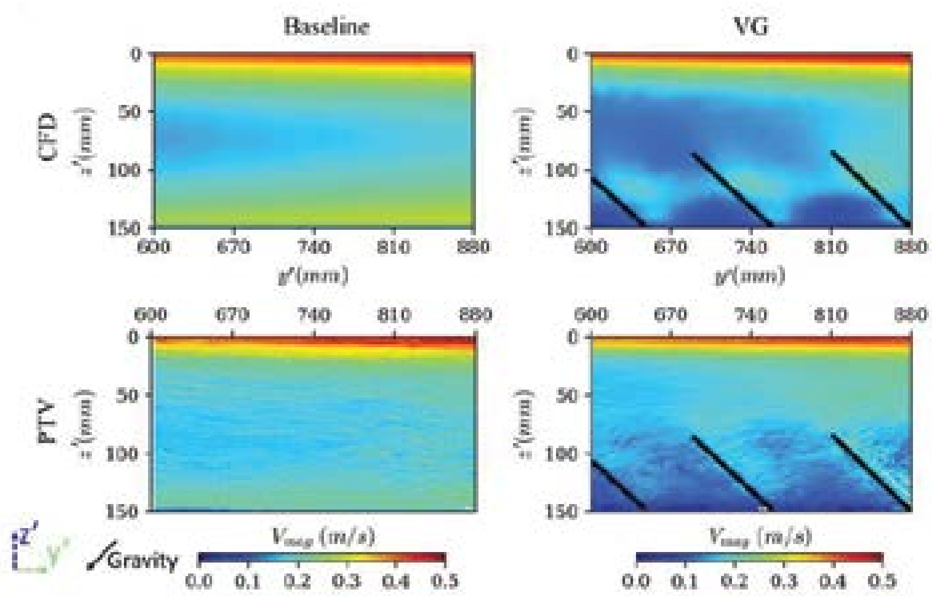

Figure 2: Comparison of mean flow field obtained from the simulations (top row), PTV experiments (bottom row), where the left and right column corresponds to baseline and a VG case.

Similar to other VG optimisation studies [9-10], the design and the arrangement of the VGs in this work is a trade-off between the flow resistance and the flow mixing effect. Different VGs arrangements were analysed to characterize the cooling performance in terms of the temperature difference ΔT between the baseline (no VGs) and VGs cases. The height of VGs over the roof gap (the ratio H/G) controls how much of the channel is occupied in the z' direction (shown in Figure 2) and thus can be regarded as the vertical filling ratio. In other direction, the horizontal filling-ratio W/Px (shown in Figure 3a) measure how much the VG is occupying the channel in the horizontal (spanwise) direction. Thus, a wider VG and smaller Px (less gap between VG spanwise) would lead to a smaller W/Px ratio leaving less space for the airflow.

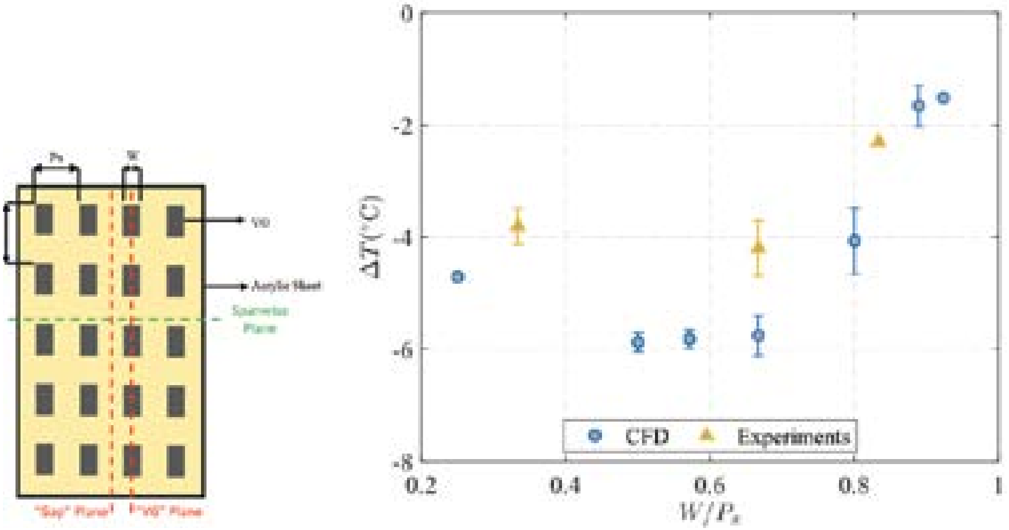

(a) (b)

Figure 3. (a) VGs arrangement; (b) The simulated and experimentally measured ΔT as a function of W/Px, for cases with H/G ~ 1.

As illustrated in Figure 3b, both computational and experimental data result in the optimal value for W/Px around 0.6, which allows an adequate level of flow mixing while maintaining a high flow rate in the roof-module channel, consequently, a high cooling potential.

The vertical motion created by the longitudinal vortexes can be viewed in the z’ component velocity plot presented in Figure 4. This vertical flow is responsible for the enhanced convective flux on the module surface and as a result, the change in the temperature distribution as shown in Figure 4. Same as that in the streamwise results [6], the flow is redirected downward behind the VGs and upwards between the VGs.

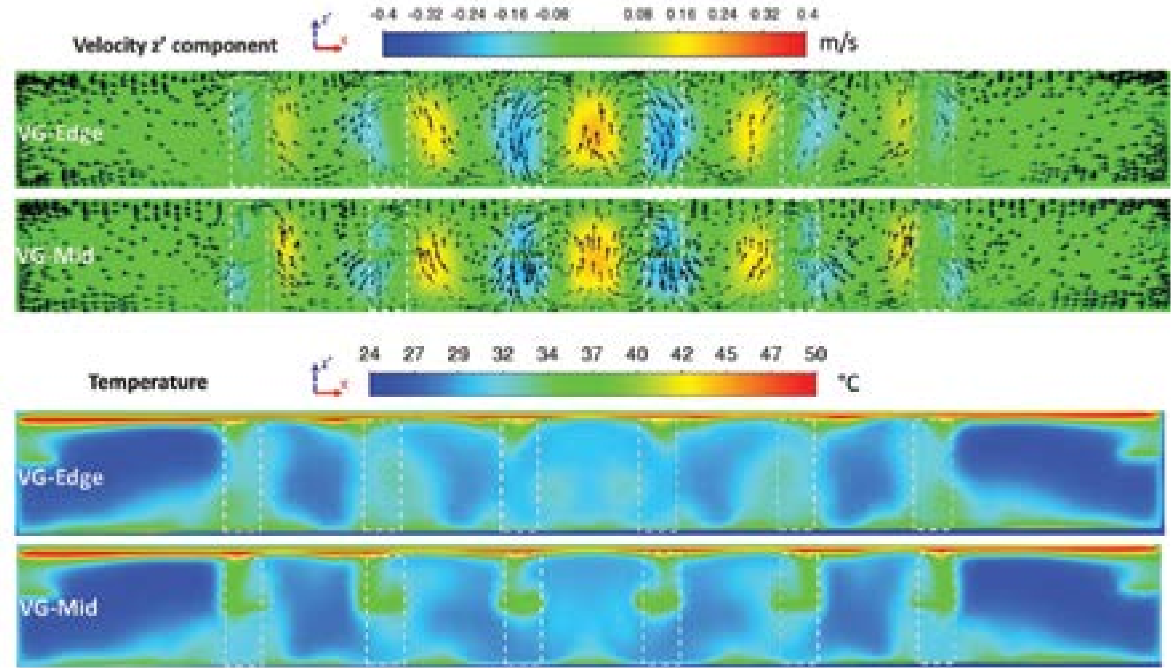

Figure 4. Simulated spanwise results in the module-roof channel for case corresponding to the low W/Px and high H/G case: (top) the vertical velocity component contours (z' direction) with 3D velocity vector; (bottom) the temperature contours at the spanwise xz' plane near the middle of the module (y'~0.8m) where the white dash line boxes are the projection of the VGs.

4. CONCLUSIONS

For an array of VGs, the ability to sustainably generate a longitudinal vortex is crucial for achieving a uniform cooling effect along the length of the module, which is highly dependent on the spacing and the aerodynamic shape of the VGs. The horizontal spacing, and therefore the density of the VGs, controls the radiation flux from the rear module surface and the effectiveness of the formed vortex. Therefore, there is an optimal spacing for each VG design. For rooftop modules with VGs attached on the roof we have found that: (1) The rectangular wing VGs reduce the module temperature by over 4 °C on a rooftop experiment setup under free convection. The trend from the simulation results agrees with the experimental results. (2) To achieve the optimal cooling effect, the VG should be as long as the roof channel is allowed without contacting the module. The VGs with a high vertical filling ratio fully utilise the high-velocity free convection boundary layer attached to the module rear surface. (3) The choice of shape and arrangement of VGs is a balance between the vortex formation and the flow resistance. A densely arranged VGs design (high horizontal filling ratio) can introduce more mixing to the channel flow at the cost of a lower overall flow rate.

For the developed BIPV system in [7] we have found that increasing the surface emissivity for the part of the roof beneath the PV panels intensifies the natural convective currents which in turn provides better cooling for PV panels and higher passive ventilation rates for the indoors. Up to a 3K decrease in the mean operating temperature of the panels and a 34% increase in the convective mass flow rate were observed by increasing the roof surface emissivity from 0.2 to 0.9 under different conditions.

REFERENCES

[1] O. Dupré, R. Vaillon, and M. A. Green, "Thermal behavior of photovoltaic devices," Phys. Eng., vol. 10, pp. 973–978, 2017.

[2] M. Hasanuzzaman, A. Malek, M. M. Islam, A. K. Pandey, and N. A. Rahim, "Global advancement of cooling technologies for PV systems: A review," Sol. Energy, vol. 137, pp. 25–45, 2016.

[3] J. Siecker, K. Kusakana, and B. P. Numbi, "A review of solar photovoltaic systems cooling technologies," Renew. Sustain. Energy Rev., vol. 79, pp. 192–203, 2017.

[4] T. M. Walsh, Z. Xiong, Y. S. Khoo, A. A. O. Tay, and A. G. Aberle, "Singapore modules-optimised PV modules for the tropics," Energy Procedia, vol. 15, pp. 388–395, 2012.

[5] Z. Zhou, S. Tkachenko, P. Bahl, D. Tavener, C. de Silva, V. Timchenko, J. Y. Jiang, M. Keevers, M. Green, Passive PV module cooling under free convection through vortex generators, Renewable Energy, vol. 190, pp. 319–329, 2022

[6] Z. Zhou, P. Bahl, S. Tkachenko, A. Hari, C. de Silva, V. Timchenko, M. A Green, Vortex Generators for Passive Cooling of Rooftop Photovoltaic Systems Under Free Convection, IEEE Journal of Photovoltaics, vol. 13, pp 743-749, 2023.

[7] H. A. Moghaddam, S. Tkachenko, G. H. Yeoh, V. Timchenko, A newly designed BIPV system with enhanced passive cooling and ventilation, Building Simulation, vol.16, pp.2093–2107, 2023.

[8] IEC, "61215-1: 2016 Terrestrial photovoltaic (PV) modules – Design qualification and type approval – Part 1: Test requirements," vol. 1, 2016.

[9] M. Fiebig, "Embedded vortices in internal flow: heat transfer and pressure loss enhancement," Int. J. Heat Fluid Flow, vol. 16, no. 5, pp. 376–388, 1995.

[10] F. A. S. da Silva, D. J. Dezan, A. V Pantaleao, and L. O. Salviano, "Longitudinal vortex generator applied to heat transfer enhancement of a flat plate solar water heater," Appl. Therm. Eng., vol. 158, p. 113790, 2019.

Sixth International Conference on Computational Methods for Energy and Thermal Problems
THERMAECOMP2024, Sept. 9-11, 2024, Budva, Montenegro
N. Massarotti, P. Nithiarasu, and I. Vušanović (Eds.)

THE ROLE OF CFD IN IMPROVING INDOOR ENVIRONMENTS AIR QUALITY, COMFORT AND SAFETY

Fausto Arpino
University of Cassino and Southern Lazio, 03043, via G. Di Biasio 43, Italy, f.arpino@unicas.it

ABSTRACT

The COVID-19 pandemic has fundamentally changed our understanding of respiratory virus transmission, highlighting the critical role of indoor environments and the necessity of effective ventilation. Traditional public health guidelines emphasized large-droplet and fomite transmission, advocating for social distancing and surface disinfection. This underestimated airborne transmission, which was acknowledged as the primary pathway for SARS-CoV-2 by major health organizations in spring 2021. Studies showed that surface disinfection had minimal impact on COVID-19 spread, while cancelling gatherings and closing schools significantly reduced transmission. As the pandemic continued, managing indoor environments became crucial. This led to a focus on indoor air quality and improved ventilation and air cleaning strategies. Computational Fluid Dynamics (CFD) techniques were vital for these efforts. Validated CFD simulations provided insights that helped optimize HVAC systems and design effective airflow patterns to ensure safety and comfort in confined spaces. This work presents mathematical and numerical modeling activities conducted in various indoor environments that have contributed to a better understanding of pollutant and viral aerosol transmission, with particular emphasis on the validation of the results obtained.

Key Words: *Heat Transfer, Finite Elements, Natural Convection.*

1. INTRODUCTION

The COVID-19 pandemic has profoundly reshaped our understanding of respiratory virus transmission, unveiling the critical role of indoor environments and the necessity for adequate ventilation in these settings. This shift is due to the recognition of airborne transmission as the primary route for many respiratory infectious diseases [1].

The transmission of respiratory viruses may occur through three basic routes. Spray transmission, traditionally known as large-droplet transmission, involves virus-laden drops (i.e., particles larger than 100 μm in diameter) emitted by an infected person and deposited on the mucosal surfaces of a susceptible subject. Inhalation transmission refers to respiratory droplets suspended in the air (particles below 100 μm in diameter, also known as aerosol or airborne droplets), which can remain airborne for extended periods and travel long distances in an indoor environment. Finally, touch transmission refers to animate or inanimate surfaces contaminated by virus-laden drops and/or droplets (i.e., fomites), being touched by people then touching their mucosa.

Historically, public health guidelines primarily addressed large droplet as transmission routes. It was not until the spring of 2021, due to the increasing scientific evidence, that major health organizations like the US CDC and WHO recognized airborne transmission as the predominant pathway for SARS-CoV-2. Environmental measures to disinfect and clean surfaces in public and semi-public places did not significantly reduce the spread of COVID-19. In contrast, the cancellation of small gatherings and the closure of educational institutions, i.e., activities characterized by high crowding in poorly ventilated indoor environments, had a significant impact on reducing the spread of the virus.

A change in the management of indoor environments is required, with greater attention to indoor air quality, and the development of better strategies for effective ventilation and air cleaning. This is backed by the findings of Buonanno et al. [2], who proved the effect of enhanced ventilation against virus transmission. Numerical modelling, particularly Computational Fluid Dynamics (CFD) techniques, is essential to achieve this goal. CFD provides detailed information on velocity, pressure and temperature fields in indoor environments, as well as spatial and temporal particle distribution, by solving well-known conservation equations. These insights, which are not achievable with experimental approaches alone, can contribute to the optimization of Heating, Ventilation and Air Conditioning (HVAC) systems and the effective design of airflow patterns within confined spaces, aiming to ensure occupants' safety and comfort. This work focuses on different indoor environments to provide insights into the various situations that individuals are likely to encounter daily. In this work both small-scale and large-scale environments are examined, as particle dynamics can significantly differ, affecting exposure and risk for vulnerable subjects. Investigations are conducted by means of CFD simulations and experimental measurements, paying particular attention to validation of numerical results.

1. MATHEMATICAL MODEL

The droplets flow evolving in the investigated indoor environments can be regarded as a dispersed dilute two-phase flow, since the spacing between droplets is sufficiently large and the particle volume fraction sufficiently low ($< 10^{-3}$) [3], [4]. Fluid-particle interaction is solved by using a Eulerian-Lagrangian approach, modelling the air (i.e., the continuous phase) with a Eulerian approach and tracking the particles (i.e., the discrete phase) individually by solving a force balance equation (Lagrangian Particle Tracking, LPT).

Particles are assumed to be spherical. The trajectory of a single particle can be expressed by the Newton Second Law:

$$m_d \frac{d\boldsymbol{u}_d}{dt} = \boldsymbol{F}_{body} + \boldsymbol{F}_{surface} + \boldsymbol{F}_{interaction} \tag{1}$$

where $\boldsymbol{F}_{body}$ is the body force and is given as the sum of gravity, $\boldsymbol{F}_G$, and virtual mass forces, $\boldsymbol{F}_{VM}$; $\boldsymbol{F}_{surface}$ is the surface force and is the sum of drag, pressure, Basset, Saffman and Magnus forces, as described by the following equation:

$$\boldsymbol{F}_{surface} = \boldsymbol{F}_D + \boldsymbol{F}_{pressure} + \boldsymbol{F}_{Basset} + \boldsymbol{F}_{Saffman} + \boldsymbol{F}_{Magnus} \tag{2}$$

$\boldsymbol{F}_{interaction}$ is the finally the interaction force, that is the sum of Brownian motion force ($\boldsymbol{F}_{BM}$), particle-particle interaction force ($\boldsymbol{F}_{pp}$), and particle-wall interaction force ($\boldsymbol{F}_{pw}$).

For particles with a small diameter, pressure, Safmann and Magnus forces can be safely neglected compared to drag forces. In addition, when the fluid density is much smaller than the particle density, the Basset force can also be considered negligible. Brownian motion force can be neglected, since the particles considered are of the order of microns in size. Particle-particle interaction forces must be considered for dense particle suspensions; particle-wall interaction forces are important in dense flows, as well as in wall-dominated dilute flows. These forces are assumed to be negligible in the proposed investigations. More information about the Eulerian-Lagrangian mathematical model are available in the scientific literature [3], [4] and are not reported here for brevity.

The particle number emission rate (ERN, particle s^{-1}), i.e., the size-dependent number of particles exhaled by the infected subject per unit time, was estimated for speaking activities based on experimental analyses by Johnson et al. [5] and Morawska et al. [6]. The original distributions were fitted into simplified distributions comprising five size ranges. Given the negligible contribution of spray-borne respiratory particles to infection risk [4], [7], [8], the five size ranges considered are limited to the airborne respiratory particle range (<90 μm).

Volume distributions and emission rates (ERV, $\mu l \cdot s^{-1}$) were calculated assuming the particles are spherical and, since evaporation occurs rapidly once particles are emitted [9], [10], the post-evaporation number and volume distributions were considered in numerical simlations. To this end, the volume particle distribution before evaporation (i.e., as emitted) was reduced to that resulting from the quick evaporation, assuming a volume fraction of non-volatiles in the initial particles of 1%. This evaporation process reduces the particle diameter to about 20% of the initial size.

2. RESULTS

The Eulerian-Lagrangian model has been applied to the analysis of droplets dispersion in different indoor environments and for different Heating, Ventilation, and Air Conditioning (HVAC) operation conditions. The first significant finding was the infection risk assessment based on CFD simulation of large and airborne droplets distribution in a close contact interaction between an infected mouth-breather subject and a susceptible subject [4]. PIV measurement for a mouth breathing case study provided the required information to choose the velocity boundary conditions employed in CFD simulations. In particular, the adopted boundary condition for the mouth-breathing receiver was verified by comparing numerical results with PIV data in terms of velocity profiles obtained at different distances from the mouth of the emitter. Experimental (PIV) and numerical (CFD) velocity contours obtained in the sagittal plane, by synchronizing the instant of time for breathing at which the maximum velocity values are reached, are presented in Figure 1, whereas PIV and CFD vertical velocity profiles in Figure 1 sagittal plane at a distance from the emitter mouth equal to 0.10 m and 0.32 m are compared in Figure 2. The peak numerical and experimental peak velocities differ by 6% and 7% at interpersonal distances of 0.10 m and 0.32 m, respectively.

Figure 3 shows velocity contours, with droplet ant airborne particles distributions at different time levels and for a distance between subjects of 0.76 m. Obtained results showed that for this distance, large droplets fall to the ground without reaching the susceptible surfaces of the receiver, while the airborne droplets are transported by the air velocity field, reach the receiver, and then are spread while rising in a vertical direction due to the effect of buoyancy forces.

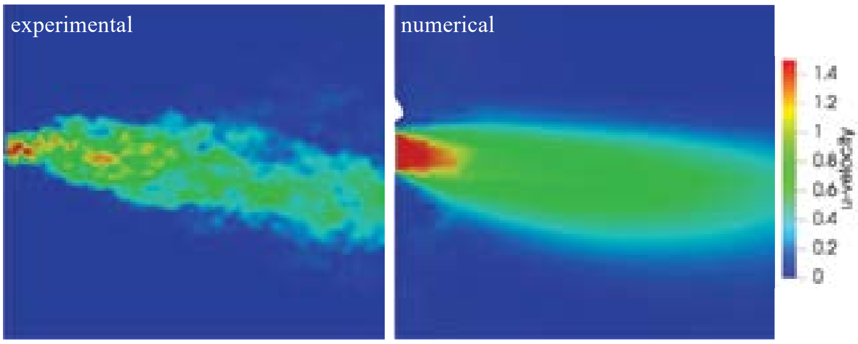

FIGURE 1. Numerical velocity contours and droplet distribution during a single breath at a distance of 0.76 m between people [4]

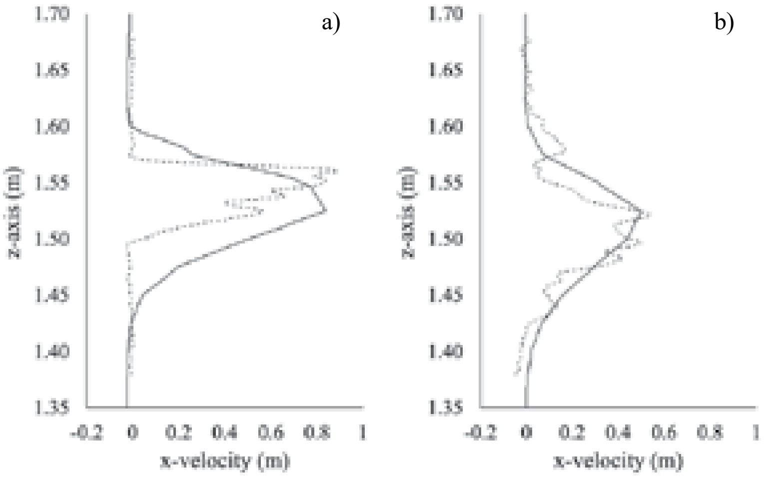

FIGURE 2. Experimental (particle image velocimetry, dotted lines) and CFD (solid lines) velocity profile comparison obtained in a sagittal plane at a distance from the emitter mouth equal to 0.10 m (a) and 0.32 m (b) [4].

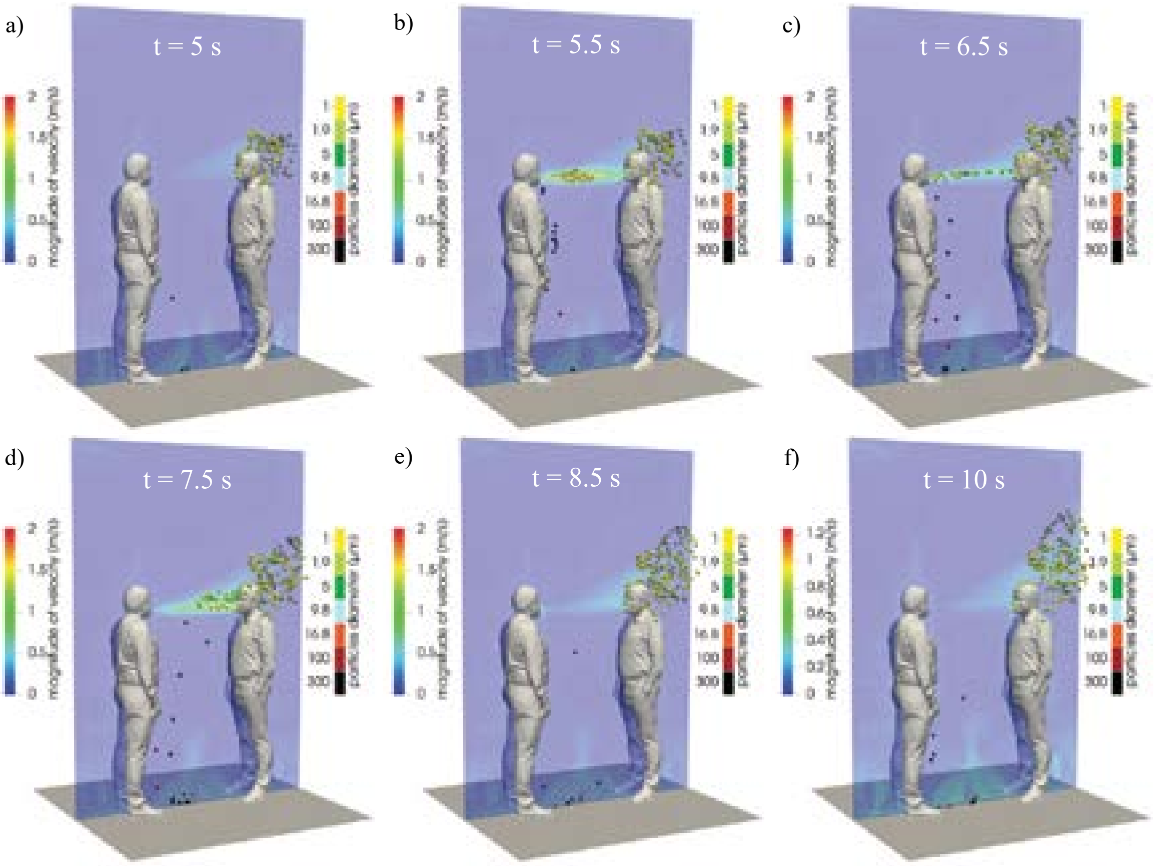

FIGURE 3. Numerical velocity contours and droplet distribution during a single breath at a distance of 0.76 m between people [4].

Figure 4 shows the dose of non-evaporated airborne droplets, that can be directly related to risk. For distances > 0.6 m, only the airborne droplet contribution to the total dose received by the infected subject is observed, demonstrating that the interpersonal distance is a key parameter in evaluating the close contact risk because the susceptible subject could fall within the highly concentrated droplet-laden flow exhaled by the infected subject. While the trajectory of large droplets is mostly affected by their inertia, and the related effect is negligible for distances > 0.6 m, the spread of airborne droplets is affected by the spread angle of the exhaled flow. At short interpersonal distances (roughly < 0.76 m) from the emission point, the dose of airborne droplets decays following the $1/L$ rule (with L representing the interpersonal distance), whereas for interpersonal distances in the range of 0.76–1.75 m, where the exhaled air flow angle becomes wider, the dose of airborne droplets decays following the $1/L^2$ rule as recognized for passive tracer-gas decay. CFD investigations allowed to evaluate the actual infection risk as a function of distance and exposure time, demonstrating the combination of these two factors is crucial for the risk assessment.

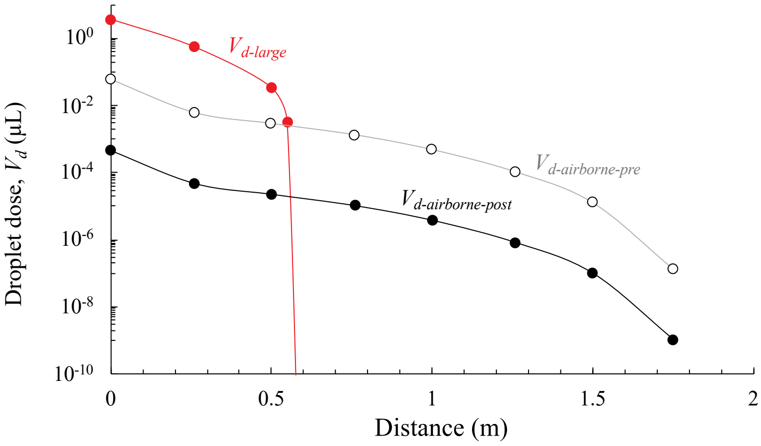

FIGURE 4. 1-min large and airborne droplet doses received by the susceptible subject (by deposition and inhalation, respectively) as a function of the distance between the two subjects [4].

The developed model has then been applied to different real-life indoor environments, such as car cabins [11], [12] and school rooms [13], characterized by significantly different characteristic size. Particle dispersion and inhalation in car cabin environment was investigated considering four occupants and three HVAC system ventilation modes: front ventilation mode (air entering the cabin through four front vents), windshield defrosting mode (air entering through one vent located under the windshield) and mixed ventilation (all the five vents enabled). All modes considered outside air intake without recirculation, and the windows closed throughout the journey. Different HVAC flow rates (from 10% to 100% of the maximum flow rate) were investigated, with the intermediate flow rate (Q50%) set at 216 m^3/h [14] When both front and windshield defrosting inlets are enabled, the airflow is split: each front vent introduces 12.5% of the flow rate, and the windshield vent introduces the remaining 50%.

The computational domain and the grid employed for mixed ventilation and front ventilation scenarios are available in Figure 5; the car model internal volume is 3.46 m^3. More details about mathematical model employed, boundary conditions, grid sensitivity analysis and results validation are available in [11], [12].

An example of obtained results is available in Figure 6, that illustrate streamlines, mean velocity contours (left), and the spatial distribution of airborne respiratory particles (right) after 30 min for the driver-infected scenario. It can be observed that the streamlines carry the respiratory particles emitted by the driver towards the passenger sitting behind him (passenger #2), resulting in higher exposure for passenger #2 as also shown by the spatial distributions of the airborne respiratory particles

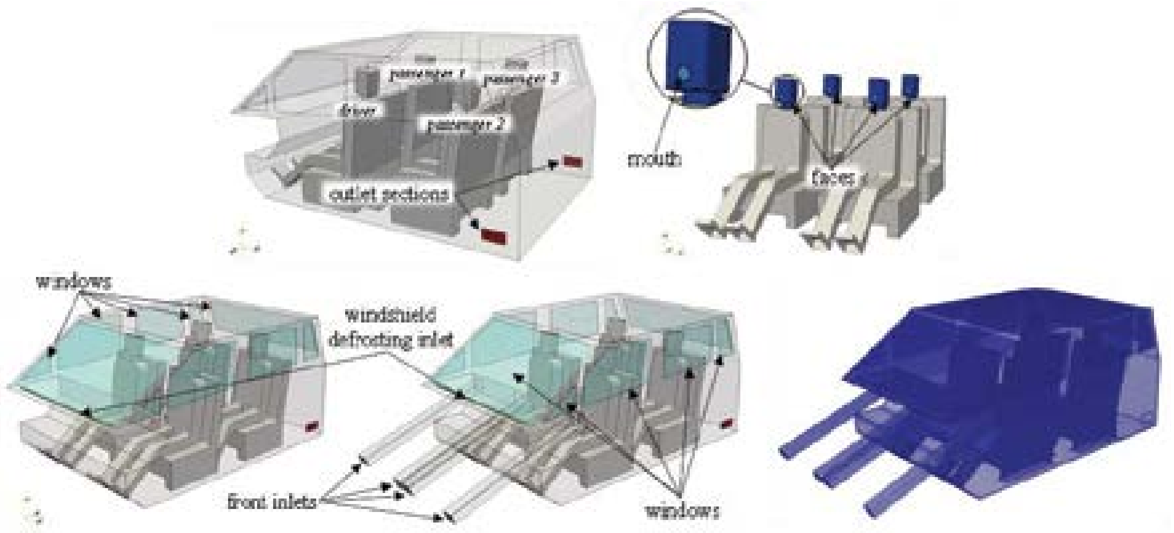

FIGURE 5. Computational domain with boundary patches, together with the computational grid employed for mixed ventilation and front ventilation scenarios [11], [12].

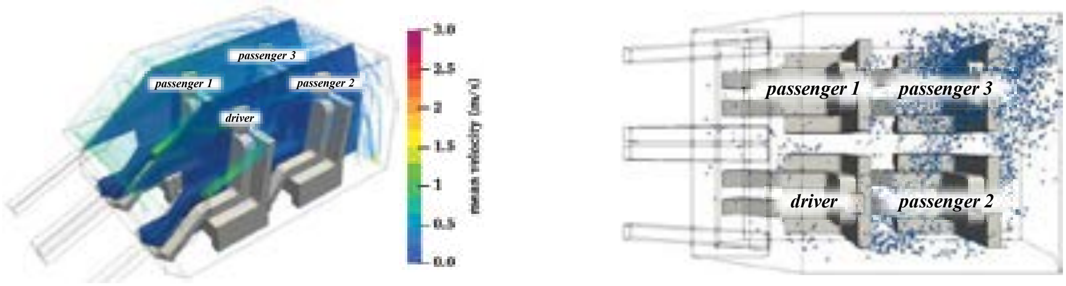

FIGURE 6. Spatial particle distribution after 30 min in case of Q50% and speaking activity. a) front ventilation mode, driver infected, b) mixed ventilation mode, driver infected c) mixed ventilation mode, passenger #3 infected. [11], [12]

CFD investigations demonstrated that, as expected, the dose and risk values are strongly influenced by the flow rate. Despite a general decreasing trend in risk as the HVAC flow rate increases, the risk for passengers sitting in the back significantly depends on specific airflow patterns at different flow rates, which can undermine the effectiveness of particle removal.

The dependence of exposure to airborne particles on HVAC operation is also evident in larger indoor environments, as in the case of a university lecture room [13]. This case study explores the spread of droplets from a source mimicking an infected person speaking continuously for two hours in a university lecture room. It evaluates the impact of different air supply rates: 3.75 Air Changes per Hour (ACH), 7.5 ACH, and 15 ACH. The study was conducted in a lecture room at the University of Naples "Parthenope," using a turbulent mixing airflow system with 8 helical swirl diffusers and 3 exhaust grilles. The room's doors and windows were kept closed, and it was unoccupied during the study to maintain consistent conditions. A picture of the lecture room and a sketch of the computational domain employed for CFD investigations are available inf Figure 7. Details about mathematical model, boundary conditions, computational grid adopted, and validation of numerical results are available in [13] and are not reported here for the sake of brevity.

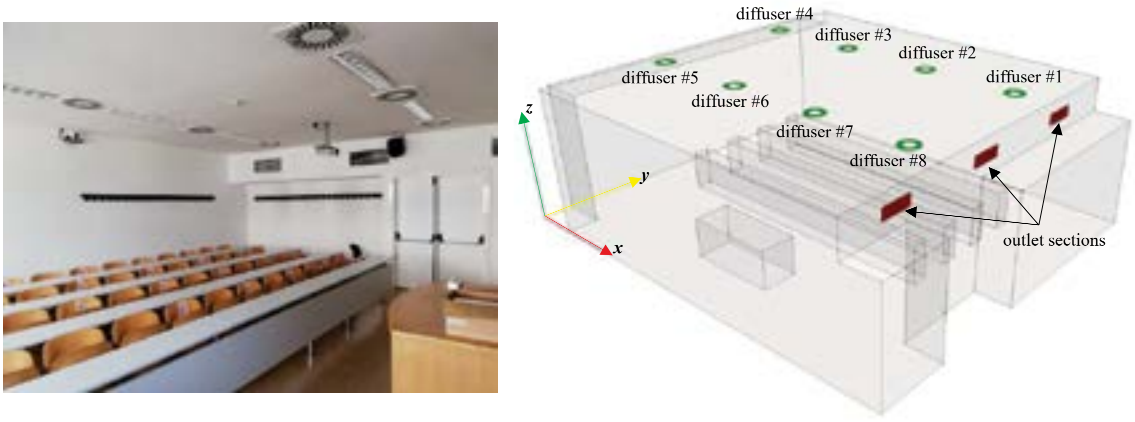

(a)

(b)

FIGURE 7. Picture (a) and 3D model (b) of the lecture room under investigation [13].

In order to numerically evaluate the average dose of particles to which occupants might be exposed during a two-hour lesson when the teacher is the infected subject, twelve control volumes were selected to calculate the average amount of airborne respiratory droplets (expressed in ml) in each volume for each investigated ACH value. Each control volume is 1.97 m wide, 0.88 m deep and 0.72 m high, extending from the benches up to a height of 1.5 m, thereby enclosing the breathing zone of the occupants and allowing to estimate their exposure to the particles emitted by the infected teacher. An example of obtained results is graphically displayed in Figure 8 for two ACH values: 3.75 (left) and 15 (right).

Obtained results show that the location of most critical control volume (i.e., with the highest parcels concentration) changes with the air supply rate. Besides, even though the overall number of droplets suspended in the air decreases when increasing ACH, there is not always a local decrease of the exposure. On the contrary, in several control volumes the particle concentration increases as the ACH value increases because of local characteristics of the air velocity field.

This behaviour may be attributed to the asymmetric disposition of the seats with respect to diffusers and to the extraction grilles, confirming the importance of using numerical investigations based in CFD techniques represent for both the design and management stages of indoor environments to optimize air quality, safety and comfort.

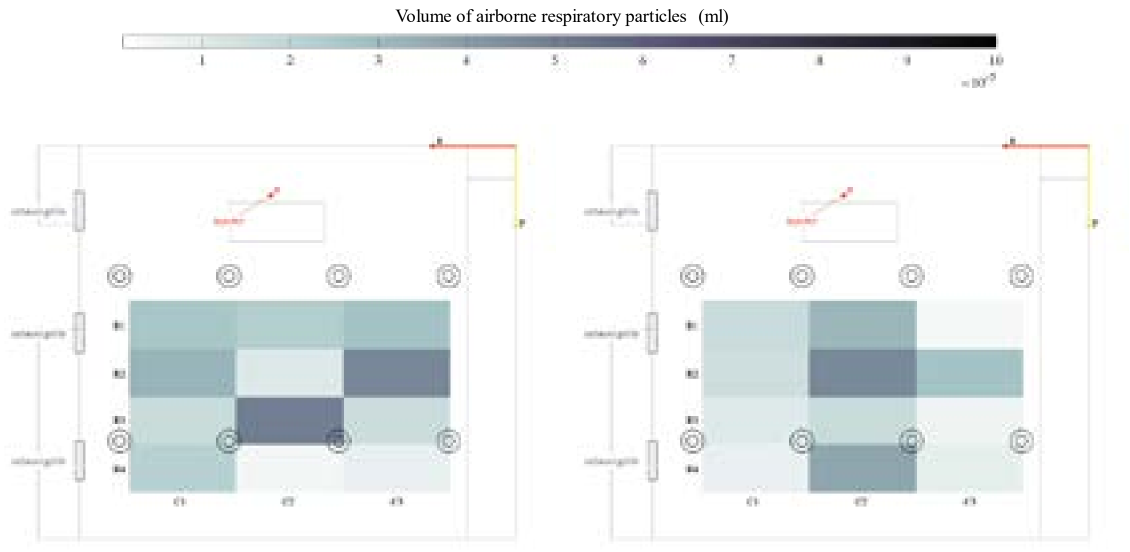

(a) 3.75 ACH

(b) 15 ACH

FIGURE 8. Colormaps of the airborne respiratory particles (expressed in ml) inside the selected control volumes, for the different AERs [13].

4. CONCLUSIONS

A Eulerian-Lagrangian mathematical and numerical model has been set to investigate pressure, velocity, temperature and particles distribution in indoor environments. The spread and distribution of virus-laden droplets, emitted by an infected subject, in three distinct situations occurring in indoor environments have been presented: a close-distance conversation between two people, a car journey, a university lecture.

CFD investigation applied on face-to-face interactions in stagnant air demonstrated that large droplets (> 100 μm) significantly contribute to the infection risk at distances less than 0.6 meters. At greater distances (0.81 m for personal and 1.06 m for social distancing), the risk primarily comes from airborne droplets. Both distance and exposure time are crucial factors; significant risk persists even with brief exposures (10 seconds) at close distances, while longer exposures (15 minutes) are needed to pose a risk at greater distances.

Findings from car-cabin investigations demonstrated the importance of using CFD approaches to properly assess individual risks in confined spaces, as fluid-dynamic conditions significantly influence airflow patterns and, consequently, the spatial distribution of the virus-laden particles within the cabin. Besides, CFD results suggested that ad-hoc designing of closed environments is achievable, especially when the spatial locations of the occupants are fixed.

Findings form lecture room simulations highlighted that the ACH alone is not sufficient to assess the effectiveness of air distribution systems and local air flow patterns must be considered when designing ventilation systems and assessing the risk of exposure to airborne diseases in indoor environments.

The application of the proposed methodology to different indoor environments demonstrated the importance of using CFD investigations to properly design and manage HVAC systems, assessing individual risks in such confined spaces, as fluid-dynamic conditions significantly influence the airflow patterns and, consequently, the spatial distribution of the virus-laden particles.

REFERENCES

[1] G. Buonanno *et al.*, Link between SARS-CoV-2 emissions and airborne concentrations: Closing the gap in understanding, *J. Hazard. Mater.*, vol. 428, p. 128279, doi: 10.1016/j.jhazmat.2022.128279, 2022

[2] G. Buonanno, L. Ricolfi, L. Morawska, and L. Stabile, Increasing ventilation reduces SARS-CoV-2 airborne transmission in schools: A retrospective cohort study in Italy's Marche region, *Front. Public Health*, vol. 10, p. 1087087, doi: 10.3389/fpubh.2022.1087087, 2022

[3] C. T. Crowe, J. D. Schwarzkopf, M. Sommerfeld, and Y. Tsuji, *Multiphase Flows with Droplets and Particles*, CRC Press, doi: 10.1201/b11103, 2011

[4] G. Cortellessa *et al.*, Close proximity risk assessment for SARS-CoV-2 infection, *Sci. Total Environ.*, vol. 794, p. 148749, doi: 10.1016/j.scitotenv.2021.148749, 2021

[5] G. R. Johnson *et al.*, Modality of human expired aerosol size distributions, *J. Aerosol Sci.*, vol. 42, no. 12, pp. 839–851, doi: 10.1016/j.jaerosci.2011.07.009, 2011.

[6] L. Morawska *et al.*, Size distribution and sites of origin of droplets expelled from the human respiratory tract during expiratory activities, *J. Aerosol Sci.*, vol. 40, no. 3, pp. 256–269, doi: 10.1016/j.jaerosci.2008.11.002, 2009

[7] K. P. Fennelly, Particle sizes of infectious aerosols: implications for infection control, *Lancet Respir. Med.*, vol. 8, no. 9, pp. 914–924, doi: 10.1016/S2213-2600(20)30323-4, 2020.

[8] S. L. Bixler *et al.*, Aerosol Exposure of Cynomolgus Macaques to SARS-CoV-2 Results in More Severe Pathology than Existing Models, doi: 10.1101/2021.04.27.441510, 2021.

[9] S. Balachandar, S. Zaleski, A. Soldati, G. Ahmadi, and L. Bourouiba, Host-to-host airborne transmission as a multiphase flow problem for science-based social distance guidelines, *Int. J. Multiph. Flow*, vol. 132, p. 103439, doi: 10.1016/j.ijmultiphaseflow.2020.103439, 2020.

[10] X. Xie, Y. Li, A. T. Y. Chwang, P. L. Ho, and W. H. Seto, How far droplets can move in indoor environments? revisiting the Wells evaporation' falling curve, *Indoor Air*, vol. 17, no. 3, pp. 211–225, doi: 10.1111/j.1600-0668.2007.00469.x., 2007

[11] G. Grossi, F. Arpino, M. Bertone, G. Cortellessa, and A. Sciacchitano, On the effectiveness of Reynolds-averaged and subgrid scale models in predicting flows inside car cabins, *Phys. Fluids*, vol. 36, no. 1, p. 015137, doi: 10.1063/5.0180823, 2024.

[12] F. Arpino, G. Cortellessa, G. Grossi, and H. Nagano, A Eulerian-Lagrangian approach for the non-isothermal and transient CFD analysis of the aerosol airborne dispersion in a car cabin, *Build. Environ.*, vol. 209, doi: 10.1016/j.buildenv.2021.108648, 2022.

[13] F. Arpino, G. Cortellessa, A. C. D'Alicandro, G. Grossi, N. Massarotti, and A. Mauro, CFD analysis of the air supply rate influence on the aerosol dispersion in a university lecture room, *Build. Environ.*, vol. 235, doi: 10.1016/j.buildenv.2023.110257, 2023.

[14] B. Pirouz, D. Mazzeo, S. A. Palermo, S. N. Naghib, M. Turco, and P. Piro, CFD Investigation of Vehicle's Ventilation Systems and Analysis of ACH in Typical Airplanes, Cars, and Buses', *Sustainability*, vol. 13, no. 12, p. 6799, doi: 10.3390/su13126799, 2021.

PARALLEL SESSIONS

Porous media correlations for thermoacoustic stacks

Armando Di Meglio, Nicola Massarotti
University of Naples "Parthenope", Italy, Centro Direzionale Napoli, 80143,
armando.dimeglio001@studenti.uniparthenope.it, nicola.massarotti@uniparthenope.it

ABSTRACT

In this work, a numerical comparison between the macroscopic porous media description of parallel plate stack and transversal pin array stack. Stack (or regenerator) is the energy core of the thermoacoustic devices. Thuse, its correct modelling affects the energy performance of the thermoacoustic device. Simulations at the pore-scale allows us to derive the macroscopic descritpion of the porous medium, using the Darcy-Forchheimer law, adapted for oscillatory flows. The results show that the stack characterized by a uniform cross section, like the parallel plate, experiences lower linear and nonlinear losses. The threshold Reynolds number that switches from Darcy to Forchheimer like porous media is lower for transversal pin array stack.

Key Words: *Thermoacoustics, porous media, stack, regenerator.*

1. INTRODUCTION

Thermoacoustics is the science which studies the interaction among acoustics, heat transfer and fluid flow [1]. The stack or regenerator [2] is a porous medium where the energy conversion between mechenical power (under the from of acoustic energy) and heat occurs in case of a thermoacoustic refrigerator or engine respectively. In the review article [3], the main numerical models for design and analysis purposes are summarized. Both in DeltaEC and CFD environments, the stack is modelled macroscopically as a porous medium. From an experimental point of view, "conventional" or "unconventional" stacks can be characterized as shown in refs. [4; 5; 6] .It is not always possible to apply the conventional porous media correlations for steady-state flow, like the Darcy-Forchheimer ones. Their validity depends on the operating frequency, the equivalent radius of the stack and thermodynamic conditions (pressure and temperature). In this article, two different kinds of stacks are firstly simulated at the microscopic level to derive the relation between pressure gradient and velocity. Then, the pore-scale results are post-processed to derive a correlation between the variables. To take into account the phase shift between pressure gradient and velocity, the same procedure adopted in ref. is used. The parallel plate stack and the transversal pin array stack are used to represent case studies of an uniform cross section stack and a tortuous stack respectively.

2. METHOD

Inspired by Darcy–Forchheimer model for steady-state problems, the general relation between macroscopic pressure gradient and superficial velocity in oscillating flows can be written as follows [7]:

$$-\nabla p = \left(a + \frac{b_R}{L_{stack}}|\mathbf{v_D}|\right)\mathbf{v_D} + \frac{\rho}{\varphi}\frac{\partial|\mathbf{v_D}|}{\partial t}\left(1 + a_V + \frac{b_V}{L_{stack}}|\mathbf{v_D}|\right) \tag{1}$$

The first term on the right hand-side represents the classical Darcy-Forchheimer model, while the second term is a correction for oscillatory flow, also known as virtual mass factors. "R" and "V" stands for "real" and "virtual", L_{stack} is the lenght of the stack, $\mathbf{v_D}$ is velocity Darcy vector, φ is the homogenous porosity, a and b the linear and nonlinear coefficients of the correlation.

The 2D computational domain including the detailed representation of the stack is pictured in Figure 1 (a) and (b). Geometrical details can be found in ref. [8]. Free fluid zones are also simulated before and after the stack to take into account the end-zone effects. A sinusoidal pressure input is given on the left boundaries while the opposite is a wall. Top and bottom boundaries are considered periodic as only three rows of parallel plates or pins are simulated. A check on the maximum Reynolds number is conducted to verify the laminar regime.

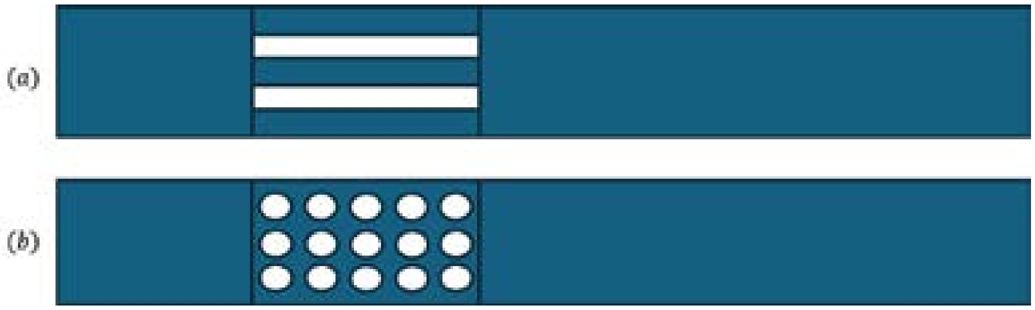

FIGURE 1. Computational domain, (a) parallel plate stack, (b) pin array stack

The simulations are carried out by varying the input pressure amplitude (i.e. the velocity inside the stack) and the frequency oscillation.

3. RESULTS

The post-processing procedure and the obtained results are valid for both stacks. Once the simulations reach the periodic steady-state, the velocity and pressure gradient are sampled. Then, the FFT is used to obtain the results in the frequency domain. Taking the velocity as a reference, the pressure gradient, calculated as difference between the pressure at the stack ends divided by the stack length, has a real component (phased with velocity) and an imaginary component (90° shifted with respect to velocity). Coefficients a, b are derived by fitting pressure drop and velocity from at least seven simulations at different pressure amplitudes (therefore velocity inside the stack) and same frequency using a polynomial curve like $y = ax + bx^2$. This is applied for both components of pressure drop and for each frequency investigated.

Previous results in ref. [8] already showed that the pressure gradient phased with velocity is characterized by a parabolic trend against velocity. This is clearly consistent with a Darcy-Forchheimer correlation of porous media. On the other hand, the opposite component, proportional to the time derivative of the velocity, is linear also at higher pressure amplitude. This means that the previous b_V is zero for both kinds of porous media. With regards to frequency, an opposite trend is found out for a and b coefficients against the frequency. a increases for higher frequency, while b reaches the maximum value when frequency approaches zero. Also this finding is confirmed for both parallel plate and transversal pin array stack.

At very low frequency steady-state results are recovered. For example, in Figure 2 the the spatial average velocity of the working fluid over the pin array stack is shown for different frequencies. The steady-state value is also considered in this graph as reference.

About the physical meaning behind the overall viscous losses, an important distinction can be made between the stacks. For a parallel plate stack, the most important source is the geometrical discontinuities between the free fluid zones and the stack. Its influence also affected the local relation between pressure gradient and velocity at the middle of the stack, if it is not long "enough". As the cross section is constant, in purely micro-channel computational domain the relation between pressure-drop and velocity is linear. On the other hand, the main source of non-linearities for the transversal pin array stack is the tortuosity.

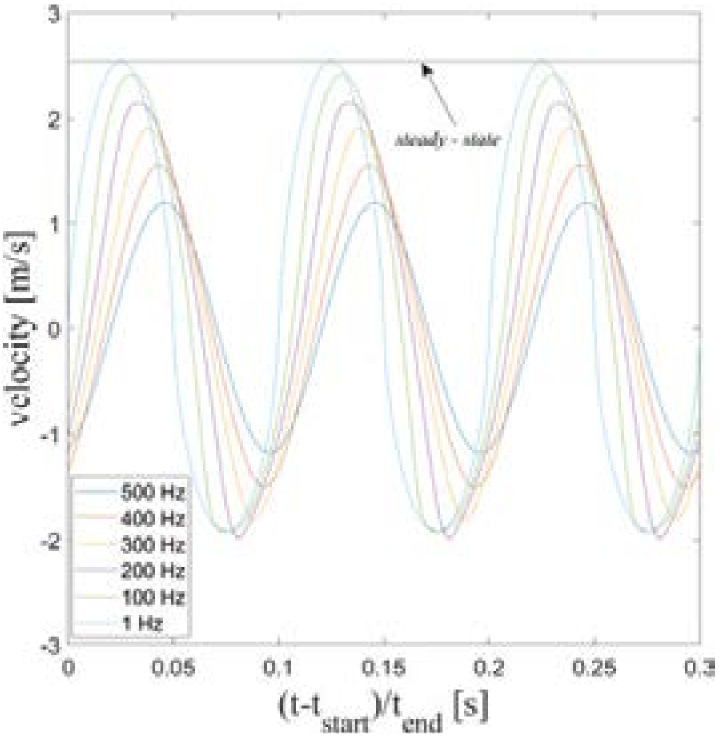

FIGURE 2. Velocity during the time at different frequencies for the transversal pin array stack

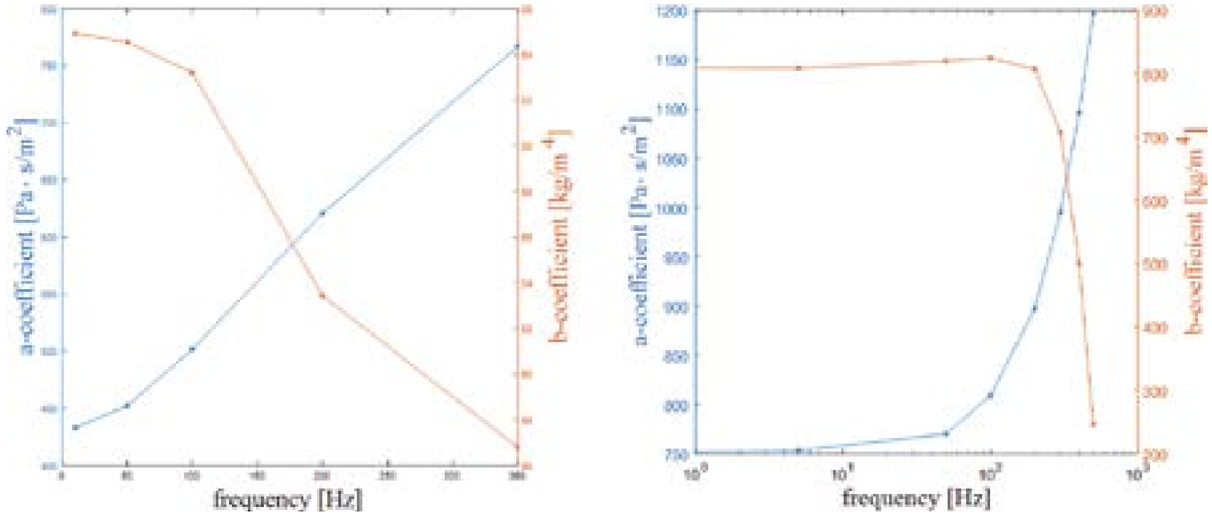

FIGURE 3. Linear and non-linear coefficients *a*, *b* against frequency: (a) parallel plate stack, (b) pin array stack

4. CONCLUSIONS

This study compares the macroscopic porous media descriptions of parallel plate and transversal pin array stacks in thermoacoustic devices, using pore-scale simulations and the Darcy-Forchheimer law adapted for oscillatory flows. The parallel plate stack, characterized by its uniform cross-section, exhibits lower overall viscous losses due to reduced geometrical discontinuities, which minimize energy dissipation from abrupt changes in flow direction. Consequently, the pressure drop across this stack follows a more predictable linear relationship with velocity, especially in purely micro-channel computational domains.

In contrast, the transversal pin array stack, with its tortuous structure, introduces significant non-linearities due to its intricate geometry, resulting in higher energy losses, particularly at the transition zones between free fluid and the porous medium. Additionally, the threshold Reynolds number, which dictates the switch from Darcy to Forchheimer-like behavior, is lower for the pin array stack, indicating a quicker onset of nonlinear flow effects that can influence the overall efficiency of thermoacoustic devices.

The study also confirms that the coefficients in the Darcy-Forchheimer model are frequency-dependent, with 'a' increasing with frequency and 'b' peaking at low frequencies. These trends are consistent across both stack configurations, underscoring the need to account for operating conditions when designing and analyzing thermoacoustic devices.

REFERENCES

[1] Geng Chen, Lihua Tang, Brian Mace, and Zhibin Yu. Multi-physics coupling in thermoacoustic devices: A review. *Renewable and Sustainable Energy Reviews*, 146:111170, 2021.

[2] Elio Di Giulio, Cong Truc Nguyen, Camille Perrot, and Raffaele Dragonetti. Wire mesh stack and regenerator model for thermoacoustic devices. *Applied Thermal Engineering*, 221: 119816, 2023.

[3] Armando Di Meglio and Nicola Massarotti. Cfd modeling of thermoacoustic energy conversion: a review. *Energies*, 15(10):3806, 2022.

[4] Marialuisa Napolitano, Elio Di Giulio, Fabio Auriemma, Rosario Aniello Romano, and Raffaele Dragonetti. Low frequency acoustic method to measure the complex bulk modulus of porous materials. *Journal of the Acoustical Society of America*, 151(3):1545 – 1556, 2022. doi: 10.1121/10.0009767.

[5] Elio Di Giulio, Marialuisa Napolitano, Armando Di Meglio, Rosario Aniello Romano, and Raffaele Dragonetti. Low frequency acoustic method to measure the complex density of porous materials. *Journal of the Acoustical Society of America*, 152(4):2220 – 2226, 2022. doi: 10.1121/10.0014762.

[6] Elio Di Giulio, Armando Di Meglio, Nicola Massarotti, Rosario Aniello Romano, and Raffaele Dragonetti. Oriented fibers stacks for thermoacoustic devices. *Applied Energy*, 373, 2024. doi: 10.1016/j.apenergy.2024.123959.

[7] Armando Di Meglio, Elio Di Giulio, Raffaele Dragonetti, and Nicola Massarotti. A novel model for macroscopic simulation of oscillating heat and fluid flow in porous media. *International Journal of Thermal Sciences*, 181:107758, 2022.

[8] Armando Di Meglio, Nicola Massarotti, Samuel Rolland, and Perumal Nithiarasu. Analysis of non-linear losses in a parallel plate thermoacoustic stack. *International Journal of Numerical Methods for Heat & Fluid Flow*, 34(1):353–377, 2024.

Sixth International Conference on Computational Methods for Energy and Thermal Problems
THERMAECOMP2024, Sept. 9-11, 2024, Budva, Montenegro
N. Massarotti, P. Nithiarasu and I. Vušanović (Eds.)

Analysis of Thermoacoustic Instability through a Macroscopic Modeling of the Stack

Elio Di Giulio, Rosario Aniello Romano, Raffaele Dragonetti
Industrial Engineering Department, University of Naples *Federico II*, Piazzale Tecchio, 80,
Napoli, 80125, Italia

ABSTRACT

Thermoacoustic devices are characterized by simple configurations and the absence of moving parts. To utilize low-grade thermal energy, significant efforts have been directed towards reducing the onset temperature of thermoacoustic engines. Various factors influence the onset characteristics of a thermoacoustic engine, including the type of the engine (traveling or standing wave), the geometry of the components, filling pressure, gas varieties, and pressure disturbances. In this work, the stability limit of thermally induced gas oscillation has been numerically investigated using a one-dimensional approach with a macroscopic model for porous materials in a Finite Element based software. This model allows the investigation of different types of non-conventional stacks (such as wire mesh and foams) and facilitates the analysis of both onset characteristics and the achieved pressure amplitude.

Key Words: *Thermoacoustics, Porous Material, Macroscopic Approach.*

1 INTRODUCTION

Thermoacoustic engines have garnered significant attention due to their simple design, potential efficiency, and the absence of moving parts, making them an attractive option for various energy conversion applications. These devices operate by converting thermal energy into acoustic energy through the working fluid within the engine. One of the critical challenges in the development of thermoacoustic engines is the utilization of low-grade thermal energy, which is often wasted due to the inefficiency of conventional energy conversion systems. The onset temperature of a thermoacoustic engine is a crucial parameter that dictates the minimum temperature difference required to initiate acoustic oscillations. Lowering this onset temperature enhances the engine's ability to utilize low-grade thermal energy sources effectively. Various factors influence the onset characteristics of a thermoacoustic engine, including the mode of the engine (traveling or standing wave), the geometry of the components, filling pressure, gas varieties, and pressure disturbances. In recent years, numerous studies have been conducted to explore these factors and improve the performance of thermoacoustic engines [1; 2; 3; 4]. However, there remains a need for comprehensive numerical investigations that can accurately predict the stability limits and onset characteristics of these engines under different conditions. In this context, the use of one-dimensional models and finite element analysis (FEA) software provides a powerful tool for simulating the behavior of thermoacoustic engines and optimizing their design. This work aims to numerically investigate the stability limit of thermally induced gas oscillation in thermoacoustic engines using a one-dimensional approach with a macroscopic model for porous materials [5]. By incorporating non-conventional stacks such as wire mesh and foams into the model [6; 7; 8; 9], this study seeks to analyze both the onset characteristics and the achieved pressure amplitude. The insights gained from this investigation will contribute to make more efficient thermoacoustic engines capable of harnessing low-grade thermal energy for practical applications.

2 POROUS MATERIAL MODELING

2.1 Viscous behaviour

The momentum equation for a porous medium in the case of oscillating flow is given by [5; 10]:

$$\frac{1}{\phi}\rho\frac{\partial u_D}{\partial t}+\frac{1}{\phi^2}(v_D\cdot\nabla)u_D=\nabla\cdot\left[-\langle p\rangle I+\frac{\langle K\rangle}{\phi}\right]+b_{sf}+b_{sf\,new} \tag{1}$$

where

$$b_{sf} = -\frac{\mu}{r_h^2}\Re\left[\frac{1}{Da}\right]u_D, \tag{2}$$

$$b_{sf\,new} = -\frac{\mu\omega}{r_h^2}\Im\left[\frac{1}{Da}\right]\frac{\partial u_D}{\partial t}. \tag{3}$$

The real part of the reciprocal of Eq. (2) is the corresponding Darcy term of the stationary flow for each frequency, for which the pressure gradient and velocity are out of phase by 180°. The imaginary part instead represents a new term indicating the phase change between pressure gradient and velocity and is proportional to the time derivative of the velocity.

The dynamic Darcy number is defined as follows:

$$Da = \phi\left(\frac{\delta_\nu}{r_h}\right)^2\frac{1-f_\nu^2}{if_\nu} \tag{4}$$

where f_ν is the viscous dynamic function depending on the fluid and the geometric characteristics of the porous material's microstructure. r_h is the characteristic radius of the microstructure. δ_ν is the viscous boundary layer depending on the fluid properties and the frequency.

2.2 Thermal behaviour

For a coupled fluid-solid problem, the reference temperature difference is $\langle T_s\rangle - \langle T\rangle$, which are integrated over the solid and the fluid medium, respectively. The thermal flux can be written as:

$$q_{sf} = \frac{h_{sf}}{r_h}(\langle T_s\rangle - \langle T\rangle) = k\frac{Nu}{r_h^2}(\langle T_s\rangle - \langle T\rangle) \tag{5}$$

In oscillating flows, the complex Nusselt number has already been studied in the literature [5]. In general, the complex Nusselt number depends on six dimensionless parameters [5]:

$$Nu = Nu\left(f_\nu,\left(\frac{r_h}{\delta_\nu}\right),f_\kappa\left(\frac{r_h}{\delta_\kappa}\right),f_s\left(\frac{r_s}{\delta_s}\right),\varepsilon_s,D,\phi\right) \tag{6}$$

Here, $f_\kappa, f_s, \varepsilon_s$ are the fluid thermal function, the solid thermal function, the heat capacity ratio, respectively.In the case of an isothermal solid (with infinite thermal capacity), the dependence on the solid properties disappears ($\varepsilon_s \to 0$). The term D is used to compare the compressibility term with the convective term. When $D \to 0$, the effects of compression are much greater than those of convection. ϕ is the porosity of the medium.

3 NUMERICAL RESULTS

The analyzed standing wave device features a circular cross-section duct at the temperature of the hot heat exchanger on the left of the stack and, an the other side, at the temperature of the cold heat exchanger on its right, see Fig.1.a. The effects of viscosity on pressure losses will be considered only within the stack, and the hot and cold heat exchangers will not be modeled. They will be considered as ideal heat sources, meaning they will not influence particle motion and will exchange heat without changing their own temperature. Thus, from a modeling perspective, they can be assimilated to Thermal Energy Reservoirs. The geometric dimensions are as follows: diameter 21 mm, cold duct length 370 mm, stack length 30 mm, hot duct length 100 mm. The 1D model analyzed in the macroscopic case employs the following physics:

- Thermal exchange in fluids, where the properties of the working fluid are defined.
- Thermal exchange in solids, where the properties of the stack are defined.
- Free thermal flow and oscillating fluid flow within the porous material, where permeability and porosity are assigned.

The numerical simulation software allows solving of thermal exchange both in solids and within fluids, at the same time. The solid volume fraction will be indicated as $(1-\phi)$ and the interstitial convective heat transfer coefficient as:

$$q_{sf} = \Re[Nu]\frac{k_0}{y_0^2}\phi \tag{7}$$

The mesh used is of the mapped type and was obtained by fixing the number of elements, resulting in a step size $\Delta x = \frac{\text{Stack length}}{\text{Number of elements}}$. This Δx is valid only within the stack, while in the remaining components, a progressively coarser mesh was assigned, as shown in Fig.1.b.. The choice to refine the mesh near the stack is due to the need to study in greater detail what happens inside it, while avoiding increasing the computational cost by refining areas that are less significant for the analysis of the results. From the pressure probe located at the hard wall condition, it is possible to observe the initiation process of the thermoacoustic phenomenon. As shown in Fig.2, the acoustic pressure tends to grow exponentially while maintaining a harmonic behavior, until it reaches a steady state where energy conversion and losses balance each other. The shape of this function resembles a sigmoid $s(t)$, represented in red colour in Fig. 2:

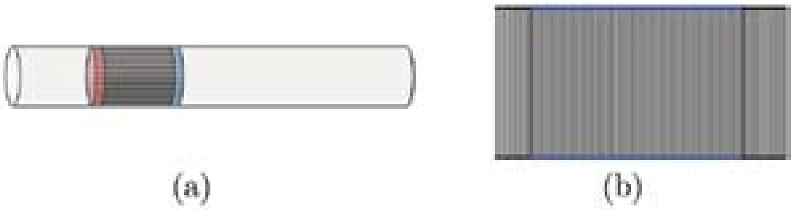

FIGURE 1. (a) Simulated standing wave device. (b) 1D Mesh of the stack.

$$s(t) = \frac{a}{1+e^{b(t-c)}} \tag{8}$$

The parameters of the sigmoid allow to numerically determine the complex frequency b ($b < 0$ condition allows to trigger the phenomenon), the initial phase shift c that helps to understand the onset time of the thermoacoustic instability, and the amplitude a of the sigmoid that provides information about the level of acoustic pressure achieved at steady state.

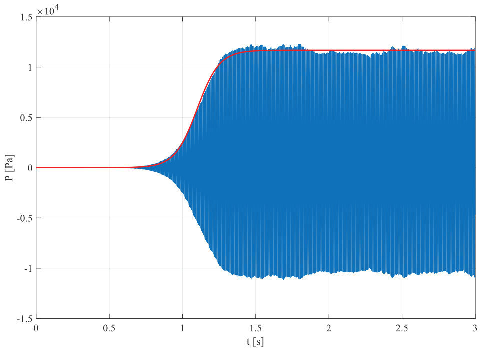

FIGURE 2. Acoustic pressure at the wall position during the thermoacoustic startup process.

4 CONCLUSIONS

This study presents a macroscopic approach to modeling the behavior of the stack within thermoacoustic devices. Utilizing finite element software, we successfully observed the onset process of the thermoacoustic phenomenon. The acoustic pressure waveform, resembling a sigmoid with oscillatory behavior, was identified, with its parameters traceable to the physical aspects of the problem, such as stack type, device geometry, and thermal inputs. Future work will focus on the analysis of complex systems with unconventional stacks, such as oriented fiber structures or membrane cells. These developments are expected to provide further insights and advancements in the design and optimization of thermoacoustic devices.

REFERENCES

[1] G. W. Swift. Thermoacoustic engines. *The Journal of the Acoustical Society of America*, 84 (4):1145, jun 1998. ISSN 0001-4966. doi: 10.1121/1.396617.

[2] Geng Chen, Lihua Tang, and Brian R. Mace. Modelling and analysis of a thermoacoustic-piezoelectric energy harvester. *Applied Thermal Engineering*, 150:532–544, mar 2019. ISSN 1359-4311. doi: 10.1016/J.APPLTHERMALENG.2019.01.025.

[3] Armando Di Meglio, Nicola Massarotti, Samuel Rolland, and Perumal Nithiarasu. Analysis of non-linear losses in a parallel plate thermoacoustic stack. *International Journal of Numerical Methods for Heat and Fluid Flow*, 34(1):353–377, jan 2024. ISSN 09615539. doi: 10.1108/HFF-02-2023-0071/FULL/PDF.

[4] Armando Di Meglio and Nicola Massarotti. CFD Modeling of Thermoacoustic Energy Conversion: A Review. *Energies 2022, Vol. 15, Page 3806*, 15(10):3806, may 2022. ISSN 1996-1073. doi: 10.3390/EN15103806.

[5] Armando Di Meglio, Elio Di Giulio, Raffaele Dragonetti, and Nicola Massarotti. A novel model for macroscopic simulation of oscillating heat and fluid flow in porous media. *International Journal of Thermal Sciences*, 181:107758, nov 2022. ISSN 1290-0729. doi: https://doi.org/10.1016/j.ijthermalsci.2022.107758.

[6] Elio Di Giulio, Armando Di Meglio, Nicola Massarotti, Rosario Aniello Romano, and Raffaele Dragonetti. Oriented fibers stacks for thermoacoustic devices. *Applied Energy*, 373: 123959, nov 2024. ISSN 0306-2619. doi: 10.1016/J.APENERGY.2024.123959.

[7] Elio Di Giulio, Camille Perrot, and Raffaele Dragonetti. Transport parameters for sound propagation in air saturated motionless porous materials: A review. *International Journal of Heat and Fluid Flow*, 108:109426, sep 2024. ISSN 0142-727X. doi: 10.1016/J.IJHEATFLUIDFLOW.2024.109426.

[8] Elio Di Giulio, Cong Truc Nguyen, Camille Perrot, and Raffaele Dragonetti. Wire mesh stack and regenerator model for thermoacoustic devices. *Applied Thermal Engineering*, 221:119816, feb 2023. ISSN 1359-4311. doi: https://doi.org/10.1016/j.applthermaleng.2022.119816.

[9] Elio Di Giulio, Armando Di Meglio, Nicola Massarotti, and Raffaele Dragonetti. Effective Thermal Conductivity Model for Tetragonal Pin Array Stack. *Journal of Fluid Flow, Heat and Mass Transfer*, 9:38 – 42, jan 2022. ISSN 23686111. doi: 10.11159/jffhmt.2022.005.

[10] Armando Di Meglio, Elio Di Giulio, Raffaele Dragonetti, and Nicola Massarotti. Analysis of heat capacity ratio on porous media in oscillating flow. *International Journal of Heat and Mass Transfer*, 179:121724, nov 2021. ISSN 0017-9310. doi: https://doi.org/10.1016/j.ijheatmasstransfer.2021.121724.

Sixth International Conference on Computational Methods for Energy and Thermal Problems
THERMAECOMP2024, Sept. 9-11, 2024, Budva, Montenegro
N. Massarotti, P. Nithiarasu, and I. Vušanović (Eds.)

Compact thermoacoustic cooler (TACOT): design and experimental qualification

Islam Ramadan, Hélène Bailliet, Martin Fontbonne
Institut Pprime, CNRS - Université de Poitiers-ENSMA, Département Fluides-Thermique Combustion, ENSIP, 6 rue Marcel Doré Bât. B17-BP 633, 86022 Poitiers Cedex, France,
islam.ramadan@univ-poitiers.fr, helene.bailliet@univ-poitiers.fr

Gaëlle Poignand
Laboratoire d'Acoustique de l'Université du Mans (LAUM), UMR 6613, Institut d'Acoustique - Graduate School (IA-GS), CNRS, Le Mans Université, France

ABSTRACT

The design and experimental qualification of a compact thermoacoustic cooler are presented. The use of two acoustic sources makes it possible to gain compactness and adjust the phase between acoustic quantities in the thermoacoustic core. The chosen architecture yields improved power densities (ratio of cooling capacity to external volume normalized by relative temperature difference across the regenerator). Results of measurements show complex temperature distribution in the thermoacoustic core region that cannot be predicted by the DeltaEC code used to design the device.

Key Word: *Thermoacoustic refrigerator.*

1. INTRODUCTION

Thermoacoustic devices usually rely on the resonance of a wave guide to reach the high acoustic levels necessary for significant thermoacoustic heat flux. Working frequencies in the range of 100 Hz correspond to metric lengths of resonators, therefore closing the door to many applications where size is a constraint. Some compact devices have been developed as the Ben & Jerry's "bellows-bounce" freezer that has a 25 cm diameter and a 48 cm length and pumps 120 W at a -20°C load temperature with a 19% of Carnot coefficient-of-performance [1]. The purpose of the present study is to present a new architecture for compact thermoacoustic coolers. The architecture of this TACOT (ThermoAcoustic Cooler for On road Transportation) was chosen following the work by Poignand, et al. [2] that proposed a two-source co-axial compact thermoacoustic refrigerator to reach compactness. To obtain high acoustic power and appropriate phase relationship between particle displacement and instantaneous temperature, a secondary electro-acoustic source is used that fits the correct acoustic impedance, equivalent to the resonator historically used. The use of two sources also makes it easy to adapt the parameters of the acoustic field to different thermal conditions by independently tuning the amplitudes and phases of the sources. Besides, the working frequency is no longer linked by quasi-standing wave or quasi-travelling wave conditions; it is set so that the wavelength is much greater than the dimensions of the resonator. Poignand et al. used an academic setup to validate the concept of a compact refrigerator [3]. It is applied in the design of the TACOT to increase the specific cooling capacity (i.e. the ratio between the cooling capacity and the total volume of the device) of thermoacoustic refrigerators. The modeling program developed at Los Alamos National Laboratory, DeltaEC [4], was used to design the refrigerator, starting from the thermoacoustic core and setting each element of the device, step by step, while ensuring that the optimal phase between particle displacement and instantaneous temperature is maintained. In the following, the design of the TACOT is presented. Then some results of measurements are given.

2. DESCRIPTION OF THE DEVICE

Figure 1 (left) shows an exploded view of the TACOT with the two electro-acoustic sources: Rix Industries, model: 1S241M colored in red in the figure, further referred to as RIX acoustic driver, and loudspeaker (Peerless, model: GBS-135F) colored in green in the figure. Both acoustic sources are connected to power amplifiers that are driven by a two-output function generator allowing the adjustment of their relative phase. Figure 1 shows the back cavities of the sources (pink and purple colored) and the housing of the thermoacoustic core (blue and gold). It makes apparent that most of the volume of the device is occupied by the RIX acoustic driver and its back cavity which corresponds to a 8-litre gas volume, the rest of the device having a 4-litre gas volume. The balance in the static pressure is ensured by an air gap around the RIX acoustic driver piston connecting those volumes.

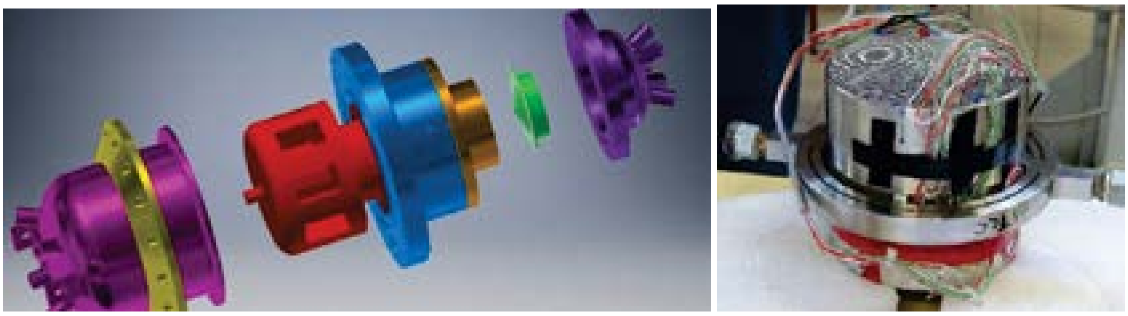

FIGURE 1. Exploded view of the TACOT and photo of its core

A photo of the thermoacoustic core (i.e. regenerator sandwiched between two heat exchangers) of the device is shown in figure 1 (right) which corresponds to the gold-colored element in figure 1 (left). Figure 2 shows the assembled schematic view along with a photo of the device. As shown in figure2, the core is connected at one end to the loudspeaker and opens on its other end on a conical element (blue-colored) that is connected to the RIX driver. As shown in Figure 1 (right), a flow straightener is placed at the junction between the cone and the core. The core hosts the regenerator (cyan-colored) and the heat exchangers. The cone has an initial diameter of 108 mm (that corresponds to the piston diameter) and a final diameter of 164 mm. The outside diameter of the regenerator and heat exchangers is 156 mm, so as to create an annulus peripheral channel (gold colored in figure 2) that connects the front of the RIX driver to the back of the loudspeaker and was designed to reach the optimum phasing between acoustic quantities in the regenerator.

FIGURE 2. Assembled schematic view and a photo of the TACOT

The regenerator is composed of a stainless steel canister that has a length of 39 mm, filled with packed stainless steel screen discs machined to a diameter of 148 mm. The copper ambient heat exchanger (AHX) extracts the heat transported by the thermoacoustic process. It is composed of fins crossed by tubes in which water flows as shown in figure 3 (left). The cold heat exchanger (CHX) is not connected to an enclosure to be cooled but it is equipped with electrical cartridges, see figure 3 (middle). This allows to estimate the cooling capacity of the refrigerator, by measuring the necessary electrical power applied to the cartridges to maintain a desired temperature. Nineteen type-K thermocouples with a 0.5 mm diameter are set at different locations in the device, mostly in the thermoacoustic core as shown in figure 3 (rigth). The refrigerator is filled with a helium-argon mixture (70% He and 30% Ar volume basis) at a static mean pressure of 40 bar. More details about the design of the TACOT, its instrumentation, and its control are available in [5].

FIGURE 3. From left to right: Ambient heat exchanger (AHX), cold heat exchanger (CHX), and thermocouple positions

3. RESULTS

The TACOT has been driven for an extended set of configurations. For all cases, the working frequency was set to the mechanical resonance frequency of the RIX driver (i.e. phase shift between the force and velocity is zero) to provide the maximum possible acoustic power. Also, at this frequency electrical resonance of the acoustic driver is achieved. The phase shift between the sources electrical input signals was set to $\Delta\varphi = \varphi_{loudspeaker} - \varphi_{RIX} = -60°$, to yield a maximum pressure amplitude in the device. Following are some details on one configuration to illustrate the gain of compactness. It corresponds to a working frequency of 47 Hz, a drive ratio (ratio of the acoustic pressure amplitude to the static pressure) of 3.6 %, a temperature difference between thermocouples number 11 (TC11=T_h) and 5 (TC5 =T_c) of 34°C, and a measured cooling capacity $\dot{Q}_C$ of 290 W. At this frequency the acoustic field in the device is compact. The measured input electrical power at the RIX driver is 180 W (over its 1600 W maximum power) and it is 12 W at the loudspeaker. The corresponding total coefficient-of-performance (COP$_{\text{total}}$), that is the ratio between the cooling capacity and the total input electric power of the acoustic sources is therefore 1.5. The thermoacoustic coefficient-of-performance (COP$_{\text{TA}}$), which takes apart the electro-acoustic efficiency and is the ratio between the cooling capacity and the acoustic power generated by the acoustic sources is 2.3. For this configuration, the power density of the device is $\rho_W = \frac{\dot{Q}_C(T_h - T_c)}{V\,T_c} = 1.43$ W/l. Here the volume V is the external volume of the refrigerator which is 24 litre, much larger than the fluid volume inside the refrigerator. For comparison, the power density of the SETAC fridge is 0.6 W/l and the power density of the Ben & Jerry's compact device is 1.26 W/l.

The results of measurements were compared to the results predicted by the design tool DeltaEC. For the above-mentioned configuration, the code shows reasonable agreement with experimental results with calculated $\dot{Q}_C = 300$ W and COP$_{\text{total}}$ = 1.2. However, as discussed, in the following, temperature measurements in the device show that the axial temperature gradient is far from the linear expectation by DeltaEC and that the temperature is not uniform across the section of the thermoacoustic core, conversely to the expectation of the 1D model. To investigate sources of discrepancy, different orientations of the device against gravity were tested and figure 4 shows the results of thermocouple measurements for two different orientations for a configuration close to the one above presented apart from the device orientation. In this figure, solid lines correspond to the results of measurements when the device has been rotated π/2 (oriented vertically) compared to figure 2 (oriented horizontally) and dotted lines to a - π/2 rotation (oriented vertically upside down), yielding a direction of the gravity field either against or similar to the device axis direction x. The insert on the left side of figure 4 shows a schematic of the thermoacoustic core orientation associated with results shown with solid lines. Let us first consider the figure 4.c, that gives the temperature distribution along the regenerator axis (TC5-8-11) together with the distributions along the two sides of the regenerator parallel to this axis (TC4-7-10 and TC6-9-12). The temperature gradient along the axis (TC5-8-11) is far from being linear and it is very influenced by the direction of the device axis against gravity (compare solid and dotted orange lines). Figure 4.c also reveals that the temperatures at a given x position are not homogenous along the transverse direction and that this inhomogeneity is more important when the axial temperature gradient is in the opposite direction to the gravity (solid line). Figure 4.b shows the temporal evolution of the thermocouples 13, 14 and 15 that are set on the outside wall of the ambient heat exchanger AHX (visible in figure 3). The difference between the temperature recorded by each thermocouple and its temperature at t=0 is plotted. After 100 seconds, the electroacoustic sources are switched on. Although some sensors recordings depict large fluctuations, the steady state average temperatures all lie within 3 to 5 K from the initial temperature, revealing a much greater homogeneity whatever the orientation than on the other side of the AHX (TC10-11-12 at x=-2 cm on the figure 4.c). Figure 4.a shows the results of measurements for the thermocouples on the outer side of the cold heat exchanger (CHX), TC1-2-3, together with the temperature in front of the acoustic driver. It shows a strong transverse inhomogeneity of the temperature and a slight dependence on the orientation of the device.

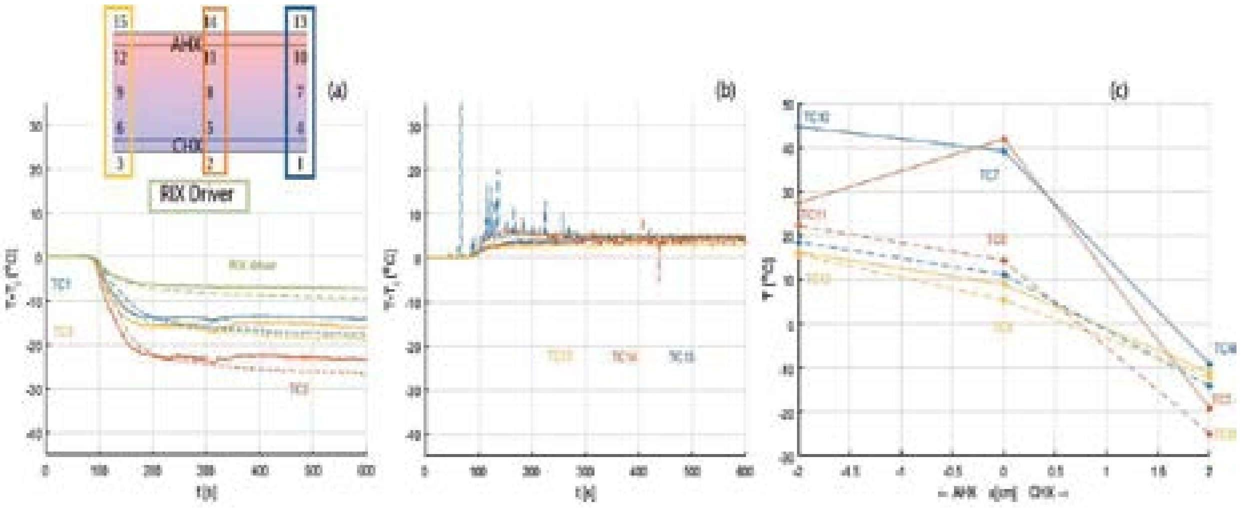

FIGURE 4. Results of thermocouple measurements

4. CONCLUSION

The TACOT refrigerator, thanks to its original architecture, gives improved specific cooling capacity. The DeltaEC code used to design the device shows its limit in describing the complex temperature distribution in the thermoacoustic core. Dedicated models are needed to better understand the behavior of the system.

REFERENCES

[1] M. Poese, R. Smith, S. Garrett, R. van Gerwen and P. Gosselin, “Thermoacoustic refrigeration for ice cream sales,” in 6th Gustav Lorentzen Natural Working Fluids, Glasgow, UK, 2004.

[2] G. Poignand, P. Lotton, G. Penelet and M. Bruneau, “Thermoacoustic, Small Cavity Excitation to Achieve Optimal Performance,” Acta Acust. United Ac., vol. 97, p. 926 – 932, 2011.

[3] G. Poignand, A. Podkovskiy, G. Penelet, P. Lotton and M. Bruneau, “Analysis of a Coaxial, Compact Thermoacoustic heat pump,” Acta Acust. United Ac., vol. 99, p. 898 – 904, 2013.

[4] J. Clark, W. Ward and G. Swift, “Design environment for low-amplitude thermoacoustic energy conversion (DeltaEC),” J. Acoust. Soc. Am., vol. 122, p. 3014, 2007.

[5] I.A. Ramadan, H. Bailliet, G. Poignand, and D. Gardner. Design, manufacturing and testing of a compact thermoacoustic refrigerator. Applied Thermal Engineering, 189:116705, 2021

Sixth International Conference on Computational Methods for Energy and Thermal Problems
THERMAECOMP2024, Sept. 9-11, 2024, Budva, Montenegro
N. Massarotti, P. Nithiarasu and I. Vušanović (Eds.)

COMPACT THERMOACOUSTIC COOLER (TACOT) : NUMERICAL APPROACH

Diana Baltean-Carlès, Catherine Weisman
Institut Jean le Rond d'Alembert, Sorbonne Université, 4 place Jussieu, 75005 Paris, France,
diana-georgiana.baltean-carles@sorbonne-universite.fr,
catherine.weisman@sorbonne-universite.fr

Yann Fraigneau
Laboratoire Interdisciplinaire des Sciences du Numérique, Campus Universitaire bât 507, Rue du Belvédère, 91405 Orsay, France, yann.fraigneau@lisn.fr

ABSTRACT

A simplified numerical model of the compact thermoacoustic cooler developed during the TACOT project is presented here. This model is based on the low Mach number approximation and is acoustically compact. The simplified configuration is two-dimensional and includes a specific model for the main acoustic source as well as the secondary source. In order to reduce the computational time the configuration is quite different from the experimental prototype in terms of length scales and acoustic power, but sufficient to obtain a fine description of main physical mechanisms. Numerical simulations specifically show the importance of gravity effects in reducing the heat pumping effect.

Key Words: *Thermoacoustic heat pump, Numerical model, Low Mach number*

1. INTRODUCTION

The TACOT (ThermoAcoustic Cooler for On road Transportation) prototype [1] is a compact thermoacoustic cooler working under high mean pressure (40 bar) in which the acoustic field is created with two acoustic sources. The main driver acts as a pressure source and the second source is a loud-speaker acting as a velocity source. The thermoacoustic core is a regenerator (mesh of stainless steel screens) placed between two heat exchangers. The overall geometry is coaxial with a peripheral channel allowing a feedback flow. The acoustic sources are functioning at the same frequency (about 50 Hz) and their amplitudes and phases are tuned independently. The working gas is a mixture composed of 30% argon and 70% helium. As commonly done in the Thermoacoustic community, the prototype was designed using the numerical code DeltaEC, based on the linear theory in which multidimensional phenomena, such as gravity and end effects, are poorly described. However, in a compact device these phenomena can become important. In this work a numerical study is performed on two-dimensional simplified geometrical configurations of the prototype. The main hypothesis in the numerical approach is that the dimensions of the thermoacoustic cooler are much smaller than the wavelength associated with the oscillation frequency of the two sources. Therefore the entire device can be considered as acoustically compact.

2. NUMERICAL MODEL AND ALGORITHM

The device being acoustically compact, a Low-Mach number approximation of Navier-Stokes equations is used, so that the pressure P is split into two parts, a thermodynamic pressure P_{th} uniform in space and a dynamic pressure $P_{dyn} = \mathscr{O}(M^2)P_{th}$ variable in time and space:

$$\frac{\partial \rho}{\partial t} + \nabla \cdot (\rho \mathbf{V}) = 0, \tag{1}$$

$$\rho \left(\frac{\partial \mathbf{V}}{\partial t} + \mathbf{V} \cdot \nabla \mathbf{V} \right) = -\nabla P_{dyn} + \nabla \cdot \tau + \rho \mathbf{g}, \tag{2}$$

$$\rho c_p \left(\frac{\partial T}{\partial t} + \mathbf{V} \cdot \nabla T \right) = \nabla \cdot \kappa \nabla T + \frac{dP_{th}}{dt}, \tag{3}$$

$$P_{th} = \rho \frac{R}{\mathscr{M}} T, \tag{4}$$

where ρ is the fluid density, $\mathbf{V}$ the velocity field and $\tau = \mu(\nabla\mathbf{V}^T + \nabla\mathbf{V}) - (\frac{2}{3}\nabla \cdot \mathbf{V})\mathbb{I})$ the stress tensor, with μ the dynamic viscosity. The term $\rho\mathbf{g}$ represents the gravity force. In the energy equation (3), T represents the temperature, c_p the specific heat at constant pressure, κ the thermal conductivity. The viscous dissipation rate is here neglected as commonly done for low-velocity flows. In the equation of state (4), $R = 8.314$ J.K^{-1}.kg^{-1} is the universal gas constant and $\mathscr{M}$ the molar mass of the gas. An integrated form of the equation of state is also used:

$$P_{th} = \frac{R}{\mathscr{M}} \frac{\int_\Omega \rho d\Omega}{\int_\Omega \frac{1}{T} d\Omega}, \tag{5}$$

since the total mass of gas inside the cavity is known at any time.
The heat equation is solved in conducting solids inside the domain.

The governing equations are solved on a staggered grid using a finite volume approach of second order in time and space. The time scheme is based on a Crank-Nicholson method where the diffusive terms are implicit. The dynamic pressure component is solved by means of an incremental projection method commonly used for the simulation of incompressible flows [2] and adapted for the low-Mach number approach by replacing the divergence-free constraint with the mass conservation constraint, equation (1). The velocity field estimated from the momentum equation (2) is then updated through the projection method in such a way that mass conservation is satisfied [3]. This leads to a Poisson's equation of the form:

$$\nabla^2 \cdot \Psi = \frac{\nabla \cdot \left(\rho^{n+1}\vec{V}^* - \frac{\partial \rho^{n+1}}{\partial t}\right)}{\Delta t}, \tag{6}$$

where $\Psi = P^{n+1}_{dyn} - P^{n}_{dyn}$ is the time increment of pressure, n denotes the time iteration, $\vec{V}^*$ is the velocity field estimated from the momentum equation (2), ρ the mass density obtained from the state equation (4) and Δt the numerical time step. In order to satisfy the mass conservation equation (1), the velocity field is updated as:

$$\vec{V}^{n+1} = \vec{V}^* - \frac{\Delta t}{\rho^{n+1}} \nabla\Psi, \tag{7}$$

3. SIMPLIFIED CONFIGURATIONS

Main geometry and physical parameters. The experimental device is simplified in order to highlight the dominant physical mechanisms and avoid prohibitive computing times. A two-dimensional rectangular cavity is introduced (Figure 1). Its dimensions are representative of a real experimental device, but not too large in order to limit the total simulation time (Table 1). On solid walls, impermeability and no-slip conditions are used for the velocity and a zero normal derivative for the dynamic pressure component. Ambient temperature $T_0 = 298$ K is set at external walls of the device, except on the left wall which is adiabatic. The gas mixture used in the experimental prototype is kept in the simulation, but the mean pressure is set to $P_0 = 10^5$ Pa in order to reduce the boundary layer widths. The fluid is a perfect gas with constant properties $c_p = 1404.97$ J.K^{-1}.kg^{-1}, $\kappa = 8.56 \times 10^{-2}$ W.m^{-1}.K^{-1} and $\mu = 2.11 \times 10^{-5}$ kg.m^{-1}.s^{-1}. The reference mass density is $\rho_0 = 0.597$ kg.m^{-3}. Simulations are conducted with or without gravity in order to assess its impact on flow dynamics and heat transfer.

Regenerator model. The regenerator is replaced by a periodic stack of plates in order to work with real solid-fluid interfaces. The stack porosity is 0.5 (smaller than in the experimental device). Plates are thermally conductive ($\kappa_s = 0.20$ W.m^{-1}.K^{-1}, $\rho_s = 2000$ kg.m^{-3}). The specific heat capacity is set to an artificially small value $c_{ps} = 10$ J.K^{-1}.kg^{-1} in order to shorten the transition period before reaching a converged mean state, since c_{ps} value has insignificant impact on the final temperature field [4]. The model equations are solved at the microscopic level: Equations (1)-(5) are solved for the fluid between plates and the heat equation is solved inside each solid plate. Continuity of temperature and heat flux at the solid-fluid interface are ensured in the model.

Heat exchangers. The ambient heat exchanger is modeled here by imposing temperature T_0 at the right end of stack. The temperature at the left end of the stack is not imposed so that it is allowed to decrease due to thermoacoustic heat pumping. With this model the mean temperature difference established over the stack is a measure of thermoacoustic effect.

Acoustic sources. The main source is the acoustic driver (AD), which governs the compression/relaxation cycle through the variation of pressure. It is modeled as an oscillating adiabatic inlet, positioned in the middle of the left domain boundary, at frequency $f_0 = 50$ Hz and amplitude $U_{AD} = 0.4\ \text{m.s}^{-1}$. The amplitude is set in order to obtain a drive ratio $Dr = 2.5\%$ (ratio between the pressure oscillation amplitude and the mean pressure). The second source is the oscillating fluid generator (OFG), which generates oscillating motion without changing the main pressure inside the domain. It is placed inside the domain on the right of the stack (Figure 1) and modeled as two back to back oscillating adiabatic inlets with frequency f_0 and amplitude $U_{OFG} = 0.1\ \text{m.s}^{-1}$. The phase shift between velocity and pressure at the OFG location is fixed $\Phi_u - \Phi_p = \frac{5}{6}\pi$ [4].

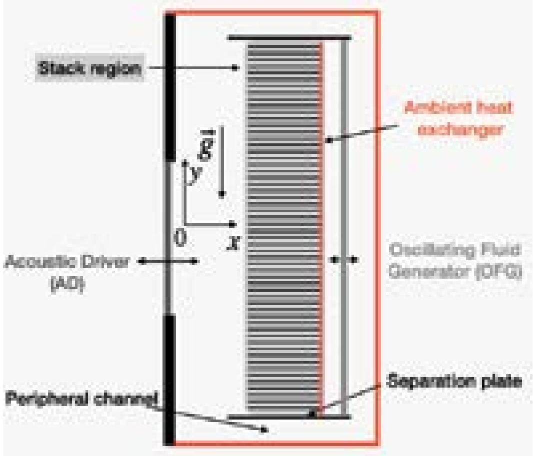

FIGURE 1. Sketch of TACOT model.

Domain length	$8.00\ 10^{-2}$m
Domain height	$1.70\ 10^{-1}$ m
Stack plate length	$3.00\ 10^{-2}$ m
Stack plate height	$1.28\ 10^{-3}$ m
Distance between plates	$1.28\ 10^{-3}$ m
Number of plates	56
Stack area height	$1.446\ 10^{-1}$ m
Distance AD-OFG	$1.16\ 10^{-1}$ m
Distance AD-stack	$3.00\ 10^{-2}$ m
AD height	$1.54\ 10^{-2}$ m
OFG height	$1.45\ 10^{-1}$ m
Peripheral channel height	$1.14\ 10^{-2}$ m

TABLE 1. Dimensions of TACOT model.

Peripheral channel and separation plates. A peripheral channel along the external walls of the cavity allows the circulation of the oscillating flow. Its height is larger than in the experimental device. The stack area is partially bounded by upper and lower separation walls, which are considered adiabatic (ideal situation).

Computational parameters. The domain is discretized according to a cartesian grid 200×1968 in the (x) and (y) directions respectively. In the x-direction, the grid is refined near walls and stack-ends. In the y-direction, cell-size variation is localized in the peripheral channel. In the stack region there are 16 cells in the fluid space between plates for correct resolution of viscous and thermal boundary layers. The time step is set to $\Delta t = 2.5 \times 10^{-5}$ s to respect a CFL-criterion of 0.5 and the L_{inf}-stability criterion related to the Crank-Nicolson scheme.

Initially the fluid is at rest (P_0, T_0, ρ_0). Numerical simulations are conducted until reaching a quasi-converged state, i.e., any averaged quantity computed over 100 cycles remains constant or its time variation can be considered as sufficiently small to be neglected.

4. RESULTS

Previous simulations performed for adiabatic external walls, in the absence of heat exchanger and with no gravity, have shown that large mean temperature difference along the stack ΔT can be obtained (about 50 K) and values agree with linear theory for small Drive ratio values [4; 5].

In the present configurations the external walls are at ambient temperature and the ambient heat exchanger is included. If gravity is not taken into account, Figure 2 shows the mean temperature field (Figure 2a) and the streamlines of mean velocity colored by amplitude (Figure 2b), when the permanent state is reached. There is symmetry with respect to the x-axis of temperature and velocity fields. Contours of temperature inside the stack are almost vertical, as assumed in linear theory. The mean velocity amplitude is maximum near corners and in the region right of the OFG, and almost zero inside the stack plates. Symmetrical counter-rotating cells appear on both sides of the stack as a result of the oscillating motion generated by both sources.

When gravity is included (Figure 3) the top-bottom symmetry is no longer true: The cold region is restricted to the lower part on the left side of the stack while the hot region extends through the stack and over the upper fluid region of the cavity (Figure 3a). The mean temperature difference over the stack plates is $<\Delta T>$=7.24 K without gravity, and 5.98 K when gravity is considered, corresponding to a decrease of about 17.4%. The fluid cooled by the thermoacoustic heat pumping effect generates a downward motion in the area left of the stack and induces a counter-clockwise peripheral flow around the stack region (Figure 3b). This is due to buoyancy effects inside the stack and in the peripheral channel.

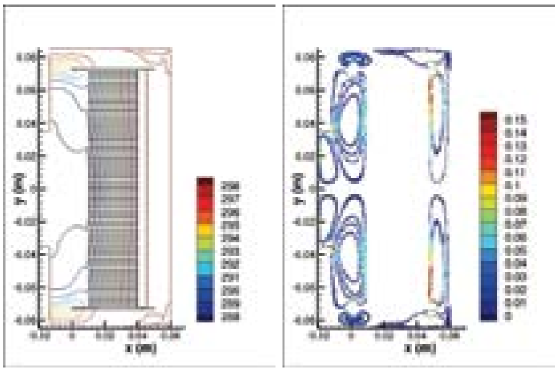

(a) (b)

FIGURE 2. : No gravity, contours of mean temperature (a), streamlines of mean velocity (b)

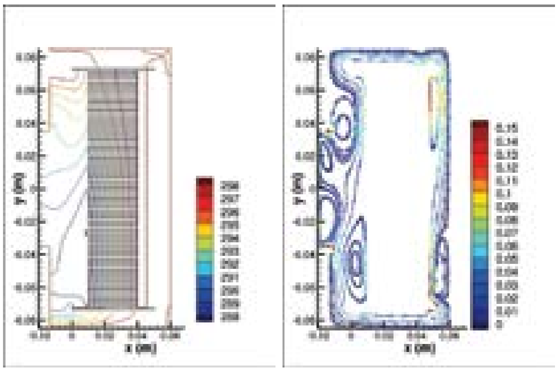

(a) (b)

FIGURE 3. : With gravity, contours of mean temperature (a), streamlines of mean velocity (b)

5. CONCLUSIONS

A simplified two-dimensional numerical model of the TACOT device was introduced. Numerical simulations performed on a specific configuration show that taking gravity into account modifies the temperature distribution, reducing the overall mean temperature difference over the stack. Top-bottom symmetry is lost and a counter-clockwise peripheral flow is observed. The model can be used to explore the influence of gravity for other configurations in order to understand the physical phenomena responsible for temperature inhomogeneity in the device and obtain a more general insight of gravity effects on thermoacoustic heat pumping.

REFERENCES

[1] I.A. Ramadan, H. Bailliet, G. Poignand, and D. Gardner. Design, manufacturing and testing of a compact thermoacoustic refrigerator. *Applied Thermal Engineering*, 189:116705, 2021.

[2] K. Goda. A multistep technique with implicit difference schemes for calculating two- or three-dimensional cavity flows. *J Comp Phys*, 30:76–95, 1979.

[3] R. Knikker. A comparative study of high-order variable-property segregated algorithms for unsteady low mach number flows. *Int J Numer Meth Fluids*, 66:403–427, 2011.

[4] Y. Fraigneau, C. Weisman, and D. Baltean-Carlès. A numerical model of thermoacoustic heat pumping inside a compact cavity. *Acta Acustica*, 7(10):15, 2023.

[5] G. Poignand, P. Lotton, G. Penelet, and M. Bruneau. Small cavity excitation to achieve optimal performance. *Acta Acust united Ac*, 97:926–932, 2011.

Sixth International Conference on Computational Methods for Energy and Thermal Problems
THERMAECOMP2024, Sept. 9-11, 2024, Budva, Montenegro
N. Massarotti, P. Nithiarasu, and I. Vušanović (Eds.)

Comparison of analytical models for Ground Heat Exchangers

Paul Christodoulides, Andreas Skaliontas, Lazaros Aresti, Georgios Florides,
Faculty of Engineering and Technology, Cyprus University of Technology, Limassol, Cyprus;
paul.christodoulides@cut.ac.cy

ABSTRACT

GSHP systems, a form of shallow geothermal energy system, are used for heating and cooling usuing Ground Heat Exchangers (GHEs) that extract/reject heat from/to the ground. In such systems, the thermal response is represented by the temperature change within the GHE and the surrounding earth as a function of heat extraction or injection. There exist several mathematical models, both analytical and numerical, in the literature that govern the thermal response of GHEs. All such models are based on Fourier's law, which allows the determination of heat flow due to conduction. Regarding numerical models, they are obviously more accurate than analytical models and can represent the GHE in greater detail. However, numerical models may be too time-consuming for building energy simulations and consequently of limited use in practical applications. In such case analytical models can play a crucial role. Analytical models can be used as alternatives to one another, depending on the case and the accuracy required to solve a problem. Some of these will be applied to an existing case study of a vertical GHE in the Mediterranean island of Cyprus and be compared to the experimental data and conclusions will be derived regarding the accuracy and suitability of each.

Key Words: G*round Heat Exchanger; GHE analytical models; GHE analytical models comparison;*

1. INTRODUCTION

Ground Source Heat Pumps (GSHPs) are one of the most well-known types of geothermal energy systems that achieve a higher performance than the conventional Air Source Heat Pumps (ASHPs). GSHP systems extract/reject heat from/to the ground through coupling a HP with Ground Heat Exchangers (GHEs), and are used for heating and cooling. GHEs essentially consist of a network of underground tubes with a circulating refrigerant fluid.

Vertical or borehole (typical configuration) GHE, used for the case study here in a U-tube configuration, exchange heat between a circulating fluid and the ground. The ground is therefore acting as an energy source, or for hear rejection. The heat exchange acts primarily as a means of conducting heat to the ground. The thermal response of a vertical GHE is represented by the temperature change within the borehole and the surrounding ground (grout and soil) as a function of heat extraction or injection. There are models that address the heat transfer problem between the fluid (circulating) and the perimeter of the borehole, including the interference between the two parts of the pipe inside the borehole and the heat transfer between the borehole and the ground [1]. This study attempts to compare available analytical models in the literature with experimental data, to determine the performance of the analytical models and whether these models can widely be applied.

2. METHODOLOGY

There are quite a few mathematical models that have been created over the years to quickly and reliably predict GHEs operation. Some of them are analytical and numerical models, all of which are based on Fourier's law, which allows the determination of heat flow due to conduction. Depending on the situation and the accuracy required, different cases require different approaches for analytical models. As for numerical models, they are generally developed to represent the borehole geometry in greater detail than analytical models [2], [3], [4]. The finite difference, finite element and finite volume methods (FDM, FEM, FVM) are usually applied in order to solve an energy balance equation. Although numerical models are more accurate, they are more expensive and require more computational time and memory. Numerical models are used to retrieve an exact solution or parametric analysis. However, most numerical models have limited flexibility in GHE models and take considerable time to calculate them. Thus, they cannot be directly integrated into building energy simulation and are therefore of limited use in practical applications.

In this study, only analytical methods are presented. Such models include (i) instantaneous line source (ILS), (ii) continuous infinite line source (CLS), (iii) continuous cylindrical source (CCS), (iv) continuous Finite line source (FLS). A comparison among different models is provided as follows [5]:

a. Instantaneous line source (ILS)

$$\Delta T = \frac{Q}{4\pi\lambda L} e^{-r^2/(4at)} \tag{1}$$

where T is temperature (K), t is time (s), r is the radial distance of a point from a reference point (the center) (m), λ is thermal conductivity (W m^{-1}K^{-1}) independent from temperature, $\alpha = \frac{\lambda}{\rho c_p}$ is thermal diffusivity (m^{2}s^{-1}) of a homogeneous isotropic solid, and Q is the amount of heat per time (W) released at time $t = 0$, and L is the length of the line / borehole.

b. Continuous infinite line source (CLS)

$$\Delta T = -\frac{Q}{4\pi\lambda L} \mathrm{Ei}\left\{-\frac{r^2}{4at}\right\} \tag{4}$$

Where the *Ei* is the exponential integral, and Euler's constant $\gamma \approx 0.57722$, where

$$\mathrm{Ei}\{-n\} = \gamma + \ln(n) - n + \frac{1}{2}n^2 + O(n^3) \tag{5}$$

or

$$\begin{aligned}\Delta T \approx \frac{Q}{4\pi\lambda L}\Bigg[&\ln\left(\frac{4at}{r^2}\right) - \gamma + 4\pi\lambda R_b \\ &+ \frac{r^2}{2at}\left(\ln\left(\frac{4at}{r^2}\right) - \gamma + 1 - \frac{amc_p}{\pi r^2 \lambda L}\left(ln\left(\frac{4at}{r^2}\right) - \gamma + 4\pi\lambda R_b\right)\right)\Bigg]\end{aligned} \tag{6}$$

where m is the mass of the borehole (kg), L the length of the borehole.

c. Continuous cylindrical source (CCS)

$$\Delta T = \frac{Q}{\pi^2 \lambda r}\int_0^\infty \left(e^{-\alpha x^2 t} - 1\right)\frac{[J_0(rx)Y_1(rx) - J_1(rx)Y_0(rx)]}{x^2[{J_1}^2(rx) + {Y_1}^2(rx)]}dx \tag{7}$$

where J_0, J_1, Y_0, Y_1 are the Bessel functions of the first and second kind, given (for $i = 1,2$) as

$$
\begin{aligned}
J_i(x) &= \sum_{k=0}^{\infty} \frac{(-1)^k}{k!\,\Gamma(k+i+1)} \left(\frac{x}{2}\right)^{2k+i} \\
Y_i(x) &= \frac{J_i(x)\cos(i\pi) - J_{-i}(x)}{\sin(i\pi)} \\
\Gamma(n) &= (n-1)!
\end{aligned}
\tag{8}
$$

d. Continuous Finite line source (FLS)

$$
\Delta T = \frac{Q}{4\pi\lambda L} \int_0^L \left(\frac{\operatorname{erfc}\left(\sqrt{\frac{r^2 + (L/2 - x)^2}{4at}}\right)}{\sqrt{r^2 + (L/2 - x)^2}} - \frac{\operatorname{erfc}\left(\sqrt{\frac{r^2 + (L/2 + x)^2}{4at}}\right)}{\sqrt{r^2 + (L/2 + x)^2}} \right) dx \tag{9}
$$

3. RESULTS

Regarding the case study, determining the thermal properties of the ground of the borehole in Limassol (real case study) of 127m depth and 152mm diameter for a U-tube of 40mm external diameter and bentonite thermal conductivity of $\lambda_b = 1.2$ W m^{-1} K^{-1}. The ground thermal conductivity λ varies between 0.6–1.5 W m^{-1}K^{-1}, while the diffusivity α varies between 0.4–0.68×10^{-6} m^2 s^{-1}. The power used for the thermal response test (TRT) was at 2900 W.

Corresponding results for the models presented above, namely the ILS, CLS, FLS, CCS, are presented in FIGURE 1, where the change in temperature with respect to time is presented. It is clearly observed that the most accurate models compared to the experimental results are CLS1 (equations 4 and 5) and CLS2 (equation 6) with an average error value of 0.0156 and 0.0194 respectively. The results of ILS, FLS and CCS are not as accurate and show an average error value of 3.309, 1.883, 3.317 respectively. It should be mentioned again that the suitability of each method depends on the physical application and most notably on the hypotheses and parameter values chosen

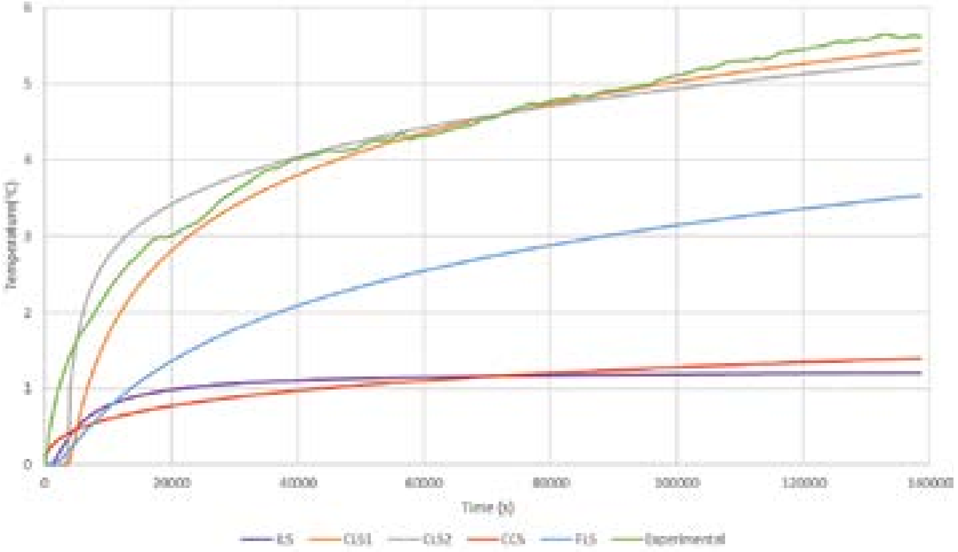

FIGURE 1. Analytical models comparison with experimental data

4. CONCLUSIONS

In this short study, different analytical models were compared against experimental geothermal data of a single U-tube borehole recorded in Cyprus. The analytical models investigated were the: Instantaneous line source (ILS), Continuous infinite line source (CLS), Continuous Finite line source (FLS), and Continuous cylindrical source (CCS).

The analytical models of GHE, observed with the highest accuracy were the CLS1 and CLS2, with very low error value (< 2%) respectively. It can be concluded that analytical models can be considered suitable in the simulation of geothermal models since they benefit much more than numerical models due to less computing time required (by computers) and are much cheaper than numerical models, however very close attention has to be placed on the selection of the parameters and the model.

ACKNOWLEDGMENT

The work presented in this paper has been undertaken in the framework of the research project WAGEs - SMALL SCALE INFRASTRUCTURES/1222/0234, which is co-funded by the Cyprus Research and Innovation Foundation and the European Regional Development Fund, under the Integrated Projects call of the "RESTART 2016-2020" Programme for Research, Technological Development and Innovation.

REFERENCES

[1] L. Lamarche and B. Beauchamp, "A new contribution to the finite line-source model for geothermal boreholes," *Energy Build*, vol. 39, no. 2, pp. 188–198, Feb. 2007, doi: 10.1016/j.enbuild.2006.06.003.

[2] L. Aresti, P. Christodoulides, and G. Florides, "A review of the design aspects of ground heat exchangers," *Renewable and Sustainable Energy Reviews*, vol. 92, pp. 757–773, 2018, doi: 10.1016/j.rser.2018.04.053.

[3] P. Christodoulides *et al.*, "Reviewing the Modeling Aspects and Practices of Shallow Geothermal Energy Systems," *Energies (Basel)*, vol. 13, no. 16, p. 4273, Aug. 2020, doi: 10.3390/en13164273.

[4] S. Javed, P. Fahlén, and J. Claesson, "Vertical Ground Heat Exchangers: A review of heat flow models," in *Proceedings of Effstock 2009: the 11th international Conference on thermal energy storages*, Stockholm, Sweden, 2009, pp. 53–78. doi: 10.1017/CBO9780511974885.006.

[5] P. Christodoulides, G. Florides, and P. Pouloupatis, "A practical method for computing the thermal properties of a Ground Heat Exchanger," *Renew Energy*, vol. 94, pp. 81–89, Aug. 2016, doi: 10.1016/j.renene.2016.03.035.

Sixth International Conference on Computational Methods for Energy and Thermal Problems
THERMAECOMP2024, Sept. 9-11, 2024, Budva, Montenegro
N. Massarotti, P. Nithiarasu, and I. Vušanović (Eds.)

Foundation Slabs as an Energy Geo-Structure in a Moderate Climate

Lazaros Aresti, Georgios Florides, Paul Christodoulides
Faculty of Engineering and Technology, Cyprus University of Technology, Limassol, Cyprus;
lg.aresti@edu.cut.ac.cy

ABSTRACT

Shallow geothermal energy is a type of Renewable Energy, used in dwellings through the employment of Ground Source Heat Pumps (GSHPs). GSHPs are coupled with the Ground Heat Exchangers (GHEs), which are responsible for the heat transfer to/ from the ground. GSHPs have not seen a major advancement in terms of wide implementation, as compared to other Renewable Energy Systems, due to the higher costs associated with them. However, the use of the foundation elements as GHEs, can contribute in a significant reduction of the costs and investment. This study computationally investigates the use of an Energy Geo-Structure (EG) system, namely the foundation slab, of a residential dwelling in Cyprus, using the COMSOL Multiphysics software. A single-family house was designed in accordance with the typical Cyprus construction elements for nearly Zero Energy Building (nZEB) characteristics. Initially, the heating and cooling loads were estimated and used as inputs to analyse the performance of the proposed system. The system under examination demonstrates steady performance and relative high Coefficient of Performance (COP) values, making it a viable renewable energy source solution for building integration.

Key Words: G*round Heat Exchanger; thermo active structures; energy geo structures; foundation GHE; foundation slab GHE;*

1. INTRODUCTION

In recent years, an increase in the popularity of Renewable Energy Systems (RES) towards the as part reduction of fossil fuels and CO2 emissions. Ground Source Heat Pumps (GSHPs), which exploits Geothermal Energy, are such examples, where the systems are utilized for space heating and cooling. In these systems, heat is transferred through a network of tubes specifically designed and place, called Ground Heat Exchangers (GHEs). GHEs function like conventional heat exchangers, where essentially, they absorb or release heat to or from the ground. Although their higher performance, compared to conventional systems, such as even the Air Source Heat Pumps (ASHPs), they have failed to flourish due to the high initial costs associated with them. GHEs are classified into two primary categories: horizontal and vertical (or borehole). The vertical kind is considered the conventional type, and it requires less ground surface area compared to the horizontal types [1].

To reduce the initial costs, recently, GSHP systems have been used in building foundations as Thermo-Active Structure (TAS) systems or Energy Geo-Structures (EGs). These systems have various applications including the energy piles, diaphragm walls, retaining walls, shallow foundations, etc. [2]. EGs are essentially foundations (with reinforced concrete or other material), that are incorporating geothermal pipes. The standard dimensions for energy piles typically range from 10 to 40 m in depth [3] and 0.3 to 1.5 m in diameter [4]. Various pipe configurations can be employed for an EGs system depending on the available space, type, and thermal requirements.

The use of foundation slabs as GHEs, has not been yet implemented in the Mediterranean island of Cyprus. Therefore, this study is intended to evaluate the potential benefits of implementing such systems. Aresti et al. [5] conducted a first examination and preliminary assessment on the energy piles system. The objective of this research is to significantly broaden the initial discoveries and, furthermore, investigate the capacity of GSHP systems by using the foundation slab in a moderate climate, such as in Cyprus, within the context of a Zero Energy Building.

2. METHODOLOGY

For this study, a computational method was selected using the COMSOL Multiphysics software, and based on the convection–diffusion equation. The 3D transient convection–diffusion equation for an incompressible fluid is used for all domains [6] (shown in equation 1), except the pipes, where a simplified 1D version is applied described in equation 2 as:

$$\rho c_p \frac{\partial T}{\partial t} + \rho c_p u \cdot \nabla T + \nabla q = Q \tag{1}$$

$$\rho A c_p \frac{\partial T}{\partial t} + \rho A c_p u e_t \cdot \nabla_t T = \nabla_t \cdot (A k \nabla_t T) + \frac{1}{2} f_D \frac{\rho A}{d_h} |u| u^2 + Q_{wall} \tag{2}$$

where ρ is the density, A is the pipe area, q is the Fourier's heat conduction, c_p is the specific heat capacity at constant pressure, T is temperature, t is time, ue_t is the tangential velocity, k is the thermal conductivity, f_D is the Darcy's friction factor, Q is the heat source, and Q_{wall} is the heat source described with the heat conduction equation.

The geometry is presented in Figure 1, where the foundation slab is included as well as he surrounding soil. The top surface of the foundation slab is assumed as insulated. One significant distinction in the foundation slab, in this example, is the system's extremely shallow depth of only 1 meter, where the ground temperatures and the foundation slab temperatures are influenced by the ambient temperature, and therefore the ambient temperature was used as a boundary condition on the upper surface of the ground domain. The pipes are placed on the lower surface of the foundation slab, represented by lines, and follow a "serpentine" configuration.

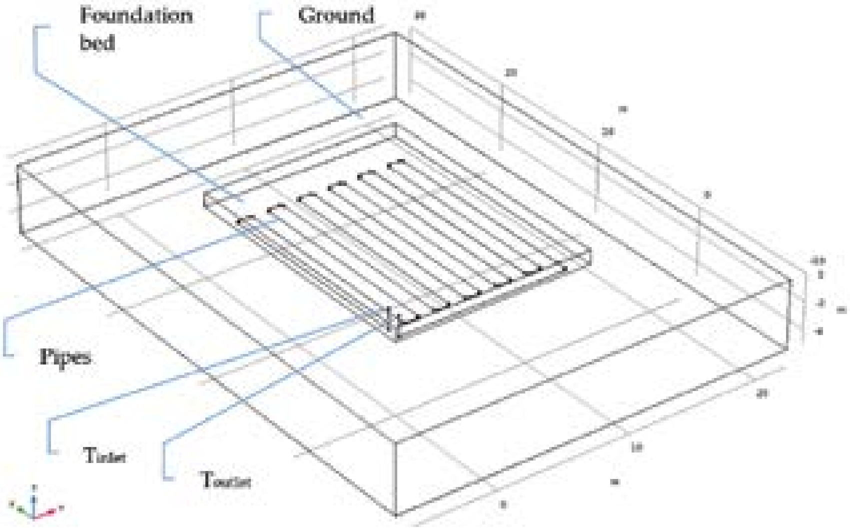

FIGURE 1. Computational model geometry and boundary conditions

3. RESULTS

The computational model is verified and validated in previous work (not shown here), and is modified to satisfy the theoretical residential model under examination. The initial computational results are represented in Figure 2, where the GHE's inlet and outlet temperatures, as well as the coefficient of performance (COP) of the GSHP is presented. By monitoring the outlet temperature, during both winter (February) and summer (July), the system consistently maintains an almost steady condition, with an observed high performance, with COP values of 4.6 in winter and 4.8 in summer.

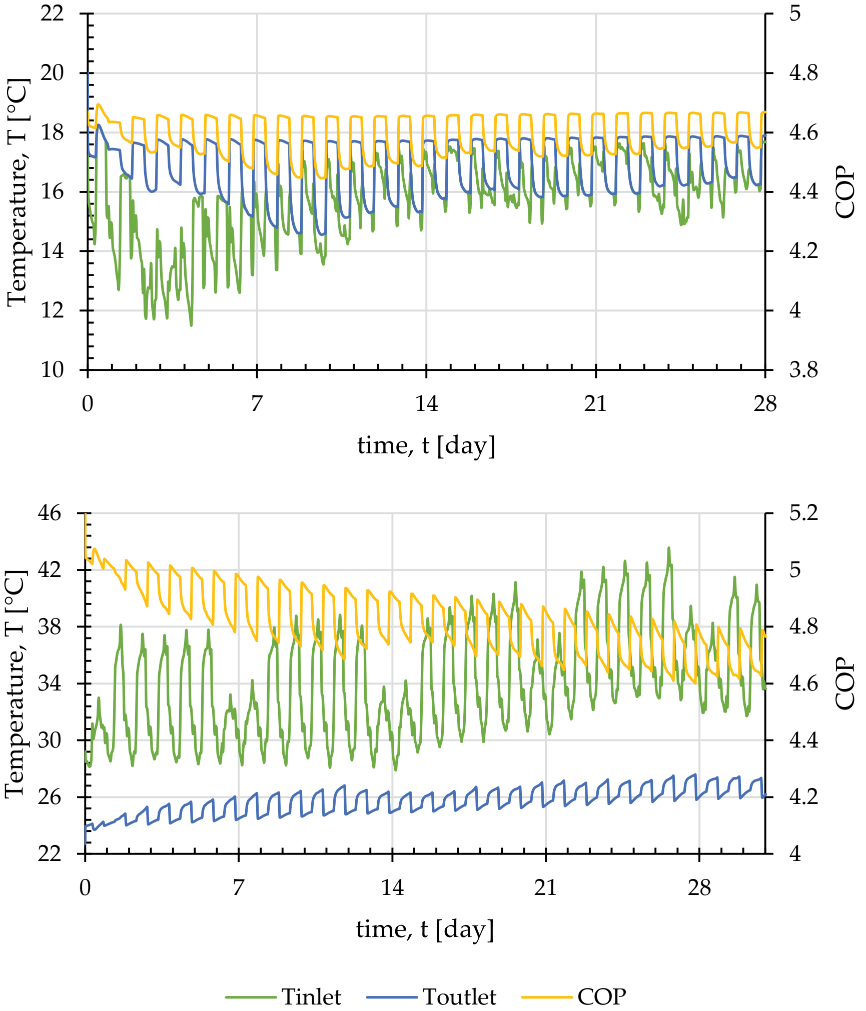

FIGURE 2 Inlet and outlet temperatures and COP values for the months of (top) February and (bottom) July.

One factor that required further investigation, is the rise in temperature of the top surface, representing the surface in contact with the dwelling's internal area. An elevation in the temperature of the dwelling's floor surface would negatively affect the cooling loads, since the heat energy rejected in the ground would circulate back through the foundation bed. This issue might be resolved by installing an insulation layer on the floor of the dwelling, the same technique applied as the rood of the dwelling.

4. CONCLUSIONS

An initial investigation for the use of the foundation slab as an Energy Geo-structure (EG) element was conducted in this research with the use of computational methods. COMSOL Multiphysics was used as the software, where the developed model, introduced the ground temperature characteristics and the local ambient temperature of a specific site. The hourly Ground Heat Exchanger's inlet and outlet temperatures were simulated for the two months, with the maximum demand in summer (July) and winter (February), based on the specified calculated loads. The results obtained indicate that the system exhibit a high coefficient of performance (COP) and maintain an almost constant conditions, with COP values ranging from 4.6 to 4.8.

ACKNOWLEDGMENT

The work presented in this paper has been undertaken in the framework of the research project WAGEs - SMALL SCALE INFRASTRUCTURES/1222/0234, which is co-funded by the Cyprus Research and Innovation Foundation and the European Regional Development Fund, under the Integrated Projects call of the "RESTART 2016-2020" Programme for Research, Technological Development and Innovation.

REFERENCES

[1] L. Aresti, P. Christodoulides, and G. Florides, "A review of the design aspects of ground heat exchangers," *Renewable and Sustainable Energy Reviews*, vol. 92, pp. 757–773, 2018, doi: 10.1016/j.rser.2018.04.053.

[2] D. Sterpi, G. Tomaselli, and A. Angelotti, "Energy performance of ground heat exchangers embedded in diaphragm walls: Field observations and optimization by numerical modelling," *Renew Energy*, vol. 147, pp. 2748–2760, Mar. 2020, doi: 10.1016/J.RENENE.2018.11.102.

[3] H. Brandl, "Thermo-active Ground-Source Structures for Heating and Cooling," *Procedia Eng*, vol. 57, pp. 9–18, Jan. 2013, doi: 10.1016/J.PROENG.2013.04.005.

[4] F. Loveridge, "The Thermal Performance of Foundation Piles used as Heat Exchangers in Ground Energy Systems," *University of Southhampton*, p. 206, 2012.

[5] L. Aresti, P. Christodoulides, L. Lazari, and G. Florides, "COMPUTATIONAL INVESTIGATION ON THE EFFECT OF VARIOUS PARAMETERS OF A SPIRAL GROUND HEAT EXCHANGER," in *12th International Workshop on Applied Modeling & Simulation, WAMS*, 30-31 October, Singapore: Liophant, 2019.

[6] L. Aresti, G. A. Florides, and P. Christodoulides, "Computational modelling of a ground heat exchanger with groundwater flow," *Bulgarian Chemical Communications*, vol. 48, no. Special Issue E, pp. 55–63, 2016.

Sixth International Conference on Computational Methods for Energy and Thermal Problems
THERMAECOMP2024, Sept. 9-11, 2024, Budva, Montenegro
N. Massarotti, P. Nithiarasu, and I. Vušanović (Eds.)

DESIGN OPTIMIZATION AND PERFORMANCE ADVANCEMENT OF GROUND-COUPLED HEAT EXCHANGER

Mohamed A. Samaha[a,b]**, Muhannad T. Ali**[a]**, Ghalib Y. Kahwaji**[a]
[a]Department of Mechanical and Industrial Engineering, Rochester Institute of Technology-Dubai
Dubai 341055, United Arab Emirates, mascada1@rit.edu, mtacad1@rit.edu, gykcad@rit.edu
[b]School of Mathematical Sciences, Rochester Institute of Technology Rochester, NY 14623, USA

Giada Boudekji, Davide Capuano
Graded S.p.A Naples 80141, Italy, davide.capuano@graded.it, giada.boudekji@graded.it

ABSTRACT

The effectiveness of utilizing Ground-Coupled Heat Exchangers (GCHE) for heat exchange with both refrigeration and heating systems has been demonstrated by several studies. In previous work (Kahwaji et al. [1–3]), optimization of the borehole heat exchanger (BHE) configuration fitted with coaxial-tubes was investigated using both numerical simulations and experimental measurements. In this paper, further modifications of the design have been implemented to enhance the performance of the heat exchanger. For the same borehole diameter, the system dimensions were optimized to maximize the overall heat conductance, improve inner to outer flow insulation and reduce the pressure drop to allow for a wider testing flowrate under different flow configurations, (four, three or two boreholes connected in series or parallel). Moreover, the inner pipe (40-m depth) was segmented into seven sections which improves the insulation effectiveness and facilitates assembly and maintenance of the system. Water-cooled A/C system is connected to the GCHE to provide a suitable heat rejection load (8 to 9 kW of condenser heat rejection). An air-cooled A/C system with the same characteristics is installed for comparison. The time-dependent water-side pressure, temperature, flowrate as well as compressor power consumptions are measured. Experimental measurements under different coolant flowrates, heat exchangers connection configurations, parallel, series, and mixed, and borehole rotations (three boreholes working with one stand by at different time intervals) were conducted. Selected cases were numerically simulated for comparison and validation. The steady sate results show that when keeping water inlet temperature, flowrate and compressor power consumption constants, the system with 4, 3 and 2 boreholes connected in series can reject 1.7, 1.54- and 1.34-times heat to the ground than that of their parallel connection counterparts. The mixed series/parallel four boreholes configuration can reject heat of about 1.34 of that of the pure parallel ones which is the same ratio as that of two BHE in parallel configuration. Thus, the series connection rejects more heat and increases the overall coefficient of performance of the system. Meanwhile, decreasing the number of boreholes results in reduction in COP under series configuration while increasing the flowrate leads to a reduction in the temperature duty and increase in the total heat rejection to the ground.

Key Words: *Ground-Coupled Heat Exchangers, Geothermal Energy, Coaxial Borehole, Boundary Layer, Soil Porous Media.*

1. INTRODUCTION

For several decades, a considerable interest in alternative, clean, renewable and sustainable resources of energy have been increasing with the aim to reduce the worldwide consumption of fossil fuels and slow its influence on the environment [4] and economy [5]. Furthermore, the increase in population and development of technology have increased the world's energy demand, which has to be met, but with satisfying the safe limit of air pollution and global warming. Improving energy utilization efficiency by 40-45% has been set as a target by the UN, EU and most countries around the world. Geothermal heat exchange is an auspicious renewable resource that could be utilized through ground-coupled heat exchangers (GCHEs) to exchange thermal energy with the ground. GCHE was demonstrated to efficiently perform for both heating and cooling applications in cold and hot climates [6]. GCHEs have a promising potential as a heat rejection method for chillers especially in hot and humid climates where operating cooling towers is costly and are not very effective such as the case of the Gulf countries that is the focus of the present work. Kahwaji et al. [1–3] have numerically simulated and experimentally measured the performance of a coaxial borehole ground-coupled heat exchanger (BHE) under Dubai, UAE real conditions for first time. They also varied the design and the system configuration to maximize the heat rejection to the ground. The proposed design of the BHE was simple and relatively inexpensive where high-density Polyethylene (HDPE) outer pipe is utilized to combat corrosion from salty ground water and reduce cost and an inner core made from UPVC is combined with the outer tube to form the heat exchanger. The BHE system is composed of four boreholes (40-m depth and 9-cm outer diameter) that can be connected in series, parallel or mixed. Water-cooled A/C system providing a maximum condenser load of 8 to 9 kW is connected to the BHE. A matching air-cooled A/C system with the same cooling characteristics is installed for comparison and estimation of the power saving. The present study is aiming at further enhancement of the performance of the heat exchanger by modifying its design to increase the heat rejection to the ground. Moreover, the performance is examined for different configurations and arrangements of the boreholes including parallel, series and mixed connections. Finally, the power saving by the proposed system is being estimated for the determination of the system feasibility in industrial applications.

2. METHODOLOGY

A couple of modifications has been implemented based on previous testing results from the existing system. The inner core of the exchanger was modified to enhance the insulation characteristics of the air gap and to minimize the pressure drop in the system which will allow achieving higher heat dissipation, better system delta temperatures and allow better flexibility in testing different borehole configurations using the same pumping setup. Furthermore, the inner core was segmented longitudinally into seven identical components to facilitate installation and maintenance. The time-dependent water-side pressure, inlet/outlet temperatures and flowrate as well as refrigeration cycle compressor power consumption are measured using calibrated sensitive pressure gauge, thermocouples, flowmeters and power-meter instrumentations. The temperature and flowrate recorded data are used to estimate the heat rejection to the ground. A predetermined set of water flow configurations comprised of one, two, three and four boreholes connected in series, two, three and four boreholes connected in parallel as well different series-parallel configurations were tested to arrive at their characteristics and propose the best. All experiments were conducted over 24 hours cycles with two days stopping periods in between to allow for ground discharge and similar starting conditions.

3. RESULTS AND DISCUSSION

Figure 1 shows the heat rejection, power consumption and COP for different BHE configurations. The results indicate that the series connection is always better than the parallel one as long as the number of boreholes, flowrate and inlet water temperature are kept the same between both connections. We reason that water flow encounters a longer path to reject heat to ground with the series connection, which advances the performance of the heat exchanger as well as the progressive lower charging temperature of the boreholes which results in a better overall temperature drop through the exchanger. The steady state results show that the system with 4 boreholes connected in series is able to reject heat of about 7 kW, which is 1.7 times as much as that of the parallel one (see Figure 1-a) when water inlet temperature is 41°C for both configurations at the design flowrate.

FIGURE 1. Heat rejection, compressor power consumption and COP with time for different configurations and connections of boreholes: (a,b) 4 BHEs with 41°C steady inlet; (c,d) 3 BHEs with 43°C steady inlet; (e,f) 2 BHEs with 46°C steady inlet; and (g,h) 4 BHEs with 41°C steady inlet. For all cases, the inlet flowrate is kept constant at the design value, 21 lit/min.

Meanwhile, for three boreholes in series, the BHE surface area and the flow path subjected to heat transfer decreases relative to that of the 4 BHEs. This increases the steady inlet water temperature to 43°C, which compensates for the heat rejection to keep it at about 7 kW (see Figure 1-c). However, the rise in water temperature little increases the condenser temperature, and hence, the compressor power (see Figure 1-c) resulting in a lower COP (see Figure 1-d). Furthermore, Figure 1-c demonstrates that the three boreholes connected in series has a steady heat rejection of 1.54 of that of the parallel one, a drop of 10% from the four boreholes configuration. This indicates the decreasing effectiveness towards the exit of the exchanger. Further reduction of the surface area and flow path when utilizing 2 boreholes in series increases the inlet water temperature to 46 °C to keep the heat rejection at 7 kW (see Figure 1-e). Consequently, the compressor power increases and COP decreases (see Figure 1-f). The two boreholes' series connection can reject 1.34 as much heat as that of the parallel one. On the other hand, when the mixed 2 series and 2 parallel boreholes configuration is implemented, a heat rejection of about 1.34 of that of the pure parallel one (same as the previous case) is observed.

4. CONCLUSIONS

The series connection of the boreholes always contributes to increasing the overall coefficient of performance, COP, up to 4.3 for the presented cases with maximum heat rejection of about 9 kW. The parallel connection possesses maximum COP about 3.0 with maximum heat rejection of about 6 kW. The mixed parallel/series connection has indicated a maximum COP of about 3.5 with maximum heat rejection of about 7.2 kW. Meanwhile, decreasing the number of the boreholes results in reduction in COP for series connection. On the other hand, increasing the flowrate leads to a reduction in the temperature duty and increase in the total heat rejection to the ground (measurements still in progress).

REFERENCES

[1] G. Y. Kahwaji, D. Capuano, G. Boudekji, and M. A. Samaha, Design and optimization of ground-coupled refrigeration heat exchanger in Dubai: Numerical approach, *Heat Transfer*, 53, 1474–1500, 2024.

[2] G. Y. Kahwaji, D. Capuano, G. Boudekji, and M. A. Samaha, Optimization of High-Capacity Ground-Coupled Heat Exchanger under Hot-Wet Climate Condition: Numerical Approach, *in Proceedings of the 6th International Conference on Energy Harvesting, Storage, and Transfer (EHST'22),* 2022, p. 116, doi: 10.11159/ehst22.116.

[3] G. Y. Kahwaji, Muhannad T. Ali, G. Boudekji, D. Capuano, Abdelrahman E. Nasreldin, Abdullah Khan, and M. A. Samaha, Maximizing Performance of Ground Coupled Heat Exchanger under Hot Wet Climate Condition: Experimental and Numerical Analysis, *in Proceedings of the 6th International Conference on Energy Harvesting, Storage, and Transfer (EHST'22),* 2022, p. 117, doi: 10.11159.ehst22.117.

[4] S. A. Alkaff, S. C. Sim, and M. N. Ervina Efzan, A review of underground building towards thermal energy efficiency and sustainable development, *Renewable and Sustainable Energy Reviews*, 60, 692–713, 2016.

[5] K. Ju K, B. Su, D. Zhou, P. Zhou, Y. Zhang, Oil price crisis response: Capability assessment and key indicator identification, *Energy*, 93, 1353–1360, 2015.

[6] A. Carotenuto, P. Marotta, N. Massarotti, A. Mauro, G. Normino, Energy piles for ground source heat pump applications: Comparison of heat transfer performance for different design and operating parameters, *Applied Thermal Engineering*, 124, 1492–1504, 2017.

Sixth International Conference on Computational Methods for Energy and Thermal Problems
THERMAECOMP2024, Sept. 9-11, 2024, Budva, Montenegro
N. Massarotti, P. Nithiarasu, and I. Vušanović (Eds.)

Exploring a Novel Geo-Exchange System on Ischia Island, Southern Italy: an Experimental Study

A. Carotenuto, V. Guida and N. Massarotti
Department of Engineering, University of Napoli “Parthenope”, Centro Direzionale, Isola C4, 80143 Napoli (NA), Italy, alberto.carotenuto@uniparthenope.it, vincenzo.guida1@studenti.uniparthrnope.it, nicola.massarotti@unipartenope.it

A. Mauro
Department of Engineering, University of Campania *Luigi Vanvitelli*, Via Roma 29, 81031 Aversa (CE), Italy, alessandro.mauro@unicampania.it

ABSTRACT

The necessity for efficient and environmentally friendly air conditioning systems is a fundamental requirement for the society. In this context, the utilization of low and medium enthalpy geothermal energy can play a crucial role. The present work describes the research activities regarding the design, realization and test of an innovative technology capable of providing thermal energy to indoor environments, without extracting fluids from the subsurface. The proposed system relies on the utilization of a downhole heat exchanger (DHE). The authors have pioneered an innovative approach to the sustainable utilization of low and medium enthalpy geothermal energy, implementing it on Ischia island, near Naples, in southern Italy. This system employs a specifically designed DHE to optimize the heat transfer with the subsurface, eliminating the need to withdraw fluids from the aquifer. The experimental setup is based on the DHE and on the above-ground system, essential for evaluating its efficiency and feeding the terminals. The heat exchanger is placed within a geothermal well, constructed with a steel casing, equipped with a filtering section positioned adjacent to the heat exchanger, in order to enhance the heat transfer performance. The experimental findings demonstrate that the heat exchanger enables the exchange more than 40 kW with the ground, yielding overall heat transfer coefficient values exceeding 435 W/m^2 K.

Key Words: *Heat Transfer, Geothermal energy, Low enthalpy, Downhole heat exchanger.*

1. INTRODUCTION

The European Union has placed a strong emphasis on boosting the utilization of renewable energy. There has been notable growth in the production of solar and wind energy, but these technologies depend greatly on weather conditions, resulting in notable fluctuations in electricity production [1]. Instead, geothermal energy is not subject to weather-induced variations.

Heat exchangers are essential to effectively exploit geothermal energy and can be installed underground in both horizontal and vertical orientations. Vertical installations are generally preferred for high heat exchange capacity in confined spaces. A downhole heat exchanger (DHE) operates by not removing geothermal fluid from the aquifer, which results in an effective and sustainable system.

Although much attention has been devoted to studying DHEs [2-5], there are still aspects concerning their interaction with wells and aquifers that require further investigation. This is due to the complexity of the entire system and the need to maximize heat transfer with the ground, without risking aquifer freezing.

Regarding experimental research on actual DHE systems, along with numerical investigations, Carotenuto and colleagues [2-3] have contributed significantly. They presented field findings from a prototype geothermal convector installed in a real well, emphasizing the significance of natural convection enhancers for such applications.

In the present work, the authors conduct on field experiments to assess the actual effectiveness of a custom-designed DHE, tailored specifically for geothermal use. This paper presents the primary outcomes of the field experiments conducted on Ischia Island, located in southern Italy.

2. DESCRIPTION OF THE EXPERIMENTAL SET-UP

The experimental set-up has been realized on Ischia island, a volcanic area with significant geothermal potential, and comprises:

(i) Downhole Heat Exchanger (DHE): The DHE is a custom-designed unit made from AISI 316L stainless steel to resist to corrosion from geothermal fluids. It measures 6 meters in length and includes internal baffles and steel tie rods for structural integrity.

(ii) Above ground heat dissipation system: This includes a dry cooler, which simulates the thermal load of an indoor heating system. The system allows to test different working conditions by dissipating the heat absorbed by the DHE.

(iii) Control and measurement apparatus: The control system features an electromagnetic flow meter, pressure transducers, Pt100 thermal probes, acquisition system and all the mechanic and electric components needed for managing and controlling the overall system. The data logger records all the temperatures within the well at different depths, such as outside the well, to analyze thermal gradients and heat transfer efficiency.

The efficiency has been calculated as follows [3]:

$$\eta = \frac{T_{top} - T_{bottom}}{T_{top} - T_m}$$

where T_m is the mean temperature, i.e. the average temperature between the inlet and outlet temperatures of the DHE, T_{top} and T_{bottom} are the temperature at the top and bottom surfaces of the DHE, respectively, and they have been measured using the temperature probes at the top and bottom caps of the DHE.

The well has a total depth of 121 meters. Filtering pipes have been installed to enhance heat transfer. The heat exchanger is positioned at a depth of 59 meters (base of the exchanger) from the ground level, with the water level located at a depth of 50 meters from the ground level. The system is equipped with five temperature probes, distributed at various depths: one at the base of the exchanger, one at an intermediate position, and one at the top of the exchanger. The remaining two probes are located 1 and 2 meters above the top of the exchanger, respectively. Figure 1 provides a schematic representation of the heat exchanger within the well.

Tests up to two weeks duration have been conducted, by varying the flow rate, employing the following values: 2375 l/h, 1875 l/h, 1500 l/h. Notably, throughout these extended tests, no freezing phenomena of the ground has been appreciated. This suggests that the combination of the DHE and the chosen installation site is well-suited for the intended application. It is worth highlighting that the system can comfortably manage a maximum flow rate up to 2500 l/h.

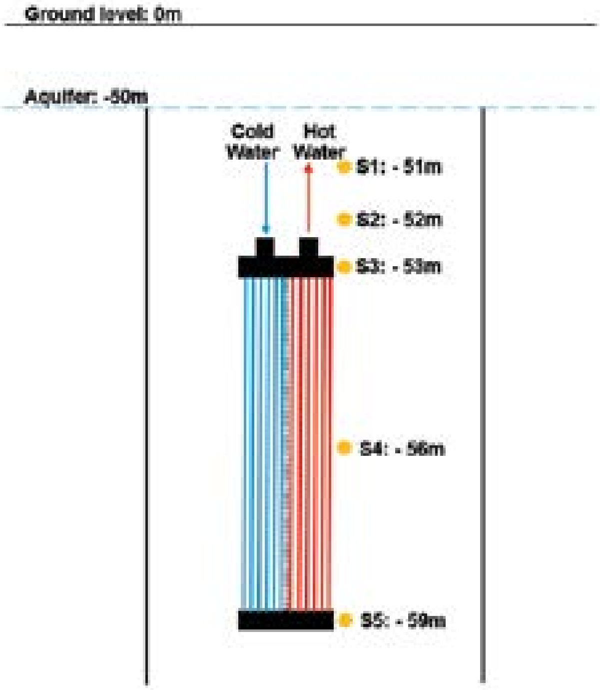

FIGURE 1. Sketch of the Down Hole Heat Exchanger within the well.

3. RESULTS

The on-site experimental tests have demonstrated the effectiveness and efficiency of the innovative DHE, achieving high efficiency, with an average value around 0.8, such as an overall heat transfer coefficient averaging 435 W/m^2K.

The temperature probes mentioned in the previous section have provided data on the groundwater temperature before and after the system is activated. Figure 2 shows the temperature profiles in the well with the system on and off.

The thermal power transferred from the ground to the DHE reaches peak values exceeding 40 kW, with an average of 36 kW. The analysis of the data presented in Figure 2 indicates a decrease in groundwater temperature during the tests, without observing any freezing phenomena of the ground. When the tests are finished, the groundwater returns to its initial temperature within few hours, thereby maintaining its ability to effectively transfer thermal power.

4. CONCLUSIONS

The outcomes from the trials conducted on the Ischia island for the innovative DHE showcase satisfactory results. This technology has demonstrated effectiveness across key performance parameters, including efficiency, overall heat transfer coefficient, and thermal power.
The authors believe that further research efforts on the analysis of DHE for geothermal applications could support the spread of sustainable use of geothermal energy in present society.

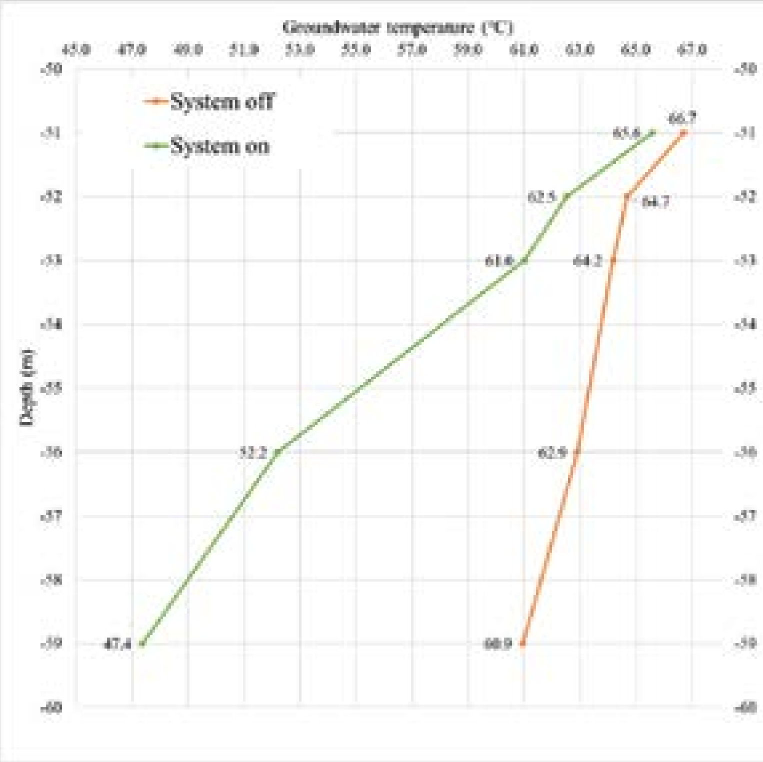

FIGURE 2. Temperature measurements in the well.

ACKNOWLEDGEMENTS

The authors gratefully acknowledge the financial support of project PRIN 2020 "Optimal refurbishment design and management of small energy micro-grids - OPTIMISM", Prot. 20204NXSZH, CUP I65F21001850006, Ministero dell'Università e della Ricerca (MUR).

REFERENCES

[1] F. Calise, M.D. D'Accadia, A. Macaluso, A. Piacentino and L. Vanoli, Exergetic and Exergoeconomic Analysis of a Novel Hybrid Solar–Geothermal Polygeneration System Producing Energy and Water, *Energy Conversion and Management*, 115, 200–2, 2016.

[2] A. Carotenuto, C. Casarosa and L. Vanoli, Optimizing the position of the tube casing slotted section for geothermal wells with a downhole heat exchanger, *Geothermics*, 30, 133 – 57, 2001.

[3] A. Carotenuto, C. Casarosa, C. and L. Martorano, The Geothermal Convector: Experimental and Numerical Results, *Applied Thermal Engineering*, 19, 349–74, 1999.

[4] G. Gola, E. Di Sipio, M. Facci, A. Galgaro and A. Manzella, Geothermal deep closed-loop heat exchangers: A novel technical potential evaluation to answer the power and heat demands, *Renewable Energy*, 198, 1193–209, 2022.

[5] J. Pássaro, A. Rebola, L. Coelho and J. Conde, Numeric study of geothermal borehole heat exchanger enhancement via phase change material macro encapsulation, *International Journal of Thermofluids*, 16, 100245, 2022.

Sixth International Conference on Computational Methods for Energy and Thermal Problems
THERMAECOMP2024, Sept. 9-11, 2024, Budva, Montenegro
N. Massarotti, P. Nithiarasu and I. Vušanović (Eds.)

Modeling temperature distribution in different grouting materials for Ground Source Heat Pumps

Fawad Ahmed, Nicola Massarotti
University of Naples 'Parthenope', Centro Direzionale Isola C4, 80143, Napoli, Italy,
fawad.ahmed001@studenti.uniparthenope.it

ABSTRACT

This study provides a numerical investigation of the subsurface temperature variation induced by different grouting materials utilized in ground source heat pump (GSHP) systems. GSHP systems have grown into a practical and sustainable heating and cooling option for buildings. The thermal properties of the ground, as well as the grouting materials used, have a significant impact on the performance of GSHP systems. In this work, numerical simulations are utilized to investigate the subsurface temperature distribution over time while using a range of grouting materials. The model employed for the simulations, takes into account the thermal conductivity, heat capacity, and thermal diffusivity of the grouting materials. The findings provide insight into the thermal behavior of various grouting materials, as well as how they can impact the efficiency and performance of GSHP systems. This study contributes to the enhancement of GSHP design and operation by making recommendations for selecting appropriate grouting materials to maximize heat transfer efficiency and system performance.

Key Words: *Sub-surface Heat Transfer, Finite Volume Method, Ground Source Heat Pump.*

1. INTRODUCTION

Ground Source Heat Pumps (GSHPs) are a popular choice for sustainable heating and cooling as the planet moves towards decarbonization. They have a long operating life and provide a variety of alternatives [1]. The efficiency and performance of GSHP systems are heavily influenced by subsurface heat transfer during heat pump operation [2]. During the operating cycle, the ground serves as either a heat transfer source (for heating) or sink (for cooling). For the GSHP to work well for long time, the characteristics of the ground must be steady [3].

The study described in this paper quantitatively evaluates subsurface temperature fluctuation for various grouting materials used in GSHP applications. The goal of these simulations is to explore the subsurface heat transfer phenomena that occurs when the GSHP system is in operation. These simulations demonstrate the subsurface temperature change in the soil during heating/cooling operations using various grouting materials. The significance of sub-surface temperature for GSHPs is critical for their long-term effectiveness [4].

The findings of this study have important implications for the design, installation, and long-term operation of GSHP systems. We want to give useful insights into the influence of grouting materials on subsurface temperature dynamics, which will improve engineering practices, optimize energy efficiency, and contribute to the long-term deployment of GSHP technology.

2. METHODOLOGY

To simulate different grouting materials for comparative analysis, a 2-D axisymmetric finite volume method (FVM) is used. The domain is discretized into 37k elements. Higher mesh density in the fluid domain improves to analyse the heat transmission between the fluid and its surroundings. The domain is a 500 x 1000 mm rectangle with the borehole and grout on the left side. The distance of the outer wall of the borehole from the axis is 95 mm and depth of 800 mm. The radius of the exterior pipe is 24 mm with 800 mm depth, while the radius of the inner pipe is 8 mm with 760 mm depth. Figure 1 shows the domain with mesh volume made of tetrahedral elements with boundary layer along the pipe walls, which captures heat transport details during simulation.

The heat transfer fluid (HTF) employed in the simulation is water, which has a thermal conduc-

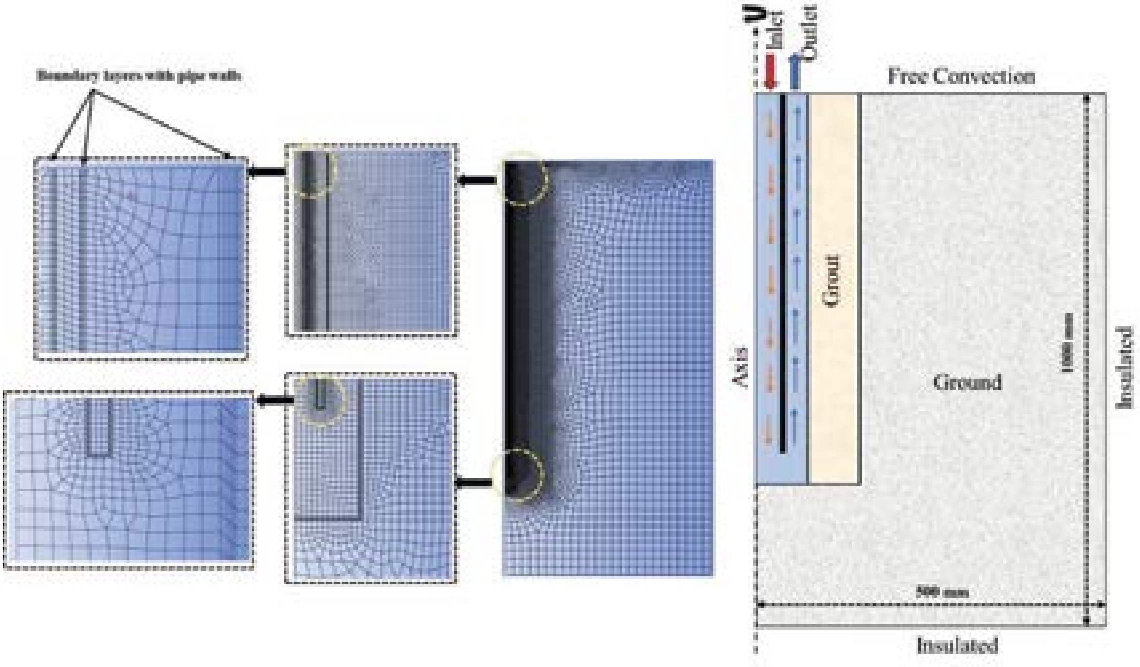

FIGURE 1. : Domain with mesh elements

tivity of 0.600 $W/m/K$, density of 1000 kg/m^3 and a specific heat capacity of 4186 $J/kg/K$. The inner pipe of the coaxial ground heat exchanger (GHE) is made of high-density polyethylene (HDPE) with a thermal conductivity of 0.421 $W/m/K$, density of 960 kg/m^3, and specific heat capacity of 2600 $J/kg/K$, whereas the outer pipe is made of steel with a thermal conductivity of 2.65 $W/m/K$, density of 2647 kg/m^3, and specific heat capacity of 830 $J/kg/K$. Table 1 shows the parameters of ground and different grout materials [5].

Materials	Thermal Conductivity $W/m/K$	Density kg/m^3	Specific heat capacity $J/kg/K$	Latent heat kJ/kg	Phase Change temperature (°C)
Ground (Silica)	2.65	2647	830	-	-
Reference (G1)	2	1520	750	-	-
Enhanced (G2)	2.7	2000	800	-	-
MEPCM (G3)	1.025	1510	1593.15	24.36	23.5 - 28.8
SSPCM (G4)	2.17	1760	1959.12	25.00	20 - 30

TABLE 1. Properties of ground and grouting materials

3. RESULTS

The model for cooling and heating is run for 8 hours, with 4 hours dedicated to cooling and 4 hours dedicated to heating. The domain's starting temperature is fixed at 18 °C. In both circumstances, the inlet flow rate remains constant at 1800 l/hr ($0.5{\cdot}10^{-3}\mathrm{m}^3/s$). The inlet water temperatures for cooling and heating processes are kept constant at 30°C and 10°C, respectively. Figure 2 shows the domain temperature of different grouting materials during a four-hour cooling operation. Sensible grouts reveal that the temperature is transmitted to the rest of the domain at the completion of the cooling procedure, and the domain's temperature is raised to almost 30 °C. The scenario for the phase change material (PCM) integrated grouts is different as compared to the sensible grouts. The temperature for micro-encapsulated phase change material (MEPCM) grout is approximately 23 °C, whereas shape-stabalized phase change material (SSPCM) is around 25 °C, which is lower than the sensible grout. This leads to the conclusion that PCM integrated grouts can store temperatures in the form of latent energy, and hence the temperature in the domain is lower than that of sensible grouts.

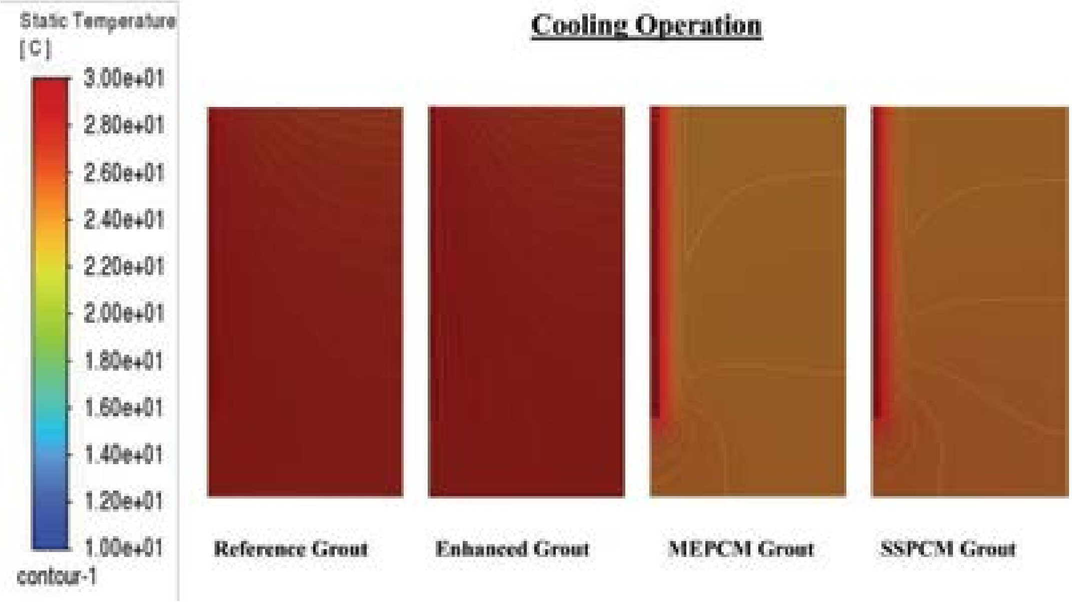

FIGURE 2. : Temperature comparison of domain for different grouting materials during 4 hours cooling operation

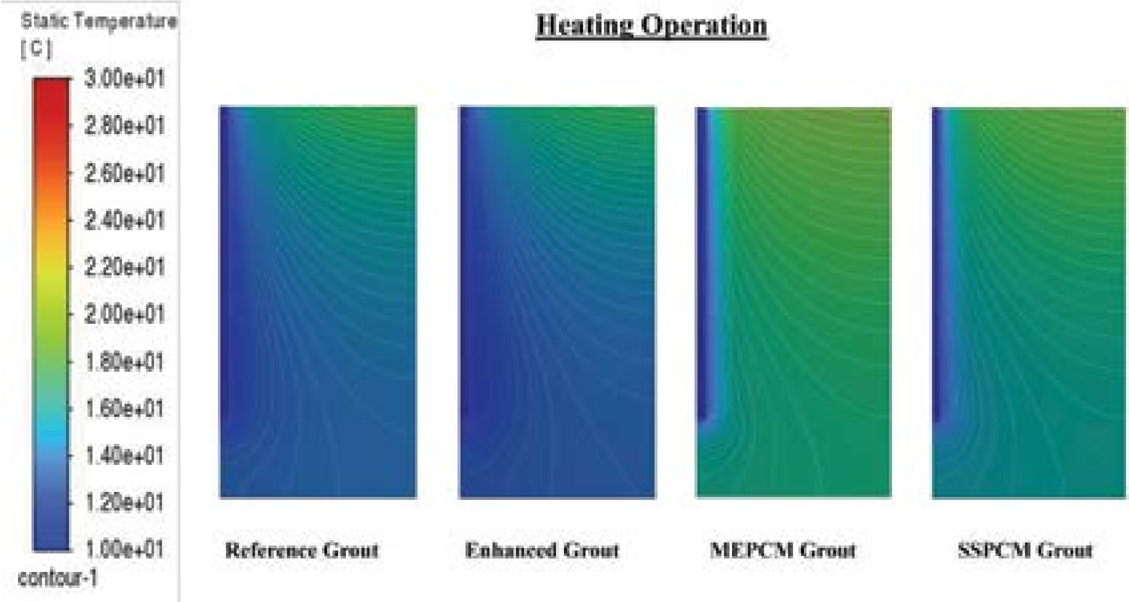

FIGURE 3. : Temperature comparison of domain for different grouting materials during 4 hours heating operation

Figure 3 depicts the temperature comparison of the domain with different grouting materials throughout the heating process. The contours clearly show that the reduction in temperature in the domain is caused by heat exchange with fluid, and the cooling impact induced by this mechanism affects virtually the whole domain. For sensible grouts, the domain temperature decreased to 13 °C during continuous operation. On the other hand, the domain temperatures for PCM integrated grouts stayed between 16 and 18 °C. This is fully justified, as temperature of the domain changes quickly in sensible grouts than in PCM integrated grouts.

4. CONCLUSIONS

The simulation presented in this paper show that including PCM into grouting material can improve the thermal performance of GSHP by mitigating their influence of subsurface temperature change. During cooling and heating operations, domain temperatures for PCM integrated grouts remained different from sensible grouts. This also demonstrates that the GSHP can operate at better efficiency for a longer period of time since the subsurface temperature remains relatively constant. Another advantage of PCM integrated grouts is their natural capacity to store energy in latent form due to the presence of PCM. This can also be employed as a energy storage mechanism near the source. In future work, the data obtained from such models can be fed to the AI model for demand estimation of such thermal systems [6].

5. ACKNOWLEDGEMENT

The work was supported by the Ministry for Education, University and Research (Italy) (MIUR) under the title of Doctoral Research Funding for Green Themes with code FSE REACT-EU CUP 165F21001390001.

REFERENCES

[1] Ioan Sarbu and Calin Sebarchievici. *Ground-Source Heat Pumps: Fundamentals, Experiments and Applications*. joe hayton, 2015. ISBN 9780128042205. doi: 10.1016/C2015-0-01812-3.

[2] Sajjan Pokhrel, Agus P. Sasmito, Atsushi Sainoki, Toshiyuki Tosha, Tatsuya Tanaka, Chiaki Nagai, and Seyed Ali Ghoreishi-Madiseh. Field-scale experimental and numerical analysis of a downhole coaxial heat exchanger for geothermal energy production. *Renewable Energy*, 182:521–535, 2022. ISSN 18790682. doi: 10.1016/j.renene.2021.10.038. URL `https://doi.org/10.1016/j.renene.2021.10.038`.

[3] Younes Noorollahi, Reza Saeidi, Mohammad Mohammadi, Ali Amiri, and Mehdi Hosseinzadeh. The effects of ground heat exchanger parameters changes on geothermal heat pump performance – A review. *Applied Thermal Engineering*, 129:1645–1658, 2018. ISSN 13594311. doi: 10.1016/j.applthermaleng.2017.10.111. URL `https://doi.org/10.1016/j.applthermaleng.2017.10.111`.

[4] Sorranat Ratchawang, Srilert Chotpantarat, Sasimook Chokchai, Isao Takashima, Youhei Uchida, and Punya Charusiri. A Review of Ground Source Heat Pump Application for Space Cooling in Southeast Asia. *Energies*, 15(14), 2022. ISSN 19961073. doi: 10.3390/en15144992.

[5] Hossein Javadi, Javier F. Urchueguía, Borja Badenes, Miguel Mateo, Ali Nejad Ghafar, Ojas Arun Chaudhari, Giedrius Zirgulis, and Lenin G. Lemus. Laboratory and numerical study on innovative grouting materials applicable to borehole heat exchangers (BHE) and borehole thermal energy storage (BTES) systems. *Renewable Energy*, 194:788–804, 2022. ISSN 18790682. doi: 10.1016/j.renene.2022.05.152. URL `https://doi.org/10.1016/j.renene.2022.05.152`.

[6] Armando Di Meglio, Nicola Massarotti, and Perumal Nithiarasu. A physics-driven and machine learning-based digital twinning approach to transient thermal systems. *International Journal of Numerical Methods for Heat and Fluid Flow*, 2024. doi: 10.1108/HFF-10-2023-0616.

Sixth International Conference on Computational Methods for Energy and Thermal Problems
THERMAECOMP2024, Sept. 9-11, 2024, Budva, Montenegro
N. Massarotti, P. Nithiarasu and I. Vušanović (Eds.)

Digital Twinning of a container-house HVAC system for controlling and optimizing energy consumption

Armando Di Meglio, Davide Maria Laudiero, Nicola Massarotti, Alessandro Mauro
University of Naples "Parthenope", Italy, Centro Direzionale Napoli, 80143,
armando.dimeglio001@studenti.uniparthenope.it,
davidemaria.laudiero@studenti.uniparthenope.it, nicola.massarotti@uniparthenope.it,
alessandro.mauro@uniparthenope.it

Perumal Nithiarasu
Zienkiewicz Institute for Modelling, Data and AI, Swansea University, Swansea, UK,
p.nithiarasu@swansea.ac.uk

ABSTRACT

This article presents a comparative study of energy consumption for an HVAC system in a container home, evaluating traditional control methods (such as on-off, PID, and PI) against an AI-based approach using reinforcement learning. Dynamic simulations were conducted to assess the performance and efficiency of each control strategy. The results demonstrate the potential advantages of AI in optimizing energy use, highlighting significant differences in consumption patterns and system responsiveness. This study provides valuable insights into the efficacy of advanced AI techniques in enhancing HVAC system performance in modern housing solutions.

Key Words: *Digital Twin, building, container house, reinforcement learning, control strategy, energy efficiency.*

1. INTRODUCTION

Container Houses (CHs), built from shipping containers, are gaining popularity for their cost-effectiveness and sustainability. These structures - versatile, modular, and structurally resilient - are suitable for various residential and commercial uses often made from recycled containers, and provide quick, affordable, and eco-friendly housing solutions globally. They are useful as temporary housing following disasters due to their rapid deployability. However, challenges such as ensuring proper thermal and acoustic insulation and meeting local building regulations must be addressed. Energy efficiency is a critical aspect of CHs, especially in emergency deployments where rapid construction can compromise comfort. Proper insulation, ventilation, and thermal comfort are essential. Studies show that adhering to Near Zero Energy Building (NZEB) standards can significantly reduce energy consumption. Artificial intelligence can play a pivotal role in finding the optimal control strategies to guarantee both thermal comfort and energy saving. Rule-based control, PID, Model Predictive Control are possible control strategies generally adopted in dynamic energy systems [1; 2; 3]. This work aims to explore the AI-based control strategy (Reinforcement Learning) and compare it with the PID-based one. More specifically, we build a simple but effective Digital Twin (DT) of the container house to control the indoor temperature by changing the power of the HVAC system, as it was similarly conducted in a previous transient thermal system [4].

2. CASE STUDY

The case study of a container house is analyzed in detail from an energy point of view in ref. [5]. The sketch of the container house geometry is shown in Figure 1. In that work, the simulations were conducted according to the European/Italian legislation for the dynamic (hourly) simulations of the building energy balance. However, to build the DT, it is needed to couple the dynamic model and the RL-based control strategy. So, a simplified model of

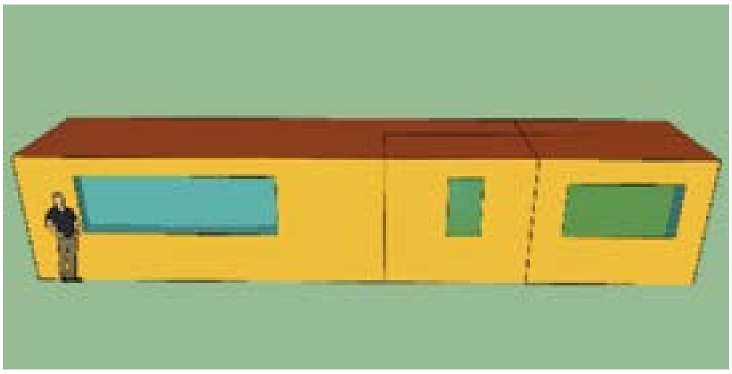

FIGURE 1. Container geometrical model

the building based on a single equation is adopted. From the commercial software EdilClima all energy flows are obtained . They can be strictly dependent on the temperature difference between indoor and external environment or they can be the heat gains due to occupancy, solar radiation, and lighting system. The general equation is the following one.

$$C\frac{dT_{in,air}(t)}{dt} = \dot{Q}_{\mathrm{int}}(t) + \dot{Q}_{\mathrm{sol}}(t) + \dot{Q}_{\mathrm{inf}}(t) + \dot{Q}_{\mathrm{vent}}(t) + \dot{Q}_{\mathrm{trans}}(t) + \dot{Q}_{HVAC}(t) \tag{1}$$

Eq. 1 represents the energy balance in a building. Here, C is the thermal capacity of the indoor space, indicating how much energy is needed to change the temperature. $C\frac{dT_{in,air}}{dt}(t)$ is the rate of change of the internal air temperature over time. The terms on the right side of the equation represent various heat gains and losses. $Q_{int}(t)$is the internal heat gain from occupants, appliances, and lighting system. $Q_{sol}(t)$ is the heat gain from solar radiation through windows; $Q_{inf}(t)$ accounts for heat loss or gain due to air infiltration; Q_{vent} represents heat exchange due to ventilation. $Q_{trans}(t)$ is the heat transfer through the building envelope (walls, floors, ceilings, windows, and doors). Last term Q_{HVAC} is the heat that has to be provided or removed by the HVAC system to balance the heat losses and maintain the internal temperature in a comfort range. The equation captures the dynamic interplay of these factors to determine how the internal temperature changes over time. The equation is simplified into:

$$C\frac{dT_{in,air}(t)}{dt} = \dot{Q}_{gains}(t) - UA_{ss}(T_{in,air} - T_{ext}) + \dot{Q}_{HVAC}(t) \tag{2}$$

UA_{ss} represents the steady-state transmittance of the building envelope. As a container house presents a very low thermal inertia, the assumption is reasonable. Q_{HVAC} is assessed by the adopted control strategy. It can be parameterised as an action between 0 and 1 and the maximum heating power of the HVAC system.

3. RESULTS

In the reference case, the control strategy is a PID. In absence of the calibration constant to tune the controller, a trial and error approach is adopted to identify the proportional, integral and derivative approach. Once the set-point of the temperature is fixed, called the difference between the indoor temperature and the set-point as e, the action can be calculated as follows.

$$e(t+\Delta t) = K_p e(t) + K_I \sum_{i=1}^{n} e_i(t) + K_D[e(t) - e(t-\Delta t)] \tag{3}$$

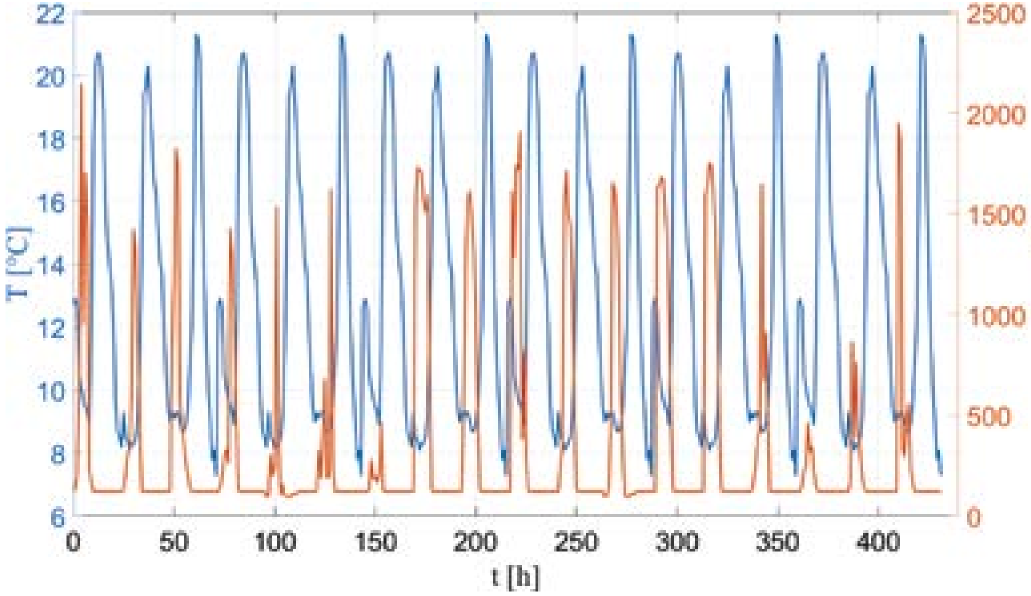

FIGURE 2. Weather data and gain for comparison and testing

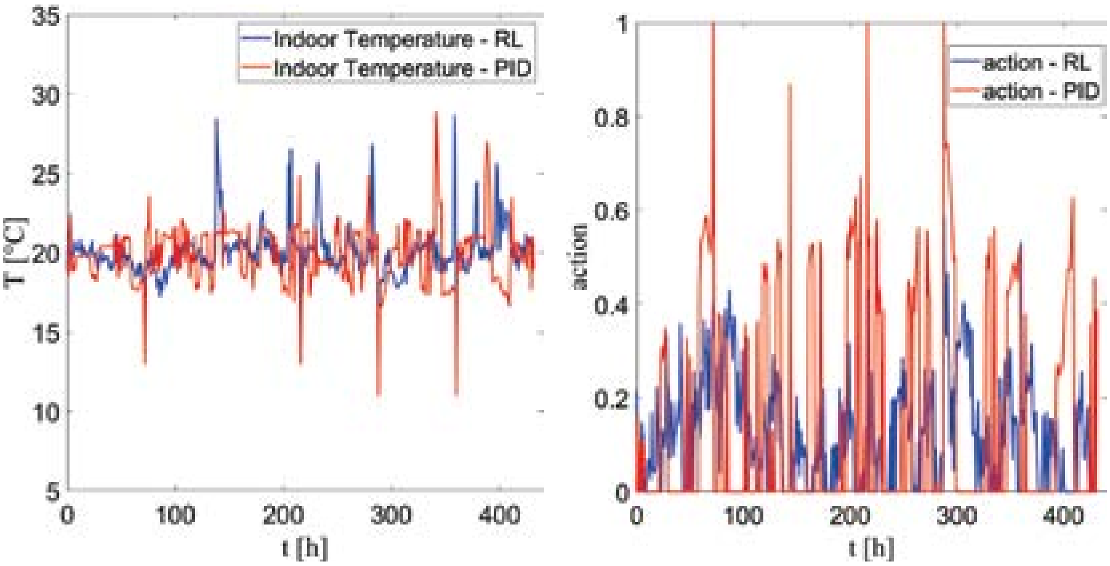

(a) (b)

FIGURE 3. Comparison RL vs PID. Indoor temperature (a), Action (or load factor)(b).

The Proximal Policy Optimization (PPO) is instead used as RL- based control strategy. PPO is an advanced reinforcement learning algorithm used for training agents in complex environments. It operates by iteratively updating the policy, balancing exploration and exploitation to maximize rewards. PPO uses a clipped surrogate objective to limit the extent of each policy update, ensuring stable and reliable learning. The algorithm collects multiple timesteps of data through interactions with the environment, then uses this data to optimize the policy, improving decision-making over time. The state is composed by the external temperature and the difference between the indoor temperature and the set point. The designed reward R, aims to minimise this difference and, at the same time, the energy consumption. The calibration constants c_1, c_2 as well as the chosen analytical functions express the relative importance between the thermal well-being and the energy consumption.

$$R(t) = e^{(-c_1|T_{in,air}(t)-T_{set}|)} - c_2 Q_{HVAC}(t) \tag{4}$$

The results are shown in Figure 3, while weather data (Naples) used for testing and heat gains are referred to the first 18 days of January (Figure 2). The RL-based control strategy allows to save approximately 18% of heating, electricity and primary energy compared to the PID-based scenario. This happens even though the distance between the indoor temperature and set-point is less in the proposed control strategy compared to the reference case.

4. CONCLUSIONS

The study demonstrates the potential of AI-based control strategies, particularly Reinforcement Learning (RL), in optimizing the energy consumption of HVAC systems in container houses. Compared to traditional PID control, the RL-based approach resulted in significant energy savings of approximately 18%, highlighting its efficiency in managing heating requirements. The use of a Digital Twin for real-time simulation and control further underscores the benefits of advanced AI techniques in enhancing energy efficiency and maintaining thermal comfort.

REFERENCES

[1] Simona Di Fraia, Armando Di Meglio, Nicola Massarotti, Laura Vanoli, Riccardo Bentivoglio, and Valerio Volpecina. Energy recovery and waste valorization in a frozen food processing facility: a case study from lazio, italy. *Energy Efficiency*, 17(3):13, 2024.

[2] Fawad Ahmed, Mariam Mahmood, Adeel Waqas, Naveed Ahmad, and Majid Ali. Thermal analysis of macro-encapsulated phase change material coupled with domestic gas heater for building heating. *Sustainable Energy Technologies and Assessments*, 47:101533, 2021. doi: https://doi.org/10.1016/j.seta.2021.101533.

[3] Luis Gabriel Gesteira, Javier Uche, Francesco Liberato Cappiello, and Luca Cimmino. Thermoeconomic optimization of a polygeneration system based on a solar-assisted desiccant cooling. *Sustainability (Switzerland)*, 15(2), 2023. doi: 10.3390/su15021516.

[4] Armando Di Meglio, Nicola Massarotti, and Perumal Nithiarasu. A physics-driven and machine learning-based digital twinning approach to transient thermal systems. *International Journal of Numerical Methods for Heat & Fluid Flow*, 2024.

[5] Rafal Damian Figaj, Davide Maria Laudiero, and Alessandro Mauro. Climate characterization and energy efficiency in container housing: Analysis and implications for container house design in european locations. *Energies*, 17(12):2926, 2024.

Sixth International Conference on Computational Methods for Energy and Thermal Problems
THERMAECOMP2024, Sept. 9-11, 2024, Budva, Montenegro
N. Massarotti, P. Nithiarasu and I. Vušanović (Eds.)

Digital twinning using novel nonlinear finite-element approach for sparse-data solution reconstruction

Wiera Bielajewa[a], Michelle Tindall[b], Perumal Nithiarasu[a*]
[a]Zienkiewicz Institute for Modelling, Data and AI, Swansea University, Bay Campus, Swansea, SA1 8EN, United Kingdom (UK)
[b]Culham Science Centre, United Kingdom Atomic Energy Authority (UKAEA), Abingdon, OX14 3DB, United Kingdom (UK)

[*]Corresponding author
Email addresses: wiera.bielajewa@swansea.ac.uk (Wiera Bielajewa), michelle.tindall@ukaea.uk (Michelle Tindall), p.nithiarasu@swansea.ac.uk (Perumal Nithiarasu)

ABSTRACT

Real-time solution reconstruction from sparse data is essential for integrating measurements from a physical experiment directly into a simulation in order to achieve digital twinning necessary for effective monitoring and control of the experiment. This paper introduces a novel inverse analysis framework based primarily on the finite element (FE) discretisation to the problems with nonlinear material properties. Furthermore, Automatic Differentiation (AD), which was utilised to calculate Jacobian matrices for gradient-based optimisation algorithms in previous works, is substituted with the variation of standard analytical procedure used in FEM solvers. This is found to be more efficient for the problems considered in the present work; to such a great degree that the near real-time operation is achieved on the local Central Processing Unit (CPU) as opposed to the supercomputer Graphical Processing Unit (GPU) that was formerly required for such rapid operation even for linear problems. The modified framework is showcased by analysing two heat conduction cases: an air-cooled stainless steel plate and a more complex water-cooled stainless steel sample the geometry of which is based on the sample tested in the fusion energy experimental facility.

Key Words: *Solution reconstruction, inverse analysis, multiple choices, sparse data, digital twinning, finite element method, nonlinear materials.*

1. INTRODUCTION

Digital twinning is a process of developing a model of a physical system, which is dynamically updated with real-time data to mimic the current behaviour of its real-world counterpart. Its principal objective is to augment sparse experimental measurements and thus potentially ensure full monitoring and control of various physical experiments. In order to achieve this objective, an effective method for reconstructing the full solution from sparse sensor measurements is needed.

More conventional inverse analysis methods focus mainly on the equation parameter estimation and tend to lack sufficient flexibility, whereas numerous approaches based on Machine Learning (ML) either require vast amounts of training data and are generally prone to developing solution bias, or need continuous training for every set of new measurements which prevent them from functioning even close to real time [1].

The present work extends the novel finite-element (FE)-based inverse analysis framework [1] to nonlinear material properties as well as trials it on a more complex geometry.

2. METHODOLOGY

After discretising the general nonlinear 3D transient heat conduction equation without a heat source and with isotropic nonlinear material properties in space and time using the standard Galerkin weighted residual method and fully implicit time discretisation scheme, the following system of equations is obtained [2]:

$$[\boldsymbol{C}] \left\{ \frac{\{\boldsymbol{T}\}^{n+1} - \{\boldsymbol{T}\}^{n}}{\Delta t} \right\} + [\boldsymbol{K}] \{\boldsymbol{T}\}^{n+1} = \{\boldsymbol{f}\}^{n+1} \tag{1}$$

where $[\boldsymbol{C}]$ and $[\boldsymbol{K}]$ are global temperature-dependent mass and stiffness matrices, respectively, while $\{\boldsymbol{f}\}$ and $\{\boldsymbol{T}\}$ are loading and temperature vectors; Δt is a time step size, and superscript n represents the n^{th} time step. Additionally, it is assumed that only Neumann boundary conditions (BCs) are applied in the form of the applied heat flux q on Γ_q and convection with convection heat transfer coefficient h on Γ_h. Therefore, the loading term $\{\boldsymbol{f}\}$ can be separated into two following parts:

$$\{\boldsymbol{f}\}^{n+1} = \{\boldsymbol{f}\}^{n+1}_q + \{\boldsymbol{f}\}^{n+1}_h \implies \{\boldsymbol{f}\}^{n+1}_q = [\boldsymbol{C}]\left\{\frac{\{\boldsymbol{T}\}^{n+1} - \{\boldsymbol{T}\}^{n}}{\Delta t}\right\} + [\boldsymbol{K}]\{\boldsymbol{T}\}^{n+1} - \{\boldsymbol{f}\}^{n+1}_h \tag{2}$$

For inverse analysis it is assumed that the material properties, ambient temperature, as well as temperature values $\{\boldsymbol{T}\}_M$ at points belonging to the measurement set M are known. The applied heat flux q is assumed to be unknown. A scalar loss function L of $\{\boldsymbol{T}\}^{n+1}$ is defined as a sum of three following terms:

(a) Residual term enforcing that $\{\boldsymbol{f}\}_q$ should be zero on the nodes inside the domain and on $\Gamma_h \setminus \Gamma_q$
$c_1 \sum_{i\in\Omega\backslash\Gamma_q} \left(\{\boldsymbol{f}\}^{n+1}_{qi}\right)^2$

(b) Measurement term $c_2 \sum_{i\in M} \left(\{\boldsymbol{T}\}_i - \{\boldsymbol{T}\}_{Mi}\right)^2$

(c) Regularisation (smoothing) term

$$\begin{aligned} c_3 \Bigg[&\sum_{i\in\Gamma_q\backslash\Gamma_{edge}} \left(\{\boldsymbol{f}\}^{n+1}_{qi} - \frac{\sum_{i\in\Gamma_q\backslash\Gamma_{edge}} \{\boldsymbol{f}\}^{n+1}_{qi}}{|\Gamma_q\backslash\Gamma_{edge}|}\right)^2 + \\ &+ \sum_{i\in\Gamma_{edge}\backslash\Gamma_{corners}} \left(\{\boldsymbol{f}\}^{n+1}_{qi} - \frac{\sum_{i\in\Gamma_{edge}\backslash\Gamma_{corners}} \{\boldsymbol{f}\}^{n+1}_{qi}}{|\Gamma_{edge}\backslash\Gamma_{corners}|}\right)^2 + \\ &+ \sum_{i\in\Gamma_{corners}} \left(\{\boldsymbol{f}\}^{n+1}_{qi} - \frac{\sum_{i\in\Gamma_{corners}} \{\boldsymbol{f}\}^{n+1}_{qi}}{|\Gamma_{corners}|}\right)^2 \Bigg] \end{aligned}$$

where $\{\boldsymbol{f}\}^{n+1}_{qi}$ is the i^{th} element in the global $\{\boldsymbol{f}\}^{n+1}_q$ vector calculated using Eq. 2. Γ_{edge} is the 3D edge of the surface where q is applied, and sharp features on Γ_{edge} discretised using one element are represented by $\Gamma_{corners}$. More details are provided by Bielajewa et al. [1]

The loss function L is minimised using gradient-based Gauss–Newton method [1]. L is a sum of squared function values, i.e. $L(\{\boldsymbol{T}\}) = \sum l_i(\{\boldsymbol{T}\})^2$, and it is necessary to calculate their Jacobian matrix $[\boldsymbol{J}]_{ij} = \partial l_i / \partial \{\boldsymbol{T}\}_j$ at every Gauss–Newton iteration. In the previous works Automatic Differentiation (AD) was used for this purpose, which necessitated the use of Graphical Processing Unit (GPU) [1]. However, for the FE equations $[\boldsymbol{J}]$ can easily be calculated analytically. Indeed, the procedure consists of the following steps:

1. Jacobian (tangent) matrix of $\{\boldsymbol{f}\}_q$, $[\boldsymbol{J}]_f$, can be analytically calculated for a given temperature vector $\{\boldsymbol{T}\}$ using Eq. 2, which is a standard FEM routine. The tangent matrices are computed for each element and subsequently assembled into the global tangent matrix.
2. Jacobian matrix of the residual term is $[\boldsymbol{J}]_{rest} = \left\{[\boldsymbol{J}]_{fi} : i \in \Omega \setminus \Gamma_q\right\}$
3. Jacobian matrix of the measurement term is $[\boldsymbol{J}]_{mt} = \{[\boldsymbol{I}_n]_i : i \in M\}$
4. Jacobian matrix of the regularisation term is $[\boldsymbol{J}]_{regt} =$

$$\begin{aligned} &= \left\{[\boldsymbol{J}]_{fi} : i \in \Gamma_q \setminus \Gamma_{edge}\right\} - \frac{1}{|\Gamma_q\backslash\Gamma_{edge}|}\left[\sum_{i\in\Gamma_q\backslash\Gamma_{edge}} [\boldsymbol{J}]_{fi1}, \sum_{i\in\Gamma_q\backslash\Gamma_{edge}} [\boldsymbol{J}]_{fi2}, \cdots, \sum_{i\in\Gamma_q\backslash\Gamma_{edge}} [\boldsymbol{J}]_{fin}\right] + \\ &\left\{[\boldsymbol{J}]_{fi} : i \in \Gamma_{edge} \setminus \Gamma_{corners}\right\} - \frac{1}{|\Gamma_{edge}\backslash\Gamma_{corners}|}\left[\sum_{i\in\Gamma_{edge}\backslash\Gamma_{corners}} [\boldsymbol{J}]_{fi1}, \cdots, \sum_{i\in\Gamma_{edge}\backslash\Gamma_{corners}} [\boldsymbol{J}]_{fin}\right] + \\ &\left\{[\boldsymbol{J}]_{fi} : i \in \Gamma_{corners}\right\} - \frac{1}{|\Gamma_{corners}|}\left[\sum_{i\in\Gamma_{corners}} [\boldsymbol{J}]_{fi1}, \sum_{i\in\Gamma_{corners}} [\boldsymbol{J}]_{fi2}, \cdots, \sum_{i\in\Gamma_{corners}} [\boldsymbol{J}]_{fin}\right] \end{aligned}$$

5. $[\boldsymbol{J}]$ is obtained by vertically concatenating weight-adjusted $\sqrt{c_1}\,[\boldsymbol{J}]_{rest}$, $\sqrt{c_2}\,[\boldsymbol{J}]_{mt}$, and $\sqrt{c_3}\,[\boldsymbol{J}]_{regt}$.

Subscripts i and j denote the i^{th} row and j^{th} column of the matrix, respectively; $[\boldsymbol{I}]$ is the identity matrix of size equal to the number of nodes in a mesh (subscript n).

3. RESULTS

Two heat conduction examples are considered in this paper: the first one is an air-cooled stainless steel plate that was analysed with an assumption of temperature-independent material properties in the previous work [1], and the second one is a water-cooled stainless steel HIVE sample, the geometry of which is based on the copper-tungsten AMAZE sample, that was tested in the fusion energy experimental facility [3]. Figure 1 shows the temperature-dependent material properties, piece-wise linearly interpolated from discrete data; water convection heat transfer coefficient h_{water} is calculated using a 1D coolant model, which is based on the coolant pressure, temperature, and velocity [4]. For h_{air} the atmospheric temperature T_{air} is equal to

20 °C, whereas for h_{water} the atmospheric temperature T_{water} is equal to 30 °C. Uniform surface heating, linearly increasing with time, is applied to both examples:

$$q(t) = \left(\frac{600000}{180}\right) t \tag{3}$$

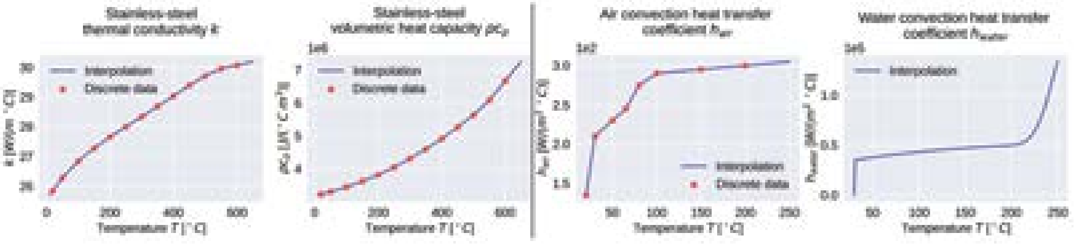

FIGURE 1. Nonlinear material properties; discrete data is not shown for h_{water} as the points are densely aggregated on the chart.

Figure 2 shows graphics of both the problems with the measurement points (locations), plate with 9 and HIVE sample with 10; Table 1 describes the applied BCs. It is assumed that the initial conditions represent a steady state, temperature of 20°C for the plate and temperature of 30°C for the HIVE sample. The simulation is run for 180s. The solutions inversely reconstructed from measurements are compared with the reference solutions produced by applying the BCs presented in Table 1 and using Newton-Raphson method. Linear hexahedral meshes with no refinement are used; second-order Gaussian quadratures are used for the element integration. The time step size used for the reference solution Δt_{ref} is 0.1s, time step size used for the solution reconstruction Δt_{rec} is equal to 2.0s. In the Gauss–Newton method used for the solution reconstruction, the initial guess for the temperature distribution at every time step is a uniform temperature equal to the average measurement value for that time step. The constants c_1, c_2, and c_3 are equal to 1.0.

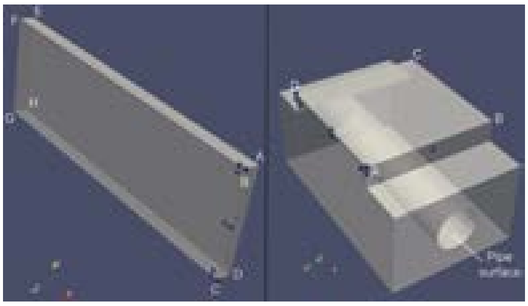

FIGURE 2. Labels for the applied BCs (Table 1) and measurement placement shown as blue spheres: plate (left) with 9 and HIVE sample (right) with 10.

TABLE 1. Applied BCs; Figure 2 shows the labels.

Plate		HIVE sample	
Surface(s)	**BC**	**Surface**	**BC**
ABCD	Uniform heat flux $q(t)$ (Eq. 3)	ABCD	Uniform heat flux $q(t)$ (Eq. 3)
BFGC, BFEA, AEHD, DHGC, EFGH	Plate-air convection h_{air}, T_{air}	Pipe surface	Sample-water convection h_{water}, T_{water}
Set	**Location**	**Set**	**Location**
Γ_q Γ_{edge} $\Gamma_{corners}$	Surface ABCD Edge ABCD Nodes A, B, C, D	Γ_q Γ_{edge} $\Gamma_{corners}$	Surface ABCD Edge ABCD Nodes A, B, C, D

An excellent similarity between the reconstructed and reference solutions is achieved for both the plate and the HIVE sample whilst maintaining the near real-time operation speed on the local Central Processing Unit (CPU), i.e. all time step runtimes are less than the time step size Δt_{rec} (Table 2, Figures 3 and 4).

4. CONCLUSIONS

In conclusion, this paper further advances the inverse analysis framework based on the conventional FE discretisations [1] in the following respects:

1. It is modified to encompass the nonlinear material properties.
2. Analytical computation of Jacobian matrices of a loss function is employed instead of AD.
3. The procedure is tested on the geometry more complex than a plate.

The solution reconstruction occurs in near real time with consistent 1.3-1.5s delay on the local CPU for the two nonlinear heat conduction cases. Further investigation may be necessary to understand when it might be beneficial to use AD in the context of this framework.

TABLE 2. Average and maximum relative solution reconstruction errors and average and maximum time step runtimes.

Case	Average relative error [%]	Maximum relative error [%]	Average time step runtime [s]	Maximum time step runtime [s]	Problem type
Plate CPU [b]	0.11	1.42	1.3	1.5 [a]	Nonlinear
Sample CPU [b]	0.15	1.22	1.3	1.5 [a]	Nonlinear
Plate GPU [1] [c]	0.15	1.33	1.2	1.3 [a]	Linear

[a] Near real-time operation, i.e. all time step runtimes are less than $\Delta t_{\text{rec}} = 2.0s$.
[b] Local CPU AMD Ryzen 7 5800X 8-Core.
[c] Supercomputer GPU NVIDIA A100 with AD for Jacobian matrices.

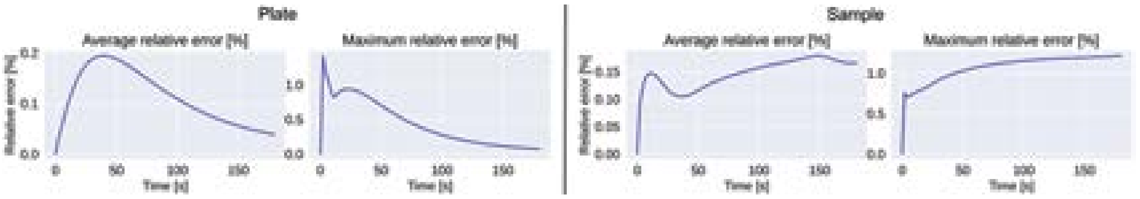

FIGURE 3. The dependence of relative errors on time for plate (left) and HIVE sample (right).

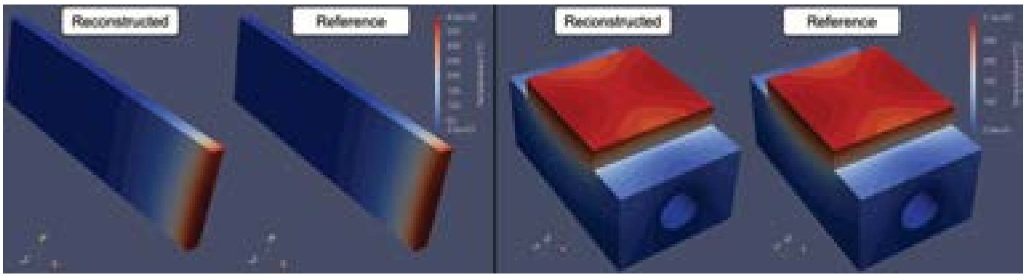

FIGURE 4. Reconstructed and reference temperature distributions for the last time instance (180s) for plate (left) and HIVE sample (right).

REFERENCES

[1] Wiera Bielajewa, Michelle Tindall, and Perumal Nithiarasu. A novel, finite-element-based framework for sparse data solution reconstruction and multiple choices. Under review, 2024.

[2] Perumal Nithiarasu, Roland W. Lewis, and Kankanhalli N. Seetharamu. *Fundamentals of the Finite Element Method for Heat and Mass Transfer*. Wiley, 2 edition, 2016. ISBN 9780470756256.

[3] David Hancock. *Employing Additive Manufacturing for Fusion High Heat Flux Structures*. Phd thesis, University of Sheffield, 2018.

[4] Theron D. Marshall, Dennis L. Youchison, and Lee C. Cadwallader. Modeling the nukiyama curve for water-cooled fusion divertor channels. *Fusion Technol.*, 35:8–16, 2001. URL `http://film2000.free.fr/TOFE.pdf`.

Sixth International Conference on Computational Methods for Energy and Thermal Problems
THERMAECOMP2024, Sept. 9-11, 2024, Budva, Montenegro
N. Massarotti, P. Nithiarasu and I. Vušanović (Eds.)

GEOGRID VIEWER FOR SUSTAINABLE EXPLOITATION OF GEOTHERMAL DIGITAL TWINS

Marina Iorio, Gianpaolo Donnarumma, Antonio Mercadante
Institute of Marine Science, National Council of Research, Calata Porta di Massa, 80133,
(Napoli) Italy, marina.iorio@cnr.it, gpdonnarumma@gmail.com, antonio.mercadante@cnr.it

Nicola Massarotti, Fawad Ahmed
Department of Engineering, University of Naples 'Parthenope', Centro Direzionale, Isola C3,
80143, (Napoli) Italy, Nicola.massarotti@uniparthenope.it,
fawad.ahmed001@studenti.uniparthenope.it

ABSTRACT

Geothermal energy can play an important part in energy transition. However, the uncertainty of the underground energy contents is the main barrier. To secure investments in this renewable energy source, this paper proposes a combination of different tools for obtaining a digital twin model for predicting energy use from subsurface resources. Integration of GeoGrid Viewer with a commercial numerical simulation tool is discussed in the paper to generate data sets for training a digital twin model. The data provided by GeoGrid is fed to the numerical tool for simulation to obtain the energy parameters for the training of a digital twin model of a reservoir located in the Campania Region (Southern Italy).

Key Words: *Digital Twin, Data integration, physics-based modeling, AI, Heat Transfer control.*

1. INTRODUCTION

Today, nearly all integrated 3D exploration software commercially available is based on an ArcGIS-style visualization and query model, where different data are overlaid as layers within the model. These software solutions have a specific market and purpose: processing subsurface information and dynamics rapidly during exploration and resource exploitation to make real-time decisions [1; 2; 3]. This work, the authors present a case study of heat storage in overlapping groundwaters (Cold and hot) and salt wedge, throughout the Geogrid Viewer, an innovative Digital Twin Type cloud software, developed as part of the RD project GEOGRID, funded by the CAMPANIA ERDF 2014/2020 program, for interactive 3D visualization of geothermal reservoirs.

2. THE GEOGRID VIEWER

All collected and geo-localized data have been visualized in the Web Application, Geogrid Viewer, especially developed, through different programming languages (e.g. PHP, HTML 5, CSS), during the GeoGrid project, to allow the integration of all multi-parameter analyzed and interpreted data in an interactive three-dimensional graphical format. The software, customizable with a wide range of tools and functionalities, also displays dynamic simulations of the reservoir during the extraction of "green" energy for more efficient and sustainable use of the resource over time [4]. The software is a tool designed to improve the assessment and sustainable use of geothermal resources, but due to its versatility, it can also be used for other underground investigation purposes by displaying simulations of dynamic 3D components of physical processes (water flows, heat variations, salinity, etc.). Cloud technology allows multiple users to use the software simultaneously and on different operating systems without the need for installation, ensuring compatibility, availability, and updates. The Geogrid Viewer, with its user-friendly interface adaptable to different displays, is innovative because: 1) it can quickly load preprocessed three-dimensional geolocated data and present interactive 3D models exportable in standard or vector formats; 2) it offers the possibility of visualizing multiparametric data of a specific complex query through unique color scales, to obtain an integrated and coherent view of the interpretation of various data sets.

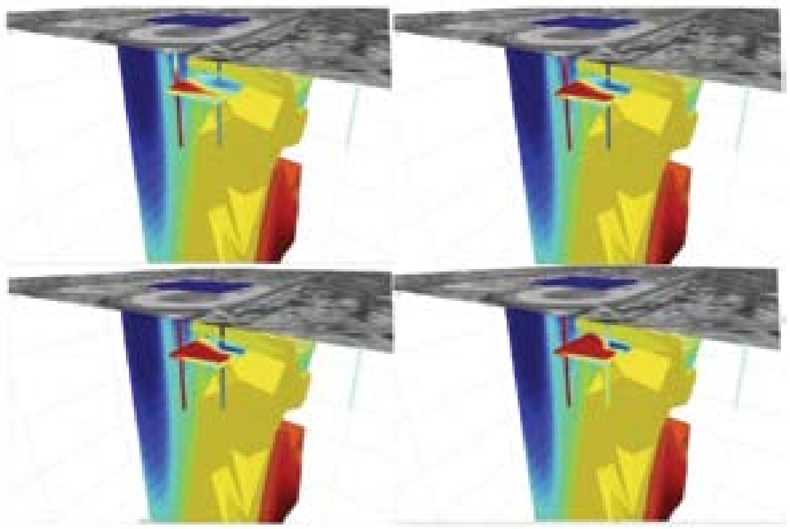

FIGURE 1. Different layers representation with GeoGrid Viewer tool

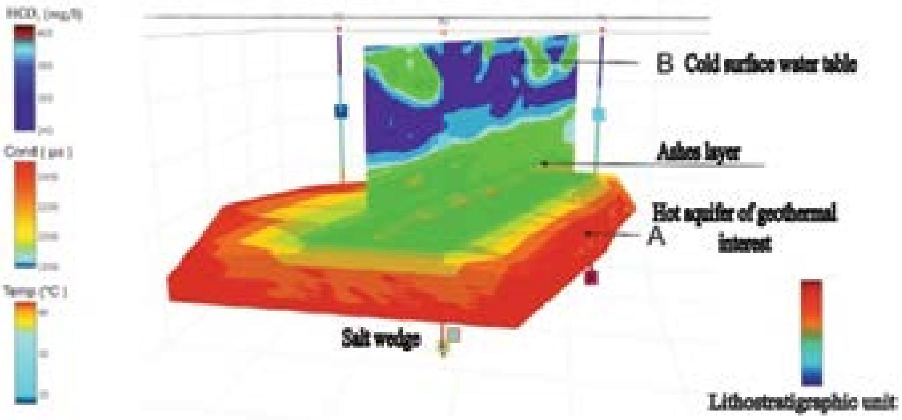

FIGURE 2. Overlapping of cold and hot aquifers located near Pozzuoli, Southern Italy

3. RESULTS

This work uses the example of the source available in Pozzuoli (Arco Felice) Phlegrean fields Campania Region in Italy and presented in Figure 2. Two overlapping aquifers and a salt wedge are integrated into the Geogrid Viewer Digital Twin for analysis of energy storage. Specifically, the multi-fold system studied is characterized by the presence of an impermeable layer consisting of fine volcanic ashes (represented in green in the tomographic section of Figure 2) identified on average between 17 and 29 m below ground level.

The study of the underground aquifer in the area under integration, aimed to recognize the geomorphological and hydrodynamic characteristics of the aquifer, as well as to calculate the groundwater transit times near well P2. The first cold aquifer consisting of sand and fill material of various origins (represented in blue in Figure 2). Below the first aquifer a fine volcanic ashes layer of 15 m constitute the impermeable layer at which base, piezometers P1, P2, and P3, intercepted a deep warm aquifer (temperatures up to 43° represented in red orange in Figure 2) with a confined nature and modest load consisting of silty sands, gravelly sands, and gravel. At the base of the deep-water body, the salt wedge, identified at about 44-45 m from the P.C. has been detected. Variable falling head permeability tests, of Lefranc type, were conducted during the installation of piezometers P1, P2, and P3 to obtain a precise characterization of the hydraulic conductivity of the different

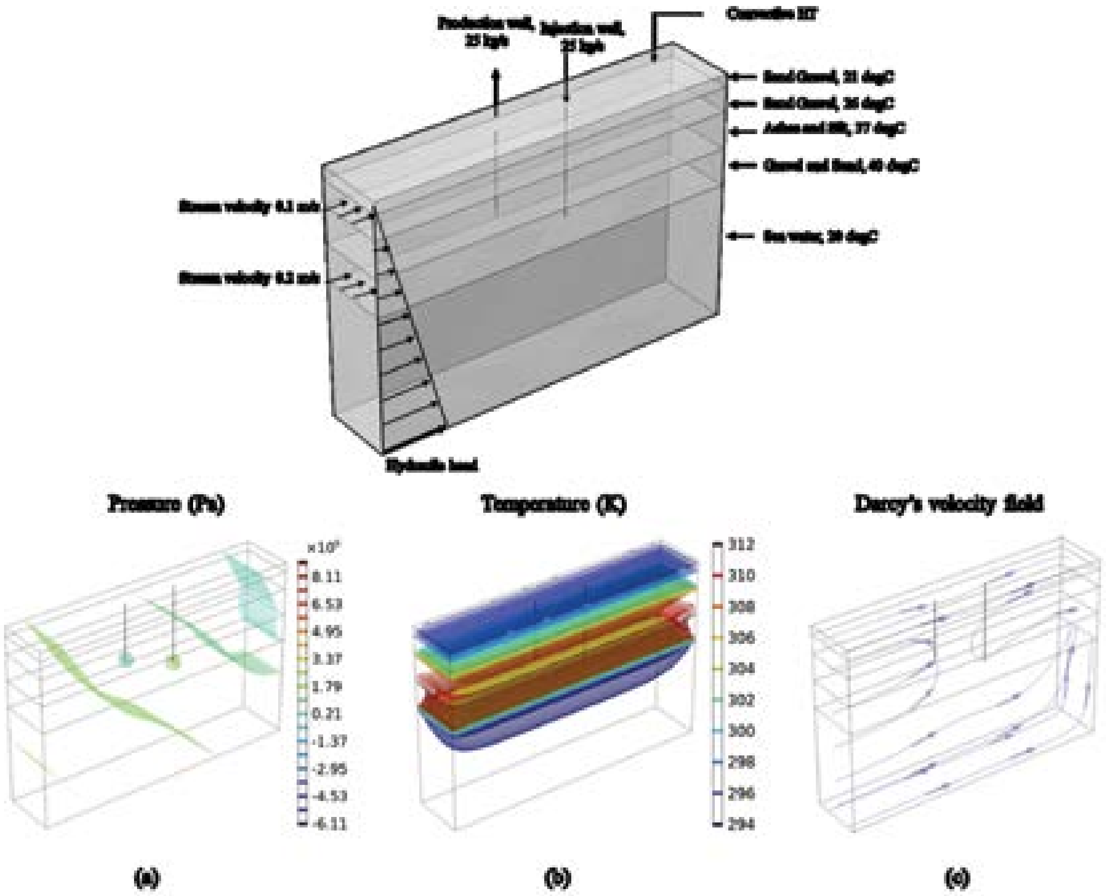

FIGURE 3. 3D Model with Boundary conditions and iso-surfaces of pressure, temperature, and Darcy's velocity field

encountered layers.

The results obtained together with a mathematical model used to post-process the data, allowed us to identify an average permeability for the warm underground aquifer and an average piezometric gradient at well P2 of 5.60

Based on the data obtained from GeoGrid Viewer, a 3D finite element numerical model for a production and injection well is simulated with given conditions to observe the behavior of Darcy's streamlines, pressure and temperatures in the domain. The details of the domain with model setting are shown in Figure 3. Figure 3 (a, b, c) presents the pressure, temperature, and Darcy's velocity field iso-surfaces obtained in the domain when production and injection wells are operating. Figure (3a) shows that the pressure at the production well is lower than the pressure at the injection well. This effect could be explain by the fact that the fluid from the hot stream is taken out for heat exchange creating a low-pressure region near the production well. On the other hand, high pressure region is formed near the injection well as the fluid is re-injected. Figure (3b) illustrates different temperature iso-surfaces due to the temperature variation of the domain according to the geological data for different underground layers while Figure (3c) shows Darcy's velocity field. The operation of production and injection wells operation can also be confirmed by Darcy's velocity field.

4. CONCLUSIONS

The application of digital twins is gaining relevance in energy systems [5]. The data obtained from the GeoGrid Viewer can be utilized for obtaining different input parameters for numerical models to simulate any proposed configuration for geothermal energy exploitation for various applications. The combination of these tools can generate data sets for training digital models for energy estimation in the future. Subsequent developments of the system may include:

• The ability to collaborate in real-time on a single 3D model

• The integration of Artificial Intelligence to automate data importation and selection from Data Lake, to create basic 3D models, and to extract complex information and hidden relationships from data.

• Parameterized temporal granularity for the visualization of reservoir simulations and exportation in video format.

Finally, digital twin can be used for sustainability analysis of low- and medium-enthalpy resource exploitation, such as for district heating and building cooling and for assessing the economic feasibility of geothermal exploitation and the development of future project facilities.

REFERENCES

[1] Marina Iorio, Michele Punzo, Alberto Carotenuto, Giuseppe Cavuoto, Alfonso Corniello, Vincenzo Di Fiore, Giampaolo Donnarumma, Maurizio Fedi, Nicola Massarotti, Nicola Pelosi, Daniela Tarallo, and Maurizio Milano. Shallow geothermal field multidisciplinary exploration: New data from campi flegrei caldera (cfc) for low—middle enthalpy resource exploitation. *Geothermics*, 121:103049, 2024. ISSN 0375-6505. doi: https://doi.org/10.1016/j.geothermics.2024.103049. URL `https://www.sciencedirect.com/science/article/pii/S037565052400138X`.

[2] F Ahmed, N Massarotti, and B Šarler. Sustainable heating and cooling for residential buildings: coaxial ground heat exchangers. *Journal of Physics: Conference Series*, 2766(1):012051, may 2024. doi: 10.1088/1742-6596/2766/1/012051. URL `https://dx.doi.org/10.1088/1742-6596/2766/1/012051`.

[3] Armando Di Meglio, Nicola Massarotti, Alessandro Mauro, and Vincenzo Trombetta. Coupled geothermal energy simulations. *Journal of Physics: Conference Series*, 2177(1):012004, apr 2022. doi: 10.1088/1742-6596/2177/1/012004. URL `https://dx.doi.org/10.1088/1742-6596/2177/1/012004`.

[4] Marina Iorio, Alberto Carotenuto, Alfonso Corniello, Simona Di Fraia, Nicola Massarotti, Alessandro Mauro, Renato Somma, and Laura Vanoli. Low enthalpy geothermal systems in structural controlled areas: A sustainability analysis of geothermal resource for heating plant (the mondragone case in southern appennines, italy). *Energies*, 13(5), 2020. ISSN 1996-1073. doi: 10.3390/en13051237. URL `https://www.mdpi.com/1996-1073/13/5/1237`.

[5] Armando Di Meglio, Nicola Massarotti, and Perumal Nithiarasu. A physics-driven and machine learning-based digital twinning approach to transient thermal systems. *International Journal of Numerical Methods for Heat Fluid Flow*, 34(6): 2229–2256, jan 2024. ISSN 0961-5539. doi: 10.1108/HFF-10-2023-0616. URL `https://doi.org/10.1108/HFF-10-2023-0616`.

Sixth International Conference on Computational Methods for Energy and Thermal Problems
THERMAECOMP2024, Sept. 9-11, 2024, Budva, Montenegro
N. Massarotti, P. Nithiarasu and I. Vušanović (Eds.)

Solution reconstruction of HIVE sample using physics-informed neural networks

Prakhar Sharma, Perumal Nithiarasu
Zienkiewicz Institute for Modelling, Data and AI, Swansea University, Bay Campus, Swansea, SA1 8EN, UK
1915438@swansea.ac.uk, p.nithiarasu@swansea.ac.uk

Michelle Tindall
Fusion Technology Facilities, United Kingdom Atomic Energy Authority, Unit 2a Lanchester Way, Rotherham, S60 5FX, UK
michelle.tindall@ukaea.uk

ABSTRACT

In this study, we apply a recently developed Physics-informed neural network (PINN)-based workflow to reconstruct field variables from sparse measurements, reducing the need for extensive pre-training and explicit BC knowledge. This workflow leverages prior experimental knowledge, and the knowledge of partial differential equations (PDEs), thus minimising large dataset requirements.

Applied to the Heat by Induction to Verify Extremes (HIVE) facility at UK Atomic Energy Authority (UKAEA), we achieved a 3.45% relative L2 error with 50 sparse measurements. When the current changes linearly from 50A to 300A, the independent steady-states approach resulted in variable errors with an average reconstruction time of 50 minutes. In contrast, the transfer learning approach consistently reduced the error and the reconstruction time to 25 minutes. This enhances feasibility in data-scarce environments and simplifies solving inverse problems.

Key Words: *Heat Transfer, Physics-informed neural networks, solution reconstruction.*

1. INTRODUCTION

Inverse problems, often ill-posed with limited data, become complex with non-linearities in partial differential equations (PDEs) and noisy data. Traditional brute-force search methods are inefficient. Physics-informed neural networks (PINNs) offer a solution but typically require many sensors or explicit boundary conditions (BCs), limiting their practicality in inverse problems.

PINNs [1] have recently become popular due to their innovative approach in solving both forward and inverse problems involving PDEs using neural networks (NNs). Unlike traditional numerical methods for PDEs, PINNs blend data-driven and physics-based techniques. This hybrid approach ensures that the initial condition (IC), BCs, and the governing PDE are inherently satisfied, allowing effective resolution of forward problems. For inverse problems, where some elements may be unknown or ambiguous, PINNs are capable of learning the missing information from sparse data.

Fusion experiments are inherently challenging and expensive, making the generation of thousands of experimental data for conventional machine learning based solution reconstruction is impractical. Additionally, the boundary conditions (BCs) in such experiments are often vague, preventing straightforward forward simulations using conventional numerical techniques to generate synthetic data.

Heat by Induction to Verify Extremes (HIVE) is an experimental facility at the UK Atomic Energy Authority (UKAEA) to expose plasma-facing components to the high thermal loads that they will experience in a fusion reactor. Samples are thermally loaded by induction heating whilst being actively cooled with pressurised water.

In this work, we focus on solution reconstruction using sparse measurements from the HIVE experiments. Our recently developed approach, which is currently under review, does not rely on additional experimental data, demonstrating the feasibility of reconstructing accurate solutions with minimal measurements.

2. MAIN BODY

2.1 The HIVE sample

Figure 1 illustrates two samples as described in Lewis's PhD thesis [2]. The left image displays a generic sample, highlighting its various components. The tile represents the plasma-facing side, while the pipe is designed for coolant flow to cool the component. The right image shows the AMAZE sample, made of Copper, featuring the coil arrangement used to replicate the thermal loads generated by the plasma.

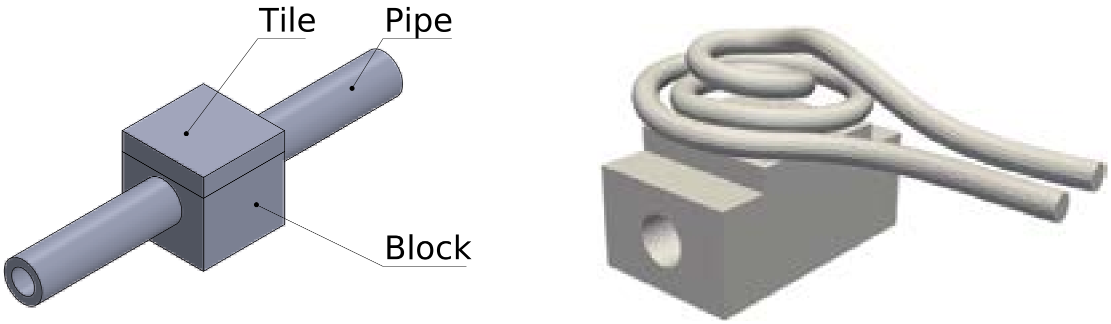

FIGURE 1. A generic sample (left) and the AMAZE sample with the coil setup (right).

To generate the reference solution, the coil emits a volumetric heat load based on the input current and its location relative to the AMAZE sample. The electromagnetic analysis of the coil was carried out using the open-source FEM solver ERMES. The coolant flowing through the pipe was simplified as a 1D problem, defined using a boiling curve that measures the heat flux (q) between the coolant and the pipe as a function of the pipe temperature (T_{wall}).

In summary, the coil serves as a heat source term (W/m^3), and the coolant acts as a heat flux term (W/m^2) for the AMAZE sample. Consequently, the temperature distribution in the tile and the block is reduced to a heat transfer problem. We are interested in the steady-state behaviour of the components tested in HIVE, as these are the conditions they will be subjected to for long periods in a fusion device. Since there is no Dirichlet boundary condition, we used the initial temperature of the coolant (30 °C) as the initial temperature in the finite element solver to obtain a solution.

2.2 The PINN-based workflow

To reconstruct the solution, we implemented a PINN-based workflow. While the detailed methodology is currently under review and cannot be discussed in full, we can provide an overview of the key steps involved in the process.

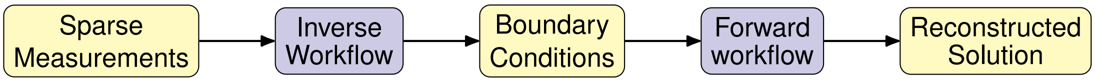

FIGURE 2. The PINN-based workflow for solution reconstruction.

Figure 2 shows a schematic diagram of the PINN-based workflow. This workflow directly reconstructs the solution from sparse measurements without requiring extensive training with numerous experiments. The sparse measurements are fed into the inverse workflow to determine the BCs, which are then used by the forward workflow to obtain the reconstructed solution by solving a forward problem. The inverse workflow requires knowledge of the PDE (Equation 1), the sparse measurements, and the approximate bounds of the solution to be reconstructed. The inverse workflow attempts to fit a high-order polynomial function to approximate the BCs.

$$\kappa \Delta u = f, \tag{1}$$

3. RESULTS

The thermo-mechanical simulation of the AMAZE sample was conducted using CodeAster, utilising the results generated by the induction heating and coolant models. The entire simulation was carried out on a platform called VirtualLab [3], which includes CodeAster, ERMES, and several meshing tools.

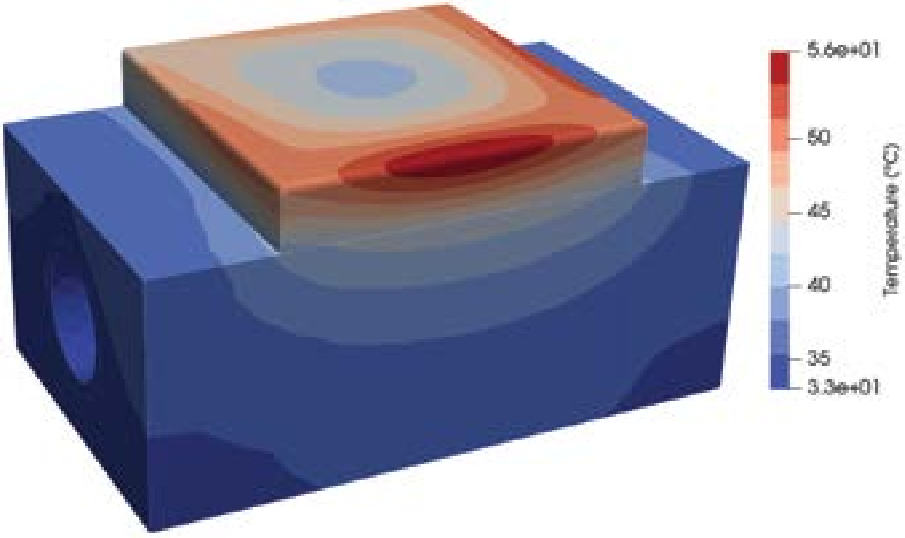

FIGURE 3. The temperature profile from the thermo-mechanical simulation of the AMAZE sample.

Figure 3 shows the temperature distribution of the AMAZE sample using the standard properties of the pipe and the coil [2]. To reconstruct the solution, we sampled 50 pseudo-random sparse measurements using the Latin-hypercube sampling. The number of sparse measurements was chosen randomly, as we have not yet explored other sampling techniques. It is possible that the solution could be reconstructed with even fewer sparse measurements.

We used an approximate BC range by increasing the bounds of the actual BCs by 25%. A multilayer perceptron (MLP) with the Adam optimiser was employed to train both the inverse and forward workflow. We tested several hyperparameters, including network size, activation function, and the order of the polynomial used to fit the BCs. Our observations indicated that a 10th-order polynomial was sufficient to capture the complexities of the BCs accurately. We also tested various activation functions such as hyperbolic tangent (Tanh), rectified linear unit (ReLU), and sigmoid linear unit (SiLU). The lowest relative L2 error of 3.45% was achieved using the ReLU activation function.

Lewis [2] used a data-driven model to reconstruct the solution of the same problem with 1000 experiments, successfully reconstructing the solution with just 3-4 sparse measurements. In contrast, we are using no additional experiments but rely on 50 sparse measurements from a single experiment.

It is important to note that while reconstructing the solution of such a complicated problem with just 50 sparse measurements without any training on numbers of experiments is exceptional, it is not practical. The small size of the sample makes it challenging to fit 50 thermocouples, as there simply isn't enough space to accommodate that many sensors.

Inverse problems are known for having non-unique solutions, and navigating from numerous local minima to the specific local minimum that generates the correct solution is a significant challenge. Additionally, the ill-posed nature of inverse problems further complicates this process as the global minimum does not necessarily represent the physical solution we are seeking. When the weights are randomly initialised, this process becomes even more time-consuming as the model has to spend more iterations finding a suitable solution. In contrast, using transfer learning with pre-trained weights significantly reduces the time required to reach an acceptable solution, as the model starts from a more informed state rather than from scratch.

To circumvent this issue, we used transfer learning by training the workflow on a simpler problem—not necessarily a low-fidelity solution of the problem at hand, but just any random BC within the approximate range of the BC and the same PDE. This approach allows the weights to be more informed about the problem they need to tackle. In this method, we only need one finite element method (FEM) solution, avoiding the necessity for multiple experiments in data-driven models.

As demonstrated in Table 1, we simulated a linear increase in the current (A) of the coil and reconstructed the solutions using both independent steady-states and transfer learning. For transfer learning, we initially used a constant thermal load of 500 W/m^3 on the tile to train the model. This constant thermal load was not used in the independent steady-state solutions but served as an initial training step to provide a baseline for the weights. For subsequent time steps with varying current values, we applied transfer learning using the model trained on the previous time step, allowing the model to progressively adapt to the changing conditions. With this approach, we were able to reconstruct the solution using just 10 sparse measurements. This methodology significantly reduced the average training time from 50 minutes to 25 minutes, compared to independently reconstructing each steady-state.

Current (A)	50	100	150	200	250	300
Independent steady-states						
Rel L2 error	3.45	5.12	2.98	4.56	3.33	5.77
Average time taken: 50 mins						
Transfer learning						
Rel L2 error	3.45	5.88	4.21	3.09	5.34	2.47
Average time taken: 25 mins						

TABLE 1. Comparison of relative L2 errors (in %) and average time taken (min) for different currents (A) using independent steady-states and transfer learning.

4. CONCLUSIONS

The PINN-based workflow demonstrated the capability to accurately reconstruct field variables from sparse measurements, significantly reducing the need for extensive experimental data. The workflow requires knowledge of the PDE, the sparse measurements, and the approximate bounds of the solution to be reconstructed. The transfer learning approach, proved effective in minimising reconstruction time and error. This methodology shows promise for efficient and practical applications in data-scarce environments. The workflow can be potentially used within the context of digital twin. Once the solution is reconstructed, it can be used to predict parameters such as temperature-dependent conductivity. This allows for proactive adjustments, such as stopping the experiment if the conductivity approaches a critical value, thereby enhancing the utility and efficiency of digital twins in monitoring and controlling experimental conditions.

REFERENCES

[1] M Raissi, P Perdikaris, and GE Karniadakis. Physics-informed neural networks: A deep learning framework for solving forward and inverse problems involving nonlinear partial differential equations. *Journal of Computational physics*, 2019.

[2] Rhydian Lewis. *Simulation driven machine learning methods to optimise design of physical experiments and enhance data analysis for testing of fusion energy heat exchanger components*. PhD thesis, Swansea University, UK, 2024.

[3] Rhydian Lewis, Ll.M. Evans, and B.J. Thorpe. Virtuallab source code. `https://gitlab.com/ibsim/virtuallab`, 2020. Source code.

Sixth International Conference on Computational Methods for Energy and Thermal Problems
THERMAECOMP2024, Sept. 9-11, 2024, Budva, Montenegro
N. Massarotti, P. Nithiarasu and I. Vušanović (Eds.)

THERMAL MANAGEMENT SYSTEM OF RAILWAY POWER ELECTRONICS THROUGH A DIGITAL TWIN OPTIMIZED VIA THE NEW *REFINE* ALGORITHM

Raffaele De Rosa, Adolfo Sentore
Department of Industrial Engineering, University of Naples “Federico II", Via Claudio 21, 80125 Napoli (NA), Italy. raffaele.derosa4@unina.it, adolfo.senatore@unina.it

Luca Romagnuolo, Emma Frosina
Department of Engineering, University of Sannio, Piazza Roma 21, 82100 Benevento (BN), Italy.
frosina@unisannio.it, lromagnuolo@unisannio.it

ABSTRACT

An automated approach for the optimization of the entire Thermal management system (TMS) of power electronics for railway applications is presented in this paper. The methodology, completely developed by the authors, involves an iterative optimization loop, managed by a batch file named *REFINE* (*Railway Electronics Fluid Integration for Network Efficiency*), which refines the liquid cold plate (LCP) design and selects appropriate pump specifications to achieve optimal cooling performance. The ultimate objective is to create an integrated model that works in both Amesim and OpenFOAM environments, that minimizes energy consumption required for cooling while guaranteeing operational temperatures of electronic components. This comprehensive approach addresses the thermal management challenges in railway systems, facilitating enhanced efficiency and reliability in a complete automatic way.

Key Words: *Digital Twin, Heat Transfer, Liquid Cold Plate, OpenFOAM, Thermal Management System, Optimization Algorithm, Simcenter Amesim.*

1. INTRODUCTION

In the realm of thermal management systems (TMSs) for high-power electronic systems such as power converters and batteries, liquid cooling systems based on liquid cold plates (LCPs), have risen to prominence as the preferred solution. This is due to their remarkable capability to efficiently dissipate heat, owing to their high heat transfer coefficients. However, optimizing TMSs in the industrial railway sector poses significant challenges necessitating advanced techniques to balance thermal performance, energy efficiency, manufacturing feasibility, and cost-effectiveness. To address these challenges, this study proposes a batch algorithm, completely developed by the authors, called *REFINE - Railway Electronics Fluid Integration for Network Efficiency*, which follows a numerical methodology already proposed in [1] to study a liquid cooling system for the converters of a high-frequency regional train. *REFINE* conducts parametric 3D CFD simulations, in the OpenFOAM environment, of an LCP with a U-type internally finned channel [2], primarily manufactured through extrusion and selects the configuration that minimizes the maximum temperature of the electronic components and the pressure drop of the LCP. Subsequently, it imports the results of the 3D CFD simulations into a lumped-parameter model of the entire liquid cooling system defined in Simcenter Amesim. Further iterations are then carried out to select the pump that ensures minimal energy consumption while maintaining electronic component temperatures within the threshold values. This approach, on one hand, allows optimizing the heat exchange performance of the LCP through a Parametric Shape Optimization (PSO), and on the other hand, enables limiting the manufacturing costs by defining an internally finned geometry that is easy and cost-effective to produce using technologies like extrusion. Furthermore, it facilitates minimizing energy consumption through the selection of a pump that matches the system resistance at the point of minimum power absorbed.

2. MATERIALS AND METHODS

The case study on which *REFINE* is applied concerns the cooling system of converters for a high-frequency train, which primarily consists of a closed-cycle circuit comprising a tank, centrifugal pump, pipework, three converter modules with their respective LCPs, radiator, and motor fan, as depicted in Fig. 1. The *REFINE* algorithm, outlined in the flowchart in Fig. 2, assigns an initialization flow rate Q as a boundary condition to a 3D CFD model developed in OpenFOAM, that is based on a parametric mesh described in the *blockMeshDict*, which automatically generates the geometry to be simulated from the input data, thus eliminating the need for CAD importation. The other boundary conditions assigned to the LCP CFD model are: a constant fluid inlet temperature of $T_{\text{in}} = 333$ K and a constant fluid outlet pressure of $p_{\text{out}} = 0$ Pa. The $k - \varepsilon$ turbulence model is employed with a turbulent intensity kinetic energy inlet of 0.05 and a turbulent dissipation rate of 0.006. To model heat transfer at all coupled walls, the boundary condition *turbulentTemperatureCoupledBaffleMixed* is used. This condition represents heat transfer through the solid wall as described by Fourier's law. The inlet thermal power in the LCP is 16 kW. In the next stage, the algorithm executes the bash script *REFINE_bash.sh*, which generates all the possible geometric combinations of the internal finning of the LCP, whose cross-sectional view is depicted in the Fig. 3, varying parameters such as the channel width between two fins (a), the fin width (b), the number of channels (n) and the fin length (l). The distance (c) between the tip of the fin and the upper surface of a plate, inserted into the channels for manufacturability reasons of the extrusion, is kept constant. This parameter, from a previous study [3], has been found to be among

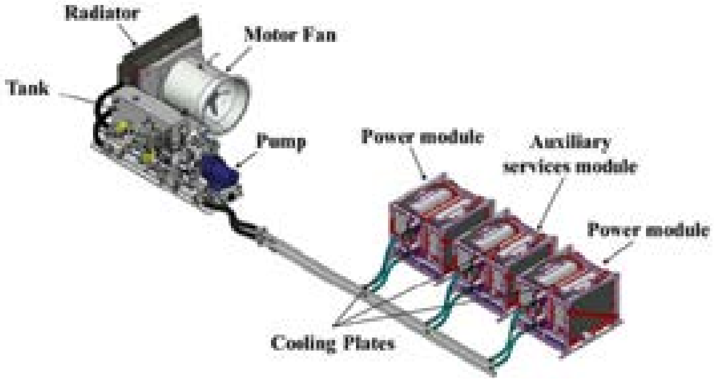

FIGURE 1. Converters hydraulic cooling system

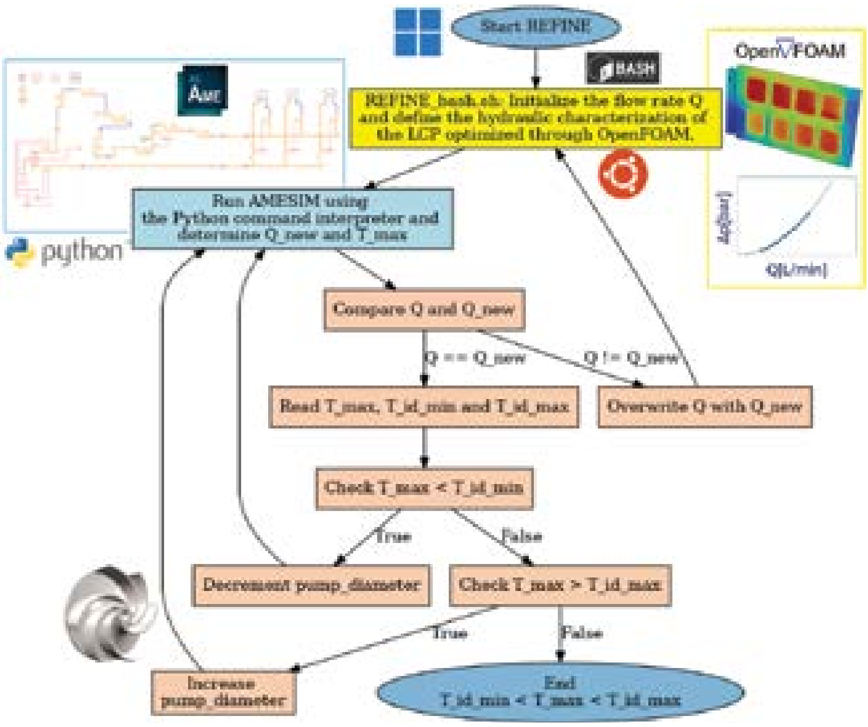

FIGURE 2. REFINE flowchart

the most significant for the performance of the LCP, and a value of 1 mm proves to be the right compromise between performance and manufacturability at reasonable costs of the product. The parameterization results in 27 different combinations. For each case, *REFINE_bash.sh* initiates the CFD simulation with OpenFOAM and selects the geometric configuration that optimizes the LCP. Since $T_{\max}$ and Δp are inversely proportional [2], the optimization is carried out using a performance coefficient (P_{c}) for each combination defined as the inverse of the sum of the normalized maximum temperature ($T_{\max_{\mathrm{N}}}$) and the normalized pressure drop (Δp_{N}):

$$P_c = \frac{1}{\left(\frac{T_{\max} - T_{\max_{\min}}}{T_{\max_{\max}} - T_{\max_{\min}}} + \frac{\Delta p - \Delta p_{\min}}{\Delta p_{\max} - \Delta p_{\min}}\right)} = \frac{1}{T_{\max_{\mathrm{N}}} + \Delta p_{\mathrm{N}}} \tag{1}$$

Subsequently, for the combination with the highest P_{c}, it calculates the overall heat transfer coefficient (h) and conducts hydraulic characterization by defining the flow-rate versus pressure drop curve ($Q - \Delta p$). These optimized LCP data generated by *REFINE_bash.sh* are then imported into an Simcenter Amesim digital twin of the entire cooling system using a Python command interpreter. This digital twin evaluates the flow rate circulating in the circuit (Q_{new}) and the temperature beneath the hottest electronic component ($T_{\max}$). Subsequently, the initialization flow rate (Q) is compared with the flow rate from the digital twin (Q_{new}). If $Q \neq Q_{\mathrm{new}}$, the process overwrites Q_{new} as new Q and returns to *REFINE_bash.sh*; otherwise, it is checked whether $T_{\max}$ falls within the threshold values $T_{\mathrm{id\_min}}$ and $T_{\mathrm{id\_max}}$. In this case, the loop terminates as it has found a configuration of the system that satisfies the requirements. If, instead, $T_{\max} > T_{\mathrm{id\_max}}$, a pump with a larger impeller, capable of generating a higher flow rate, is selected from the library implemented in *REFINE*. Conversely, if $T_{\max} < T_{\mathrm{id\_min}}$, a pump with a smaller impeller is selected from the *REFINE* library to generate a lower flow rate and achieve energy savings. After redefining the pump and re-optimizing the LCP, the loop terminates when $T_{\mathrm{id\_min}} < T_{\max} < T_{\mathrm{id\_max}}$ is verified.

FIGURE 3. Parameters of the internal finned channel. a) Dependent variable; b) 3.5 mm, 4.0 mm, 4.5 mm; n) 17, 18, 19; l) 5 mm, 6 mm, 7 mm; c) 1 mm.

3. RESULTS

The *REFINE* algorithm, on one hand, provided an optimized LCP (Tab. 1), in terms of maximum temperature and pressure drop, with internally finned channels, that can be easily manufactured through extrusion. On the other hand, it redefined the pump that feeds the entire system, taking into account the upgrade of the LCP. The results of the optimized liquid cooling system for converters are reported in Tab.2, where, the first row refers to the most critical LCP, positioned in the auxiliary services module that dissipates 16 kW of heat, while the second row is related to the entire hydraulic system showed in Fig.1. The new system configuration obtained through *REFINE* has allowed achieving a maximum temperature under the hottest components of 85.5°C, which is within the maximum and minimum threshold temperatures, enabling a transition from a pump with a 139mm impeller to one with a 122mm impeller. This reduction results in a significant change in the operating condition of the pump, shifting from 133 L/min - 2.38 bar in the initial system [1] to 111 L/min - 1.70 bar in the optimized system with *REFINE*. Taking into account

	a [mm]	b [mm]	l [mm]	n	P_c
Optimized LCP	2.2	4.5	6	17	1.96

TABLE 1. Optimized LCP configuration

	P_{diss} [kW]	Q [L/min]	h [W/(m^2 K)]	$T_{\max}$ [°C]	Δp [bar]	P_{absorb} [kW]
LCP	16	37	3060	85.5	0.22	/
Entire sys	32	111	/	85.5	1.70	0.7

TABLE 2. Results for the single LCP and the entire cooling system

the pump efficiency, which is approximately 0.45 in both cases, the absorbed power decreases from 1.2 kW in the initial configuration to 0.7 kW in the optimized one. Considering that about 600 units of the examined high-frequency regional train have been produced, and on average each unit incorporates two pumps, a total electrical power saving of 600 kW is achieved. Furthermore, since each train operates for 18 hours per day, the overall energy saved by the entire fleet would amount to 10.8 MWh per day. The single CFD-dataset, including 27 simulations to find the best configuration and 20 simulation to perform the characterization, takes 20 hours using 12 threads of an Intel Xeon CPU E5-2640 v2 2.00 GHz processor with DDR3 192 GB RAM. In this case, starting from a pump with a 139 mm impeller and a flow rate of 40 L/min, the code converges in three iterations. The parameter that most influences the convergence time is the initial impeller diameter, while it does not depend on the initial flow rate. Furthermore, it was observed that the optimum LCP configuration does not strongly depend on the flow rate, this means that, regardless of the initial flow rate value, Q_{new} is redefined after the first pass in the Amesim model.

4. CONCLUSIONS

The proposed method offers a systematic approach to optimizing thermal management systems in railway power electronics. The integration of CFD simulations with a lumped parameters digital twin facilitates a comprehensive solution to the challenges of balancing thermal performance, energy efficiency, and cost-effectiveness. In particular, CFD simulations allows for detailed analysis of fluid flow and heat transfer within the system, while the digital twin provides an accurate representation of the entire cooling system. Furthermore, since, in the circuits with centrifugal pumps, the circulating flow rate depends on the pressure drops introduced by all the component, enabling the communication between the CFD model of the LCP and the entire cooling system allows for obtaining the exact boundary conditions for the CFD model in terms of inlet velocity. Indeed, it must be considered that by altering the geometry of the finned channels, the pressure drop introduced by the component also changes. Consequently, the flow rate circulating in the system varies, directly affecting the inlet velocity in the CFD model. The entire optimization process is facilitated by consolidating Python and Bash scripts into a single REFINE.bat script. This integration enables a fully automated procedure that adopts a holistic optimization approach, taking into account both local and system-wide effects. The result is a systems that lead to a significant energy savings.

REFERENCES

[1] R De Rosa, L Belli, E Frosina, P Venanzio, L Romagnuolo, and A Senatore. Predictive model of cooling system for railway electric propulsion: validation of design choices and last mile analysis. *Journal of Physics: Conference Series*, 2385:012062, 2022. doi: 10.1088/1742-6596/2385/1/012062.

[2] R De Rosa, E Frosina, L Romagnuolo, and A Senatore. Doe optimization of a liquid cold plate used in a thermal management system for power converters in the railway sector through 3d cfd analysis. *Journal of Physics: Conference Series*, 2648:012097, 2023. doi: 10.1088/1742-6596/2648/1/012097.

[3] R De Rosa, M Bernagozzi, A Georgoulas, L Romagnuolo, E Frosina, and A Senatore. An open-source algorithm for automatic geometrical optimization of extruded liquid cold plates for enhanced thermal management in railway electronics. *Submitted to Applied Thermal Engineering*, 2024.

Sixth International Conference on Computational Methods for Energy and Thermal Problems
THERMAECOMP2024, Sept. 9-11, 2024, Budva, Montenegro
N. Massarotti, P. Nithiarasu, and I. Vušanović (Eds.)

CYLINDRICAL BATTERY THERMAL MANAGEMENT WITH DIFFERENT PHASE CHANGE MATERIAL SOLUTIONS

Francesco Piccirillo, Marcello Iasiello, Nicola Bianco

Dipartimento di Ingegneria Industriale, Università degli Studi di Napoli Federico II, Piazzale Tecchio, 80, 80125 Napoli, Italy, francesco.piccirillo@unina.it, marcello.iasiello@unina.it, ni.bianco@unina.it

Wilson K. S. Chiu

School of Mechanical, Aerospace and Manufacturing Engineering, University of Connecticut, 191 Auditorium Road, 06269, Storrs, CT, USA, wilson.chiu@uconn.edu

ABSTRACT

Phase change materials (PCMs) are considered for battery thermal management systems (BTMS). This study proposes a coupled electrochemical-thermal model of a cylindrical battery incorporating a molten salt PCM, specifically sodium thiosulfate pentahydrate, within a hollow mandrel. For safety, the battery's operating maximum temperature limit is set at 50 °C. The study compares the time it takes to reach this temperature limit across different configurations: without PCM, with PCM applied externally, and with PCM applied both externally and internally in place of the mandrel. The PCM volumes used internally and externally are selected to properly compare the effectiveness. The best performance is obtained in the case of PCM placed both internally and externally, but twice the volume is used. Externally placed PCM performs better than internally placed PCM, but will result in a larger battery dimension.

Key Words: *Cylindrical battery, Electrochemical-thermal Model, Battery thermal management system, Phase Change Material, Numerical Model*

1. INTRODUCTION

Battery thermal runaway and aging problems are factors that affect battery performance and safety. For this reason, battery thermal management systems (BTMS) using phase change materials (PCMs) are studied in depth. An innovative thermal management method could be to insert PCM inside the battery, in the hollow mandrel. Few experiments and numerical models [1] - [2] are present in the literature with this solution. Therefore, an electrochemical-thermal model in a finite element environment is proposed in this study, where thermal management is performed through a numerical analysis with a molten salt PCM, sodium thiosulphate pentahydrate (STP), inserted in different positions: internally, externally, and internally/externally. A pseudo-two dimensional (P2D) electrochemical model is coupled with a two-dimensional thermal model to simulate this problem. The models will be briefly described in the next section. Subsequently, the results in terms of battery temperature for the different PCM placements are presented.

2. ELECTROCHEMICAL-THERMAL MODEL

The electrochemical model analyzed, also called pseudo-two dimensional (P2D), is based on Fuller's theory [3]. It considers the anode and cathode as porous electrodes filled with electrolyte. The model includes two interconnected dimensions, cell thickness x and particle radius r. The first dimension allows the model to describe charge transport in the electrodes and electrolyte and charge transfer reactions at the electrode/electrolyte interface, while along the second dimension describes Li-ion diffusion within spherical particles.

The electrochemical model is coupled with a two-dimensional thermal model using a finite element method. Heat generation is derived from calculations in the electrochemical model. Additionally, some parameters in the electrochemical model, such as open circuit voltage and entropic heat generation, depend on the average temperature that is calculated in the thermal model. The equations for the model are described in [4].

3. PCM MODEL

The effectiveness of PCMs derives from the exploitation of latent heat coming from phase change. For this purpose, it is important to use a PCM model which simulates its behaviour during the three phases: a solid zone, a liquid zone, and a mushy zone where both phases coexist. In this model, volume changes during the melting process and natural convection phenomena are assumed to be negligible. The energy conservation equation is given by:

$$\left(\rho c_p\right)_{PCM}\left(\frac{\partial T}{\partial t}\right) = \nabla \cdot \left(k_{PCM}\nabla T\right) + S_h \tag{1}$$

Where T is temperature [K], t is the time [s] and ρ_{PCM}, $c_{p,PCM}$, and k_{PCM} are respectively the PCM density [kg m^{-3}], heat capacity [J kg^{-1}] and thermal conductivity [W m^{-1} K^{-1}].

To account for latent heat, a generation term S_h is assumed to be:

$$S_h = -\rho_{PCM} H_l \frac{\partial \varphi}{\partial t} \tag{2}$$

Where H_l is the latent heat [J kg^{-1}] and φ is the liquid fraction in the mushy zone:

$$\varphi(T) = \frac{V_{liq}}{V} = \begin{cases} 0 & if\ T \leq T_s \\ \dfrac{T - T_s}{T_L - T_s} & if\ T_s < T < T_L \\ 1 & if\ T \geq T_L \end{cases} \tag{3}$$

Where V_{liq} [m^3] is the PCM liquid volume fraction, V [m^3] is the PCM volume, T_s [K] is the solidification temperature, and T_L [K] is the melting temperature. Finally, it can be defined a general PCM phase-dependent thermal parameter Y, which stands for ρ, c_p, and k.

$$Y_{PCM} = Y_{solid}\left(1 - \varphi(T)\right) + Y_{liquid}\varphi(T) \qquad Y = \rho,\ c_p, k \tag{4}$$

Where Y_{solid} and Y_{liquid} are calculated respectively at the solid and liquid phase.

Three BTMS cases with PCM are studied (figure 1). In the first case, PCM is inserted inside a hollow mandrel, in the second case, PCM is placed outside the battery in an external casing, and finally, PCM is applied both inside the mandrel and outside the battery simultaneously. All results are compared to a reference case without PCM. Due to their thinness and high thermal conductivity, the hollow mandrel and outer PCM casing are not considered in the thermal model. The PCM used is sodium thiosulfate pentahydrate (STP), a molten salt with a melting temperature of 48°C. All necessary parameters for the PCM model are detailed in references [5] - [6]. A molten salt is chosen over paraffins, since the latter are easily flammable and safety-related problems can occur with their use. The volume of PCM is kept consistent across internal and external use cases. For standardized analysis conditions, a 0.22 mm thickness of PCM is used for external applications.

4. RESULTS

A comparison based on the numerical results of [4] is made, where a charge/discharge cycle (500 s per full cycle, starting with the charge phase, at ± 80 A/m^2) is applied for a 18650 cylindrical battery with lithium cobalt oxide (LCO) cathode. It has a nominal capacity C_{nom} of 12 Ah and an initial state of charge (SOC) of 30%. All the battery's electrical and thermal parameters are taken from [4]. The average battery temperature is calculated using an external convective heat transfer coefficient h, simulating natural convection (8 - 10 W/m^{2}K, with an ambient temperature T_{amb} = 20 °C). The mesh used consists of 6102 elements, and grid consistency and timestep are verified with two different meshes and timestep that are respectively twice and half of the employed ones. Figure 2 shows the dimensions of the analyzed battery (a) and the comparison results (b).

A charge/discharge cycle is applied (500 seconds per full cycle, starting with the charge phase, at ±50 A/m^2 with an initial State of Charge of 30%) with an external heat transfer coefficient of 10 W/m^{2}K, an external temperature of 20 °C, and maintained temperature continuity at the interfaces. A battery operating temperature limit T_{lim} of 50 °C is assumed; above this temperature, the battery will shut down for safety reasons. Figure 3 (a) shows the maximum battery temperature T_{max} in all configurations, showing different times t_{stop} to reach T_{lim}. Without PCM, the battery reaches the limit temperature T_{lim} in the shortest time, after 2475 s. Performance is improved by inserting a PCM internally, extending the operating time by 1000 s, even more if inserted externally (t_{stop} = 3926 s) or internally/externally (t_{stop} = 5459 s). In Figure 3 (b), the percentage improvement $I = \frac{t_{stop} - t_{stop,ref}}{t_{stop,ref}}$ of all BTMS solutions is compared to the reference case.

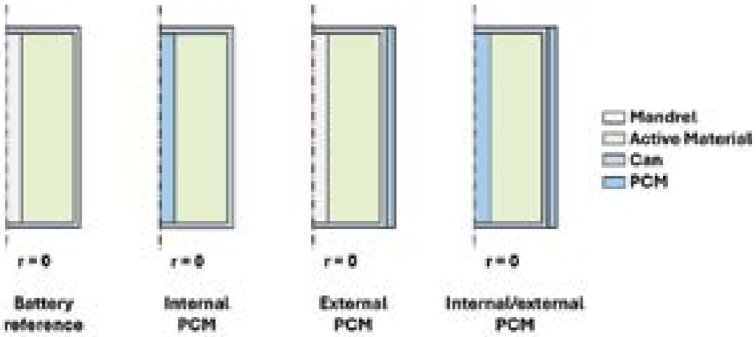

FIGURE 1. Battery reference composition and three proposed BTMS configurations

(a)

Description	Symbol	Value
Cell radius	r_{cell}	9 mm
Cell height	h_{cell}	65 mm
Mandrel Radius	r_{man}	2 mm
Can thickness	d_{cell}	0.25 mm

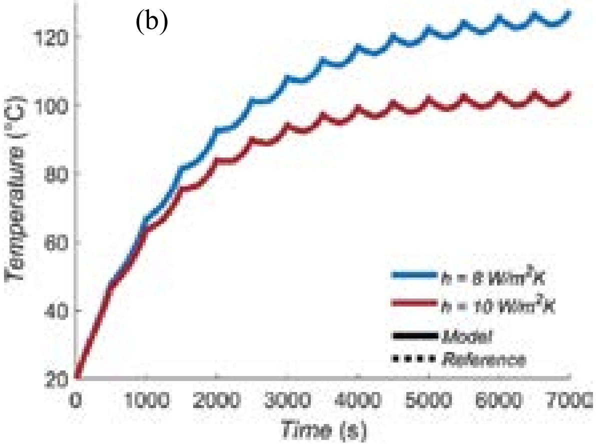

FIGURE 2. Dimensions of the analyzed battery (a) and comparison results (b)

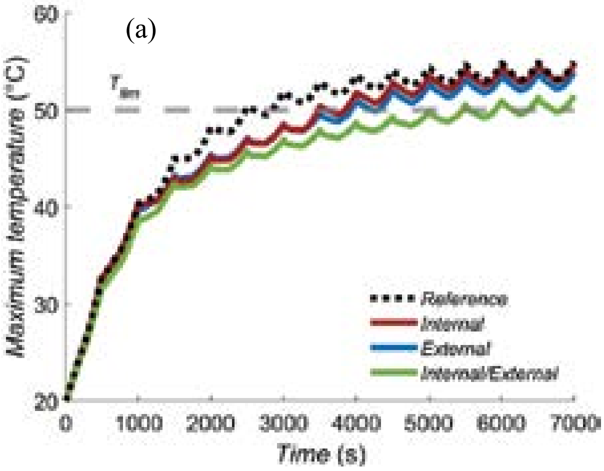

(b)

BTMS configuration	Improvement I
Internal	40.5 %
External	58.6 %
Internal/External	120.5 %

FIGURE 3. Maximum battery temperature for all the cases analysed (a), percentage improvement I of all BTMS solutions is compared to the reference case (b)

Superior performance of the externally-positioned PCM is due to convective heat exchange with the environment, which delays the attainment of the melting temperature. The simulation continues even after the maximum temperature of 50 °C is reached, as its operation is not affected. However, if the temperature continues to rise uncontrollably, thermal runaway reactions may occur.

5. CONCLUSIONS

An electrochemical-thermal model of a cylindrical battery with various PCM battery thermal management systems is developed using a finite element method. The systems include internal PCM inserted in a hollow mandrel, external PCM, and a combination of both internal and external PCM. Using PCM as a BTMS significantly improves performance by extending the time taken to reach a maximum temperature. With internal PCM, there is an increase in performance and space-savings due to the compact design. However, for better performance, placing the PCM externally is more beneficial. It is observed that the t_{stop} time still increases when PCM is inserted both internally and externally, but a double PCM volume has been used compared to the previous cases. This results in additional weight and should be considered in the construction of a battery pack.

REFERENCES

[1] Zhao, R., Gu, J., & Liu, J. (2017). Optimization of a phase change material based internal cooling system for cylindrical Li-ion battery pack and a hybrid cooling design. *Energy*, *135*, 811-822.

[2] Gou, J., Liu, W., & Luo, Y. (2019). The thermal performance of a novel internal cooling method for the electric vehicle battery: An experimental study. *Applied Thermal Engineering*, *161*, 114102.

[3] Fuller, T. F., Doyle, M., & Newman, J. (1994). Simulation and optimization of the dual lithium ion insertion cell. *Journal of the electrochemical society*, *141*(1), 1.

[4] Cianciullo, M., Vilardi, G., Mazzarotta, B., & Bubbico, R. (2022). Simulation of the Thermal Runaway Onset in Li-Ion Cells—Influence of Cathode Materials and Operating Conditions. *Energies*, *15*(11), 4169.

[5] Hadjieva, M., Stoykov, R., & Filipova, T. Z. (2000). Composite salt-hydrate concrete system for building energy storage. *Renewable Energy*, *19*(1-2), 111-115.

[6] Landini, S., Leworthy, J., & O'Donovan, T. S. (2019). A review of phase change materials for the thermal management and isothermalisation of lithium-ion cells. *Journal of Energy Storage*, *25*, 100887.

Sixth International Conference on Computational Methods for Energy and Thermal Problems
THERMAECOMP2024, Sept. 9-11, 2024, Budva, Montenegro
N. Massarotti, P. Nithiarasu, and I. Vušanović (Eds.)

Efficient explicit time stepping enthalpy methods for phase change problems

[1]Igor Vušanović, [2]Vaughan R Voller

[1]University of Montenegro, George Washington St. bb, 81000 Podgorica, Montenegro, igorvus@ucg.ac.me

[2]Department of Civil, Environmental, and Geo-Engineering, University of Minnesota, Minneapolis, MN 55455, USA, vole001@umn.edu

ABSTRACT

Due to the need to track a moving front, the numerical solution of phase change problems is challenging. A particular phase change problem of interest is the melting of an initially solid material. A problem that not only requires the tracking of the melt front but also requires the coupled solution of the Navier-Stokes flow equations in the liquid phase. One effective numerical approach is based on an enthalpy-porosity formulation, that through the definitions of a heat content variable, combining latent and sensible heats, and a porosity source term in the flow equations, allows for solutions on fixed numerical grids. While explicit time step solutions of enthalpy-porosity schemes are easily implemented, they can be, due to time step stability limitations, computationally costly. In this study, we present a numerical scheme that combines an explicit time stepping solution of the enthalpy-porosity formulation with the SIMPLE Navier-Stokes algorithm. We then demonstrate how this scheme overcomes the time step limitation, through employing multiple (n) explicit enthalpy solutions steps of time $\Delta\tau_{exp}$ (a value within the stability limit) for every SIMPLE step of time $\Delta\tau = n\Delta\tau_{exp}$. In applications to the classic gallium melting benchmark [4], we show that when n=300 the efficiency of the basic (n=1) explicit scheme can be increased by 1.5 orders of magnitude, with less than 0.28% change in the prediction accuracy.

Key Words: *Phase change, enthalpy method, explicit scheme, SIMPLE.*

1. INTRODUCTION

The classic phase change problem, the Stefan problem, involves the heat conduction-controlled melting of a pure solid [5,6]. The core numerically difficulty in this problem rests in tracking the position of the melt front. A common numerical solution approach is to use a so-called enthalpy formulation [6,7]. In such an approach, the position of the melt, on a fixed numerical grid, is tracked by providing a constitutive relationship between the temperature and a liquid fraction index term $0 \leq g \leq 1$. An important extension of the Stefan problem are problems that, in addition to heat conduction, also consider the advective heat transfer in the liquid melt, requiring solution of both a temperature and flow field. Numerical solution of this class of problems can be achieved by using the so-called enthalpy-porosity approach, Brent et al. [1]. In these approaches an enthalpy formulation of the heat balance is solved to obtain the temperature and liquid fraction field, followed by a solution of the momentum and continuity equations for the flow field. An important part of this solution is the treatment of the melt range as a porous media, a device that allows the velocity filed to be switched off as the liquid fraction $g \rightarrow 0$. Typically, enthalpy-porosity techniques employ an implicit time stepping scheme for solving the enthalpy heat balance and a time implicit pressure correction scheme (e.g., SIMPLE [2]) for the flow field. While in general these schemes can be efficient, cases where the non-linear relationship between the temperature and liquid fraction involves sharp changes and jumps require carefully designed iteration strategies. Such complications can be averted by using a mixed time stepping scheme, solving the enthalpy formulation with explicit time stepping followed by an implicit time stepping solution for flow (e.g.,SIMPLE). Of course, the immediate disadvantages of this mixed time stepping is the stability restriction on the size of the time step ($\Delta\tau < \Delta\tau_{\mathrm{exp}}$) leading to inefficient solutions. In this light, the objective of this paper, is to propose, what we refer to as a hybrid method, a method that retains the advantage of an explicit solution of the heat equation with only a limited loss in efficiency.

In studying the classic benchmark problem of melting an initially solid gallium block [4] we demonstrate that an optimum application of this scheme involves a trade-off of choosing a large enough value of n to improve efficiency of the solution without detriment to the accuracy.

2. PHYSICAL AND MATHEMATICAL MODEL

To motivate the development of our approach we consider the classic benchmark problem of the melting of a Gallium block, introduced by Gau & Viskanta [4], see Figure (1). Using appropriate scaling, the problem domain, 1x1.4 is size, is initially solid at the dimensionless temperature of $T_0 = -0.18$, which is below the dimensionless melt temperature of $T_m = 0$. Melting is induced by raising and fixing the left-hand vertical wall to a temperature above the melting temperature $T_L = 1$. As meting advances, the right-hand vertical wall is kept fixed at $T_R - 0.18$, while the top and bottom horizonal walls are insulated.

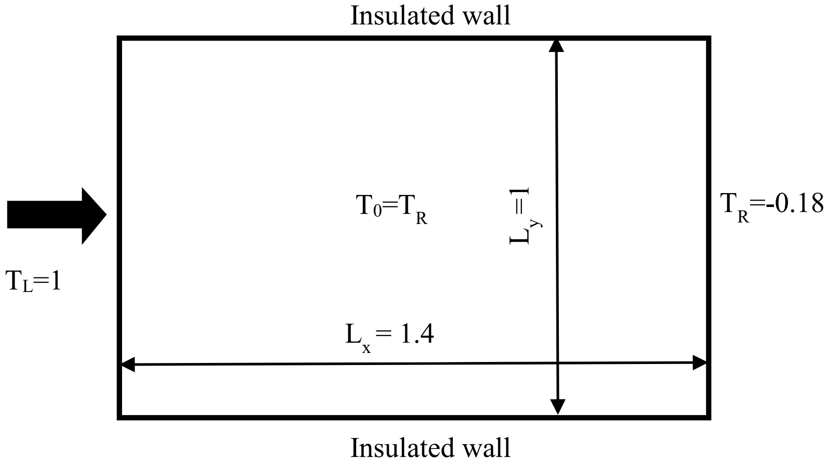

FIGURE 1. Physical model for Gallium melting problem

In this study, we use non-dimensional form of mixture continuum model composed by mass, momentum and heat balance as follows:

- Mass balance:

$$\frac{\partial u}{\partial x}+\frac{\partial v}{\partial y}=0, \tag{1}$$

- Momentum in x and y directions:

$$\frac{\partial u}{\partial \tau}+u\frac{\partial u}{\partial x}+v\frac{\partial u}{\partial y}=\frac{\partial^2 u}{\partial x^2}+\frac{\partial^2 u}{\partial y^2}-\frac{\partial p}{\partial x}-\frac{1}{k}\frac{(1-g)^2}{g^3}u, \tag{2}$$

$$\frac{\partial v}{\partial \tau}+u\frac{\partial v}{\partial x}+v\frac{\partial v}{\partial y}=\frac{\partial^2 v}{\partial x^2}+\frac{\partial^2 v}{\partial y^2}-Gr\cdot T-\frac{\partial P}{\partial y}-\frac{1}{k}\frac{(1-g)^2}{g^3}v, \tag{3}$$

- Energy balance:

$$\frac{\partial h}{\partial \tau}+u\frac{\partial T}{\partial x}+v\frac{\partial T}{\partial y}=\frac{\partial}{\partial x}\left(\left[\frac{1}{Pr}\right]\left(\frac{\partial T}{\partial x}\right)\right)+\frac{\partial}{\partial y}\left(\left[\frac{1}{Pr}\right]\left(\frac{\partial T}{\partial y}\right)\right), \tag{4}$$

$$h=T+g\cdot St^{-1}. \tag{5}$$

$$g=\begin{cases}1\ if\ \ T\geq 0\\ 0\ if\ T<0\end{cases} \tag{6}$$

where u and v are the flow velocities in the x and y directions, p is pressure, T is temperature, h is the mixture enthalpy, and g is the liquid fraction (note the Heaviside definition with temperature). The last terms in equations (2) and (3) are the porosity terms, when the liquid fraction approaches zero these terms will dominate the equations and force the velocities to zero as the full solid state is reached, and (k) is the permeability constant, in this study was set on value $k = 3.56x10^{-11}$. For gallium melting, the dimensional groups in these equations are: Grashof number $Gr = 2.81x10^{-7}$, Prandtl number $Pr = 0.0216$, Stefan number $St = 0.0391$.

3. SOLUTION METHOD

The control volume finite difference solution method proposed by Brent et al [1], used iterative implicit time stepping for solving the energy balance in eq. (4) and the implicit SIMPLE [2] method to solving for the velocity field. Here we propose replacing the iterative implicit solution of the energy balance used by Brent with an explicit scheme. In this way, for given previous time fields of velocity (u^{old}, v^{old}), temperature (T^{old}) and liquid fraction (g^{old}), we can explicitly calculate the enthalpy field at time $t^{old} + \Delta\tau_{exp}$ ($\Delta\tau_{exp}$ is a stable time step) in one step. From this we can immediately calculate time updates for the liquid fraction and temperature as:

$$T = min(h, max(h - St^{-1}),0)), \tag{7}$$

$$g = min(1, max(St(h - T), 0)). \tag{8}$$

At this point we can continue and use SIMPLE to calculate the velocity field at time $\tau^{old} + \Delta\tau_{exp}$. However, since we can expect that, due to the stability criterion, $\Delta\tau_{exp}$ to be small this scheme will require many time steps. Here we propose to reduce this load by adopting a ***hybrid scheme***. The essential concept is in each time step, make n successive explicit solutions of the enthalpy formulation with a time step $\Delta\tau_{exp}$,*without* updating the flow field. Only when we have the estimated temperature and liquid fractions at time $t^{old} + n\Delta\tau$, do we make a SIMPLE solution, with time step $n\Delta\tau_{exp}$, to obtain an updated flow field. Note. in the SIMPLE solution, we declare convergence when the maximum mass error in any control volume CV becomes less than 10^{-4} % of the control volume area.

4. RESULTS AND CONCLUSION

To demonstrate the proposed hybrid scheme in the solution of the gallium melting problem, we use the same grid size as in Brent et al research [1], $n_y \, x \, n_x = 30 \, x \, 42$. In the calculations, a stable explicit time step is set as $\Delta\tau_{exp} = 2.4x10^{-6}$ (0.4 times the limit) calculations continue to the point where ~0.78 of the cavity is melted. The results, CPU performance and accuracy, for various choices of n =1, 10, 20, 50, 100, 200, and 300 are shown on Fig. 2. With CPI performance in Fig 2 (A), we note dramatic reduction in CPU time as n is increased. We evaluate accuracy, by comparing predictions of the evolution of the liquid fraction in the cavity using values of n >1 against the n=1 prediction, see Fig 2(B). We note a choice of *n*=300 provides a CPU speed up of over 1.5 orders of magnitude with only a slight deviation in the liquid fraction evolution predictions; with *n*=300 the prediction of the cavity liquid fraction, at 80%, differs by less than 0.28% from the prediction with *n*=1. Thus, in the context of the gallium benchmark, we conclude that the proposed hybrid scheme can offer a dramatic improvement in CPU performance without significantly compromising the accuracy of the solution. Our next step is to compare the hybrid method with a that uses an implicit scheme for the heat balance.

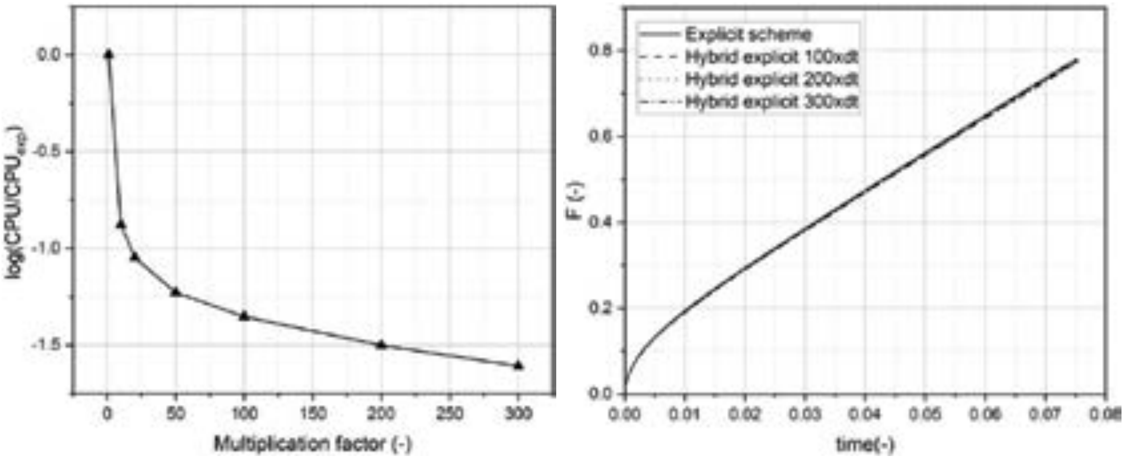

$a)$ $b)$

FIGURE 2. (a) Example CPU usage as ratio of full explicit scheme $(n = 1)$. (b) Predictions of the time evolution of the domain liquid fraction $(F = \sum_{nodes} g\Delta V)$.

REFERENCES

[1] A.D. Brent, V.R. Voller, K.J. Reid, Enthalpy-porosity technique for modeling convection diffusion phase change: application to the melting of a pure metal, *Numerical Heat Transfer*, 13, 297–318, 1988.

[2] S.V. Patankar, *Numerical heat Transfer and Fluid Flow*, Hemisphere, Washington, 1980.

[3] V.R. Voller, A. Mouchmov, M. Cross, An explicit scheme for coupling temperature and concentration fields in solidification models, *International Journal of Heat and Mass Transfer*, 28 (1), 79–94, 2004.

[4] C. Gau, R. Viskanta, Melting and solidification of a metal system in a rectangular cavity, *International Journal of Heat and Mass Transfer*, 214 27 (1), 113–123, 1984.

[5] J. Stefan, Über die Theorie der Eisbildung. *Monatshefte für Mathematik* 1(1), 1–6, 1890

[6] J. Crank, *Free and Moving Boundary Problems*, Clarendon Press, Oxford, 1984.

[7] P.H. Price, M.R. Slack, The effect of latent heat on numerical solutions of the heat flow equation, *British Journal of Applied. Physics*, 285–287, 1954.

Sixth International Conference on Computational Methods for Energy and Thermal Problems
THERMAECOMP2024, Sept. 9-11, 2024, Budva, Montenegro
N. Massarotti, P. Nithiarasu, and I. Vušanović (Eds.)

HIGH FIDELITY AND SIMPLIFIED MODELING OF HYDROPHOBIC SURFACES PERFORMANCES FOR ANTI-ICING APPLICATIONS

Giulio Croce,
University of Udine, 33100 Udine, giulio.croce@uniud.it

Nicola Suzzi

University of Udine, 33100 Udine, nicola.suzzi@uniud.it

ABSTRACT

Hydrophobic and super-hydrophobic coatings are currently considered promising tools to enhance the performances of thermal devices for in-flight icing protection. Two different simulation approaches are considered: the first is a high-fidelity phenomenological model, following the evolution of every droplet from its impact and possible rebound on the wing surface, through the evolution in the form of static droplets, running ones, rivulets or film. The second exploits the statistical local average distribution of droplet sizes in the different regimes obtained from the first model, allowing for a conventional eulerian based model of the water layer. Heat and mass balances are applied in both approaches, including phase changes. Both strategies are successfully compared with literature experimental data predicting the performances of a thermal anti-icing device.

Key Words: *Heat Transfer, hydrophobic coating, in-flight icing.*

1. INTRODUCTION

Current commercial numerical prediction tools for in-flight icing simulation are based on the Messinger model [1], although extended to 3-D arbitrary surfaces [2], coupled with Lagrangian or Eulerian [3] droplet flow field analysis. Messinger model assumes that the runback water layer is a continuous film driven by the shear stress and provides reliable and accurate results in several applications. Unfortunately, it intrinsically neglects any wettability effect and thus cannot assess hydrophobic coating performances. The main difficulty in the simulation of such coatings is that it involves an inherently multi-scale problem: wettability operates at a small scale, at most of the order of the single impinging droplet, but the local impinging mass flow, shear stresses, and heat transfer convective coefficients require state-of-the-art CFD computation around a whole wing or a whole aircraft. Since it is not practical to manage the large-scale computations with a grid fine enough to resolve the single droplet evolution (e.g., via VOF approach), a kind of intermediate bridge is required to derive average integral corrections from the small scale and transfer them to a coarser grid for the standard CFD solution of the large scale thermal and flow field. Here, a hierarchical approach is followed: first, given a coating of known wetting properties (i.e. contact angles), a high fidelity, small-scale model defines statistical distributions of relevant properties (rebounding droplet fractions, average runback water velocities, wet area fractions, coalesced droplet diameter distribution) as a function of the local fluid dynamic conditions. This step is performed via a phenomenological model describing the evolution of a droplet population. Then, statistical correlations are extracted by this small-scale computation campaign, providing integral corrections to the larger-scale CFD simulation.

2. HIGH FIDELITY MATHEMATICAL MODEL

In-flight icing occurs when an airplane flies through a cloud of supercooled droplets, which can freeze on impact on the surface, or flow along it in the form of moving droplets, rivulets, or films freezing at some downstream location. Such a phenomenon requires the simulation of the water evolution on the surface through all its transformations: impact on the surface, possible rebound on a super-hydrophobic surface, eventually followed by a later secondary impact, transition between still and moving droplets regimes, rivulets onset, their merge into continuous film, phase change due to freezing and evaporation. A small-scale, high-fidelity phenomenological model, fully described in [4], is used and. A Lagrangian tracking method evaluates first droplet's impact distribution (i.e. collection efficiency). A correlation based on the local Weber number [4,5] verifies if the impinging droplets rebound (with hydrophobic surfaces and fast-coming droplets), in which case a correlation based on the local streamwise shear stress derivatives offers an estimate of the distance at which the droplet hits the surface at a secondary impact location [4], correcting the collection efficiency from the tracking model. Primary to secondary impact distance is small but plays a role in the small airfoil used for the validation in the following paragraphs. Then, we generate a random distribution of droplets, at a density defined by the computed collection efficiency. Droplets are assumed spherical caps with constant static contact angle ϑ for the evaluation of active surface in the heat transfer computations, while their moving threshold is determined by the hysteresis between advancing and receding contact angles. Droplet growth due to coalescences or further impinging, shear stress driven movement, rivulet transition and their coalescence into a film are modeled. The procedure was developed to predict roughness evolution for rime ice [6] and was applied to a wide range of heat and mass transfer processes [7]. A force balance on one half of the droplet detects the onset of droplet elongation, leading to rivulet transition [8]. Rivulets are modeled as a series of overlapping droplets, thus modeling the entrainment of individual droplets into the rivulet with the same approach used for droplet coalescence. Droplet velocities derive from a power balance, rivulet, and film ones from the assumption of constant shear stress along the water layer thickness. Fig.1 shows a typical outcome for different surfaces subjected to the same droplet mass flow and diameter. The hydrophilic case yields larger droplets, still or moving (the latter identified by the dry surface left behind) and the onset of rivulets (identified as overlapping droplet clusters). The hydrophobic case shows smaller droplets, no rivulets, and dry traces from quick individual droplets.

FIGURE 1. Typical droplet evolution on (left) hydrophilic and (right) superhydrophobic surfaces. Air velocity and drag forces from left to right.

The energy balance equation for each droplet includes the convective heat transfer to the air, the heat flux provided by the de-icing heaters, the heat transfer related to phase changes (freezing on the solid-droplet interface and evaporation on the spherical cap surface exposed to the air). Freezing occurs after a short time lag due to the time required by the nucleation process to cover the whole substrate-droplet contact area [9]. Rivulet energy balances include the correction due to the difference between the base area (where freezing occurs) and free surface one (where convective heat transfer occurs)

3. SIMPLIFIED STATISTICAL MODELING

The starting point is an average balance for the mass m on a surface control volume of the coarse CFD grid, i.e. including a large number of droplets/rivulets:

$$\frac{d(m^{ds}+m^{dm}+m^{r})}{dt} = -\dot{m}_{out}^{dm} - \dot{m}_{out}^{r} + \dot{m}_{in}^{dm} + \dot{m}_{in}^{i} + \dot{m}_{in}^{r} - \dot{m}^{f} - \dot{m}^{ev} \quad (1)$$

$$\dot{m}_{out}^{d} = S_{dm}\dot{m}''^{i}_{in} + \dot{m}_{start}^{d} + \dot{m}_{in}^{*d} \quad (2)$$

$$\dot{m}_{out}^{r} = S_{r}\dot{m}''^{i}_{in} + \dot{m}_{start}^{r} + \dot{m}_{in}^{*r} \quad (3)$$

where the superscripts identify the still droplet (*ds*), moving droplets (*dm*), impinging droplets (*i*), rivulets (*r*), freezing (*f*), evaporating (*ev*) masses and mass flows. Subscripts identify incoming mass from upstream control volumes (*in*) outcoming mass (*out*), rivulet and droplets originating from the present control volume (*start*). From a large campaign of high fidelity results we derive a statistical distribution of droplet radii, in terms of number of droplets of radius *r* per unit surface N'''_{ds}

$$N'''_{ds} = f(r_{max}, r) \tag{4}$$

In the coalescence regime, eq.(4) assumes the well-known shape of the Rose correlation. Then, we check for the value of r_{max} required to accommodate the water mass per unit surface.

$$m" = \int_{r_0}^{r_{max}} \rho V_d(\vartheta, r) N'''_{ds}(r, r_{max}) dr = \frac{\pi}{3}(1-cos\vartheta)^2(2+cos\vartheta)\rho f(r_{max}) \tag{5}$$

$$f = \int_{r_0}^{r_{max}} r^3 N'''_{ds}(r, r_{max}) dr \tag{6}$$

If $r_{max} < r_{move}$ we have still droplet regime, with zero average water velocity, if $r_{max} > r_{move}$ have starting droplets. In the latter case we evaluate moving droplets mass and average velocity from an energy balance involving local shear stress, radius and contact angles as in [4]:

$$u_d = f(\tau, r, \vartheta) \tag{7}$$

$$\dot{m} = \overline{u_d} \int_{r_{move}}^{r_{max}} \rho V_d(\vartheta, r) N"_d(r, r_{move}) dr \tag{8}$$

3. VALIDATION AND RESULTS

High fidelity and statistical, simplified model results are compared with experimental data from [10] in the case of small airfoil, a scaled model of a wind turbine profile (15cm cord). Testing conditions offer freestream air temperature and velocities of -5°C and 40 m/s, liquid water content is 2 grams per m^3 of air, 30μm diameter droplets. The de-icing heater covers 30% of the cord, roughly corresponding to the impinging area. The heat flux is the minimum required to clear the heated area: 3.2 kW/m^2 in the hydrophilic case, 2.7 kW/m^2 in the hydrophobic case. Hydrophilic and hydrophobic advancing/receding contact angles are 105°/50°, 159°/154° respectively.

FIGURE 2. Airfoil high fidelity computational domain within the rectangle, heater covers green area

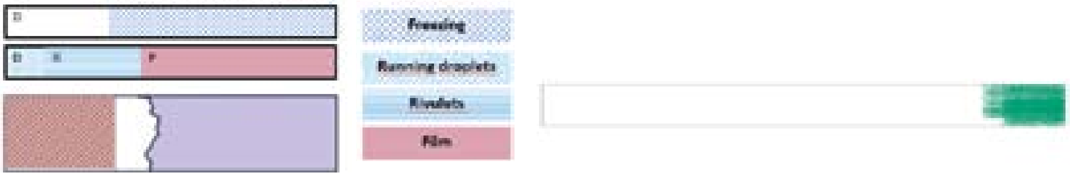

FIGURE 3. Hydrophilic surface: top left trace of frozen beads, middle left, water regimes from simplified model; bottom left, iced area derived from [10]. Right: high fidelity iced bead traces

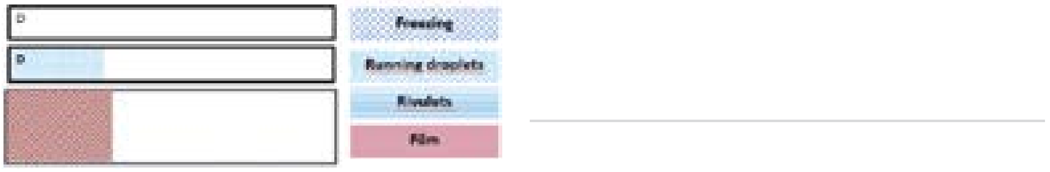

FIGURE 4. Hydrophobic surface: top left trace of frozen beads, middle left, water regimes from simplified model; bottom left, iced area derived from [10]. Right: high fidelity iced bead traces

Experiments show that the hydrophobic surface requires less power and prevents freezing of runback water beyond the impinging area, due to quicker drainage, droplet rebound, efficient evaporation. Numerical computation with the high-fidelity model covers the red zone depicted in Fig.2, the simplified model includes the whole airfoil surface. External shear stress, pressure gradients, and flow fields around the profile come from a CFD solution. The following Figs(3,4) show a view of the upper surface of the airfoil, comparing the numerical results from both models (left, the simplified one, right, the high fidelity) in terms of iced area with the experimental data from [10] reported at the bottom left: purple area is the frozen region, dashed red the heated area. Both the proposed models capture the ice topology (runback water ice on the hydrophilic case, clean hydrophobic surface), which depends on the complexity and variety of different water layer topologies produced by different coatings. Predicted ice boundary in the hydrophilic case is a bit upstream of the experimental data, due to the effect of substrate longitudinal conduction which was not considered.

4. CONCLUSIONS

Both the proposed high-fidelity and statistically simplified models capture the iced region, controlled by the complexity and variety of different water topologies produced by different coatings. As such, the simplified approach may be an effective and efficient tool for integrating wettability effects into the ice accretion prediction over complex geometries.

REFERENCES

[1] B.L. Messinger, Equilibrium Temperature of an Unheated Icing Surface as a Function of Air Speed, *Journal of Aeronautical Sciences*, 29–42, 1953.

[2] Y. Bourgault, H. Beaugendre, W.G. Habashi, Development of a shallow-water icing model in FENSAP-ICE, *Journal of Aircraft*, 37, 640-646, 2000.

[3] Y. Bourgault, Z. Boutanios, W.G. Habashi, Three-dimensional Eulerian approach to droplet impingement simulation using FENSAP-ICE, Part 1: Model, algorithm, and validation, *Journal of Aircraft*, 37, 95-103, 2000.

[4] G. Croce, N. Suzzi, M. Pretto, P. Giannattasio, Numerical Modelling of Droplets and Beads Behavior over Super-Hydrophobic and Hydrophilic Coatings under in-Flight Icing Conditions, *Applied Sciences*, 12, 2022.

[5] P. Attané, F. Girard and V. Morin: An energy balance approach of the dynamics of drop impact on a solid surface, *Physics of Fluids*, 19, 2007.

[6] G. Croce, E. De Candido, W.G. Habashi, J. Munzar, M.S. Aubé, G.S. Baruzzi, C. Aliaga, FENSAP-ICE: Analytical model for spatial and temporal evolution of in-flight icing roughness, *Journal of Aircraft*, 47, 1283-1289, 2010.

[7] N. Suzzi, G. Croce, Numerical simulation of dropwise condensation over hydrophobic surfaces using vapor-diffusion model, *Applied thermal Engineering*, 214, 2022.

[8] F. Wang and X. Cheng: Modeling approach of flowing condensate coverage rate on inclined wall for aerosol wash down, *Nuclear Engineering and Design*, 355, 2019.

[9] M. Sun, W. Kong, F. Wang and H. Liu, Impact freezing modes of supercooled droplets determined by both nucleation and icing evolution, *International Journal of Heat and Mass Transfer*, 142, 2019.

[10] L. Gao, Y. Liu, L. Ma, H. Hu, A hybrid strategy combining minimized leading edge electric-heating and superhydro/ice-phobic surface coating for wind turbine icing mitigation, *Renewable Energy* 140, 943-956, 2019.

Sixth International Conference on Computational Methods for Energy and Thermal Problems
THERMAECOMP2024, Sept. 9-11, 2024, Budva, Montenegro
N. Massarotti, P. Nithiarasu, and I. Vušanović (Eds.)

NUMERICAL ANALYSIS OF PASSIVE COOLING OF PV PANELS USING PCM

Boris Hrnčić, Igor Vušanović
University of Montenegro - Faculty of Mechanical Engineering, Bulevar Džordža Vašingtona bb,
81000 Podgorica, Montenegro, borish@ucg.ac.me, igorvus@ucg.ac.me

ABSTRACT

The efficiency of photovoltaic (PV) panels decreases with increasing temperatures, posing a challenge to their performance in hot regions with high solar irradiance. This study investigates the effectiveness of utilizing Phase Change Materials (PCMs) for passive cooling of PV panels, with case study in the climatic conditions of Podgorica, the capital of Montenegro. Through a numerical simulation spanning one year, the temperature variations of PV panels are analysed, revealing substantial thermal stress during peak solar exposure. To mitigate these effects, a comparative analysis is conducted between scenarios with and without PCM integration. Results demonstrate that incorporating a 1 cm layer of PCM with a melting temperature of 25 degrees Celsius leads to almost 9% increase in total electricity output over the course of a year. Furthermore, economic analysis indicates a promising payback period of approximately 7 years for implementing PCM-based cooling systems, highlighting their potential as a cost-effective solution for enhancing PV panel efficiency in Mediterranean climates.

Key Words: *Passive cooling, PCM, PV panels.*

1. INTRODUCTION

Since the climate crisis is getting worse, many countries in the world are making efforts to put an end to fossil fuel use, one that mainly comes from PV technology and wind farms which are also the strongest technological base for renewable energy production [1]. The number of countries striving for a reduction of greenhouse gas emissions and mitigating the effects of global warming has provoked a substantial growth in PV installations across the globe. Nevertheless, it must be pointed out that PV panels furnish with the efficiency and reliability to the different factors out of which the environmental one represents the most important one. In particular, temperature changes affect them.

One of the mail problems of PV systems is that their efficiency is largely decreased by high temperature environments. In the world, where on hand, there is an upsurge of average temperatures, because of the climate change, there is degradation being exerted on the performance of the PV panels. This issue requires some new and affordable cooling mechanisms to make the panels more productive.

In this case of using different PV technologies including monocrystalline, polycrystalline, and thin-film, the ratio of their average efficiencies varies. The conversion ratio, monocrystalline silicon PV panels, tends to be very high when compared to the rest of the types i.e. 15% to 22%. Thus, they are more preferred for household and commercial applications. Although polycrystalline silicon panels have differences in efficiencies which are usually from 13 to 18 percent, amorphous silicon and cadmium telluride thin-film technologies which are the next technologies behind are 7% to 13%. While these disparities are clearly present, the capacity for PV technologies to suffer performance degradation as temperatures rise should bring out the universal need for breakdown cooling mechanisms toward the achievement of the highest power generation.

2. METHOD

The numerical model employed in this study utilizes a one-dimensional explicit scheme to simulate the temperature distribution within photovoltaic (PV) panels. The model considers the thermal behaviour of PV panels both with and without a layer of Phase Change Material (PCM) on the backside of panel. To simulate the temperature of the panel itself, excluding PCM, the thermal properties of silicon 3 cm thick were used. Thermal properties of PCM are taken for commercially available PCM with a melting temperature of 25 degrees Celsius manufactured by Rubitherm and designated as RT25 HC [2]. Simulations with PCM were performed in cases where the PCM layer has a thickness of 1 cm and 3 cm. The thermal properties of the used PCM are given in Table 1:

Thermal properties	Unit	Value
Main melting temperature	[°C]	25
High melting temperature	[°C]	26
Low melting temperature	[°C]	22
Main congealing temperature	[°C]	25
High congealing temperature	[°C]	26
Low congealing temperature	[°C]	22
Density solid phase	[kg/m^3]	880
Density liquid phase	[kg/m^3]	770
Specific heat capacity (solid and liquid)	[kJ/kgK]	2
Heat conductivity (solid and liquid)	[W/mK]	0.2
Phase change heat	[kJ/kg]	230

TABLE 1. The thermal properties of the PCM

For PV panels without PCM, the heat transfer equation governing the temperature distribution $T(t,x)$ within the panel is given by:

$$\rho c_p \frac{\partial T}{\partial t} = k \frac{\partial^2 T}{\partial x^2}, \tag{1}$$

Where: ρ – density of material [kg/m^3], c_p – specific heat capacity [J/kgK], k – thermal conductivity [W/mK], t – time [s], x - the spatial coordinate along the thickness of the panel [m].

When PCM is present on the backside of the PV panel, the heat transfer equation in PCM layer is modified to account for the latent heat storage/release during phase change. The enthalpy-based approach is utilized, and the heat transfer equation becomes:

$$\frac{\partial h}{\partial t} = \alpha \frac{\partial^2 T}{\partial x^2} \tag{2}$$

Where $h = cT + gL$ represents the mixture enthalpy with included latent heat *(L)* of phase change within the PCM, with liquid fraction of PCM (g), and $\alpha = k/\rho c$ is the thermal conductivity of PCM. To solve the equation, a time step of 0.001 seconds was chosen, which satisfies the stability conditions. The spatial step was chosen to be 0.001 m. Hourly temperature data for Podgorica was used as boundary condition on both sides PV panel with convection coefficient of 15 [W/m^{2}K]. The intensity of solar radiation on the south side at a slope of 35 degrees, was also used as part of boundary condition but only on the side of the panel exposed to the sun. Climate data is taken from Meteonorm software [3].

Based on the value of the temperature of the PV panel, the intensity of solar radiation and the characteristics of the panel, the annual production of electricity was calculated. The power production P was calculated based on following equation:

$$P = V_{oc} \cdot I_{sc} \cdot FF \tag{3}$$

Where V_{oc} stands for open-circut voltage, I_{sc} stands for the short-circuit current and FF for fill factor. All of these values depend on panel characteristics, temperature and solar iridance. Calculations were made in the case of using panels LX-680-700W M132/210 [4].

3. RESULTS

The calculation results showed a significant decrease in the maximum temperatures that the PV panel reaches, as well as an increase in the energy output on a daily and annual basis. In order to see the temperature reduction of the PV panel in the case without PCM and with PCM layers of 1 and 3 cm, July 21 was taken as a reference day. The daily hourly change in panel temperature for July 21 is presented in Figure 1:

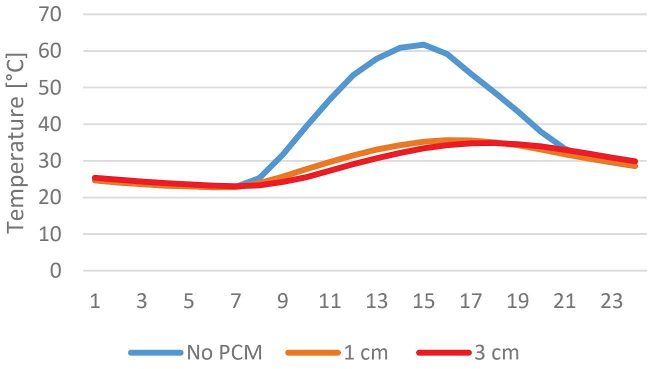

FIGURE 1. Hourly temperature of PV panel for July 21

It can be seen from the Figure 1 that in the case when no PCM is used, the maximum temperature of the panel reaches 62 °C, in the case of a layer of 1 cm PCM temperature is 36 °C, and in the case of a layer thickness of 3 cm temperature is 35 °C. This shows a large difference compared to the case without PCM, but the difference is very small between the cases when a 1 cm layer and a 3 cm layer are used. Hourly power output of PV panel for July 21 is presented in Figure 2:

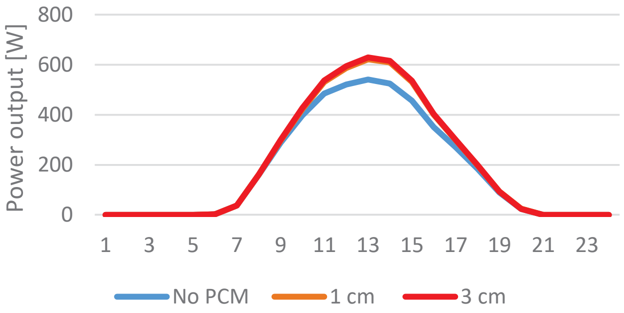

FIGURE 2. Hourly power output of PV panel for July 21

Figure 2 shows a clear difference in panel power output between the cases without and with PCM, but again the difference in the cases between 1 cm and 3 cm is very small.

If we look at the total annual energy production for all three cases, the following results were obtained: 1101 kWh case without PCM, 1200 kWh case with 1 cm PCM and 1220 kWh case with 3 cm PCM. Considering the panel area of 3.1 square meters and the density of PCM material, a layer of 1 cm would weigh about 27.5 kg and with an average price of 2 euros per kg [5], the total investment in PCM per panel would be about 55 euros. With an average selling price of electricity of 8 cents per kWh, the payback period of the investment would be about 7 years. In the case of a 3 cm thick PCM layer, the payback period would be much higher because the total energy produced is not drastically higher compared to the case with a 1 cm thick layer.

4. CONCLUSIONS

The integration of Phase Change Materials (PCMs) presents a promising approach to mitigate the efficiency loss experienced by photovoltaic (PV) panels due to elevated temperatures. This study, conducted in the climatic conditions of Podgorica, Montenegro, highlights the potential of PCM-based passive cooling systems for enhancing PV panel performance.

Through numerical simulations spanning a year, it was observed that PV panels experience significant thermal stress during peak solar exposure. However, the incorporation of a 1 cm layer of PCM with a melting temperature of 25 degrees Celsius led to a notable improvement in total electricity output, with an approximate increase of 9% over the course of a year.

Furthermore, economic analysis revealed a favourable payback period of approximately 7 years for implementing PCM-based cooling systems. Considering the potential increase in energy production and the relatively low cost of PCM materials, PCM integration emerges as a cost-effective solution for enhancing PV panel efficiency, particularly in Mediterranean climates.

REFERENCES

[1] “Pathways for the energy mix – World Energy Outlook 2023 – Analysis - IEA.” https://www.iea.org/reports/world-energy-outlook-2023/pathways-for-the-energy-mix (accessed May 08, 2024).

[2] “Rubitherm GmbH.” https://www.rubitherm.eu/en/productcategory/organische-pcm-rt (accessed Jan. 30, 2024).

[3] Meteotest, “Documents - Meteonorm (en).” https://meteonorm.meteotest.ch/en/meteonorm-documents (accessed Dec. 05, 2020).

[4] “Downloads - LUXOR SOLAR.” https://www.luxor.solar/en/downloads.html (accessed Apr. 30, 2024).

[5] A. Bland, M. Khzouz, T. Statheros, and E. I. Gkanas, “PCMs for residential building applications: A short review focused on disadvantages and proposals for future development,” *Buildings*, vol. 7, no. 3, 2017, doi: 10.3390/buildings7030078.

Sixth International Conference on Computational Methods for Energy and Thermal Problems
THERMAECOMP2024, Sept. 9-11, 2024, Budva, Montenegro
N. Massarotti, P. Nithiarasu, and I. Vušanović (Eds.)

SENSITIVITY STUDY IN SIMULATIONS OF MELTING IN A CYLINDRICAL GEOMETRY

Anthony G. Straatman, Maryam Hemmat, Kyle Teather
Department of Mechanical & Materials Eng., Western University, London, Canada N6A 5B9
agstraat@uwo.ca, mhemmat@uwo.ca, kteather@uwo.ca

ABSTRACT

This study considers the sensitivity of numerical simulations of melting in a truncated cylindrical geometry to the parameters chosen within the enthalpy-porosity model. The study focuses on two main parameters: the mushy zone coefficient, A_{mush}, and the thermal expansion coefficient, β, which is considered as an aggregate adjustable parameter that can be used to control the convective intensity in the melted region. The study shows that using this approach, a model can be calibrated to predict the main features of the melting process and the melting time, which are important for using the model for other heating conditions and enclosure shapes.

Key Words: *Phase change material, Enthalpy-porosity model, numerical simulation.*

1. INTRODUCTION

Understanding the heat transfer during melting and freezing of Phase Change Materials (PCMs) is important for the successful evolution and application of thermal storage systems. Thermal storage systems, also called thermal batteries, can store heat derived from solar or waste heat sources to be later used for water, space and process heating. The use of PCM's in thermal batteries has several advantages; first, PCM's melt and freeze at near constant (liquidus and solidus) temperatures facilitating charging and discharging processes. Second, PCM's consume and discharge large amounts of heat during the melting and freezing processes, respectively, thereby facilitating a high density of energy storage, and third, PCM's come in a variety of compositions that can be tailored to melt/freeze at temperatures suitable for a particular application.

Melting and freezing of PCM's are sophisticated heat transfer processes that require specialized modelling techniques to carry out [1]. Among approaches used, the enthalpy-porosity model has gained popularity and has been used extensively in recent years (see, for example [1-3]). The enthalpy-porosity model tracks liquid and solid regions of a melting PCM using a liquid fraction, f, wherein computational cells containing pure liquid have a value $f = 1$, and cells containing pure solid have a value $f = 0$. Where an interface between liquid and solid PCM exists, a cell can contain both liquid and solid resulting in a value $1 \leq f \leq 0$. In these cells, the mushy zone coefficient is active in that it directly influences a sink term in the fluid momentum equation, having the impact of slowing the melted fluid as if it were in the presence of a wall. The impact of the mushy zone coefficient depends on the value assigned to it, which may be loosely related to the perceived form of the interface, and the "thickness" of the interface, which is dictated largely by the temperature difference between the liquidus and solidus temperatures prescribed in the simulations; i.e. if the liquidus and solidus are prescribed the same temperature, the interface is sharp and the mushy zone coefficient affects the melted fluid in only a narrow band of cells that contain the interface. If a temperature difference is prescirbed between the liquidus and solidus, the interface region thickens and the mushy zone coefficient has a larger influence. The other source term-related parameter that can be used to calibrate the outcome of simulations with experiments is the thermal expansion coefficient, β. Though β is nominally a physical property of the PCM material, its association with the buoyancy term in the momentum equations makes it useful to consider it as more of a control parameter for convective intensity in the melted region. In this study, it is considered an aggregate parameter that accounts for the subtle changes in viscosity and density with temperature that would also influence momentum [4].

The present study investigates the sensitivity of the mushy zone coefficient and thermal expansion parameter on the melt front shape, melting features and melting time for a paraffin-based PCM in a truncated cylindrical enclosure. The results are compared to similar experimental results to show the efficacy of the enthalpy porosity model in these calculations. Of specific interest is the sensitivity of these parameters on the computed outcomes.

2. MAIN BODY

The truncated cylindrical geometric model employed in this study mimics the physical model considered in the experiments of Teather & Siddiqui [5]. The cylindrical PCM cavity shown in Figure 1 is formed using an acrylic shell of 6.35 mm thickness (shown as a thick black line in Figure 1a), with a 70 mm inside diameter, and depth 12.5 mm. The cylinder contains a small air gap at the top to facilitate expansion/contraction of the PCM during the physical experiments and is immersed in a water bath of a fixed temperature during the melting process. The computational analogue of this model is shown in Figure 1b, wherein the air gap is ignored leaving a flat upper surface of PCM. The properties of the PCM considered are given in Table 1.

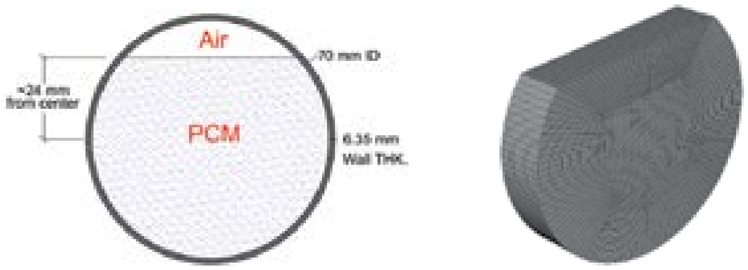

a- Physical geometry b- Computational mesh

FIGURE 1. Computational model of truncated cylinder under consideration.

TABLE 1: Thermophysical properties of Rubitherm RT26.

Property	Typical Value	Unit
Melting Temperature	298 - 299	[K]
Congealing Temperature	299 - 298	[K]
Heat Storage Capacity* ± 7.5%	180	[kJ/kg]
Specific Heat Capacity	2000	[J/kg/K]
Density Solid	880	[Kg/m^3]
Density Liquid	750	[Kg/m^3]
Heat Conductivity	0.2	[W/m/K]

* Combination of latent and sensible heat in a temperature range of 19ºC to 34ºC

Simulations were conducted using the enthalpy-porosity model available in the commercial software ANSYS Fluent 2022 R1. The front and back faces of the model in Figure 1b were considered adiabatic walls, the flat upper surface as a slip surface with a convection condition (convection coefficient h= 6.2 W/m^2/K [6]), and the outer acrylic cylinder shell as an isothermal wall of constant temperature 306.05 K to mimic the lowest temperature condition considered in [5]. The acrylic shell separating the constant-temperature water bath from the PCM was modelled as a thin shell with specific heat C_P= 1470 J/kg/K, conductivity k= 0.2 W/mK and density ρ = 1190 kg/m^3 [6]. The mesh shown in Figure 1 has 59,900 hexahedral cells and is grid-independent to within 0.76% in terms of overall melting time. The transient simulations were conducted using the SIMPLE algorithm with second-order upwinding and a fixed time step size of 1s. Other details are available in [6].

3. RESULTS

Figure 2a shows the impact of the mushy zone coefficient on liquid fraction variation during the melting process with a constant thermal expansion coefficient $\beta = 0.0005$ K^{-1}. Initially, the mushy zone coefficient has a minor effect due to sensible heat transfer dominance, but after approximately 2500 seconds, higher coefficient values are observed to hasten melting, which highlights the inverse correlation between the mushy zone coefficient and convective intensity. Figure 2b shows the impact of the thermal expansion coefficient on liquid fraction during the melting process with a constant mushy zone coefficient $A_{mush} = 10^5$. Here, it is evident that higher values result in more intense convection, leading to a higher liquid fraction and reduced overall melting time.

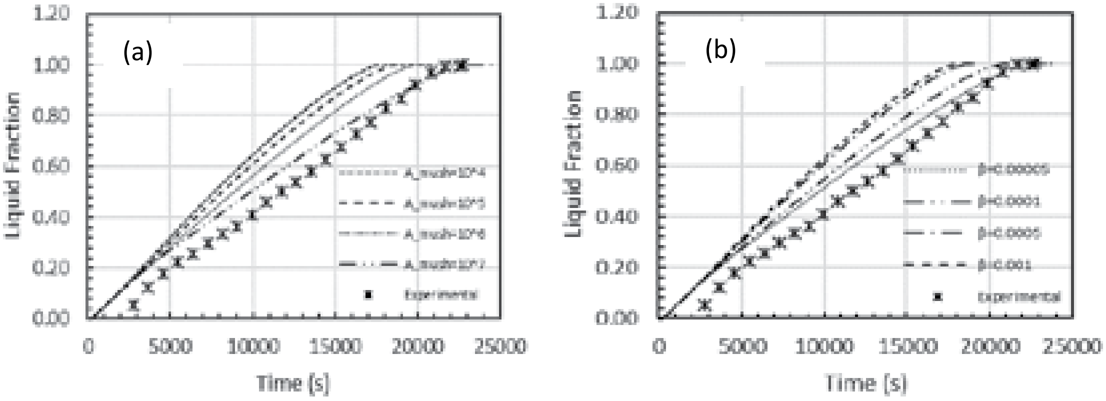

FIGURE 2. The influence of mushy zone coefficient (a) and thermal expansion coefficient (b) on the total melting process of RT26 in the truncated cylinder with an initial temperature Ti= 296 K exposed to a constant water bath temperature T= 306.5 K.

From the plots in Figure 2, it is tempting to select the highest A_{mush} and the lowest β to coincide with the experiments, but closer scrutiny of the flow patterns and melt shape suggest that an ideal combination of parameters leads to a result that better mimics the heat transfer process, while preserving the approximate melting time. Figure 3 shows images of the melt shape and flow patterns for several different times in the melt process compared to the experimental results of [5]. The "calibrated" model has $A_{mush} = 10^6$, $\beta = 0.0001$ K^{-1} and with solidus and liquidus temperatures of 298 and 299 K, respectively. To be consistent with the experiments [5], the plots are compared at dimensionless times derived as: $\tau + = (t - t_{start})/(t_{end} - t_{start})$, where t is time and t_{start}/t_{end} are the times at the start/end of the melting process. Figure 3 shows that as the melting process progresses, a pair of robust symmetric counter-rotating vortices emerge along the cavity's walls, driven by the combined effects of buoyancy-driven fluid motion. The heated wall induces upward fluid movement near its surface, while along the solid-liquid interface, cooling occurs as heat transfers to the solid, causing the denser liquid to descend along the solid resulting in the generation of vortices on both sides of the solid mass. These features of the melting process are important to capture and enable the calibrated model to perform well at other heating conditions.

4. CONCLUSIONS

A sensitivity study on the mushy zone coefficient and the thermal expansion coefficient, herein considered a convective intensity parameter, within the scope of the enthalpy-porosity model shows

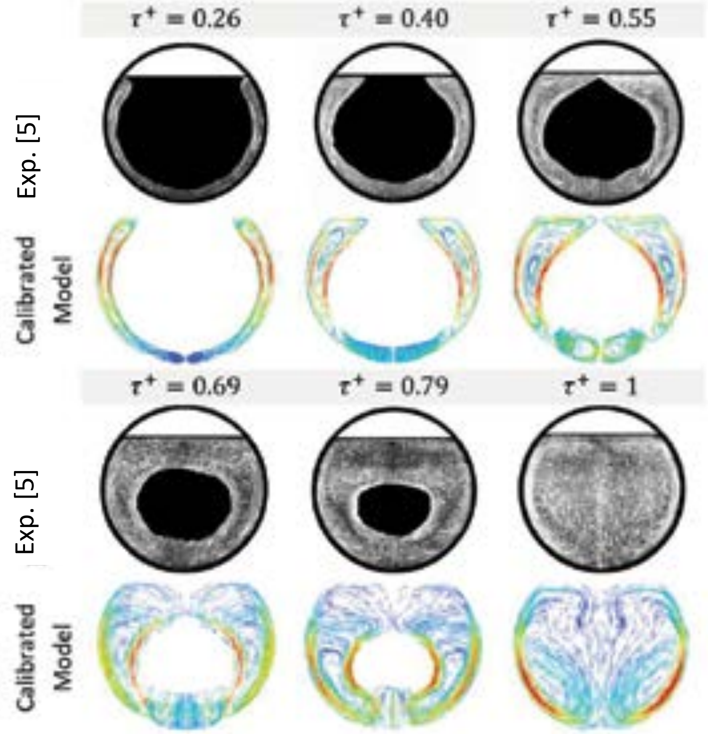

FIGURE 3. The Illustrations of calibrated model predictions and experimental liquid flow patterns in the melting process: the numerical results employ a refined localized color scale to illustrate the entire range of motions, with a specific focus on highlighting convective structures.

that a suitable combination produces a calibrated model that captures the main features of the melting process. Additional computations (not provided) show that the calibrated model commutes well to other heating conditions and to other shaped enclosures containing the same PCM material.

REFERENCES

[1] V. R. Voller and C. Prakash, A fixed grid numerical modelling methodology for convection-diffusion mushy region phase-change problems, *Int. J. Heat Mass Trans.* 30, 1709–1719, 1987.

[2] H. Sattari, A. Mohebbi, M. M. Afsahi, and A. Azimi Yancheshme, CFD simulation of melting process of phase change materials (PCMs) in a spherical capsule, *Int. J. Refrig*. 73, 209–218, 2017.

[3] D. Ghosh and C. Guha, Numerical and experimental investigation of paraffin wax melting in spherical cavity, *Int. J. Heat Mass Trans*. 55, 1427–1437, 2019.

[4] C. Jaffray, K. Siddiqui and A. G. Straatman, An efficient method for modelling thermal energy storage in packed beds of spherically encapsulated phase change material, *J. Energy Storage*, 81, 110462, 2024.

[5] K. Teather and K. Siddiqui, An Experimental Investigation of Constrained Melting of a Phase Change Material (PCM) in Circular Geometries, Part I: Velocity Characterization, *J. Energy Storage* 86 (part A), 111516, 2024.

[6] M. Hemmat, An investigation into modelling of melting and solidification of phase change materials, M.E.Sc. Thesis, Western University, London, Canada, 2023.

Sixth International Conference on Computational Methods for Energy and Thermal Problems
THERMAECOMP2024, Sept. 9-11, 2024, Budva, Montenegro
N. Massarotti, P. Nithiarasu, and I. Vušanović (Eds.)

OPTIMIZATION OF COLBURN AND FANNING FRICTION FACTORS IN AN OFFSET STRIP PLATE-FIN HEAT EXCHANGER USING GENETIC ALGORITHM

Vinay Pratap Singh Negi, Sarvesh Khandelwal, Chennu Ranganayakulu
Department of Mechanical Engineering, Birla Institute of Technology and Science Pilani, Pilani Campus, Rajasthan, 333031, India. Email: p20210456@pilani.bits-pilani.ac.in, f20201990@pilani.bits-pilani.ac.in c.ranganayakulu@pilani.bits-pilani.ac.in

ABSTRACT

Among the most efficient and thermally effective heat exchangers are plate fin compact heat exchangers (PFCHEs), which are highly compact and possess a greater surface area density. This study aims to optimize the Colburn *'j'* factor and Fanning friction factor *'f'* for compact heat exchangers with offset strip fins (OSFs) utilizing Genetic algorithm (GA), which represent heat transfer and pressure drop performance, respectively. The MATLAB code provides multi-objective optimization algorithm designed to determine the optimal design parameters for a plate-fin heat exchanger using the NSGA-II (non-dominated sorting genetic algorithm-II). Five design variables define the heat exchanger's characteristics: fin height *(h)*, fin length *(l)*, fin spacing *(s)*, fin thickness *(t)*, and Reynolds number *(Re)*. Colburn *'j'* factor provides heat transfer coefficient, whereas Fanning friction factor *'f'* will be used to calculate fin pressure drop. The accuracy of models can be determined by their ability to predict data points consistently by calculating mean square error (MSE). Both objective functions have demonstrated strong performance in fitting and predicting the two variables, with R-squared values of over 97% for Colburn *'j'* factor and 94% for Fanning friction factor *'f'* respectively.

Key Words: *Colburn 'j' factor, Compact heat exchanger, Fanning friction factor 'f', Genetic algorithm, Heat Transfer, NASGA-II, Plate-fin heat exchanger.*

1. INTRODUCTION

Energy efficiency has become a critical concern in recent times, mainly because of the substantial increase in energy demands. As a result, numerous industrial facilities and businesses must comply with government emission regulations, which can be fulfilled by utilizing energy-efficient equipment. High-performance compact heat exchangers (CHEs) are crucial in the aerospace industry for improving heat transfer rates, as these applications typically have strict weight and space limitations. There are several types of fins surfaces have been developed for CHEs in different applications such as simple fins, offset strip fins (OSFs), louvered fins, and wavy fins. OSFs, louvered fins, and wavy fins are commonly utilized as heat transfer surfaces in various systems [1]. These fins work by creating interrupted channels that lead to the initiation and development of laminar boundary layers. Consequently, the surface compactness is high, and there is a significant enhancement in heat transfer. The dissipation of these boundary layers takes place in the fin wakes. Plate-fin compact heat exchangers (PFCHEs) are widely utilized in several industries, such as aerospace, electronics, automobile, power machinery, and chemical engineering, due to their small size and light weight design. For an example the primary objective of the environmental control system (ECS) in commercial aircraft is to deliver a specific quantity of clean air at a designated pressure and temperature. This is done to ensure that the cabin maintains conditions that guarantee the comfort of passengers and crew. PFCHEs are the main components of the ECS which fulfil the requirement of cabin cooling by removing the heat of the hot air as shown in Figure 1.

Researchers have conducted numerous experimental and numerical studies on PFCHEs, including different plate-fin geometries. Kays and London [2] studied various plate-fin geometries and determined the Colburn *'j'* and Fanning friction *'f'* factors. In this study, an OSFs for optimization by utilizing *'j'* and *'f'* factors with those reported by Chennu & Paturu [3] and Liu et al. [4]. The MATLAB code provides multi-objective optimization algorithm designed to determine the optimal design parameters for a PFCHE using the NSGA-II (non-dominated sorting genetic algorithm-II). The Reynolds numbers in the laminar zone ranged from 300 to 800, while in the turbulent region, ranged from 1000 to 15000. The investigation was conducted in both regions.

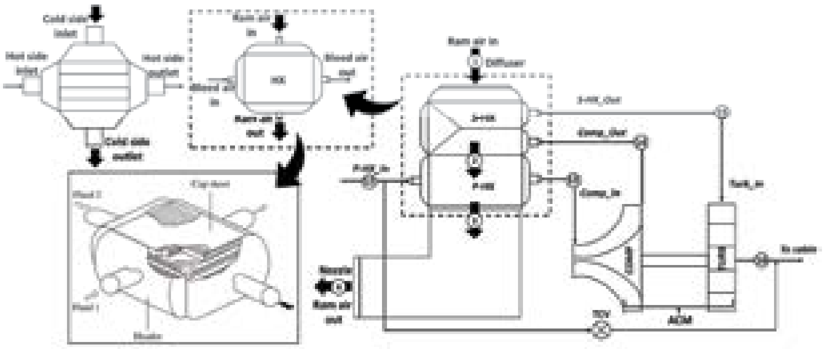

FIGURE 1. PFCHEs arrangements in aircraft ECS

2. MAIN BODY

As depicted in Figure 2, the geometric attributes of the three-dimensional OSFs flow channel are determined by the following parameters: fin height *(h)*, fin spacing *(s)*, fin thickness *(t)*, and offset strip length *(l)*. The flow cross-section aspect ratios, $\alpha = s/h$, $\gamma = t/s$, and, $\delta = t/l$ provide dimensionless representations of these variables. The primary requirements for optimizing the PFCHEs are adequate heat dissipation capacity and minimal flow resistance. The Colburn *'j'* factor measures the enhancement of heat transfer efficiency, while the Fanning friction factor *'f'* indicates smooth flow with minimal resistance in the channel. As a result, optimizing the Colburn *'j'* factor and Fanning friction factor *'f'* were approached as a multi-objective optimization problem due to the conflicting objectives involved.

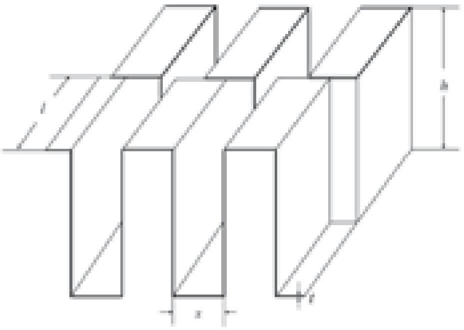

FIGURE 2. OSFs dimensional description

The correlations for Colburn *'j'* factor and Fanning friction factor *'f'* obtained from the CFD analysis for both laminar and turbulent regions are given below [3], design parameters from the input vector *'x'*.

For laminar region (300 ≤ Re ≤ 800)

$$j = 0.661(Re)^{-0.651}(s/h)^{-0.343}(t/s)^{-0.538}(t/l)^{0.305} \tag{1}$$

$$f = 10.882(Re)^{-0.79}(s/h)^{-0.359}(t/s)^{-0.187}(t/l)^{0.284} \tag{2}$$

For turbulent region (1000 ≤ Re ≤ 15000)

$$j = 0.185(Re)^{-0.396}(s/h)^{-0.178}(t/s)^{-0.403}(t/l)^{0.29} \tag{3}$$

$$f = 2.237(Re)^{-0.236}(s/h)^{-0.347}(t/s)^{-0.151}(t/l)^{0.639} \tag{4}$$

Therefore, the optimization of the Colburn factor *'j'* and Fanning friction factor *'f'* were treated as a multi-objective optimization problem due to the presence of two conflicting objectives. The design took into account of OSFs height *(h)*, length *(l)*, spacing *(s)*, thickness *(t)*, and Reynolds number *(Re)*. With the Colburn factor *'j'* and the Fanning friction factor *'f'* in mind, we can develop the desired objective function.

$$\mathrm{F}(x) = \mathrm{F}(x_1, x_2, x_3, x_4, x_5) = \mathrm{F}(h,\ l,\ s,\ t,\ Re) \tag{5}$$

The constraint handling of design parameter variables was created based on the parameter range of heat transfer performance given in Table 1.

	h	*l*	*s*	*t*	*Re*
Lower bound	5	3	1	0.15	300
Upper bound	10	6	2	0.3	15000

TABLE 1. Constraint handling design parameters of lower and upper bound

The following goal functions were selected for optimization: the highest Colburn factor and the lowest Fanning friction factor given in Equations (6) and (7). This objective function seeks to minimize the negative Colburn factor and friction factor for a specified design parameter set and Reynolds number. This feature is critical for assessing how well various optimization settings for the PFCHE work, as it directs the search for the best possible solutions using the NSGA-II details are given in Table 2.

$$\max j\,(x_i) = \max \mathrm{F}(h, l, s, t, Re) \tag{6}$$

$$\min f(x_i) = \min \mathrm{F}(h, l, s, t, Re) \tag{7}$$

Population size	Evolution generation	Crossover probability	Pareto fraction	Plot function
1000	30	0.99	0.35	@gaplotpareto

TABLE 2. Parameters of NSGA-II

The provided Colburn *'j'* Factor and Fanning friction *'f'* factor functions are crucial parts of the PFCHEs optimization process. The Colburn *'j'* factor function utilizes a non-linear extrapolation technique between Reynolds numbers 800 and 1000 to determine the appropriate Colburn factor based on quadratic extrapolation coefficients derived from known values at those specific Reynolds numbers. For Reynolds numbers outside that range, it calculates Colburn *'j'* factor using the provided formula. Similarly, the Fanning friction factor *'f'* function employs a similar non-linear extrapolation approach for Reynolds numbers between 800 and 1000.

3. RESULTS

The use of this method leads to the multi-objective optimization of the original OSF-PFCHE, as evidenced by the optimized geometric parameters displayed in Table 3, which illustrates the contrast between the original and optimized models. The graph in Figure 3 depicts a clear decline in the *j/f* ratio as the Reynolds number increases. This reduction is linear until the Reynolds number reaches 700, at which point the scattering of points becomes more widespread. As flow rates increase, the *j/f* ratio becomes less predictable, which is indicative of the heat transfer performance and fluid friction characteristics of the system. The Pareto front graphic in multi-objective optimization illustrates the trade-off between the *'j'* factor (heat transfer efficiency) and the *'f'* factor (pressure loss). The curve suggests that enhancing heat transfer efficiency often leads to increased pressure loss in heat exchanger design modifications.

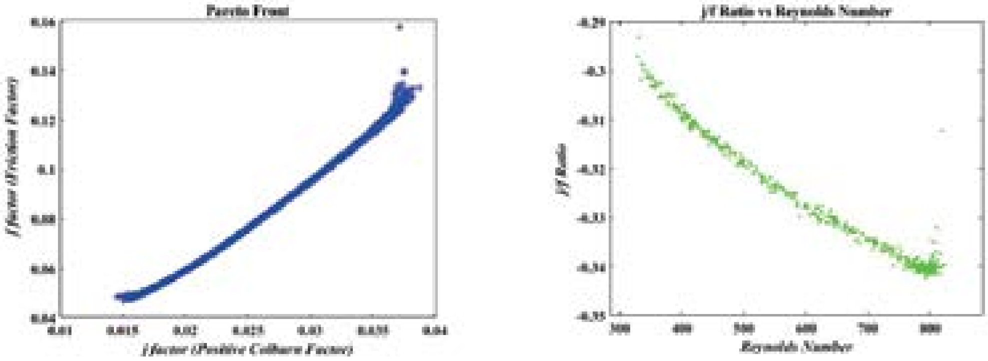

(a) (b)

FIGURE 3. Optimized results: (a) Friction factor vs. Colburn factor; (b) *j/f* ratio vs. Reynolds Number

The accuracy of models is evident from the low mean square error (MSE) values, which suggest that they can accurately predict the data points. Both objective functions have demonstrated strong performance in fitting and predicting the two variables, with R-squared values of over 97% for Colburn *'j'* factor and 94% for Fanning friction factor *'f'* respectively.

h	l	s	t	Re
9.67	3.63	1.95	0.157	336
5.48	5.50	1.81	0.163	806

TABLE 3. Geometric parameters of optimization model

4. CONCLUSIONS

The optimization technique effectively balances performance attributes by discovering ideal heat exchanger topologies, as shown by the fluctuation in design parameters. Machine learning models effectively predict outcomes, making them suitable for use as surrogate models in optimization processes. The MATLAB code employs the NSGA-II algorithm to improve the design parameters of an OSF-PFCHE for multiple objective optimizations. The algorithm effectively balances two objectives: optimizing heat transfer efficiency (as measured by the Colburn factor) and minimizing pressure drop (as gauged by the Fanning friction factor). The performance of the objectives is assessed using design parameters and the Reynolds number.

REFERENCES

[1] R. Chennu, "Numerical analysis of compact plate-fin heat exchangers for aerospace applications," *Int J Numer Methods Heat Fluid Flow*, vol. 28, no. 2, pp. 395–412, 2018, doi: 10.1108/hff-08-2016-0313.

[2] W. M. Kays and A. L. London, "Compact heat exchangers," 1984.

[3] R. Chennu and P. Paturu, "Development of heat transfer coefficient and friction factor correlations for offset fins using CFD," *Int J Numer Methods Heat Fluid Flow*, vol. 21, no. 8, pp. 935–951, 2011, doi: 10.1108/09615531111177732.

[4] C. Liu, W. Bu, and D. Xu, "Multi-objective shape optimization of a plate-fin heat exchanger using CFD and multi-objective genetic algorithm," *Int J Heat Mass Transf*, vol. 111, pp. 65–82, 2017, doi: 10.1016/j.ijheatmasstransfer.2017.03.066.

Sixth International Conference on Computational Methods for Energy and Thermal Problems
ThermaEComp2024, Sept. 9-11, 2024, Budva, Montenegro
N. Massarotti, P. Nithiarasu, and I. Vušanović (Eds.)

A POROUS-MEDIUM APPROACH FOR THE THERMAL ANALYSIS OF MICROCHANNEL HEAT SINKS

Nonino Carlo, Savino Stefano
Università degli Studi di Udine, DPIA,
Via delle Scienze 206, 33100 Udine, Italy
carlo.nonino@uniud.it, stefano.savino@uniud.it

ABSTRACT

This paper presents an original method for using the commercial code Ansys Fluent for the thermal analysis of microchannel heat sinks based on the porous-medium approach and the local thermal non-equilibrium model. What is new is how heat transfer at the solid porous matrix boundaries is accounted for, because with the original code those boundaries can only be treated as adiabatic. The sample application concerns a double-layered cross-flow microchannel heat sink.

Key Words: *Microchannels, Heat sinks, Porous-medium.*

1. INTRODUCTION

CFD has been and still is essential for the optimization of liquid-cooled microchannel heat sinks. However, in the past most numerical simulations have been conducted for the case of micro heat sinks with one or two layers of channels all parallel to each other. This allowed exploiting existing symmetries to make reference to very simplified geometries consisting of a single half-channel or two stacked half-channels. Consequently, more complex heat sink geometries comprising all microchannels and/or manifolds have rarely been studied because their domain discretization requires a very large number of cells, thus resulting in prohibitive computational efforts.

Alternatively, the thermal analysis of an entire microchannel heat sink can be carried out in an approximate way using an approach where an entire layer of microchannels is treated as a porous medium characterized by empirically determined properties so that the same thermal behavior can be achieved. The validity of this approach has been demonstrated in the past, especially when combined with the local thermal non-equilibrium (LTNE) method. This type of analysis can be conducted using commercial software that offers the LTNE option. However, one of the most popular of these codes (Ansys Fluent) cannot be used for this purpose because, while featuring the LTNE model, it does not allow for taking into account the heat transfer between the solid porous matrix and the adjacent solid parts of the domain [2].

In this paper, an original method is presented to circumvent the problem and allow the use of the porous medium approach combined with the LTNE model of Ansys Fluent. The method is then validated by comparing results obtained in the case of a double-layered cross-flow microchannel heat sink studied using the porous medium approach with those obtained from the detailed thermal analysis performed with an in-house finite element (FEM) code for a case with 50 microchannels per layer.

2. HIGHLIGHTS OF THE NUMERICAL PROCEDURE

According to the porous medium model with LTNE, two thermal energy equations are solved, one for the fluid and one for the solid medium. These two equations are coupled by a source/sink term that appears in both of them but with opposite signs

$$S_{\mathrm{LNTE}} = \pm\, h_{\mathrm{fs}} A_{\mathrm{fs}} (T_{\mathrm{f}} - T_{\mathrm{s}})$$

where h_{fs} is the heat transfer coefficient for the solid/fluid interface, A_{fs} is the interfacial area density, and T_f and T_s are the temperatures of the fluid and the solid medium, respectively [1].

Since with Ansys Fluent a porous solid zone can only exchange heat with the fluid through the term S_{LNTE} and not with its surroundings, the proposed method to circumvent the problem exploits one row (in 2D) or one layer (in 3D) of cells of the porous solid-fluid part of the discretized domain in contact with the solid region to somehow short-circuit the fluid itself and allow indirect heat transfer between the boundaries and the solid porous medium. A very high value of h_{fs} (order of 10^8 W/m^{2}K) and a thermal conductivity of the liquid equal to that of the solid are specified in this very thin layer (less than 1% of the channel height) to allow heat transfer through the boundaries of the solid porous matrix with a negligible interface resistance. In addition, a very high value is also assigned to the viscosity of the fluid in the thin layer so that the velocity field vanishes, and the solid-fluid layer virtually behaves as if it were completely solid.

The value of h_{fs} in the remaining part of the fluid domain is assumed to vary with the axial coordinate, decreasing exponentially to account for the entrance effect. The coefficients of the exponential expression are a function of velocity and were determined empirically based on comparisons of results of 3D simulations for a single microchannel of the heat sink and those of calibration tests of a 2D porous-medium model. As for the solution of the momentum equations, the superficial velocity porous formulation is used where the porous medium is modeled by the addition to the Navier-Stokes equations of a source term that includes the contributions of viscous and inertial losses. This formulation is the default in Ansys Fluent and is not described here [1].

3. VERIFICATION

The verification tests were conducted with reference to the thermal analysis of a double-layered cross-flow microchannel heat sink such as the one shown in Figure 1(a), comprising 50 microchannels in each layer, with footprint dimensions of 10 × 10 mm^2. The heat flux applied to the base is 100 W/m^2, while the top is adiabatic. The height and width of each microchannel are 0.5 mm and 0.1 mm, respectively, whereas the thickness of all solid walls is 0.1 mm as well; the equivalent porosity is equal to 0.5. The solid material is silicon, and the fluid is water. Three values of the average microchannel velocity are considered, namely, 0.5 m/s, 1.0 m/s, and 2.0 m/s, all corresponding to laminar flow conditions [2]. Figure 1(b) shows the three-dimensional domain used for the simulations based on the porous-medium approach. The computational domain corresponding to one-half (given the existing symmetries) of a microchannel of one layer used for the simulations required for the calibration of the porous model is shown in Figure 1(c), while the two-dimensional partly porous domain corresponding to the microchannel in Figure 1(c) is depicted in Figure 1(d). A reliable in-house FEM code [2] was used for the detailed simulations concerning the domain illustrated in Figure 1(a), which yielded the reference results, while Ansys Fluent was employed for all the other calculations. The hexahedral or rectangular grids used for discretization of the computational domains consist of 22,100,000 elements for the one shown in Figure 1(a), 1,060,000 for that in Figure 1(b), 57,000 for that in Figure 1(c), and 5,200 for that in Figure 1(d).

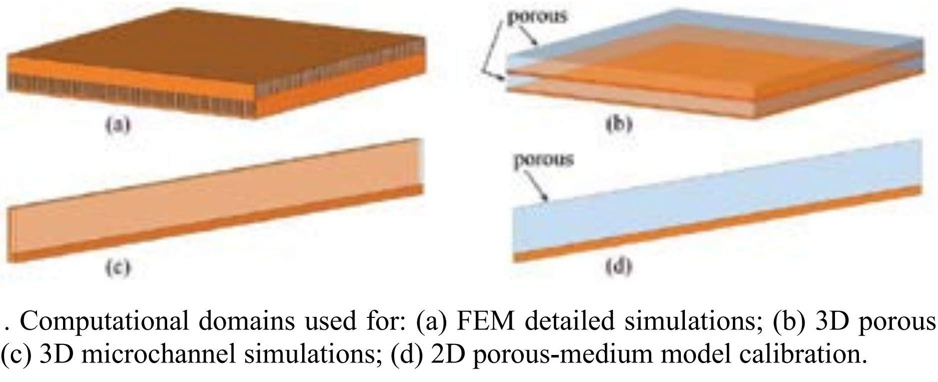

FIGURE 1. Computational domains used for: (a) FEM detailed simulations; (b) 3D porous-medium solution; (c) 3D microchannel simulations; (d) 2D porous-medium model calibration.

The porous medium parameters were determined by trial and error based on the comparison of the results obtained from the 3D simulations concerning a single microchannel (see Figure 1(c)) and the 2D solutions obtained using the domain of Figure 1(d). The values thus obtained were used to compute the solutions based on the porous medium approach with the domain of Figure 1(b), to be compared with the reference FEM solutions relative to the domain of Figure 1(a).

A qualitative comparison between the solutions obtained with the proposed procedure and the reference FEM solutions can be made based on Figure 2 and Figure 3 where temperature maps on the heated base surface and the mid-plain of the solid layer between the two layers of microchannel are shown. Dark grey and light grey arrows indicate the directions of flow in the lower and upper microchannel layers, respectively. Quantitative comparisons can instead be made based on the data shown in Table 1 concerning the average outlet bulk temperature values in the two microchannel

		Lower L.	Upper L.	Heated base		Mid-plane	
Method	V [m/s]	T_{bulk} [K]	T_{bulk} [K]	$T_{\min}$ [K]	$T_{\max}$ [K]	$T_{\min}$ [K]	$T_{\max}$ [K]
FEM [2]	0.5	311.40	307.89	307.57	321.07	302.58	315.30
Present		311.37	307.86	307.61	320.62	302.84	314.90
FEM [2]	1.0	306.06	303.64	306.60	314.80	301.88	309.15
Present		306.01	303.62	306.45	314.55	301.98	308.96
FEM [2]	2.0	303.20	301.67	305.77	311.68	301.33	306.19
Present		303.15	301.67	305.39	311.54	301.28	306.13

TABLE 1. Comparisons of average outlet bulk temperatures T_{bulk} and minimum and maximum temperatures $T_{\min}$ and $T_{\max}$ on different surfaces and for different velocities V.

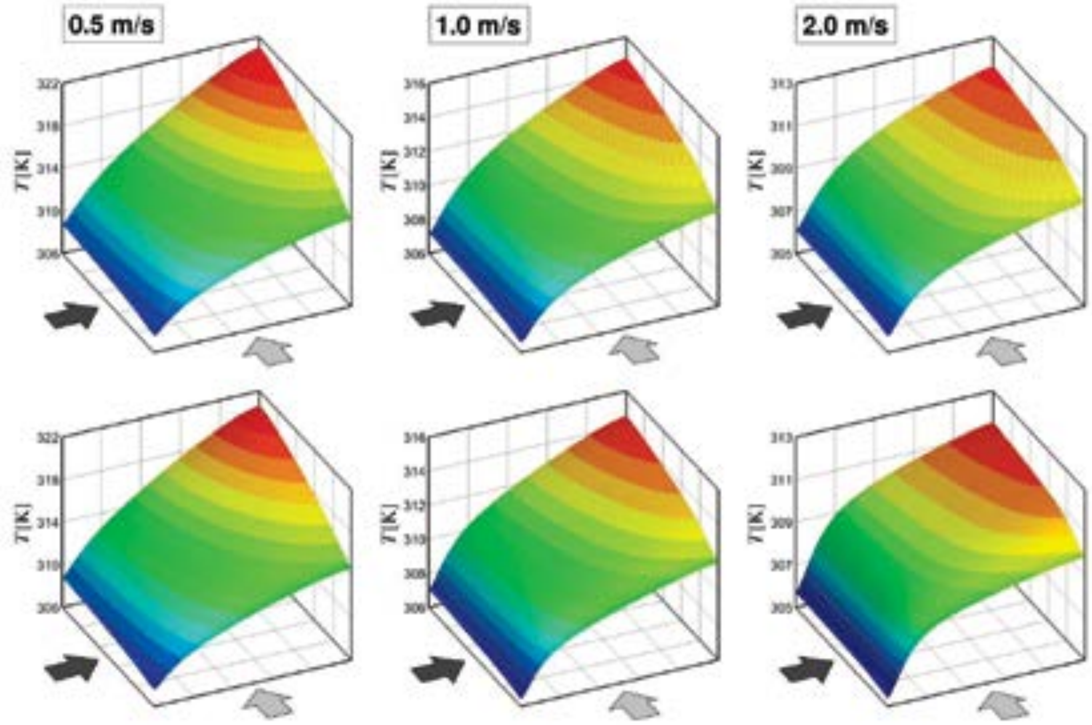

FIGURE 2. Heated base temperature distributions for different average microchannel velocities (top: FEM detailed analysis; bottom: LTNE porous-medium approach).

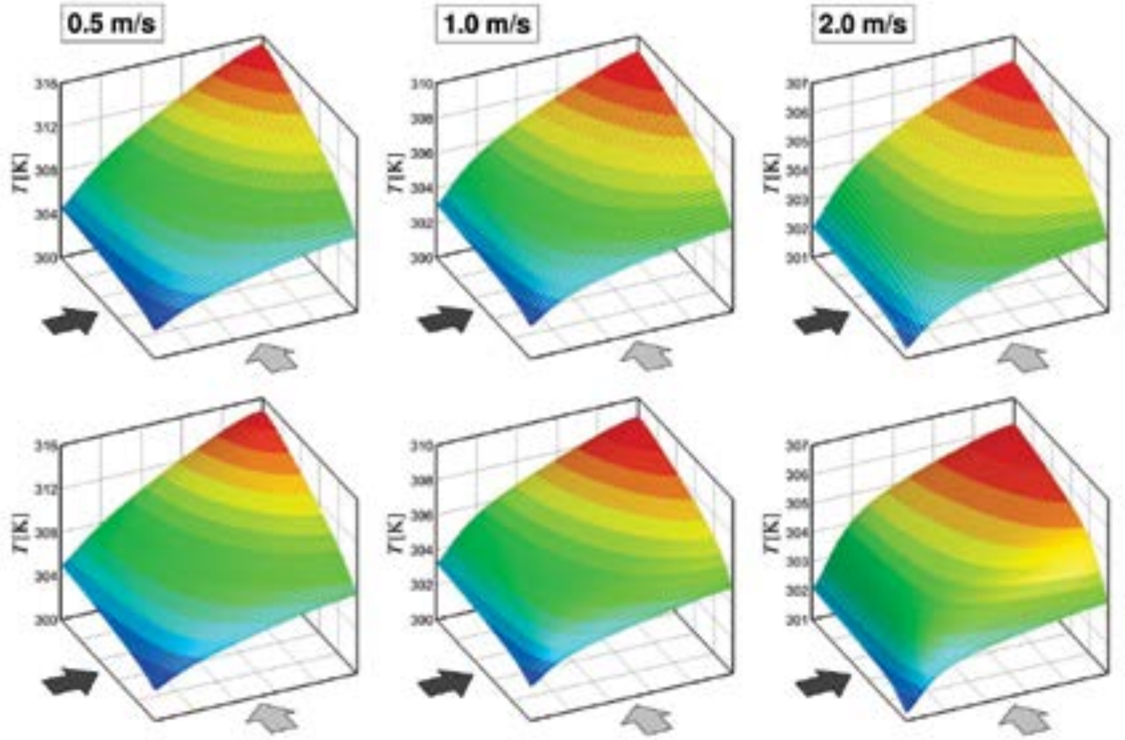

FIGURE 3. Mid-plane temperature distributions for different average microchannel velocities (top: FEM detailed analysis; bottom: LTNE porous-medium approach).

layers and the minimum and maximum temperature values on the heated base surface and the mid-plane of the solid layer between the two layers of microchannels. The good agreement of both qualitative and quantitative comparisons demonstrates the validity of the proposed method for the thermal analysis of liquid-cooled microchannel heat sinks with a reduced computational effort.

4. CONCLUSIONS

A method based on the porous-medium approach and local thermal non-equilibrium was presented for using the commercial software Ansys Fluent for thermal analysis of microchannel heat sinks. The comparison of the results obtained with those given by a detailed analysis of a double-layered cross-flow microchannel heat sink conducted employing a previously developed FEM procedure was used to verify the method. The good agreement between the results demonstrates the reliability of the proposed procedure which can then be used confidently for the thermal performance analysis of micro heat sinks with complex geometries with substantial savings in the computational effort.

REFERENCES

[1] Ansys, Inc., *Ansys Fluent User's Guide, Release 2023/R2*, 2023.

[2] C. Nonino and S. Savino, Temperature uniformity in cross-flow double-layered microchannel heat sinks, *Fluids*, 5, 143, 2020. doi:10.3390/fluids5030143

Sixth International Conference on Computational Methods for Energy and Thermal Problems
THERMAECOMP2024, Sept. 9-11, 2024, Budva, Montenegro
N. Massarotti, P. Nithiarasu, and I. Vušanović (Eds.)

CFD INVESTIGATION OF HEAT AND MASS TRANSPORT IN SOLID OXIDE FUEL CELLS

Giorgio Grossi, Fausto Arpino, Christian Canale, Gino Cortellessa, Giorgio Ficco
Department of Civil and Mechanical Engineering, University of Cassino and Southern Lazio, Via G. Di Biasio 43, Cassino, 03043, FR, Italy. E-mail address: giorgio.grossi@unicas.it

Reza Hamidi Jahromi
Department of Engineering, University of Naples "Parthenope", Centro Direzionale, Isola C4, 80143 Naples, Italy

Davide Pumiglia
ENEA Department of Energy Technologies and Renewable Sources; Laboratory of Energy Storage, Batteries and Hydrogen Production & Use Technologies (TERIN-PSU-ABI), Research Centre Casaccia; Rome, Italy

ABSTRACT

This study conducts 3D numerical simulations to examine the complex multi-physics phenomena in an anode-supported planar solid oxide fuel cells (SOFCs), using the open-source OpenFOAM toolbox. The numerical model, validated against data from the scientific literature, is employed to evaluate the temperature gradient within the solid regions of the cell under different operating conditions. A single-unit model in a counter-flow configuration is considered for the investigations. Results indicate that the operating temperature has a minimal effect on the distribution of temperature gradients, with the maximum gradient occurring at the cathode inlet section. This work represents the first stage of a larger research project aimed at investigating, both numerically and experimentally, the effects of various factors on the performance of anode-supported SOFCs, including the presence of contaminants and their impact on material aging.

Key Words: *Computational Fluid Dynamics (CFD), Fuel Cells, Validation, Heat Transfer.*

1. INTRODUCTION

Green hydrogen plays a crucial role in the transition to renewable energy sources due to its versatility and compatibility with clean energy technologies such as fuel cells and electrolysers. These devices are promising replacements for traditional fossil fuel-based technologies but require detailed investigation of mass and energy transport phenomena and electrochemical processes for optimization. Numerical simulations, particularly using Computational Fluid Dynamics (CFD), provide a detailed description of these phenomena, which are challenging and costly to study experimentally. Solid Oxide Fuel Cells (SOFCs) are particularly attractive due to their high operating temperatures, which allow the use of less expensive catalysts, enable the processing of various fuels, and offer cogeneration possibilities, making them suitable for stationary applications. Despite advancements, SOFCs still face reliability issues and high production and operating costs.

Building on previous research activities [1–3], this study uses CFD simulations to investigate a single-unit model of an anode-supported planar SOFC using the open-source OpenFOAM toolbox. The numerical model is validated with existing data and then used to evaluate the temperature gradient within the cell under different operating conditions. In fact, being it strictly related to thermal stresses, temperature gradient can significantly affect cell performance in terms of stability and lifetime [4,5]. This research is the first stage of a broader project aimed at studying the effects of various factors on SOFC performance, including contaminants and material aging.

2. METHODOLOGY

Numerical simulations are conducted using the *openFuelCell2* tool, developed by Zhang et al. [6].
Mass, momentum, energy and species conservation equations are solved for anode and cathode parts, considering porous electrodes and including a source term for heat generation from electrochemical reactions. The model assumptions include steady-state conditions, incompressible flow, negligible buoyancy forces, homogeneous properties for porous materials, and laminar flow (based on the typical values of Reynolds number for SOFCs). For the electric regions, ions transport across the electrolyte and electron conduction through electrodes and interconnects follow a Poisson-type relationship. Activation overpotential is calculated using the Butler-Volmer equation. The model's detailed mathematical description is based on the work of Zhang et al. [6].

3. CASE STUDY AND NUMERICAL SETUP

The study examines a planar anode-supported SOFC in a counter-flow configuration, whose schematic is available in Figure 1. Boundary conditions include specified mass species fractions, velocities, and fixed temperatures at the anodic and cathodic inlets, with pressure specified at the outlets. The fuel is a mixture of hydrogen and water (80% H_2 and 20% H_2O by mass), while the oxidant is air. The inlet velocity of air is set to 2.0 m/s, while the fuel inlet velocity is equal to 0.05 m/s. The computational grid, shown in Figure 2, consists of 1,348,800 hexahedral elements and is refined in porous regions to accurately describe mass and species transport. It was realized with the *blockMesh* utility available in OpenFOAM. The solution is considered converged when the scaled residuals are below 10^{-6} for all variables.

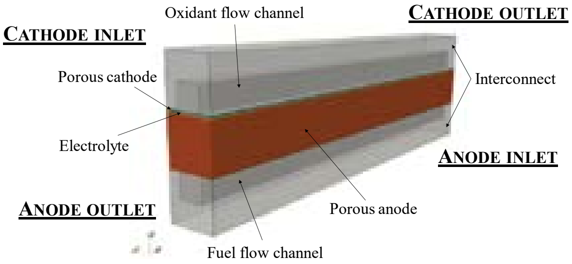

FIGURE 1. Geometry model of the anode-supported SOFC under study

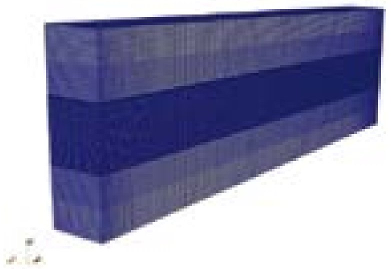

FIGURE 2. Computational grid employed for numerical simulations, composed of 1,348,800 cells

The model is validated by reproducing a polarization curve for a cell temperature of 1023 K. The validated model is then applied to simulate heat transfer with the environment at two distinct temperatures, specifically 973 K and 923 K, assuming a convection heat transfer coefficient of 10 W/(m² K) and that the flow streams enter the cell at the same temperature as the surrounding environment. For these specific analyses, the mean cell current density is fixed at 0.8 A/cm². The primary properties of the cell components used for validation can be found in the work of Mauro et al. [3].

3. RESULTS

The validation of the numerical model shows a good match with the polarization curve provided by Mauro et al. [3], as shown in Figure 3. The comparison is made for the following average cell current densities: 0.1 A/cm^2, 0.2 A/cm^2, 0.4 A/cm^2, 0.6 A/cm^2, 0.7 A/cm^2, 0.8 A/cm^2, 0.84 A/cm^2, 0.88 A/cm^2, 0.92 A/cm^2. A discrepancy is observed in the activation region (i.e., at low current densities) and the mass transport region (i.e., at high current densities). The discrepancy in the mass transport region is due to the absence of calculations for concentration losses. For the activation losses, the disagreement is likely caused by the assumption of a constant exchange current density. It is important to note that the results presented here are preliminary, and both issues will be addressed in future work. Nonetheless, these limitations do not impact the results in the ohmic region, where the average current density considered for evaluating temperature gradients (i.e., 0.8 A/cm²) falls.

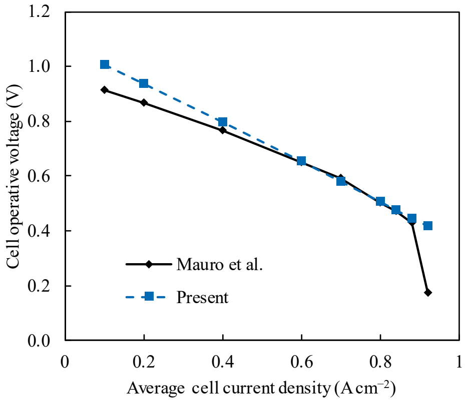

FIGURE 3. Operative cell voltage as a function of average current density, compared with Mauro et al. [3].

The study then predicts temperature gradients within the cell's solid regions at two distinct operating temperatures. The numerically predicted contours of temperature gradient are provided below for an operating temperature of 973 K (Figure 4a) and 923 K (Figure 4b), on the x-z plane crossing the computational domain in its middle.

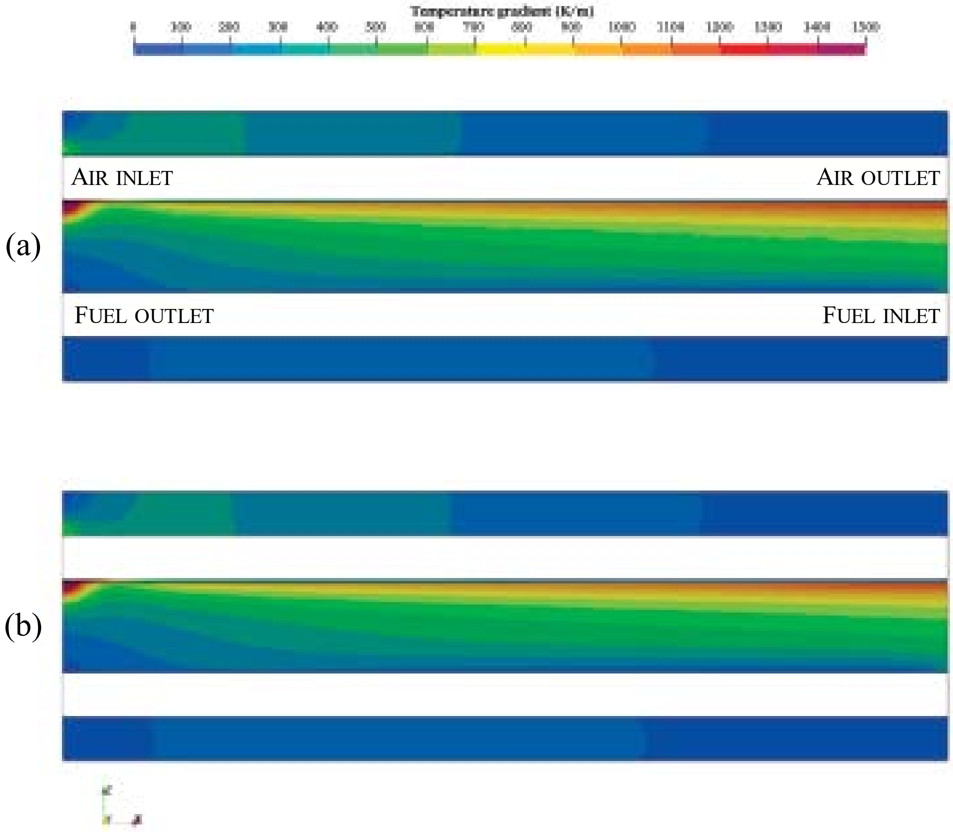

FIGURE 4. Predicted contours of temperature gradient within the solid regions, for an operating temperature of (a) 973 K and (b) 923 K.

Contours are quite similar in the two simulated conditions, with maximum values of 7891 K/m for a temperature of 973 K and 7547 K/m for a temperature of 923 K. The upper limit of the legend has been set to 1500 K/m to ensure a better representation of the results and highlight the gradients.

The maximum temperature gradient is located at the air inlet section, corresponding to the highest heat generation by electrochemical reactions near the fuel inlet section. This suggests that the air inlet section acts as a cold spot, which could be mitigated by supplying the oxidant at higher temperatures to achieve a more uniform temperature distribution and reduce thermal stresses.

The results indicate that the operating temperature has a marginal effect on the temperature gradient distribution, with contours being quite similar in both simulated conditions.

4. CONCLUSIONS

This study presents CFD simulations of a single-unit model of an anode-supported planar SOFC, carried out in the OpenFOAM environment using the *openFuelCell2* tool, developed by Zhang et al. [6]. The numerical model is validated against existing data and applied to predict temperature gradients within the cell under different operating conditions. The findings reveal that operating temperature has a limited impact on temperature gradient distribution, with maximum gradients located at the cathode inlet section. Future research will focus on further exploring this phenomenon and studying the impact of various factors on SOFC performance, including the presence of contaminants and their effect on material aging.

ACKNOWLEDGEMENTS

This research was funded by the European Union - NextGenerationEU from the Italian Ministry of Environment and Energy Security, POR H2 AdP MEES/ENEA with involvement of CNR and RSE, PNRR - Mission 2, Component 2, Investment 3.5 "Ricerca e sviluppo sull'idrogeno", CUP: I83C22001170006.

REFERENCES

[1] F. Arpino, A. Carotenuto, N. Massarotti, P. Nithiarasu, A robust model and numerical approach for solving solid oxide fuel cell (SOFC) problems, International Journal of Numerical Methods for Heat & Fluid Flow 18 (2008) 811–834. https://doi.org/10.1108/09615530810898971.

[2] F. Arpino, N. Massarotti, Numerical simulation of mass and energy transport phenomena in solid oxide fuel cells, Energy 34 (2009) 2033–2041. https://doi.org/10.1016/j.energy.2008.08.025.

[3] A. Mauro, F. Arpino, N. Massarotti, Three-dimensional simulation of heat and mass transport phenomena in planar SOFCs, International Journal of Hydrogen Energy 36 (2011) 10288–10301. https://doi.org/10.1016/j.ijhydene.2010.10.023.

[4] K. Wiranarongkorn, A. Banerjee, O. Deutschmann, A. Arpornwichanop, Performance analysis and temperature gradient of solid oxide fuel cell stacks operated with bio-oil sorption-enhanced steam reforming, International Journal of Hydrogen Energy 45 (2020) 12108–12120. https://doi.org/10.1016/j.ijhydene.2020.02.120.

[5] S. Zeng, M. Xu, J. Parbey, G. Yu, M. Andersson, Q. Li, B. Li, T. Li, Thermal stress analysis of a planar anode-supported solid oxide fuel cell: Effects of anode porosity, International Journal of Hydrogen Energy 42 (2017) 20239–20248. https://doi.org/10.1016/j.ijhydene.2017.05.189.

[6] S. Zhang, S. Hess, H. Marschall, U. Reimer, S. Beale, W. Lehnert, openFuelCell2: A new computational tool for fuel cells, electrolyzers, and other electrochemical devices and processes, Computer Physics Communications 298 (2024) 109092. https://doi.org/10.1016/j.cpc.2024.109092.

Sixth International Conference on Computational Methods for Energy and Thermal Problems
ThermaEComp2024, Sept. 9-11, 2024, Budva, Montenegro
N. Massarotti, P. Nithiarasu, and I. Vušanović (Eds.)

ENERGY RETROFIT IMPACT IN EUROPEAN CONTAINER HOUSES: A SIMULATION STUDY

Vincenzo Bianco[1], Alberto Carotenuto[1], Furio Cascetta[2], Davide Maria Laudiero[1*], Alessandro Mauro[1,2]

[1]Department of Engineering, University of Naples "Parthenope",
vincenzo.bianco@uniparthenope.it; alberto.carotenuto@uniparthenope.it;
davidemaria.laudiero@studenti.uniparthenope.it;

[2]Department of Engineering, University of Campania "L. Vanvitelli",
furio.cascetta@unicampania.it; alessandro.mauro@unicampania.it

ABSTRACT

This study examines the effectiveness of retrofit solutions to improve energy efficiency in container houses across various European climates. Using geographic and climatic data from 22 locations, it compares two envelope configurations of standardized containers, utilizing sandwich panels made of steel and polyurethane. Using dynamic simulations in TRNSYS, the energy payback periods are quantified based on the embodied energy of the insulating materials. The results reveal significant variability in payback periods depending on specific climate conditions, underscoring the importance of customizing retrofit solutions for these housing types. Furthermore, the possibility of extending the analysis to calculate carbon payback using a similar methodology is suggested.

Key Words: Container Houses, Embodied energy, Payback period.

1. INTRODUCTION

Container Houses (CHs), utilizing shipping containers as primary structural components, are gaining increasing global popularity for numerous valid reasons. These structures represent a cost-effective alternative to traditional construction, especially when recycled containers are used. They offer significant benefits including rapid assembly, reduced costs, and environmental sustainability. The accumulation of over 17 million unused containers at ports worldwide, due to high storage and disposal costs, underscores the urgent need to rethink their use, given their durability [1].

CHs are particularly valued as temporary housing solutions following disasters, thanks to their ability to be quickly assembled [2]. However, this speed can sometimes compromise the energy efficiency of the buildings, as highlighted by Costa et al., who noted that the need for rapid construction post-disaster may overlook fundamental energy efficiency principles, potentially deteriorating the comfort of the occupants [3]. This underscored the importance of incorporating retrofit measures that not only meet immediate housing needs but also ensure long-term energy efficiency.

In this context, retrofit measures have proven to be essential tools for reducing operational energy consumption related to seasonal climatization, thus enhancing the efficiency of existing buildings. Research conducted by Mirabella et al. [4] has shown that the embodied energy in insulating materials used in retrofits is often overlooked in decision-making processes, mainly due to the difficulty in obtaining detailed information. This demonstrates the importance of considering the entire lifecycle of construction materials [5].This study aims to investigate the effectiveness of retrofit solutions applied to container houses in different European climatic contexts, examining how specific climate conditions influence the adaptability and energy efficiency of these innovative housing solutions.

2. MAIN BODY

For this analysis, 22 locations across Europe were examined, ensuring a comprehensive representation of geographical and climatic diversity. The sample selection, as shown in Figure 1, encompasses different climates, ranging from the coldest to the most temperate and warm. These locations are listed in Table 1.

Figure 1. Focus Areas

AREAS			
1.	AMSTERDAM	12.	MADRID
2.	ATHENS	13.	MARSEILLE
3.	BARCELONA	14.	MILAN
4.	BERLIN	15.	NAPLES
5.	BUDAPEST	16.	PARIS
6.	CAGLIARI	17.	PRAGUE
7.	DUBLIN	18.	ROME
8.	HAMBURG	19.	SOFIA
9.	ISTANBUL	20.	VIENNA
10.	KRAKOW	21.	WARSAW
11.	LISBON	22.	ZAGREB

Table 1. Selected Areas

The study examined container dimensions according to international and European standards, selecting containers from Hapag-Lloyd, a major German ocean carrier. The specifications for the container include interior dimensions of 12.03 m in length, 2.35 m in width, and 2.39 m in height.

In the study, a comparison was conducted between two configurations of the container's building envelope under examination. In the first configuration, the base layer consists of a single sandwich panel covering the entire surface of the building envelope. The sandwich panel is composed as follows: Steel (1 mm) - Polyurethane (2 cm) - Steel (1 mm). In the second configuration, three sandwich panels placed side by side were considered to cover the entire area of the building envelope. This comparison forms the basis of the study to effectively assess the energy efficiency intervention of the opaque envelope component, considering the embodied energy of the materials.

	One sandwich panel		Three sandwich panels		
Building element	Transmittance [W/m^{2}K]	Thickness [m]	Transmittance [W/m^{2}K]	Thickness [m]	A [m^2]
External wall	0.927	0.022	0.258	0.144	69.02
Horizontal elements	0.927	0.022	0.258	0.144	56.54

Table 2. Main characteristics of the container envelope

2.2 Methodology

The methodology used to compare the embodied energy in insulation materials with the reduction in operational energy resulting from retrofit solutions is explored, with the goal of quantifying the energy savings achieved. Initially, the embodied energy is assessed and then compared with the energy savings during the operational phase, thereby calculating the energy payback period. This methodology can also be applied to assess the environmental impact of carbon, which is influenced by the specific energy mix of each country. Only the essential data needed to determine the energy return time are presented here, analysing the operational energy savings (OE) over a specified period, calculated according to (1).

$$OE_i = \sum_i (E_{OP} - E_{OPS}) \tag{1}$$

where E_{OP} [MJ/m^2] is defined as the annual operational energy for heating of the non-refurbished container, and E_{OPS} [MJ/m^2] is the operational energy for heating of the refurbished container.

Defining 'EE' as the Embodied Energy of materials, it is then possible to determine the energy payback time, denoted as 'n', in the following way:

$$EE - \sum_{i=1}^{n} OE_i = 0 \tag{2}$$

Where the energy payback period, denoted as 'n', is the number of years required for the savings in operational energy (OE) to offset the initial embodied energy (EE) investment.

3. RESULTS

To evaluate the embodied energy of materials used in energy efficiency improvements, the quantity of materials used after the insulation intervention was first defined. Initially, the structure consisted of a single sandwich panel made of steel-polyurethane-steel. Subsequently, we calculated the amount of material, considering both polyurethane and steel, in relation to a structure composed of 3 sandwich panels. The values used to calculate the embodied energy (EE) are listed in the following table.

Material	Polyurethane	Steel
EE_I [MJ/kg]	110	35
ρ [kg/m3]	30	8000
s [cm]	6	0,2
λ [W/(m k)]	0,028	17

Table 3. Materials properties used for energy retrofit.

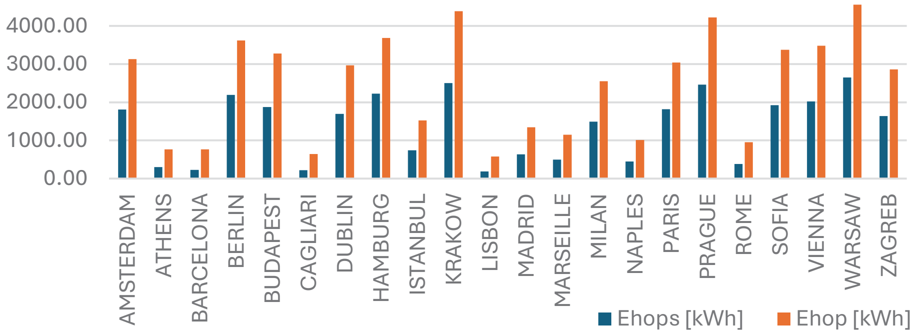

Figure 2. Thermal Load

Once the thermal loads have been obtained through dynamic modeling in the TRNSYS environment, it is possible to determine the payback period of the energy investment 'n'.

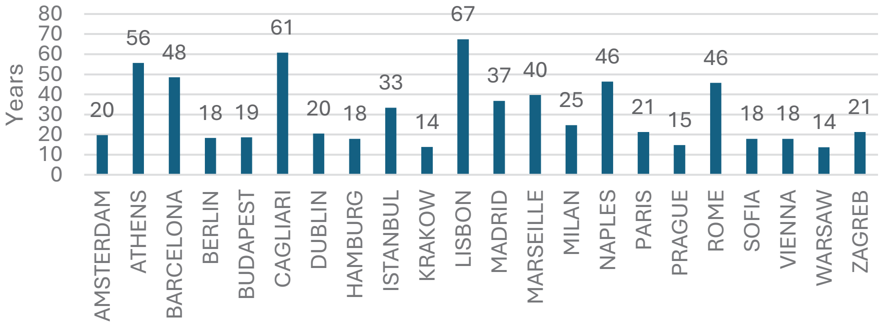

Figure 3. Energy payback

3. CONCLUSION

This study highlights the significance of energy retrofit solutions for container houses across various European climatic contexts. It has been distinctly observed that the energy payback period varies significantly depending on the location, thereby underscoring the need for tailored strategies to enhance energy efficiency. For instance, cities like Berlin, Budapest, Krakow, and Warsaw exhibit payback periods of less than 20 years, making interventions on the building envelope energetically beneficial. In contrast, warmer locations such as Athens, Cagliari, and Lisbon experience payback periods exceeding 50 years, suggesting that retrofit strategies may require a different approach.

These differences not only reflect the climatic variability across European regions but also directly influence the effectiveness of the adopted retrofit solutions. By expanding the analysis to include the carbon payback time using a similar methodological approach, a more comprehensive assessment of the environmental impact of retrofit solutions could be achieved.

This methodology enables the assessment of different insulating materials in sandwich panels, optimizing retrofit solutions for container houses. Such models can be crucial for designers and policymakers, helping them choose the best retrofit approaches based on specific climatic zone. Customizing these solutions and selecting the right materials are key to enhancing energy efficiency and reducing the environmental impact across Europe.

Acknowledgments: Prof. Mauro and Dr. Laudiero gratefully acknowledge the financial support of project PRIN 2020 "Optimal refurbishment design and management of small energy micro-grids - OPTIMISM”, Prot. 20204NXSZH, CUP I65F21001850006, Ministero dell’Università e della Ricerca (MUR). Prof. Bianco, Prof. Cascetta and Prof. Mauro acknowledge Erasmus+ SHERLOCK Project (#101105629), funded by the European Union. Views and opinions expressed are however those of the author(s) only and do not necessarily reflect those of the European Union or the European Education and Culture Executive Agency (EACEA). Neither the European Union nor EACEA can be held responsible for them.

REFERENCES

[1] L. M. M, G. Student, R. SHIBASAKI Eng, T. B. KADONO Eng, and H. IEDA Eng, “An estimation of the international container shipping transport volumes among asian counrties by global trade analysis project model and its applications to fta and transport improvement scenarios.”

[2] Y. Hong, “A study on the condition of temporary housing following disasters: Focus on container housing,” *Frontiers of Architectural Research*, vol. 6, no. 3, pp. 374–383, Sep. 2017, doi: 10.1016/J.FOAR.2017.04.005.

[3] B. B. F. da Costa, C. F. P. Silva, A. C. F. Maciel, H. D. P. Cusi, G. Maquera, and A. N. Haddad, “Simulation and Analysis of Thermal Insulators Applied to Post-Disaster Temporary Shelters in Tropical Countries,” *Designs (Basel)*, vol. 7, no. 3, Jun. 2023, doi: 10.3390/designs7030064.

[4] N. Mirabella *et al.*, “Strategies to improve the energy performance of buildings: A review of their life cycle impact,” *Buildings*, vol. 8, no. 8. MDPI AG, Aug. 12, 2018. doi: 10.3390/buildings8080105.

[5] S. Abd Alla, V. Bianco, L. A. Tagliafico, and F. Scarpa, “Life-cycle approach to the estimation of energy efficiency measures in the buildings sector,” *Appl Energy*, vol. 264, p. 114745, Apr. 2020, doi: 10.1016/J.APENERGY.2020.114745.

Sixth International Conference on Computational Methods for Energy and Thermal Problems
THERMAECOMP2024, Sept. 9-11, 2024, Budva, Montenegro
N. Massarotti, P. Nithiarasu, and I. Vušanović (Eds.)

HARNESSING WASTE HEAT AND SOLAR THERMAL INTEGRATION FOR SUSTAINABLE BREWERY COOLING: A CASE STUDY APPROACH

Musannif Shah[1], Valeria Palomba[1], Andrea Frazzica[1], Mikel Arenas-Larrañaga[2], Daniel Carbonell[2,3]

[1]Istituto di Tecnologie Avanzate per l'Energia CNR ITAE, 98126, Messina, Italy,
musannif.shah@itae.cnr.it, valeria.palomba@cnr.it, andrea.frazzica@cnr.it

[2]SPF Institut für Solartechnik, OST – Ostschweizer Fachhochschule, CH-8640 Rapperswil, Switzerland, mikel.arenas@ost.ch, extern.carbonell@ost.ch

[3]DCarbo Energy Consulting S.L., 08212, Sant Llorenç Savall, Barcelona, Spain,
daniel.carbonell@dcarbo.es

ABSTRACT

Industrial waste heat refers to the thermal energy generated in an industrial process that is not put into practical use and is either lost, wasted, or dumped. The brewery industry consumes a significant amount of energy, mostly dedicated to cooling purposes. This paper explores a novel hybrid design that harnesses thermal energy from potential wastewater sources and integrates high vacuum flat plate (HVFP) solar thermal collectors with adsorption cooling technology to provide process cooling in a specific brewery case study (Browar Glubczyce). The studied brewery produces up to 50000 m^3 of beer annually. Following each wort boiling cycle, the entire volume is cooled to fermentation temperature (e.g., 8 °C). The proposed system exploits thermal power (e.g., 350 kW) from wastewater sources at approximately 80 °C, supplemented by an array of 70 kW HVFP thermal collectors to augment the primary heat source, raising the supply temperature to 100 °C for a 200-kW capacity adsorption chiller. A preliminary analysis based on the simulation of this hybrid system suggests potential annual energy savings and reductions in CO_2 emissions.

Key Words: *Waste heat recovery, Low-grade heat, Brewery, Adsorption cooling.*

1. INTRODUCTION

The potential of low-grade waste heat and solar thermal technologies for industrial cooling remains less explored. In 2020, the industrial sector in the European Union (EU) accounted for 26.1% of the total energy consumption. The primary energy sources employed for fulfilling this demand are electricity (32.9%) and fossil fuels (48.5%), leading to a substantial dependence on fossil fuels, predominantly imported from non-EU countries [1]. Approximately, 150 TWh/y of electricity is used for process cooling [2], primarily in industries such as food and beverage, tobacco, and light chemicals. In these industries, cooling can account for up to 50% of electricity consumption, typically for temperatures above 0 °C. The industrial cooling energy market is projected to experience a Compound Annual Growth Rate (CAGR) of 6.1% in the US market between 2023 and 2033 [3].

Breweries are large-scale industrial facilities that consume a significant amount of energy. Brewing and fermentation are both considered energy-intensive processes in beer production. In particular, brewing requires a significant amount of heat demand, with the wort kettle alone accounting for one-third of the steam used by the entire plant. Additionally, the fermentation process demands a considerable amount of cooling energy, constituting approximately 60 to 70% of the total cooling capacity, which is supplied by a refrigeration system [4].

Conventionally, vapor compression chillers powered by electricity continue to dominate the industrial process cooling market due to their widespread availability and reliability, while thermally-driven technologies are limited to a niche market [5]. However, approximately 300 TWh/y of waste heat sources are available from industrial processes in the EU [6]. From this waste heat, around 35% is below 200 °C leaving a significant potential for integrating thermally driven cooling technologies. In addition, the adoption of solar thermal energy to support the supply of cooling energy is increasingly appealing due to its sustainability, technical feasibility, and economic advantages. However, its implementation is still limited [7].

The industrial sector presents favourable conditions for the use of solar thermal energy, as the load is often consistent throughout the year and existing storage facilities can be utilized. However, despite these advantages, the adoption of solar thermal systems in industrial companies remains limited globally, with such systems accounting for only 12% of the installed capacity worldwide [8]. Therefore, it is essential to explore the potential of integrating solar thermal energy based on the For such applications, adsorption cooling systems are considered highly reliable thermally driven cooling technologies due to their numerous advantages [9]. These systems can operate using low-grade waste heat, utilize natural refrigerants like water, have minimal moving mechanical parts, require low maintenance, and are environmentally friendly [10].

This paper focuses on a case study to assess the potential of low-grade thermal energy recovery in cooling applications for the brewery industry. This work proposes a novel hybrid system that uses thermal energy from the hot wort stream and solar thermal collectors to operate an adsorption chiller. Moreover, the study also aims to evaluate the energy performance of the system and optimization of the key components of the system using pytrnsys simulation tool [11].

2. MAIN BODY

The proposed system demonstrates a solution for thermally driven industrial cooling technology based on the adsorption process, being able to exploit low-grade waste and renewable energy, to increase the overall energy performance and efficiency of the system. The main objective of this work is to propose a cost-competitive industrial cooling solution for a case study brewery industry

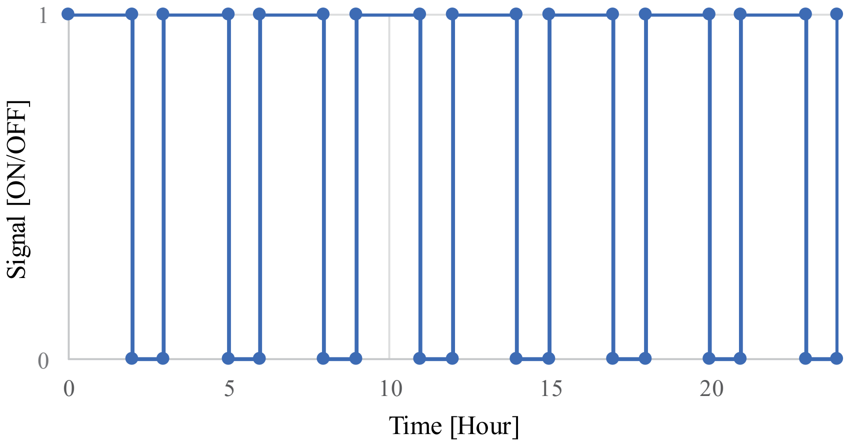

FIGURE 1: Operational control of the system

(e.g., Browar Glubczyce, Poland). The analysis of the system is being carried out in pytrnsys, a Python-based framework based on TRNSYS called pytrnsys [11]. This tool allows to develop, run, and post-process of TRNSYS simulations in a more user-friendly way. The brewery case study has an annual beer production capacity of up to 50,000 m^3. The mashing and boiling are conducted by heating 35 m^3 of beer wort using process steam approximately 800 times per year. Afterward, the entire volume of the wort is cooled from 98 °C to the fermentation temperature of 8 °C within an average duration of 2 hours for each batch, achieved through a two-stage cooling process. The operational control of the batch-wise cooling of the wort is shown in the Figure 1. In the first stage, the cooling water sourced from a deep well at 15 °C lowers the wort temperature, whereas, in the later stage, an adsorption chiller cools further the wort to the required temperature. The system also comprises an existing ammonia cooling system needed to reach the final temperature. The estimated cooling capacity of the adsorption chiller for the temperature range of 6/15 °C and flow rate of 17.1 m^3/h is 200 kW. Figure 2 shows the schematic layout of the proposed system. A series of heat exchangers (HE) are installed to lower the temperature of the wort after the mashing stage from 98 °C to 8 °C. For instance, a closed loop of water recovers thermal energy from hot wort (e.g., HE1) to supply the driving thermal energy to the adsorption chiller followed by a supplementary array of solar thermal collectors to achieve the design driving temperature of the chiller. The cooling water that comes from the deep well at 15 °C is chilled in an adsorption chiller and supplied at 6 °C (point 10) to HE2 which cools down the wort to the required temperature. The ammonia chiller is only activated when the adsorption chiller is not able to achieve the wort set point temperature.

3. PRELIMINARY RESULTS

The proposed system layout for the case study brewery at Browar Głubczyce, Poland showcases the integration of waste heat recovery from process wort and solar thermal technologies to meet the brewery's cooling demands. The implementation of an adsorption chiller driven by the recovered thermal energy from the hybrid system is expected to yield significant energy savings and reduce

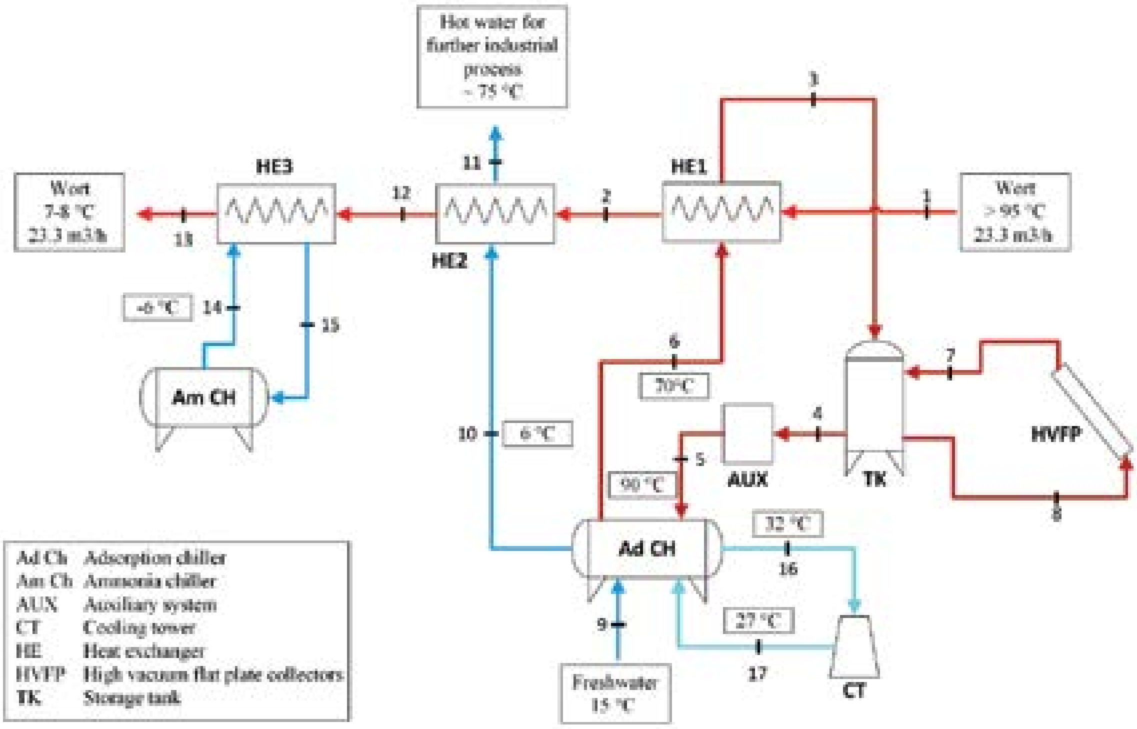

FIGURE 2: Schematic layout of the system

CO_2 emissions. Preliminary simulations indicate potential annual electricity savings from 64 MWh to 161 MWh and a reduction of 51 t/y of CO_2 emissions at full plant operation.

ACKNOWLEDGMENT

This project has received funding from the European Union's Horizon Europe research and innovation program under grant agreement No 101138697 (RE-WITCH)

REFERENCES

[1] "Final energy consumption in industry - detailed statistics - Statistics Explained." Accessed: Mar. 25, 2024. [Online]. Available: https://ec.europa.eu/eurostat/statistics-explained/index.php?title=Final_energy_consumption_in_industry_-_detailed_statistics#Paper.2C_pulp_and_printing_industry

[2] M. Rehfeldt, C. Rohde, T. Fleiter, F. Toro, and F. Reitze, "A bottom-up estimation of heating and cooling demand in the European industry".

[3] "Industrial Cooling Systems Market Size, Share & Trends | 2033." Accessed: Mar. 25, 2024. [Online]. Available: https://www.futuremarketinsights.com/reports/industrial-cooling-systems-market

[4] "Efficient use of energy and resource through conservation and recovery in breweries".

[5] M. Kılıç, "Evaluation of Combined Thermal–Mechanical Compression Systems: A Review for Energy Efficient Sustainable Cooling," *Sustain.*, vol. 14, no. 21, Nov. 2022, doi: 10.3390/SU142113724.

[6] M. Papapetrou, G. Kosmadakis, A. Cipollina, U. La Commare, and G. Micale, "Industrial waste heat: Estimation of the technically available resource in the EU per industrial sector, temperature level and country," *Appl. Therm. Eng.*, vol. 138, no. July 2017, pp. 207–216, 2018, doi: 10.1016/j.applthermaleng.2018.04.043.

[7] L. Kumar, M. Hasanuzzaman, and N. A. Rahim, "Global advancement of solar thermal energy technologies for industrial process heat and its future prospects: A review," *Energy Convers. Manag.*, vol. 195, pp. 885–908, Sep. 2019, doi: 10.1016/J.ENCONMAN.2019.05.081.

[8] D. Tschopp, Z. Tian, M. Berberich, J. Fan, B. Perers, and S. Furbo, "Large-scale solar thermal systems in leading countries: A review and comparative study of Denmark, China, Germany and Austria," *Appl. Energy*, vol. 270, p. 114997, Jul. 2020, doi: 10.1016/J.APENERGY.2020.114997.

[9] A. Caprì, A. Frazzica, and L. Calabrese, "Recent Developments in Coating Technologies for Adsorption Heat Pumps: A Review," *Coatings 2020, Vol. 10, Page 855*, vol. 10, no. 9, p. 855, Sep. 2020, doi: 10.3390/COATINGS10090855.

[10] V. Palomba, A. Bonanno, V. Brancato, A. Frazzica, and R. Herrmann, "Design of adsorption chillers under rolling conditions in naval applications: Experimental and numerical approaches," *Appl. Therm. Eng.*, vol. 248, p. 123224, Jul. 2024, doi: 10.1016/J.APPLTHERMALENG.2024.123224.

[11] "pytrnsys — pytrnsys documentation." Accessed: Mar. 27, 2024. [Online]. Available: https://pytrnsys.readthedocs.io/en/latest/

INVESTIGATION OF MULTIPLE ORC PLANT CONFIGURATIONS FOR WASTE HEAT STREAM RECOVERY

Biagio Morrone, Saif Serag
Department of Engineering - Università della Campania "L. Vanvitelli" Aversa (CE) 81031 - Italy
biagio.morrone@unicampania.it; saifhadimohsen.serag@unicampania.it

Hélène Ageorges
Université de Limoges, CNRS, IRCER, UMR 7315, F-87000 Limoges, France
helene.ageorges@unilim.fr

ABSTRACT

Organic Rankine Cycle (ORC) is a promising technology for converting low-grade waste heat into power. This study investigates the performance of a Parallel Dual stage Organic Rankine Cycle (PDORC) system using R1233zd and R1234ze as working fluids compared with a Basic ORC (BORC). Numerical simulations were performed to evaluate thermal efficiency and net power output under various operational conditions. The motivation for considering a PDORC comes from the exploitation of two different heat sources with diverse temperatures from a marine internal combustion engine. The results indicate that the PDORC configuration with R1234ze and R1233zd achieves higher thermal efficiency under certain conditions. The R1233zd performs better than the other fluid, in terms of efficiency, extracted power and lower mass flow rate of the organic fluid.

Key Words: *ORC, PDORC, Cycle Efficiency, Waste Heat Recovery, Electrical Energy Production.*

1. INTRODUCTION

The global industrial sector is a cornerstone of modern economies, driving significant advancements in technology, infrastructure, and overall societal progress. However, it also stands as one of the largest consumers of energy, accounting for a substantial portion of global energy demand. A critical issue associated with industrial energy use is how exploit of waste heat, which, when not effectively recovered and utilized, results in substantial energy losses and adverse environmental impact [1]. The efficient recovery of waste heat leads to reduction of fuel consumption and greenhouse gas emissions, aligning with the global push towards more sustainable and environmentally friendly industrial practices [2].

Organic Rankine Cycles (ORC) gained considerable attention as a viable technology for converting low to medium-temperature waste heat into power. ORC operates on the same principles as the traditional Rankine cycle but using organic working fluids with lower boiling points compared to water, more suitable for exploiting and converting lower temperature heat sources. This characteristic enables ORC systems to be efficiently applied to a wide range of industries [3].

Despite the advantages of ORC technology, the efficiency and economic viability of these systems are highly dependent on the specific configuration of the ORC plant and the available waste heat stream. A comprehensive investigation into diverse ORC plant configurations is essential to identify the most effective approaches for maximizing energy recovery from waste heat streams [4]. Two working fluids have been selected, R1233zd(E) and R1234ze(E), which belong to the "isentropic" family [5]; their T-s diagrams are plotted in Fig. 1. These fluids have garnered attention due to their favorable thermophysical properties, low global warming potential (GWP) and Ozone Depletion Potential (ODP). Their main thermodynamic and environmental properties are reported in Table (1).

Fluid	Critical Temperature (°C)	Critical Pressure (bar)	Normal boiling point (°C)	ODP	GWP (IPCC AR4)	Health Impact	Flammability	Reactivity
R1233zd(E)	166.4	36.2	18.3	0	5	Very Low	Low	Very Low
R1234ze(E)	109.4	36.4	-18.9	0	7	Low	High	Very Low

TABLE 1. Main thermodynamic and environmental properties of the investigated fluids

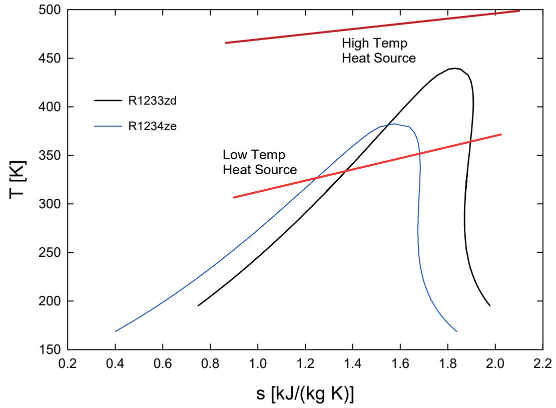

FIGURE 1. T-s diagrams for R1233ze(E) and R1234zd(E) organic fluids and the two-temperature level heat sources plots.

The objective of the investigation is to evaluate the thermodynamic efficiency of two ORC different configurations, by using two different temperature level waste heat sources from a marine internal combustion engine, aiming to identify the setup for maximizing waste heat recovery under various operational conditions. ORC configurations investigated are the basic ORC (BORC) and Parallel Dual stage ORC (PDORC) with double pressure level.

2. METHODOLOGY

The BORC is displayed in Fig. 2(a), a classical Rankine cycle configuration, whereas the PDORC under investigation comprises: Low (LT HX) and High-Temperature (HT HX) Evaporators, Low (LPT) and High-Pressure (HPT) Turbines, Condenser, and Low (LPP) and High-Pressure (HPP) Pumps, is schematized in Fig. 2(b).

In PDORC the stream is split between Low- and High-Pressure branches (LP and HP). The vapour from the HT HX evaporator passes through the HPT turbine, after that it mixes with the fluid from the low-pressure branch, LT HX. Then, stream expands in the LPT turbine. After that, the fluid enters the condenser, where it is condensed. Condensed fluid is then pumped in the two lines (HPP and LPP). Assuming steady-state operation, negligible heat losses to the environment and assigned isentropic efficiency for turbines and pumps, the energy and exergy calculations were accomplished. In addition, the same thermal performance of the heat exchangers (LT HX and HT HX) for both the organic fluids and both the configurations has been assumed.

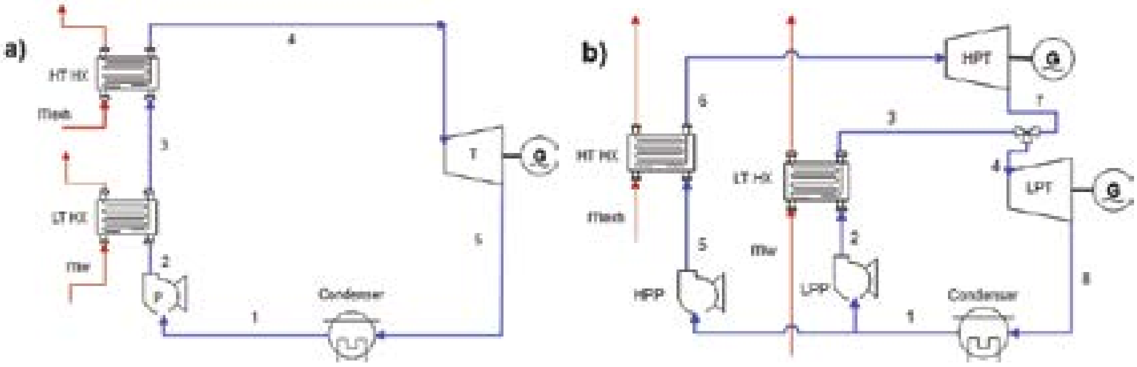

FIGURE 2. a) BORC and b) PDORC, with low- and high-pressure lines

3. RESULTS

The investigation considers two different temperature level heat sources, and for this reason the PDORC has been contemplated. One heat source is liquid water from cooling jacket of a marine internal combustion engine, the other corresponds to the exhaust gases from the same engine. Table 2 shows the inlet conditions of the two heat source streams.

TABLE 2. Main data properties of the heat sources

Fluid	Tin (°C)	$\dot{m}$ (kg/h)
Jacket Water	90	150,000
Exhaust gases	230	170,000

Figure 3 displays the extracted power $\dot{W}$ [kW] from the ORC as a function of the maximum cycle pressure. When the BORC is considered, p_{max} represents the high pressure of the cycle, whereas for the PDORC, it represents the highest high-level pressure (HP). The maximum pressure values of the organic fluid are constrained by the jacket water and the exhaust gases inlet temperatures. For this reason, when the BORC is considered, it is not possible to increase it above a fixed value which depends on the chosen fluid. The R1233zd, Fig. 3(a) shows power as a function of the maximum pressure ranging between 550 and 707 kW for the BORC, whereas when considering the PDORC the extracted power is between 720 and 806 kW depending on the maximum pressure value. The R1234ze shows smaller power values, between 520 and 665 kW for the BORC, whereas for the PDORC the extracted power ranges between 648 and 667 kW. It is clear that the increment of extracted power is larger for R1233zd fluid. By considering the BORC and the maximum value of the extracted power for R1233zd, the results show percent increments between 1 and 14% when the PDORC is considered. In contrast, the R1234ze fluid shows a different trend. In fact, the extracted power by the PDORC can be lower than that of the best BORC value. When the best condition is run, with a p_{HP} of 33.4 bar, the percent increment of the PDORC extracted power is less than 1% compared with the best BORC performance. When the cycle efficiency is considered, the BORC configuration ranges between 0.100 and 0.135 for the R1233zd and between 0.100 and 0.126 for the R1234ze. When the PDORC is considered, the efficiency spans between 0.136 and 0.154 for the R1233zd, whereas it is between 0.125 and 0.127 for the R1234ze. Thus, the PDORC shows larger efficiency differences between the two investigated fluids.

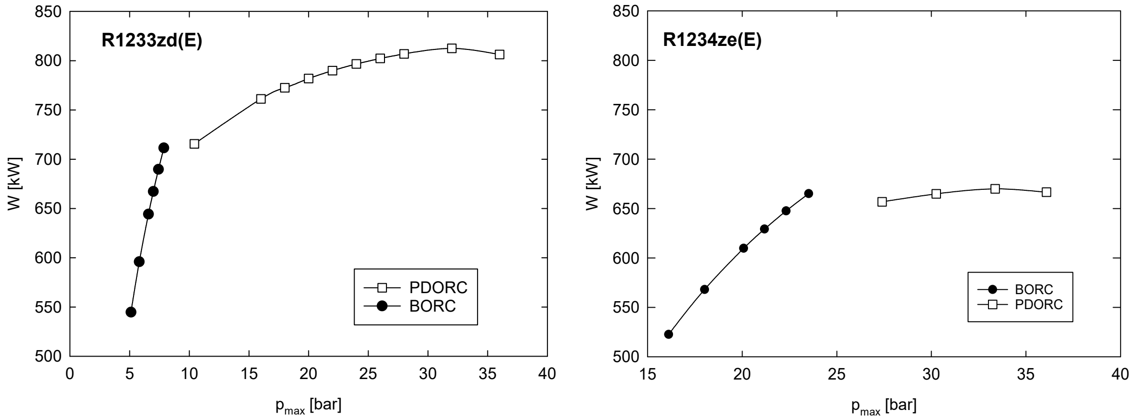

FIGURE 3. ORC power as a function of the maximum cycle pressure: (a) R1233zd; (B) R1234ze.

4. CONCLUSIONS

A comparison between two ORC configuration plants (BORC and PDORC) is presented, by exploiting two different temperature level waste heat sources from a marine internal combustion engine. Two fluids have been studied, R1233zd and R1234ze, with very low GWP and ODP indexes. The performance of R1233zd organic fluid is better than that of R1234ze. The difference is noticeable especially when the comparison is accomplished for the PDORC configuration, for which the performance of R1233zd fluid shows large increments of order 1 to 14%.

5. ACKNOWLEDGMENT

Università della Campania "L. Vanvitelli" is gratefully acknowledged for the grant "*2024 Call for Visiting Professors/Researchers*" for supporting the mobility of prof. H. Ageorges.

REFERENCES

[1] Rissman J. et al., Technologies and policies to decarbonize global industry: Review and assessment of mitigation drivers through 2070, *Applied Energy*, Volume 266, 2020, ISSN 0306-2619, doi.org/10.1016/j.apenergy.2020.114848

[2] Suand Z. et al., Opportunities and strategies for multigrade waste heat utilization in various industries: A recent review, *Energy Conversion and Management*, Volume 229, 2021, doi.org/10.1016/j.enconman.2020.113769

[3] Zhang H. et al., Thermodynamic and thermoeconomic analyses of the energy segmented stepped utilization of medium- and low-temperature steam based on a dual-stage organic Rankine cycle, *Applied Thermal Engineering*, Volume 219, 2023, doi.org/10.1016/j.applthermaleng.2022.119488.

[4] Pezzuolo A. et al., The ORC-PD: A versatile tool for fluid selection and Organic Rankine Cycle unit design, *Energy*, Volume 102, 2016, doi.org/10.1016/j.energy.2016.02.128.

[5] Mariani A., M.L. Mastellone, B. Morrone, M. V. Prati, and A. Unich, An Organic Rankine Cycle Bottoming a Diesel Engine Powered Passenger Car, *Energies*, Vol.15, 2022, doi.org/ 10.3390/en15217912.

Sixth International Conference on Computational Methods for Energy and Thermal Problems
THERMAECOMP2024, Sept. 9-11, 2024, Budva, Montenegro
N. Massarotti, P. Nithiarasu, and I. Vušanović (Eds.)

LIFE CYCLE BASED COMPARISON OF DIFFERENT SOLUTIONS FOR URBAN PASSENGERS' TRANSPORTATION

N. Massarotti[1], R. Santagata[1,2,*], L. Vanoli[1]
[1]Department of Engineering, Parthenope University of Naples, Centro Direzionale, Isola C4, 80143, Napoli, Italy
[2]Faculty of Engineering and Computer Science, Pegaso University, Centro Direzionale, Isola F2, 80143, Napoli, Italy
nicola.massarotti@uniparthenope.it; *remo.santagata@unipegaso.it; laura.vanoli@uniparthenope.it

ABSTRACT

The significant pressure on the transportation systems in urban environments is calling for accurate planning and feasible solutions. In particular within cities with great historical and socio-economic values, also interested by important touristic flows, a correct balance between efficiency and environmental load is a paramount topic. This work analyses different solutions for road passenger transport in Naples, Italy. The results highlight how important is a careful planning, and how energy sources can drive the environmental impacts.

Key Words: *Road Transport, Hydrogen bus, Electric bus, Life Cycle Assessment, Energy sources.*

1. INTRODUCTION

Urban environments can be taken in consideration as dynamic systems, developing according to internal and external factors and to policies and decisions. They are characterized by increasing population and are contributing to global issues such as greenhouse gas emissions and loss of biodiversity [1]. The city population increased from 25% in the '50s, to around 50% in 2020, with projections of about 58% within the next 50 years [2]. The increase in urban population density brings several socio-economic and environmental issues [3], including health problems [4]. Furthermore, tourism is becoming one of the most prominent characteristics within interested cities, shaping the urban experience due to the development of service economies and bringing issues as increased pollution and waste, use of resource, transport demands [5] and increasing housing prices. Many European cities have been interested by massive tourism flows in the last year, such as Naples, in Southern Italy, that have seen an increase of 60% in bookings for touristic trips. This framework calls for feasible solutions in the urban planning and in the management of urban services, such as urban transportation, in order to maintain acceptable levels of wellbeing for residents and visitors. The present work analyses the road transport within the city of Naples, studying, from a life cycle perspective, the environmental impacts of different solution for bus transport. The Life Cycle Assessment (LCA) method is used to compare the environmental load of diesel, electric and hydrogen powered buses, considering the number of passengers moved and the distance covered annually. The results are of significant relevance both from a local, regulatory point of view, and as a basis for others urban cities worldwide.

2. MATERIALS AND METHODS

With around 1 million inhabitants, Naples is the third city in Italy for population, after Rome and Milan. It spans over an area of about 117 km^2, around one of the largest European historical city centres, dating back to the Magna Grecia. It is home of different Universities, among which the University of Naples Federico II represents one of the most ancient universities in the world. Furthermore, Naples is the capital of the 3 million inhabitants metropolitan city and is the destination of a significant flow of tourism both national and international. These, and other features, put the local transportation system under a significant stress. The urban and extra urban Neapolitan transportation system is managed by ANM s.p.a. (Azienda Napoletana Mobilità - https://www.anm.it/), that manages road vehicles, the Line 1 and Line 6 metros, and funicular railways. In addition, the metro Line 2 is managed by the Italian statal railway company Trenitalia (https://www.trenitalia.com/), while the regional metropolitan system is managed by EAV s.p.a. (Ente Autonomo Volturno). The Road transport system by ANM involves 87 urban and 20 suburban routes, employing 399 buses, almost all diesel powered, with a small fraction of methane powered vehicles. These buses are responsible for the transport of more than 32 million passengers annually, for an overall distance of more than 11 million kilometres [6].

In this work, a comparison among different solutions is carried out, to understand the best alternatives for assuring the movement of people throughout the urban territory with the least environmental impacts. Based on literature data, the environmental load of the transportation for diesel, electric (E-Bus) and hydrogen (H2Bus) powered buses. The study is carried out by means of the LCA method, a highly standardized method for the environmental assessment of human dominated processes [7,8]. The analysis is performed by using the Simapro software [9], with the Ecoinvent 3.6 database [10] and the ReCiPe 2016 v.1.04 impact method [11]. The diesel bus is modelled according to the Ecoinvent database, the E-Bus is modelled according to [12] and is accounted for using energy from the Italian electricity mix, the H2Bus according to [13], using hydrogen fuel produced by means of methane steam reforming, which is how about 95% of the European hydrogen is produced. The Functional Unit (FU) chosen for the study is the transportation of 1 person for 1 kilometre, the boundaries considered includes the production of buses and fuels, and their operation through a lifespan of 15 years.

3. RESULTS

Table 1 reports the ReCiPe midpoint results, i.e. the emission potentials, for the transportation of 1 passenger for 1 kilometre related to the Diesel bus, the E-Bus and the H2Bus. It is clear how the results are very category dependent. Considering the Diesel Bus as a benchmark in a Business-as-Usual perspective, the E-Bus shows better performances in some categories such as, among the others GWP (-67%, equals to more than 27 thousand tons of CO_2 eq. avoided annually), PMFP (-16%, about 3 tons of PM2.5 eq. avoided annually), and FSP (-68%, almost 9 thousand tons of oil eq. avoided annually). In other categories, the E-Bus performs worse than the Diesel one, in particular in toxicity related categories, the use of land and the water consumption. A similar behaviour is recognizable also regarding the H2Bus. The latter show a reduction of 42% in GWP, equals to more than 17 thousand tons of CO_2 eq. avoided annually, 13 tons of PM2.5 avoided annually, 30 m^2 of land and more than 3700 tons of oil eq. avoided annually. It is important to notice that the reported environmental impacts are dependent almost entirely on the production of the energy used for their operations. The production of diesel fuel is contributing for an overall 84% to the total impacts, the Italian electricity and the production of hydrogen show the 99.99% of the load on the total impacts of the E-Bus and of the H2Bus. This is of course due to the absence of emissions for the operations of the E-Bus and the H2Bus. The relevance of the energy source is quite significant, as the performance of the different analysed systems could be much improved by simply making the energy used more sustainable, e.g. using electricity from renewable sources, and electrolysis or thermochemical processes for hydrogen production, among others.

Figure 1 shows the ReCiPe normalized results, highlighting the unitless magnitude of the potential emissions in the different impact categories. The most impacted categories, in addition to the toxicity related ones, are FSP, in particular with relation to the Diesel and the H2 buses, FEP within the E-Bus and GWP, in particular for the Diesel and H2Bus.

TABLE 1. ReCiPe Midpoint (H) characterized results for 1 passenger.km by Diesel Bus, E-Bus and H2Bus.

Impact category	Abb.	Unit	Diesel Bus	E-Bus	H2Bus
Global warming	GWP	kg CO$_2$ eq	1.24E+00	4.07E-01	7.20E-01
Stratospheric ozone depletion	ODP	kg CFC11 eq	7.44E-07	3.22E-07	2.23E-07
Ionizing radiation	IRP	kBq Co-60 eq	1.19E-02	4.61E-02	1.80E-03
Ozone formation, Human health	OFHP	kg NO$_x$ eq	1.58E-03	7.49E-04	3.63E-04
Fine particulate matter formation	PMFP	kg PM$_{2.5}$ eq	5.69E-04	4.80E-04	1.73E-04
Ozone formation, Terrestrial ecosystems	OFTP	kg NO$_x$ eq	1.63E-03	7.61E-04	3.87E-04
Terrestrial acidification	TAP	kg SO$_2$ eq	1.72E-03	1.42E-03	5.10E-04
Freshwater eutrophication	FEP	kg P eq	1.48E-05	1.16E-04	1.47E-05
Marine eutrophication	MEP	kg N eq	1.30E-06	1.14E-05	1.08E-06
Terrestrial ecotoxicity	TETP	kg 1,4-DCB	5.83E-01	4.66E-01	3.13E-01
Freshwater ecotoxicity	FETP	kg 1,4-DCB	2.60E-03	1.16E-02	6.82E-03
Marine ecotoxicity	METP	kg 1,4-DCB	4.20E-03	1.51E-02	9.01E-03
Human carcinogenic toxicity	HCTP	kg 1,4-DCB	3.59E-03	9.77E-03	3.81E-03
Human non-carcinogenic toxicity	HNTP	kg 1,4-DCB	6.87E-02	2.39E-01	9.12E-02
Land use	LUP	m^{2}a crop eq	1.02E-02	1.51E-01	9.27E-03
Mineral resource scarcity	MSP	kg Cu eq	3.78E-04	4.41E-04	5.57E-04
Fossil resource scarcity	FSP	kg oil eq	3.90E-01	1.23E-01	2.76E-01
Water consumption	WCP	m3	1.83E-04	8.41E-03	2.17E-03

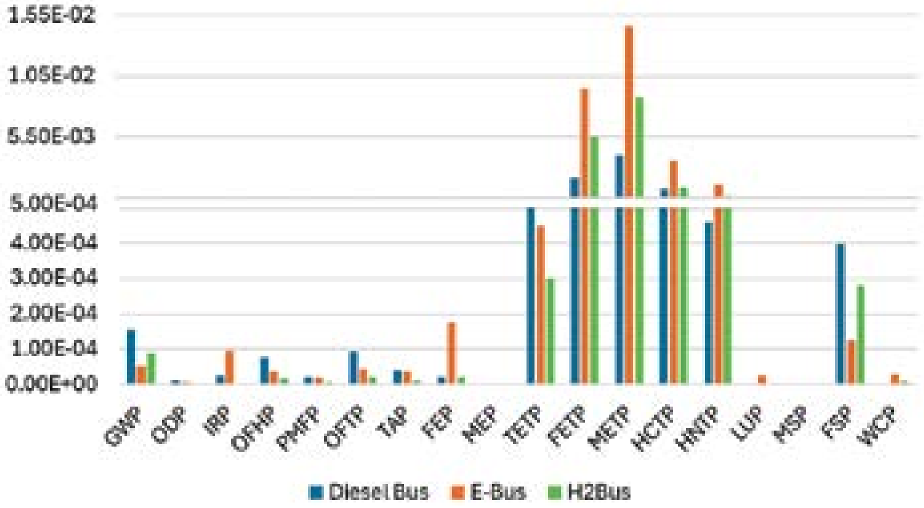

FIGURE 1. ReCiPe Midpoint (H) normalized results for 1 passenger.km by Diesel Bus, E-Bus and H2Bus.

Table 2 reports the ReCiPe Endpoint impacts related to the three investigated options. It is clear how the E-Bus and the H2Bus represent better environmental options with much less effect on human health, ecosystems and resource use compared to the Diesel one. The E-Bus in particular show slightly inferior impacts than the H2Bus with respect to human health and resource use.

TABLE 2. ReCiPe Endpoint (H) results for the 1 passenger.km by Diesel Bus, E-Bus and H2Bus.

Damage category	Unit	Diesel Bus	E-Bus operation	H2 Bus operation
Human health	DALY	1.54E-06	7.83E-07	8.13E-07
Ecosystems	species.yr	4.17E-09	3.02E-09	2.06E-09
Resources	USD2013	1.76E-01	3.65E-02	9.85E-02

4. CONCLUSIONS

The balance between environmental impacts and efficiency of urban transportation systems in urban environments is of great relevance and represents an important topic nowadays, in particular in cities heavily interested by touristic flows. This work analysed different solutions for city road transport, comparing diesel buses, electric buses and hydrogen powered buses. The results confirmed the electric and hydrogen buses as the most feasible solutions, and highlighted how the energy mix used within the systems performances is important.

REFERENCES

[1] Bille RA, Jensen KE, Buitenwerf R. Global patterns in urban green space are strongly linked to human development and population density. Urban For Urban Green 2023;86:127980. https://doi.org/10.1016/J.UFUG.2023.127980.
[2] UN-Habitat. World Cities Report 2022. Envisaging the Future of Cities. 2022.
[3] Santagata R, Zucaro A, Viglia S, Ripa M, Tian X, Ulgiati S. Assessing the sustainability of urban eco-systems through Emergy-based circular economy indicators. Ecol Indic 2020;109. https://doi.org/10.1016/j.ecolind.2019.105859.
[4] Baumann O, Brooks-Cederqvist B. Multimodal assessment of effects of urban environments on psychological wellbeing. Heliyon 2023;9:e16433. https://doi.org/10.1016/J.HELIYON.2023.E16433.
[5] Klepej D, Marot N. Considering urban tourism in strategic spatial planning. Annals of Tourism Research Empirical Insights 2024;5:100136. https://doi.org/10.1016/J.ANNALE.2024.100136.
[6] ANM s.p.a. La Carta della Mobilità 2023. 2023.
[7] ISO. UNI EN ISO 14040 - Environmental management - Life cycle assessment - Principles and framework 2006.
[8] ISO. UNI EN ISO 14044: Life cycle assessment — Requirements and guidelines 2006.
[9] Oele M. What’s new in SimaPro 9.1? - SimaPro 2020.
[10] Wernet G, Bauer C, Steubing B, Reinhard J, Moreno-Ruiz E, Weidema B. The ecoinvent database version 3 (part I): overview and methodology. Int J Life Cycle Assess 2016:pp.1218–1230.
[11] Huijbregts MAJ, Steinmann ZJN, Elshout PMF, Stam G, Verones F, Vieira MDM, et al. ReCiPe 2016 v1.1 A harmonized life cycle impact assessment method at midpoint and endpoint level Report I: Characterization. Bilthoven, The Netherlands: 2017.
[12] BYD. Environmental Product Declaration - Electric bus - K9UD. 2023.
[13] Agostinho F, Serafim Silva E, Silva CC da, Almeida CMVB, Giannetti BF. Environmental performance for hydrogen locally produced and used as an energy source in urban buses. J Clean Prod 2023;396:136435. https://doi.org/10.1016/J.JCLEPRO.2023.136435.

Sixth International Conference on Computational Methods for Energy and Thermal Problems
ThermaEComp2024, Sept. 9-11, 2024, Budva, Montenegro
N. Massarotti, P. Nithiarasu, and I. Vušanović (Eds.)

PREDICTION OF CO_2 EMISSIONS INSIDE A BUILBING WITH MACHINE LEARNING BASED ON EXPERIMENTAL DATA

Eugenia Rossi di Schio, Vincenzo Ballerini, Christian Sentimenti, Paolo Valdiserri
Alma Mater Studiorum – University of Bologna. Department of Industrial Engineering DIN. Viale Risorgimento 2, I-136 Bologna, Italy. eugenia.rossidischio@unibo.it; vincenzo.ballerini2@unibo.it; christian.sentimenti@studio.unibo.it; paolo.valdiserri@unibo.it

ABSTRACT

Controlling CO_2 emissions in buildings is of vital importance for the indoor air quality of the people who inhabit them. However, it is not always possible to have CO_2 sensors, and therefore air exchange must occur using other information. In this paper, we implement a machine learning method to derive predictive information about CO_2 from experimental data. The measurements, primarily of temperature and relative humidity, were taken within an apartment, in this initial analysis focusing specifically on the living area. A decision tree method was then applied by employing a Matlab script, to derive the CO_2 emissions. The obtained results were compared with experimental CO_2 emission data, showing an excellent agreement.

Key Words: *Machine learning, Decision Tree, CO_2 emissions, Temperature, Relative humidity.*

1. INTRODUCTION

In enclosed environments, the concentration of CO_2 can increase rapidly if there is inadequate ventilation to remove exhaled air and replace it with fresh air from the outside. Elevated concentrations of CO_2 can lead to fatigue, headaches, and difficulty concentrating, negatively impacting the well-being and productivity of occupants. Therefore, monitoring and controlling CO_2 levels in enclosed spaces is crucial to ensuring a healthy and comfortable environment [1-3].

Monitoring and controlling CO_2 levels is not always simple: indeed, experimental measurements require economic investments and especially infrastructure for sensors, and therefore, are not always easily achievable. In this framework, predictive models can provide a valid alternative and guide CO_2 reduction activities, such as opening windows or introducing forced ventilation. This aspect is even more interesting when activities with low repeatability occur in buildings, such as apartments [4]. In a school [5-6], for example, predicting behaviours based on schedules is easier. On the contrary, it is more difficult to have repeatable behaviours in a lived-in house, making predictive models even more important.

We focus on the decision tree among the machine learning predictive models in the present work. As is well known, decision trees are powerful tools for classification and regression tasks, and they are known for their intuitive structure and ability to handle diverse data types. Each node in a decision tree represents a feature, and branches depict possible outcomes, leading to leaf nodes with class labels or numerical values. Constructing a decision tree involves recursively selecting features that maximise data homogeneity using metrics like Gini impurity or information gain. However, decision trees are prone to overfitting, mitigated by techniques like pruning or ensemble methods. Despite their simplicity, decision trees find applications across various domains due to their interpretability and effectiveness in capturing complex decision boundaries, and offer accessible yet powerful solutions to diverse problems. Decision tree models have recently been applied to HVAC contexts [7-8], but not to forecast carbon dioxide emissions.

In the present paper, we apply the decision tree method to predict CO_2 emissions inside an apartment based on experimental data of temperatures and relative humidity.

2. MATERIALS AND METHODS

This analysis aims to apply a machine learning algorithm to predict carbon dioxide emissions, starting from experimentally collected data. The measures were performed on a residential building located in Bologna, Italy (latitude 44°29′38″, longitude 11°20′34″). This apartment, depicted in Figure 1(a) for its floor plan and Figure 1(b) for its 3D view, occupies the ground floor of a four-story condominium constructed in 1992. Featuring an independent entrance, the apartment comprises three distinct thermal zones: an entrance/living area (covering 24.5 m^2), a bedroom (spanning 7.2 m^2), and a windowless bathroom (with a floor area of 7.0 m^2). The total floor area of the apartment measures 38.7 m^2, with a room height of 3.00 m, except for the entrance area, where a false ceiling reduces the height to 2.70 m. Positioned above garages, the apartment has another unit above (also constituting a heated thermal zone), and it is surrounded by three external walls, and one side facing the unheated stairwells of the condominium. The net heated volume of the apartment is 112.4 m^3 (with a gross volume of 160.2 m^3), and the gross dispersing surface S (which includes surfaces facing the outside and unheated rooms) measures 140.5 m^2, resulting in an S/V ratio of 0.88. Details regarding the main envelope elements are provided in Table 1. We focused on the "living room".

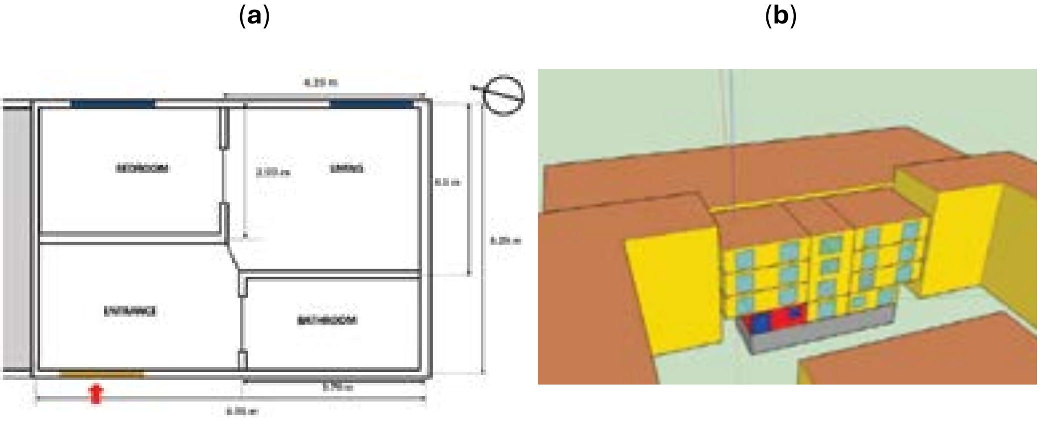

FIGURE 1. The layout of the apartment (a) and the position of the apartment in the building block: the analysed apartment is depicted in red, while the grey construction represents the underground garages (b).

Component	Thickness [m]	U-value [W/(m^2 K)]
Dividing wall	0.10	2.074
External walls	0.30	0.667
Inter-floor	0.42	0.595

TABLE 1. Main features of the envelope elements

The apartment is fully equipped with sensors, namely:

- 10 kOhm Negative Temperature Coefficients (NTC) at 25°C with 1% accuracy [9];
- Temperature and humidity sensors DHT11 and AHT10 [10, 11];
- CO2 sensor MHZ14A [12];
- BME 680 gas sensor [13].

The readings from these sensors are taken by Wi-Fi microcontrollers based on ESP8266 [14].

In detail, the sensor MHZ14A measures the CO_2 concentration in ppm, with an uncertainty of ± (50 ppm + 5% reading value). A detailed explanation of the experimental setup is reported in [15].

The available data are the air temperature measured in the living room, at ceiling level (260 cm high), at person level (150 cm from the floor), and at ankles level (15 cm from the floor), as well as the relative humidity, the atmospheric pressure and the air conductivity (employing BME680 gas sensor [15]). The collected data display a granulometry of 1 measure per minute approximatively. Experimental data on CO_2 emissions in ppm are also available and used only to test the effectiveness of the proposed methodology. We applied the decision tree methodology via a Matlab script.

3. RESULTS

In Figure 2, a comparison between the predicted results and the experimental benchmark data is reported. Data relating to a linear forecasting model, whose formula is shown in eq. (1), data relating to a nonlinear model (eq. 2), and data relating to the forecast model that uses the decision tree were considered. The values of the coefficient of determination R^2 were respectively 0.408, 0.422, and 0.900, while the RMSE was 431 ppm, 425 ppm and 152 ppm respectively. The decision tree model has therefore proven to be very accurate in predicting CO_2.

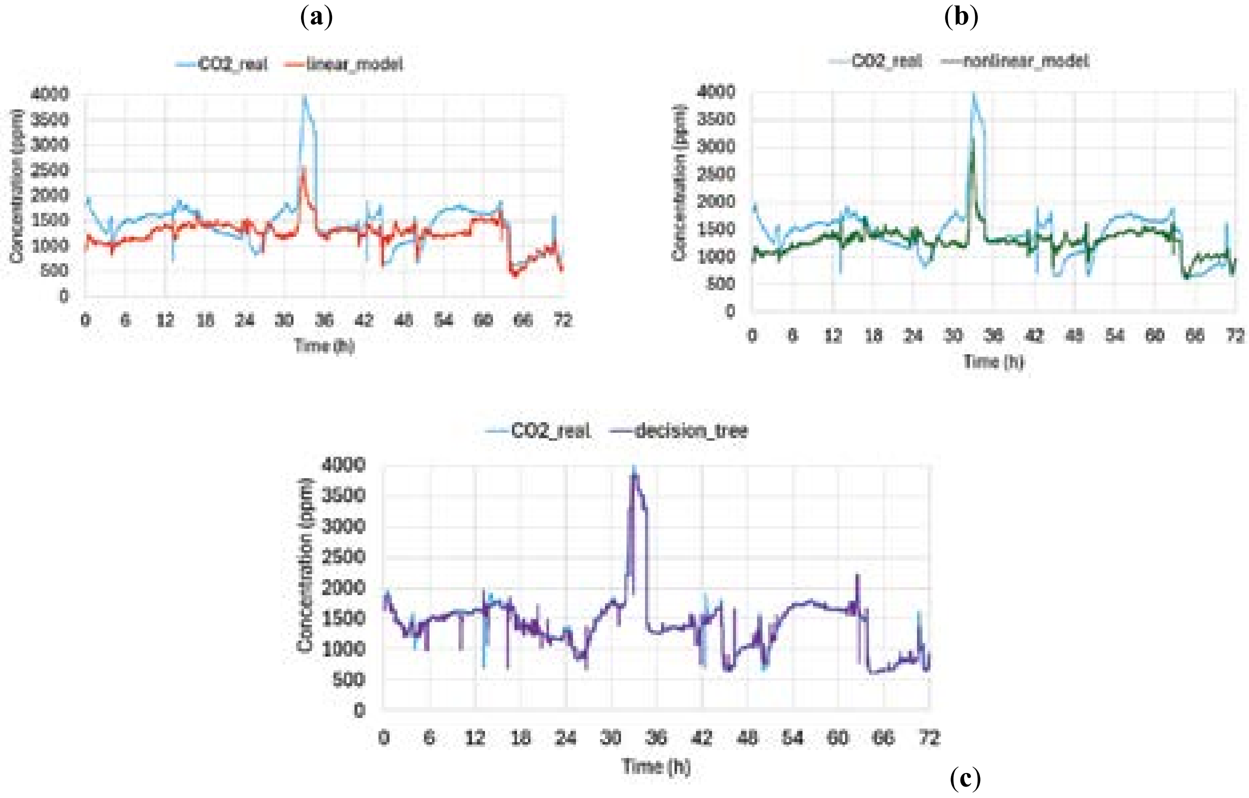

FIGURE 2. Comparison between experimental and predicted data for a linear model (**a**), a non-linear model (**b**) and the decision tree model (**c**).

In eqs. (1) and (2), b_i represents constant coefficients, while the other terms refers to the predictors.

$$y_{co2} = b_1 RH_i + b_2 t_{125,i} + b_3 t_{15,i} + b_4 P_i + b_5 \tag{1}$$

$$y_{co2} = b_1 + b_2 RH_i + b_3 * (t_{125,i} - t_{15,i}) + b_4 P_i + b_5 (t_{125,i} - t_{15,i})^2 + b_6 \exp(b_7 RH_i + b_8 (t_{125,i} - t_{15,i})) \tag{2}$$

4. CONCLUSIONS

In this study, we employed a machine learning approach to extract predictive insights regarding CO_2 levels from experimental data. Data were collected from measurements within an apartment located in Bologna, and were primarily centered on temperature and relative humidity measured in the living area. Subsequently, predictions via a Matlab script to estimate CO_2 emissions were made by employing a linear model, a non-linear model and a decision tree algorithm. Comparison with experimental CO_2 emission data revealed a strong concordance, validating our methodology and revealing that the decision tree algorithm ensures the best fit. In this case, we obtained a coefficient of determination R^2=0.900. Further analysis will investigate the dependence of the predicted results on the set of experimental data available, as well as the use of different learning machine algorithms.

REFERENCES

[1] B. Dong, V. Prakash, F. Feng, and Z. O'Neill, A review of smart building sensing system for better indoor environment control. *Energy and Buildings 199*, 29-46, 2019.

[2] N. Mahyuddin, and H. Awbi, A review of CO2 measurement procedures in ventilation research. *International Journal of Ventilation* 10(4), 353-370, 2012.

[3] G. Marques, C.R. Ferreira, and R. Pitarma, Indoor air quality assessment using a CO2 monitoring system based on internet of things. *Journal of medical systems* 43(3), 67, 2019.

[4] G. Guyot, M.H. Sherman and I.S. Walker, Smart ventilation energy and indoor air quality performance in residential buildings: A review. *Energy and Buildings* 165, 416-430, 2018.

[5] V. Ballerini, E. R. di Schio, P. Valdiserri, C. and M. Dongellini, A Long-Term Dynamic Analysis of Heat Pumps Coupled to Ground Heated by Solar Collectors. *Applied Sciences* 13(13), 7651, 2023.

[6] V. Ballerini, B. Lubowicka, P. Valdiserri, D.A. Krawczyk, B. Sadowska, M. Kłopotowski, and E.R. di Schio, The Energy Retrofit Impact in Public Buildings: A Numerical Cross-Check Supported by Real Consumption Data. *Energies* 16(23), 7748, 2023.

[7] R. Yan, Z. Ma, Y. Zhao, …, and G. Kokogiannakis, G.,A decision tree based data-driven diagnostic strategy for air handling units. *Energy and Buildings* 133, 37-45, 2016.

[8] A. Kusiak, M. Li, and F. Tang, Modeling and optimization of HVAC energy consumption. *Applied Energy*, 87(10), 3092-3102, 2010.

[9] Conrad Electronic SE. NTC, Datasheet: https://www.mouser.com/datasheet/2/758/DHT11-Technical-Data-Sheet-Translated-Version-1143054.pdf (Accessed on May 14, 2024).

[10] Mouser Electronics. DHT11 Humidity and temperature sensor: https://www.mouser.com/datasheet/2/758/DHT11-Technical-Data-Sheet-Translated-Version-1143054.pdf (Accessed on May 14, 2024).

[11] ASAIR AHT10 Manual: https://server4.eca.ir/eshop/AHT10/Aosong_AHT10_en_draft_0c.pdf (Accessed on May 14, 2024).

[12] Winsen. Intelligent Infrared Carbon Dioxide Module (Model: MH-Z14A): https://www.winsen-sensor.com/d/files/MH-Z14A.pdf (Accessed on May 14, 2024).

[13] BOSCH. BME680 Low power gas, pressure, temperature & humidity sensor: https://cdn-shop.adafruit.com/product-files/3660/BME680.pdf (Accessed on May 14, 2024).

[14] AZ-Delivery C1 Mini NodeMcu, based on ESP8266: https://cdn.shopify.com/s/files/1/1509/1638/files/Betriebsanleitung-AZ-C1miniV1.2_2.pdf?v=1590603445 (Accessed on May 14, 2024).

[15] V. Ballerini, C. Biserni, G. Fabbri, P. Guidorzi, E.R. di Schio, and P. Valdiserri, The Use of Arduino and PID Control Approach for the Experimental Setup of HVAC Temperature Testing, *Journal of Robotics and Control (JRC)* 5(2), 482-489, 2024.

Sixth International Conference on Computational Methods for Energy and Thermal Problems
THERMAECOMP2024, Sept. 9-11, 2024, Budva, Montenegro
N. Massarotti, P. Nithiarasu and I. Vušanović (Eds.)

All Mach number two-phase Riemann solver for compressible flows based on six-equation model

Ghanshyam Bharate, J.C. Mandal
Aerospace Engineering Department, IIT Bombay, India, mandal@iitb.ac.in

ABSTRACT

This paper presents the development of an all-Mach-number Riemann solver for two-phase flow using a six-equation model. The formulation includes a straightforward low Mach number correction based on velocity reconstruction. The effectiveness of the proposed correction is demonstrated by solving a standard two-phase subsonic nozzle problem.

Key Words: *Diffuse interface method, two-phase flows, six-equation model, low-Mach number, Riemann solver.*

1. INTRODUCTION

The diffuse interface method (DIM) has gained popularity for simulating flows involving dispersive multiphase mixtures and interfaces separating pure fluids. One major advantage of using DIM is its ability to handle compressible multiphase flows with significant pressure and density gradients. However, the method faces efficiency and accuracy issues in the incompressible limit $(Ma \to 0)$ [1]. The primary cause of this low Mach number problem is the incorrect scaling of pressure. Asymptotic analysis of the original governing equations in the limit $Ma \to 0$ suggests that pressure should scale with the square of the Mach number [1]. Nevertheless, numerical results at low Mach numbers $(Ma << 1)$ do not align with this trend.

Previous researchers [1, 2] have employed preconditioning approaches to address the unphysical behavior of DIM in the low Mach number limit $(Ma \to 0)$. While preconditioning methods can mitigate the low Mach number problem, they come with drawbacks such as the global cutoff Mach number problem and severe restrictions on computational time steps. In this work, we present a straightforward solution procedure for computing accurate low Mach number two-phase flows using the diffuse interface method.

2. GOVERNING EQUATIONS

There are various models of DIM existing in literature [3]. Because of the robustness and volume fraction positivity the six-equation model found to be a better choice among the different multiphase models [4]. The system of equations for single-velocity six-equation model can be written as

$$\frac{\partial \mathbf{U}}{\partial t} + \nabla \cdot (\mathbf{F}, \mathbf{G}) + \sigma = \mathbf{S}$$

$$\mathbf{U} = \begin{bmatrix} \alpha_1 \\ \alpha_j \rho_j \\ \rho u \\ \rho v \\ \alpha_j \rho_j e_j \end{bmatrix}, \quad \mathbf{F} = \begin{bmatrix} 0 \\ \alpha_j \rho_j u \\ \rho u^2 + p \\ \rho uv \\ \alpha_j \rho_j e_j u \end{bmatrix}, \quad \mathbf{G} = \begin{bmatrix} 0 \\ \alpha_j \rho_j v \\ \rho uv \\ \rho v^2 + p \\ \alpha_j \rho_j e_j v \end{bmatrix}$$
$$\sigma(\mathbf{U}) = \begin{bmatrix} \mathbf{u} \cdot \nabla \alpha \\ 0 \\ 0 \\ 0 \\ \alpha_j p_j \nabla \cdot \mathbf{u} \end{bmatrix}, \quad \mathbf{S}(\mathbf{U}) = \begin{bmatrix} \mu (p_1 - p_2) \\ 0 \\ 0 \\ 0 \\ (-1)^j \mu p_I (p_1 - p_2) \end{bmatrix} \tag{1}$$

Here $\alpha_j, \rho_j, p_j, e_j$ are the volume fraction, density, pressure, and specific internal energy of the phase j, respectively. The velocity vector is represented by $\mathbf{u} = (u, v)$. ρ and p denotes the mixture density and mixture pressure, respectively. The non-conservative terms accommodated inside the σ vector. The single-velocity model also contain some pressure relaxation terms, which are grouped into source vector $\mathbf{S}$. The parameter μ controls the rate of relaxation. For computing equilibrium flows, the single-velocity model (1) is solved in the limit of stiff pressure relaxation $(\mu \to \infty)$.

3. NUMERICAL METHOD

In order to solve above system of equations (1) with relaxation terms, the operator splitting approach is used. In this method the solution at $n+1$ time level is obtained using hyperbolic $(\mathscr{L}_H)$ and relaxation operator $(\mathscr{L}_R)$ sequentially. The solution at $n+1$ time level in terms of operators can be written as

$$\begin{gathered} \mathbf{U}^{n+1} = \mathscr{L}_R \mathscr{L}_H \left(\mathbf{U}^n\right) \\ \text{where} \quad \mathscr{L}_H : \frac{\partial \mathbf{U}}{\partial t} + \nabla \cdot (\mathbf{F}, \mathbf{G}) + \sigma(\mathbf{U}) = 0, \quad \mathscr{L}_R : \frac{\partial \mathbf{U}}{\partial t} = \mathbf{S} \end{gathered} \tag{2}$$

In the first step, the multiphase system (1) is solved without any relaxation terms using an hyperbolic operator. The finite volume discretization of mass and momentum conservation equations appearing in the system (1) can be written as

$$\begin{gathered} \frac{\mathrm{d}\mathbf{Q}_i}{\mathrm{d}t} + \frac{1}{\Omega_i} \sum_{l=1}^{4} \mathrm{T}_{il}^{-1} \mathbf{F}\left(\hat{\mathbf{Q}}_L, \hat{\mathbf{Q}}_R\right) \Delta s_{il} = 0 \\ \hat{\mathbf{Q}} = \mathrm{T}_{il}\mathbf{Q} = \begin{bmatrix} \alpha_1\rho_1 \\ \alpha_2\rho_2 \\ \rho u_n \\ \rho u_t \end{bmatrix}, \quad \mathrm{T}_{il} = \begin{bmatrix} 1 & 0 & 0 & 0 \\ 0 & 1 & 0 & 0 \\ 0 & 0 & n_x & n_y \\ 0 & 0 & -n_y & n_x \end{bmatrix} \end{gathered} \tag{3}$$

Here $\hat{\mathbf{Q}}_L$ and $\hat{\mathbf{Q}}_R$ are the set of normal state variables at the left and right side of the cell interface and T is the rotational invariance matrix. For volume fraction and phasic internal energy equations, semi-discrete formulations can be written as

$$\begin{gathered} \frac{d(\alpha_1)_i}{dt} + \frac{1}{\Omega_i} \sum_{l=1}^{4} (u_n)_i \, (\alpha_1)_{il} \, \Delta s_{il} = 0 \\ \frac{d(\alpha_j\rho_j e_j)_i}{dt} + \frac{1}{\Omega_i} \sum_{l=1}^{4} \left[(\alpha_j\rho_j e_j u_n)_{il} + (\alpha_j p_j)_i \, (u_n)_{il}\right] \Delta s_{il} = 0, \quad j = 1, 2 \end{gathered} \tag{4}$$

In above formulation (4), the terms with subscript i are computed using cell averaged variables. On the other hand, quantities with subscript il are obtained at the cell interface. The cell interface quantities in (3) and (4) can be obtained using any Riemann solver. In this work we are using HLLC solver. The detailed description of the solver and other required expressions can be found in the literature [4]. Since, the conventional Riemann solver is known to produce undesired results at low Mach number, a low Mach number correction is proposed in the subsequent section.

4. Low Mach number correction

Researchers [5, 6] have found that scaling the velocity difference across the cell interface can correct the unphysical behavior observed at low Mach numbers. In order to implement this idea, we use reconstructed velocities suggested by the Thornber et al. [7] in left $\mathbf{Q}_L$ and right state $\mathbf{Q}_R$

variables. The expressions for the reconstructed normal and tangential velocities are as follows:

$$
\begin{aligned}
u^r_{nL} &= \frac{u_{nR}+u_{nL}}{2} - f(M)\frac{u_{nR}-u_{nL}}{2}, \quad & u^r_{tL} &= \frac{u_{tR}+u_{tL}}{2} - f(M)\frac{u_{tR}-u_{tL}}{2} \\
u^r_{nR} &= \frac{u_{nR}+u_{nL}}{2} + f(M)\frac{u_{nR}-u_{nL}}{2}, \quad & u^r_{tR} &= \frac{u_{tR}+u_{tL}}{2} + f(M)\frac{u_{tR}-u_{tL}}{2}
\end{aligned}
\tag{5}
$$

Here, $f(M)$ is function of local Mach number, which can be taken as

$$
f(M) = \min\left(1, \max\left(\frac{\sqrt{u^2_{nL}+u^2_{tL}}}{a_L}, \frac{\sqrt{u^2_{nR}+u^2_{tR}}}{a_R}\right)\right) \tag{6}
$$

5. RESULTS

Given that the current solver reverts to the original HLLC solver presented in reference [4], which demonstrated accurate results for high Mach number test cases, we have focused our attention on very low Mach number flows to verify its performance. We considered a two-phase nozzle problem, in which water-air mixture flows in the two-dimensional symmetric nozzle at very low Mach number. The nozzle geometry is taken from the similar test case presented in the literature [1]. The computational domain is discretized with 100 × 25 quadrilateral cells. The inflow water-air mixture is defined as

$$
\alpha_{air} = 10^{-3}, \quad \rho_{air} = 1\ \text{kg/m}^3, \quad \rho_{water} = 1000\ \text{kg/m}^3, \quad P_0 = 10^6\ \text{Pa}
$$

A fixed pressure P_0 is imposed on the outlet. The inflow velocity is based on the selected Mach number. The numerical results obtained with and without low Mach number correction are compared in the FIGURE 1. As the nozzle is symmetric about the middle vertical axis, the flow inside the nozzle should also be symmetric. However, the numerical results by standard numerical scheme (on the left in FIGURE 1) does not follow the exact solution. From the pressure contours shown on the right in FIGURE 1, it becomes apparent that the correction presented in this work rectifies the accuracy problem of numerical scheme at very low Mach number ($M = 0.01$).

FIGURE 1. Pressure contours for subsonic nozzle problem

In addition to the qualitative comparison, quantitative results are also presented in the FIGURE 2. The plots shown in the FIGURE 2 contains pressure profile of top and bottom boundary of the nozzle. Additionally, average pressure values over the channel height are also computed and compared with the exact quasi-one dimensional solution. The comparison presented on the right in FIGURE 2 suggests that numerical results obtained with the low Mach number correction are in agreement with the exact solution.

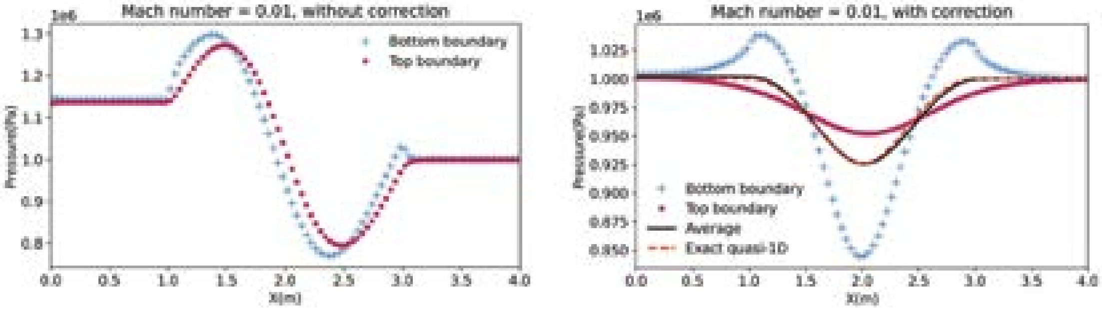

FIGURE 2. Pressure profiles for subsonic nozzle problem

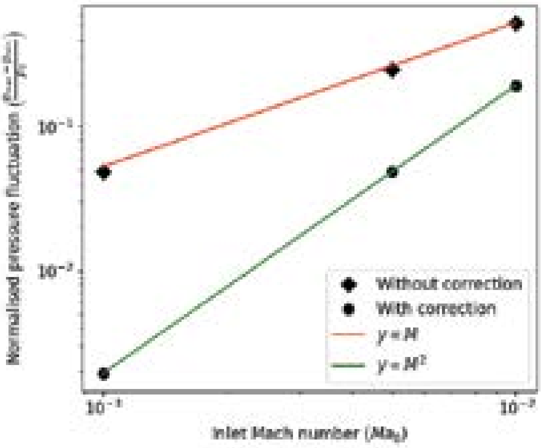

FIGURE 3. Log-log plot of computed normalised pressure fluctuations vs inlet Mach number

To demonstrate that the pressure scaling in the numerical results exhibits the correct behavior, we have plotted the variation of normalized fluctuation with respect to inlet Mach number in FIGURE 3. As shown in FIGURE 3, the pressure scaling of the numerical results obtained after applying the low Mach number correction follows the order of the square of the Mach number, which aligns with the correct behavior predicted by asymptotic analysis. [1].

6. CONCLUSIONS

This paper presents a straightforward correction based on velocity reconstruction for computing low Mach number two-phase flows using a six-equation model. A comparison of numerical results obtained with and without the low Mach number correction demonstrates that the proposed method effectively addresses the issues encountered at very low Mach numbers.

REFERENCES

[1] Marica Pelanti. Low mach number preconditioning techniques for roe-type and hllc-type methods for a two-phase compressible flow model. *Applied Mathematics and Computation*, 310:112–133, 2017.

[2] S LeMartelot, Boniface Nkonga, and Richard Saurel. Liquid and liquid–gas flows at all speeds. *Journal of Computational Physics*, 255:53–82, 2013.

[3] Richard Saurel and Carlos Pantano. Diffuse-interface capturing methods for compressible two-phase flows. *Annual Review of Fluid Mechanics*, 50(1):105–130, 2018.

[4] Richard Saurel, Fabien Petitpas, and Ray A. Berry. Simple and efficient relaxation methods for interfaces separating compressible fluids, cavitating flows and shocks in multiphase mixtures. *J. Comput. Phys.*, 228:1678–1712, 2009.

[5] Felix Rieper. A low-mach number fix for roe's approximate riemann solver. *Journal of Computational Physics*, 230(13):5263–5287, 2011.

[6] Kai Oßwald, Alexander Siegmund, Philipp Birken, Volker Hannemann, and Andreas Meister. L2roe: a low dissipation version of roe's approximate riemann solver for low mach numbers. *International Journal for Numerical Methods in Fluids*, 81(2):71–86, 2016.

[7] Ben Thornber, Andrew Mosedale, Dimitris Drikakis, David Youngs, and Robin JR Williams. An improved reconstruction method for compressible flows with low mach number features. *Journal of computational Physics*, 227(10):4873–4894, 2008.

Sixth International Conference on Computational Methods for Energy and Thermal Problems
THERMAECOMP2024, Sept. 9-11, 2024, Budva, Montenegro
N. Massarotti, P. Nithiarasu, and I. Vušanović (Eds.)

AN ELECTRONEUTRALITY-PRESERVING APPROACH FOR MULTI-IONIC TRANSPORT USING FINITE ELEMENT METHODS APPLIED TO THE ELECTROLYTIC NEUTRAL PICKLING OF STAINLESS STEEL

Alvaro Bossio, Maarten Blommaert, Martine Baelmans
Department of Mechanical Engineering - KU Leuven, Celestijnenlaan 300, 3001 Leuven, Belgium,
alvaromanuel.bossiocastro@kuleuven.be,

Jan Fransaer
Department of Material Science - KU Leuven, Kasteelpark Arenberg 44, 3001 Leuven, Belgium,
jan.fransaer@kuleuven.be,

Ruben Gielen
Aperam Stainless Belgium, Swinnenwijerweg 5, 3600 Genk, Belgium,
ruben.gielen@aperam.com

ABSTRACT

A numerical scheme is proposed for the solution of the tertiary current distribution in the electrolytic neutral pickling of stainless steel. The mathematical model accounts for the transport of $N \geq 2$ ionic species subjected to convection due to a known velocity field, molecular diffusion, and electromigration due to an unknown electric potential field. The concentrations of the ionic species and the electric potential are also coupled through the electroneutrality condition. Boundary conditions obey the Tafel equation. Concentration overpotentials were found to represent in general a small fraction of the cell voltage for typical industrial conditions. The effects of the concentration gradients start to be appreciable for $Pe < 10^8$, and $i_{avg}^{cath} > 3$ kA m^{-2}.

Key Words: *Multi-ionic transport, Concentration overpotential, Electrolytic pickling, Finite Elements.*

1. INTRODUCTION

Electrolytic neutral pickling (ENP) is a process used in the production of flat stainless steel to remove undesired oxides formed on the material surface during annealing. Compared to alternative technologies such as electrolytic acid pickling, or molten salt pickling, ENP barely affects the underlying alloy, and constitutes, in general, a lower hazardous process both for personnel and facilities [1]. However, ENP suffers from poor current and energy efficiencies [2], which has caused it to become the bottleneck process for a wide range of products.

Numerical simulations of the ENP process have been addressed in the past with different levels of complexity. Primary (PCD) and secondary current distribution (SCD) models [3] are simple, but assume concentrations of ionic species to be uniform. The effect of concentration gradients in the electrolyte, however, may be important at high current densities, small electrode-to-strip separation, and low strip velocity. Tertiary current distribution (TCD) models account for these effects. TCD problems share some similarities to conjugate heat transfer problems, as both types of problems require the coupled solution of a Laplace equation in a solid (the electrode), and the transport of one or more scalar equations in the fluid (the electrolyte). However, TCD problems include additional challenges. First, the ionic species present in the electrolyte are not only transported by diffusion and convection, but also by electromigration, due to the electric field developed between the two terminal electrodes. This electric field is unknown a priori and should satisfy the electroneutrality condition (i.e. net charge in the electrolyte is zero). Second, Schmidt numbers *Sc* (i.e. analogous to *Pr* in heat transfer) for ionic species are around 10^3, thus diffusion boundary layers appear even in conditions of creeping flow. Finally, the conjugate conditions at the electrode/electrolyte interface often include nonlinear relations arising from electrochemical kinetics theory.

TCD models have already been explored for ENP [4]. However, the solution approach proposed earlier has several limitations. The electroneutrality condition is imposed by excluding an arbitrary ionic species. As a result, the solution depends on the choice of the excluded species, and the conservation of the excluded species is violated. Moreover, an *ad-hoc* isotropic artificial diffusion (IAD) stabilization scheme is used for the transport of the ionic species. This scheme cannot be directly generalized to other geometries, and is excessively diffusive, which may lead to an underestimation of the concentration gradients at the electrode surfaces.

2. DESCRIPTION OF THE MODEL

The present work considers a simplified ENP cell similar to that proposed in Ref. [4]. The cell is assumed sufficiently long in the spanwise direction, so that a 2D approximation is valid. The terminal anode and cathode are equipotential and fixed in the upper plate, while the stainless steel moves in the lower plate. The electrolyte between these plates is assumed to follow laminar Couette flow. A schematic representation of the geometry is shown in Figure 1.

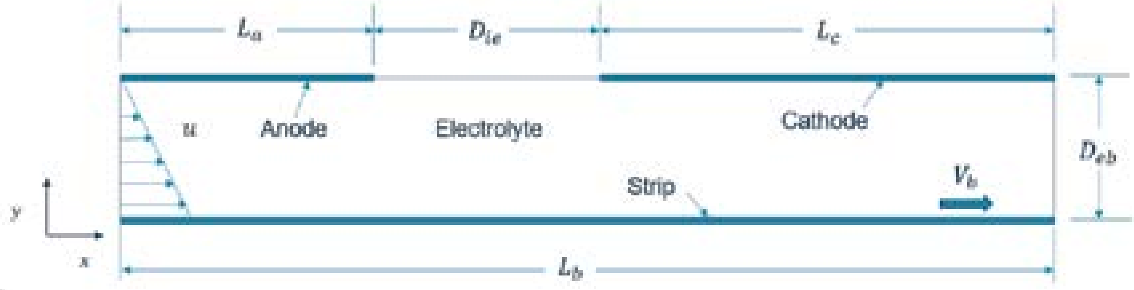

FIGURE 1. Schematic representation of the geometric domain.

The mathematical problem consists of two coupled subproblems. In the stainless steel subdomain, the electrical potential ϕ_s satisfies Laplace's equation. In the electrolyte subdomain, the concentrations of the dissolved species $c_i,\ i = 1, \dots, N$, and the electric potential ϕ_e, which determines the electric field, obey the Nernst-Planck equation, together with the electroneutrality condition. At the surface of the electrode surfaces, the current density $\boldsymbol{j}$ is required to satisfy the Tafel equation [5]. Effects of chemical reactions taking place in the electrolyte are not considered.

The problem is discretized using the open-source finite element solver FEniCS [6]. Some important implementation aspects are given below:

1. Since the electroneutrality condition is not explicit in the electric potential, the linearized subproblem for the electrolyte is a saddle-point problem. To address this problem numerically, an electroneutrality-preserving predictor-corrector scheme [7] is implemented.
2. To avoid the appearance of spurious oscillations, which is a typical issue for convection-dominated problems, SGS stabilization [8] and localized mesh refinement are implemented.

3. RESULTS

Numerical simulations were run for values of average cathodic current density $i_{\text{avg}}^{\text{cath}}$ ranging between 0 and 5 kA m^{-2}, and a Peclet number $Pe = V_b D_{eb} / D_{H^+}$ between 10^8 and 10^{10}. To assess the effect of the concentration gradients, the average concentration overpotential is calculated for each separated electrode surface. Profiles of concentration overpotentials relative to cell voltage at the anode and the cathode are shown in Figure 2. As expected, the contribution of these overpotentials increases as *Pe* decreases, e.g. due to a reduction in the strip velocity or the channel height.

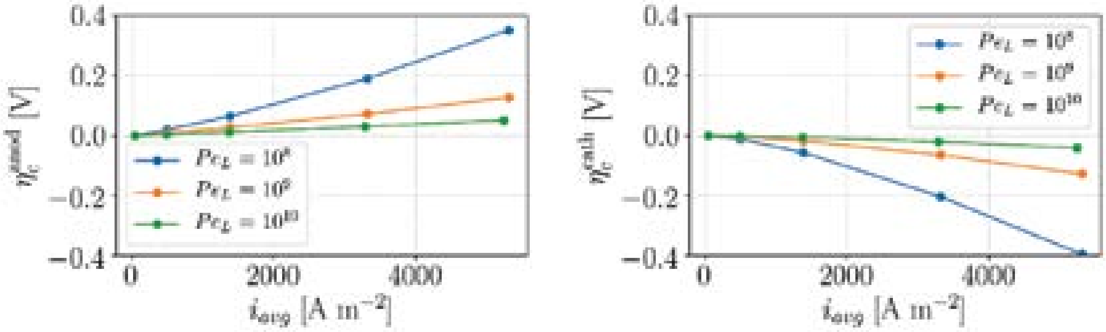

(a) Concentration overpotentials at the anode surface.

(b) Concentration overpotentials at the cathode surface.

FIGURE 2. Concentration overpotentials at the (a) anode surface, and (b) at the cathode surface, as a function of the average current density for different values of *Pe*.

A benchmark between SCD and TCD approximations gives small errors for typical industrial conditions ($Pe \approx 10^9, i_{avg}^{cath} \approx 1$ kA m^{-2}). Appreciable differences ($> 5\%$) are observed for $Pe < 10^8$, and $i_{avg}^{cath} > 3$ kA m^{-2}, as can be seen in Figure 3.

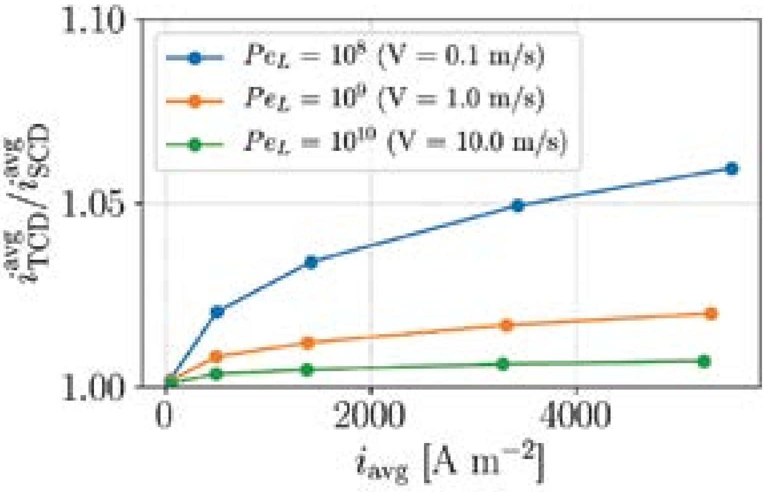

FIGURE 3. Concentration overpotentials at the (a) anode surface, and (b) at the cathode surface, as a function of the average current density for different values of *Pe*.

4. CONCLUSIONS

An electroneutrality-preserving multi-ion transport model was implemented and solved using finite element methods to study the effect of mass-transfer on the electrolytic neutral pickling for stainless steel. The method avoids the choice of an arbitrary species to impose electroneutrality and reduces artificial diffusion with respect to previous solution approaches. Concentration overpotentials were found to represent a small fraction of the cell voltage for typical industrial conditions. The effects of the concentration gradients start to be appreciable for $Pe < 10^8$, and $i_{avg}^{cath} > 3$ kA m^{-2}.

REFERENCES

[1] M. Vynnycky, "Pickling: Electrochemical," in *Encyclopedia of Iron, Steel, and Their Alloys*, no. June, Taylor and Francis, 2016, pp. 2516–2531. doi: 10.1081/e-eisa-120050930.

[2] V. I. Dunaevskii, V. T. Stepanenko, M. Y. Shnol', and L. N. Bespal'ko, "Rate of removal of scale and subscale layer in electrolytic pickling of stainless steels in Na2SO4 solution," *Zaschita Metallov*, vol. 21, no. 3, pp. 431–436, 1985.

[3] N. Ipek, N. Lior, M. Vynnycky, and F. H. Bark, "Numerical and experimental study of the effect of gas evolution in electrolytic pickling," *Journal of Applied Electrochemistry*, vol. 36, no. 12, pp. 1367–1379, 2006, doi: 10.1007/s10800-006-9201-4.

[4] N. Ipek, A. Cornell, and M. Vynnycky, "A mathematical model for the electrochemical pickling of steel," *Journal of the Electrochemical Society*, vol. 154, no. 10, pp. 108–119, 2007, doi: 10.1149/1.2764233.

[5] J. Newman and K. E. Thomas-Alyea, *Electrochemical Systems*. John Wiley, 2004.

[6] A. Logg, K. Mardal, and G. N. Wells, *Automated Solution of Differential Equations by the Finite Element Method. The FEniCS Book*. 2011. doi: 10.1007/978-3-642-23099-8.

[7] Y. -K Kwok and C. C. K. Wu, "Fractional step algorithm for solving a multi-dimensional diffusion-migration equation," *Numerical Methods for Partial Differential Equations*, vol. 11, no. 4, pp. 389–397, 1995, doi: 10.1002/num.1690110407.

[8] G. Bauer, V. Gravemeier, and W. A. Wall, "A stabilized finite element method for the numerical simulation of multi-ion transport in electrochemical systems," *Computer Methods in Applied Mechanics and Engineering*, vol. 223–224, pp. 199–210, 2012, doi: 10.1016/j.cma.2012.02.003.

Sixth International Conference on Computational Methods for Energy and Thermal Problems
THERMAECOMP2024, Sept. 9-11, 2024, Budva, Montenegro
N. Massarotti, P. Nithiarasu, and I. Vušanović (Eds.)

CVFEM SOLUTION FOR THE VORTICITY-STREAM FUNCTION FORMULATION: MATLAB IMPLEMENTATION FOR LID DRIVEN CAVITY FLOW

Esad Tombarević, Milan Šekularac, Igor Vušanović, Uroš Karadžić
University of Montenegro, Faculty of Mechanical Engineering, Džordža Vašingtona bb,
Podgorica 81000, Montenegro
esad.tombarevic@ucg.ac.me, milan.sekularac@ucg.ac.me,
igor.vusanovic@ucg.ac.me, uros.karadzic@ucg.ac.me

ABSTRACT

The Control Volume Finite Element Method (CVFEM) seamlessly merges the geometric versatility of the Finite Element Method (FEM) with the intuitive nature of the Control Volume Method (CVM), rendering it potent for tackling heat and fluid flow complications within intricate domain geometries. This study focuses on discretizing the vorticity-stream function formulation using the CVFEM approach and presents a MATLAB implementation. The code's accuracy is validated against the well-established benchmark of lid-driven cavity flow, incorporating appropriate boundary conditions. Notably, the CVFEM solution exhibits commendable conformity with benchmark solutions across Reynolds numbers of 100 and 400. This work represents a computational stride towards establishing a collocated methodology primed for addressing three dimensional fluid flow challenges.

Key Words: *CVFEM, vorticity-stream function approach, lid driven cavity flow.*

1. INTRODUCTION

In the realm of fluid dynamics, two primary approaches stand out in the quest to understand and simulate flow fields: the direct solution of the Navier-Stokes equations and the vorticity-stream function formulation. The former entails solving the complete set of Navier-Stokes equations, which govern the motion of viscous fluid. This approach provides a comprehensive understanding of fluid behaviour by simultaneously determining the pressure and velocity fields. However, due to the coupled nature of these equations, sophisticated numerical techniques are often required. One prevalent method is the SIMPLE algorithm and its variants, which iteratively solve the discretized equations for velocity and pressure fields [1]. Those algorithms incorporate pressure correction steps to ensure mass conservation and fulfil the continuity equation.

Conversely, the vorticity-stream function formulation offers an alternative perspective by decoupling the velocity and pressure fields, expressing the flow solely in terms of vorticity and stream function. This simplification provides computational advantages, especially in scenarios where rotational structures dominate or when dealing with two-dimensional, incompressible flows.

2. GOVERNING EQUATIONS

The integral form of the governing equation offers a direct path to deriving the discrete equations of the Control Volume Finite Element Method (CVFEM), expressed in terms of nodal values located at the centres of polygonal control volumes. To derive the vorticity equation, one manipulates the momentum balance equations, computing their curl to introduce the vorticity as the curl of the velocity field $\omega = \dfrac{\partial v_y}{\partial x} - \dfrac{\partial v_x}{\partial y}$. This process effectively eliminates pressure from the resulting equations, yielding the vorticity equation, which governs the evolution of vorticity in the flow.

$$\int_V \left[\nabla \cdot (\mathbf{v}\omega) - \nu \nabla^2 \omega\right] dA = 0 \tag{1}$$

The relationship between vorticity and the stream function, defined by $v_x = \dfrac{\partial \psi}{\partial y}$ and $v_y = -\dfrac{\partial \psi}{\partial x}$, can be established through the Poisson equation

$$\nabla^2 \psi = -\omega \tag{2}$$

The integral form of the equations (1) and (2) suitable for CVFEM discretization, is obtained by using the divergence theorem to transform the volume to surface integral

$$\int_A \left[\omega \mathbf{v} \cdot \mathbf{n} - \nu \nabla \omega \cdot \mathbf{n}\right] dA = 0 \tag{3}$$

$$-\int_V \omega dA = \int_A \nabla \psi \cdot \mathbf{n} dA \tag{4}$$

The vorticity equation (3) can be interpreted as a steady-state advection-diffusion equation, while the stream function equation (4) can be regarded as a steady-state diffusion equation with a volume source. The general form of the discretized equations is:

$$\left[a_i^{\omega} + B_{C_i}^{\omega}\right]\omega_i = \sum_{j=1}^{n_i} a_{i,j}^{\omega}\omega_{S_{i,j}} + B_{B_i}^{\omega} \tag{5}$$

$$\left[a_i^{\psi} + Q_{C_i}^{\psi} + B_{C_i}^{\psi}\right]\psi_i = \sum_{j=1}^{n_i} a_{i,j}^{\psi}\psi_{S_{i,j}} + Q_{B_i}^{\psi} + B_{B_i}^{\psi} \tag{6}$$

where *B*'s account for boundary conditions and *Q*'s for the source term. Determining the coefficients of the discretized equations and the treatment of boundary conditions and sources is beyond the scope of this extended abstract. Details can be found in Voller [2]. The vorticity and stream function equations are coupled via the boundary condition in equation (5) and the source term in equation (6), and are solved iteratively in a nested loop until appropriate convergence is achieved.

3. RESULTS

The accuracy of the analysis, solution procedure, and computer program was assessed by comparing the results with well-known numerical benchmark solution by Ghia, Ghia and Shin (1982) for lid-driven flow in a square cavity. The benchmark employs the coupled strongly implicit multigrid (CSI-MG) method to solve the vorticity-stream function formulation of the two-dimensional, incompressible Navier-Stokes equations. Their seminal work provides detailed insights into the flow characteristics, including streamline patterns for primary, secondary, and additional corner vortices, vorticity contours, as well as tabulated data for the v_x-velocity along a vertical line, v_y-velocity along a horizontal line passing through the geometric centre of the cavity, and vorticity along the moving boundary. The comparison serves as a robust validation of the methodology and implementation, ensuring the fidelity of results against a well-established benchmark in the field.

Comparisons are presented below for Re=100 and Re=400, which are well below Re=1000. Under these conditions, viscous effects dominate over inertial effects.

Figures 1 and Figure 2 depict the streamline patterns, whereas Figures 3 and Figure 4 illustrate the vorticity patterns. Consistently, identical contour levels were applied for both the CVFEM and the benchmark solution across all cases. It can be concluded that the qualitative agreement between the CVFEM and the benchmark solution, regarding contour levels and the representation of primary and additional vortices, is very good.

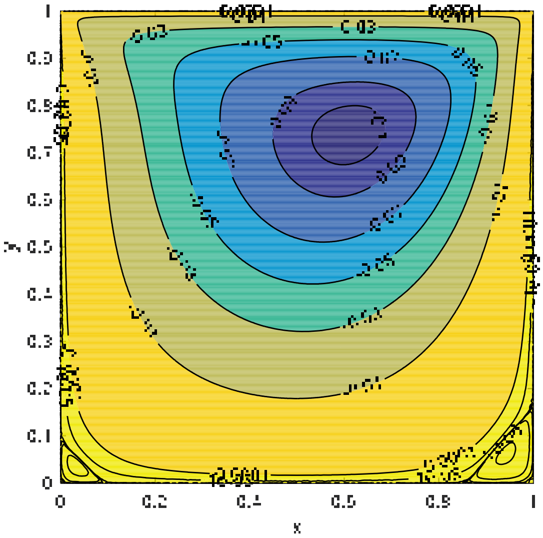

FIGURE 1. Streamline patterns for Re=100

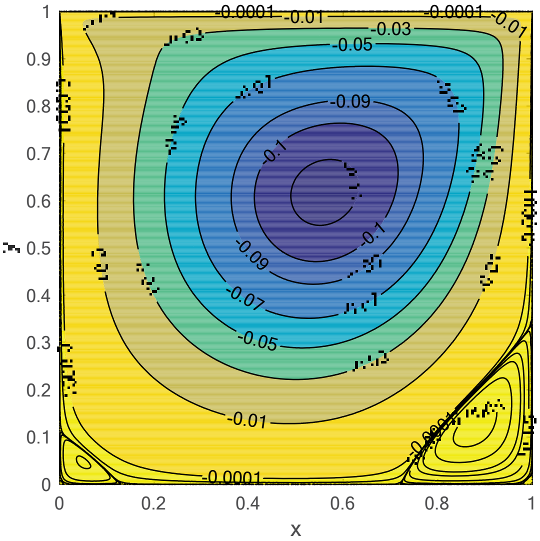

FIGURE 2. Streamline patterns for Re=400

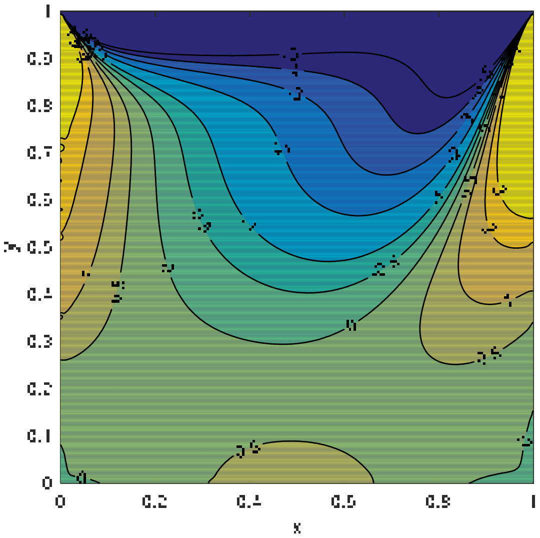

FIGURE 3. Vorticity patterns for Re=100

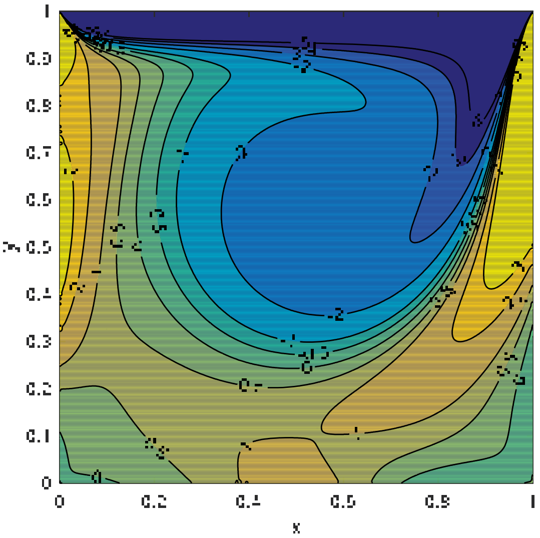

FIGURE 4. Vorticity patterns for Re=400

A more comprehensive quantitative analysis is provided by examining the tabulated data for v_x velocity along the x=0.5 line and v_y velocity along the y=0.5 line (Figure 5 and Figure 6). It is important to highlight that in the simulation with Re=400, a finer mesh was employed compared to the case with Re=100. Despite the utilisation of a finer mesh, it is noteworthy that the agreement with the benchmark solution is relatively weaker for the higher Reynolds number scenario. This observation suggests potential areas for enhancement, such as refining the iterative scheme, revisiting convergence criteria, or possibly incorporating a more sophisticated treatment of the vorticity boundary condition.

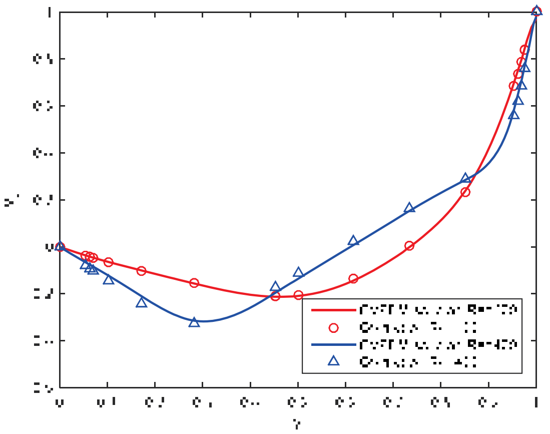

FIGURE 5. v_x velocity along the vertical line through the geometric centre of cavity

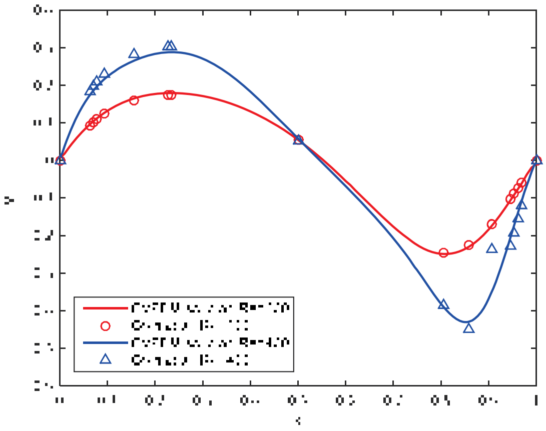

FIGURE 6. v_y velocity along the horizontal line through the geometric centre of cavity

4. CONCLUSIONS

The developed CVFEM MATLAB code for the vorticity-stream function formulation of shear-driven flow in a cavity shows commendable agreement with established benchmark solution for Reynold numbers of 100 and 400. Currently, the code prioritizes readability and comprehensibility, laying a strong foundation for further adaptations and translations into other programming languages. While its efficiency and accuracy are noteworthy, further enhancements can be pursued through the implementation of more sophisticated iteration schemes and convergence checks. After these arrangements, the code will be tested for higher Reynolds numbers, and the analysis will determine the need for finer meshes or better approximation of the boundary conditions.

The adaptation of a vorticity-stream function approach underscores a longstanding tradition in computational fluid dynamics, particularly for two-dimensional incompressible flows. However, transitioning from two-dimensional to three-dimensional fluid flow simulation poses inherent complexities, as both the vorticity and stream function evolve into three-component vectors. Nonetheless, this work serves as a precursor for authors to address such challenges, laying the groundwork for developing a CVFEM code using a collocated methodology capable of tackling three-dimensional fluid flow phenomena.

To facilitate collaboration and further research, the MATLAB code developed herein will be made available upon request to the authors or through publication on platforms like ResearchGate. This endeavour not only contributes to the academic community's toolbox for fluid dynamics simulations and fosters collaborative innovation to tackle complex fluid flow challenges.

REFERENCES

[1] S. Patankar, *Numerical Heat Transfer and Fluid Flow*, Hemisphere Publishing, 1980.

[2] V. Voller, *Basic Control Volume Finite Element Methods for fluids and solid*s, World Scientific, 2009.

[3] U. Ghia, K.N. Ghia and C.T. Shin, High-Re solutions for incompressible flow using the Navier-Stokes equations and a multigrid method, *Journal of Computational Physics*, 48, 387-411, 1982.

Sixth International Conference on Computational Methods for Energy and Thermal Problems
ThermaEComp2024, Sept. 9-11, 2024, Budva, Montenegro
N. Massarotti, P. Nithiarasu, and I. Vušanović (Eds.)

Experimental and numerical analysis of a side-mirror model through PTV and CFD technique

Canale Christian, Arpino Fausto, Cortellessa Gino, Grossi Giorgio
University of Cassino and Southern Lazio, Via G. di Biasio 43, 03043 Cassino (FR), Italy, christian.canale@unicas.it

Sciacchitano Andrea
TU Delft, Department of Aerospace Engineering, Delft, The Netherlands,A.sciacchitano@tudelft.nl

ABSTRACT

Turbulent particulate flows are present in many natural and industrial processes. The need to fully understand the dominant phenomenon of interaction between the dispersed phase and the carrier flow is clear. This article proposes a study of the fluid dynamics of a simplified side mirror through the Particle Tracking Velocimetry approach in the wind tunnel facility of the TU Delft University. A Computational Fluid Dynamics numerical model was developed and compared against the experimental data.

Key Words: *Computational Fluid Dynamics, Particle Tracking Velocimetry, Fluid Dynamics.*

1. INTRODUCTION

Particle transport within these environments is a highly complex and multifaceted phenomenon with many engineering, medical, and environmental applications. Examples include the automotive sector, indoor particle dispersion, and air-borne pollutants [1] in shared environments. It is crucial to develop a reliable design-based tool for predicting and understanding these flows, as it has the potential to greatly enhance the accuracy and efficiency of prototype-based analyses. Numerous studies have been conducted in the scientific literature, evaluating various strategies to analyze particle-laden flows. Kim et al. [2] investigated the fluid dynamics of different side mirror geometries, assessing the impact of three configurations on the fluid dynamics using the Particle Tracking Velocimetry (PTV) technique. Elhimer et al. [3] developed an innovative technique for simultaneous measurement of the particle velocity in a three-dimensional turbulent flow to compare the differences between Particle Image Velocimetry (PIV) and PTV measurements. Chen [4] conducted a numerical investigation to evaluate the performance of ventilation systems in indoor building environments, aiming to find the best computational fluid dynamics (CFD) solution for particle dispersion analysis. This research activity presents an experimental campaign conducted in the TU Delft wind tunnel to study the fluid dynamics of simplified mirror models. A CFD numerical model, developed in an OpenFOAM environment, will be compared against the experimental data to validate the numerical results and conduct a preliminary study of the fluid dynamics

2. MATERIALS AND METHODS

An experimental campaign was conducted in a low-speed and open jet wind tunnel (W-Tunnel) of the Aerodynamic Laboratories of the Aerospace Engineering Department at TU Delft aiming at the analysis of the fluid dynamics of a side mirror model, which was mounted on a black-covered supporting plate of 1m x 0.8 m x 0.01 m dimensions, placed forty centimetres out of the W-Tunnel exit. A 45° edge cut was created on the plate's leading edge to avoid the separation of the fluid coming from the exit of the wind tunnel.

The wind tunnel is characterized by a square contraction ratio of 1:9 and a 40×40 cm^2 cross-section, yielding a maximum velocity of 35 m/s. The velocity profile was measured in the freestream region using the three-dimensional Particle Tracking Velocimetry technique (PTV). A freestream velocity of 10 m/s was used for the experimental study, defining a Reynolds number of 66000. The side-view mirror model is characterized by 10 cm height and 5 cm width and it is immersed in the turbulent boundary, defining a blockage ratio of 1.4%. The dimension of the measurement volume is 0.3m x 0.3m x 0.3 m. The side mirror model, represented by a half cylinder with a quarter sphere on top, is the simplest configuration studied in the automotive sector's scientific literature ([2], [5]). In this preliminary study, an computational fluid dynamics (CFD) study has been performed by employing the open-source OpenFOAM code. The Unsteady Reynolds-averaged Navier-Stokes (URANS) approach was employed to solve the mass and momentum equations. The Shear Stress Transport (SST) k–ω turbulence model, as documented in [6], proved to be the most appropriate model for accurately predicting the velocity and pressure within the computational domain. For brevity, this section does not document the specifics of the URANS turbulence model utilized, but such information can be found in [7]. The pressure-velocity coupling was solved with the Pressure Implicit with Splitting of Operators (PISO) algorithm, enabling the processing of fully transient phenomena with a real-time step. The control of the time step is provided by defining the Courant number following the numerical approach described by Arpino et al [8]. The boundary conditions of the numerical simulations are presented in Figure 1:

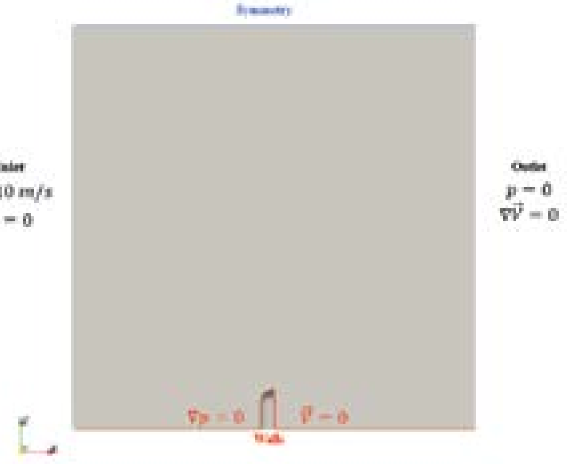

FIGURE 1. Boundary conditions of the numerical simulation.

A hexahedral-based structured grid was generated by employing the OpenFOAM tool "snappyHexMesh". The mesh was selected based on a comprehensive sensitivity analysis, to get a proper evaluation of the grid size and characteristics. The sensitivity analysis was conducted by doubling the number of elements in each step, as presented in TABLE 1

TABLE 1. Characteristics of the three meshes used for the sensitivity analysis

	Mesh 1	**Mesh 2**	**Mesh 3**
Number of elements	$1.21 \cdot 10^6$	$2.08 \cdot 10^6$	$4.46 \cdot 10^6$
Maximum Skewness	0.96	0.96	0.97
Average non-orthogonality	37.24	36.92	36.66

The mesh was selected by comparing the three computational domains, on the stagnation streamline and the top of the side mirror. The sensitivity analysis was performed by evaluating the average error from the reference (mesh 3), which was considered the reference for the sensitivity analysis. The average error was calculated as the difference between the reference value and the tested computational domain, performing a 5.85% error for the comparison between 3 and 1, and a 2.15% error for the comparison between 3 and 2.

3. RESULTS

These results have been obtained by processing the Helium Filled Soap Baubles (HFSB) tracers in the W-tunnel at 10 m/s.

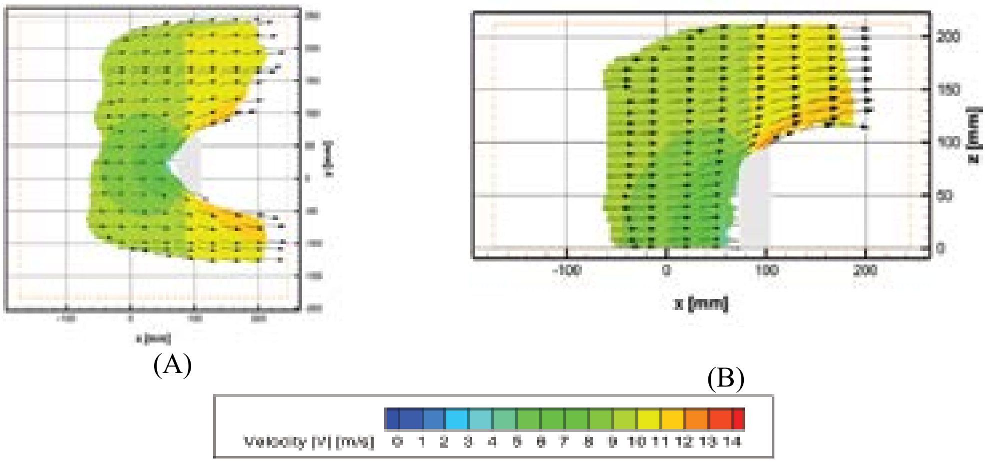

(A) (B)

FIGURE 2. (A) An x-z slice of the binning results of the upstream region around the model. (B) An x-y slice of the binning results of the upstream region around the model.

The fluid dynamics of the side mirror model were analyzed using the time-averaged velocity field approach. Figure 2 shows the time-averaged velocity measurements along the centerline of the horizontal plane at y = 45 mm and the vertical plane at z = 0 mm. The flow accelerates above the main recirculation region due to the blockage induced by the wake, as visible in the orange zone above and sideways of the side mirror model. The Davis software was used for the upstream and downstream views to evaluate the uncertainty of the mean-velocity measurement. The uncertainty evaluation considered the instantaneous velocity components and the maximum standard deviation of the velocity component was determined to be 0.14 m/s. As a result, the uncertainty is defined with a 1.4% margin for the mean flow component in the turbulent wake region for a single measurement at a freestream velocity of 10 m/s.The experimental data and the numerical simulations were compared in two different steps. The results are presented in FIGURE 3 (A) and (B), evaluating an average error for both configurations of 3.1% from the experimental results.

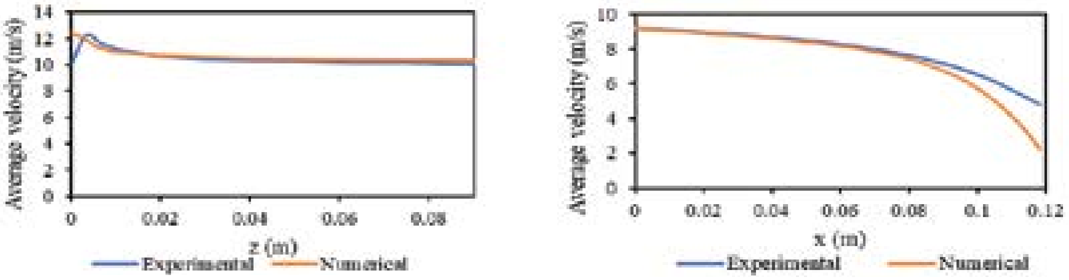

(A) (B)

FIGURE 3. (A) Comparison between the experimental and numerical data on the z-axis at y = 0. (B) Comparison between the experimental and numerical data on the z-axis at y = 0

Another comparison between experimental and numerical results is presented, in which the iso line of the average velocity field for the upstream study. In FIGURE 4 the black line represents the experimental isoline, while the coloured lines are the numerical ones.

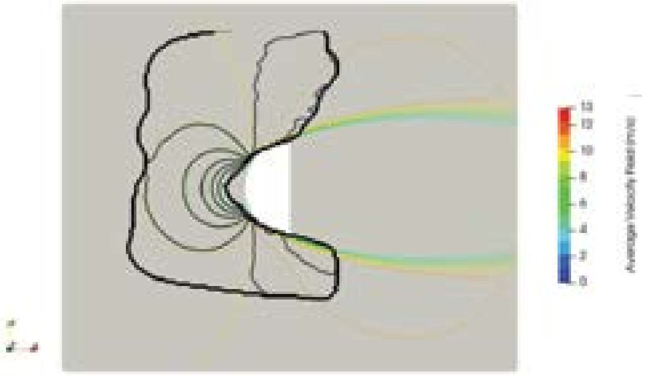

FIGURE 4. Velocity isoline comparison for the experimental (black) and numerical (coloured) data

The accordance of the two fluid dynamics, clearly visible from the isoline comparison, and the low average error comparison consent us to validate the numerical model against the experimental data.

4. CONCLUSIONS AND FUTURE DEVELOPMENTS

The present research is part of a preliminary study of the fluid dynamics of a side mirror model, whose measurements were conducted in a wind tunnel facility of the TU Delft laboratories. The experimental campaign aimed at the generation of a data set useful for the study of a simplified model, whose boundary conditions and setup characteristics are easily replicable. A PTV methodology was applied using the STB algorithm with four high-speed cameras and HFSB tracers in wind tunnel experiments. The analysis aimed, also, at the generation of a URANS numerical model developed in the OpenFOAM environment, which can describe the fluid dynamic of the case. The experimental campaign was conducted by testing also Air-Filled Soap Baubles (AFSB) and water droplets. These experimental results will be investigated in further developments of the present research, aiming at the evaluation and validation of the Lagrangian model, which is not presented in this research and is still under development.

REFERENCES

[1] C. Poelma, J. Westerweel, e G. Ooms, «Particle–fluid interactions in grid-generated turbulence», *J. Fluid Mech.*, vol. 589, pp. 315–351, ott. 2007, doi: 10.1017/S0022112007007793.

[2] D. Kim, M. Kim, E. Saredi, F. Scarano, e K. C. Kim, «Robotic PTV study of the flow around automotive side-view mirror models», *Experimental Thermal and Fluid Science*, vol. 119, p. 110202, nov. 2020, doi: 10.1016/j.expthermflusci.2020.110202.

[3] M. Elhimer, O. Praud, M. Marchal, S. Cazin, e R. Bazile, «Simultaneous PIV/PTV velocimetry technique in a turbulent particle-laden flow», *J Vis*, vol. 20, fasc. 2, pp. 289–304, mag. 2017, doi: 10.1007/s12650-016-0397-z.

[4] Q. Chen, «Ventilation performance prediction for buildings: A method overview and recent applications», *Building and Environment*, vol. 44, fasc. 4, pp. 848–858, apr. 2009, doi: 10.1016/j.buildenv.2008.05.025.

[5] W. Fu e Y. Li, «Experimental Study on a Generic Side-View Mirror with Slotted Cylindrical Foot», *JAFM*, vol. 16, fasc. 2, pp. 363–374, feb. 2023, doi: 10.47176/jafm.16.02.1424.

[6] F. R. Menter, «Two-equation eddy-viscosity turbulence models for engineering applications», *AIAA Journal*, vol. 32, fasc. 8, pp. 1598–1605, ago. 1994, doi: 10.2514/3.12149.

[7] K. Hanjalić, Y. Nagano, e M. J. Tummers, A c. di, *Turbulence, heat and mass transfer 4: proceedings of the Fourth International Symposium on Turbulence, Heat and Mass Transfer, Antalya, Turkey, 12 - 17 October, 2003*. New York, NY: Begell House, 2003.

[8] F. Arpino, G. Cortellessa, G. Grossi, e H. Nagano, «A Eulerian-Lagrangian approach for the non-isothermal and transient CFD analysis of the aerosol airborne dispersion in a car cabin», *Building and Environment*, vol. 209, p. 108648, feb. 2022, doi: 10.1016/j.buildenv.2021.108648.

Sixth International Conference on Computational Methods for Energy and Thermal Problems
THERMAECOMP2024, Sept. 9-11, 2024, Budva, Montenegro
N. Massarotti, P. Nithiarasu, and I. Vušanović (Eds.)

Heat Conduction Simulation via the Meshless Fragile Points Method (FPM) and Various Explicit/Implicit ODE Numerical Solvers

Rade Grujičić[1], Vidosava Vilotijević[1], Igor Vušanović[1], Mirko Komatina[2]
[1] University of Montenegro, Faculty of Mechanical Engineering, Dzordza Vasingtona bb 81000 Podgorica, Montenegro
[2] University of Belgrade, Faculty of Mechanical Engineering, Kraljice Marije 16, 11120 Belgrade, Serbia
Emails: radeg@ucg.ac.me, vidosavav@ucg.ac.me, igorvus@ucg.ac.me, mkomatina@mas.bg.ac.rs

ABSTRACT

This paper explores the possibilities of applying the Fragile Points Method (FPM) to simulate transient heat conduction problems in combination with several explicit and implicit numerical methods for solving ordinary differential equations (ODEs). Through an analysis of rough time complexity, computational time, and estimated errors of the numerical solution, a comparison of methods for solving ODEs was conducted. When compared to explicit methods, implicit ones appear to be more suitable for stiff problems while maintaining similar computational costs.

Key Words: *Fragile Points Method, Heat Conduction, Numerical Simulations.*

1. INTRODUCTION

Although many physical processes are well described by partial differential equations (PDEs), analytical solutions are lacking for most of them. Additionally, analytical results are often limited to simplified models that do not always accurately represent the real behaviour of the system. To address these issues, numerous numerical methods have been developed over the last several decades for solving PDEs and simulation purposes.

One of the newer methods is the Fragile Points Method (FPM), introduced by Dong et al. in [1]. While retaining the essential advantages over classical mesh-based methods, it offers computational improvements compared to other meshless methods. Its main features are discontinuous polynomial trial functions, which enables easy, precise, and fast integration with simple Gaussian quadratures.

Thus far, the FPM has demonstrated a great potential in solving various problems. One of them is heat conduction in anisotropic nonhomogeneous media. This paper represents an extension of previous research performed by Guan et al. [2], which confirmed the stability and convergence of FPM for heat conduction simulation. As transient problems are addressed, FPM provides only a semi-discrete solution, i.e. discretization in the spatial domain. To incorporate discretization in the time domain, this research introduces several explicit/implicit schemes. The primary novelty lies in comparing these schemes in terms of accuracy and computational complexity.

2. GOVERNING EQUATION, BOUNDARY CONDITIONS AND INITIAL CONDITION

The equation governing transient heat conduction in anisotropic nonhomogeneous media is:

$$\rho(\mathbf{r})c(\mathbf{r})\frac{\partial u}{\partial t}(\mathbf{r},t) = \nabla\cdot[\mathbf{k}(\mathbf{r})\nabla u(\mathbf{r},t)] + Q(\mathbf{r},t), \qquad \mathbf{r}\in\Omega, t\in[0,T], \tag{1}$$

where: Ω represents a domain, $\mathbf{r}$ is a position vector, t denotes time, $\rho(\mathbf{r})$ stands for density, $c(\mathbf{r})$ is a specific heat capacity, $u(\mathbf{r},t)$ represents temperature field, $\mathbf{k}(\mathbf{r})$ denotes a thermal conductivity tensor, $Q(\mathbf{r},t)$ is a density of heat sources, and ∇ is a gradient operator.

Dirichlet, Neumann, and Robin boundary conditions are analyzed in the following forms:

$$\begin{gathered} u(\mathbf{r},t) = g_{\mathrm{D}}(\mathbf{r},t), \qquad \mathbf{r} \in \Gamma_{\mathrm{D}}, \\ [\mathbf{k}(\mathbf{r})\nabla u(\mathbf{r},t)] \cdot \mathbf{n} = \mathbf{g} \cdot \mathbf{n} = g_{\mathrm{N}}(\mathbf{r},t), \qquad \mathbf{r} \in \Gamma_{\mathrm{N}}, \\ h(\mathbf{r})[u_{\mathrm{R}}(\mathbf{r}) - u(\mathbf{r},t)] = g_{\mathrm{R}}(\mathbf{r},t), \qquad \mathbf{r} \in \Gamma_{\mathrm{R}}, \end{gathered} \tag{2}$$

where: $\mathbf{n}$ represents the outer normal vector of the domain, $h(\mathbf{r})$ denotes a heat transfer coefficient, and $u_{\mathrm{R}}(\mathbf{r})$ is the temperature outside the convective boundary.

The initial condition is specified as:

$$u(\mathbf{r},t)|_{t=0} = u(\mathbf{r},0), \qquad \mathbf{r} \in (\Omega \cup \partial\Omega). \tag{3}$$

3. DISCRETE FORM OF THE GOVERNING EQUATION

For the purpose of this research, piecewise linear trial functions are employed. Test function is given a shape of trial function to ensure the symmetry of matrices. The semi-discrete form of the governing equation, obtained through discretization in the spatial domain, has the following structure [2]:

$$\mathbf{C}\dot{\mathbf{u}} + \mathbf{K}\mathbf{u} = \mathbf{F}, \tag{4}$$

where: $\mathbf{C}$ is a global heat capacity matrix, $\mathbf{K}$ denotes a global thermal conductivity matrix, $\mathbf{u}$ is a vector of temperatures in nodes, $\dot{\mathbf{u}}$ stands for a time derivative of temperature at nodes, and $\mathbf{F}$ is the heat flux vector. $\mathbf{C}$ and $\mathbf{K}$ matrices are constant, while the $\mathbf{F}$ vector can generally be variable, depending on the heat sources and boundary conditions. The procedure for determining $\mathbf{C}$, $\mathbf{K}$ and $\mathbf{F}$ is described by Guan et al. in [2].

To complete the numerical solution, several ODE numerical solvers are involved. Table 1 presents the full-discrete governing equation obtained with FPM and ODE solvers.

Explicit	Forward Euler (FE)	$\mathbf{u}_{m+1} = \mathbf{u}_m + \Delta t\mathbf{C}^{-1}(\mathbf{F}_m - \mathbf{K}\mathbf{u}_m)$
	Runge-Kutta 4th order (RK)	$\mathbf{u}_{m+1} = \mathbf{u}_m + \frac{\Delta t}{6}\mathbf{C}^{-1}(\mathbf{k}_1 + 2\mathbf{k}_2 + 2\mathbf{k}_3 + \mathbf{k}_4)$ $\mathbf{k}_1 = \mathbf{F}_m - \mathbf{K}\mathbf{u}_m$ $\mathbf{k}_2 = \mathbf{F}_{m+0.5\Delta t} - \mathbf{K}(\mathbf{u}_m + 0.5\Delta t\mathbf{k}_1)$ $\mathbf{k}_3 = \mathbf{F}_{m+0.5\Delta t} - \mathbf{K}(\mathbf{u}_m + 0.5\Delta t\mathbf{k}_2)$ $\mathbf{k}_4 = \mathbf{F}_{m+\Delta t} - \mathbf{K}(\mathbf{u}_m + \Delta t\mathbf{k}_3)$
Implicit	Backward Euler (BE)	$\mathbf{u}_{m+1} = (\mathbf{E} + \Delta t\mathbf{C}^{-1}\mathbf{K})^{-1}(\mathbf{u}_m + \Delta t\mathbf{C}^{-1}\mathbf{F}_{m+1})$
	Trapeze Rule (TR)	$\mathbf{u}_{m+1} = \left(\mathbf{E} + \Delta t\frac{1}{2}\mathbf{C}^{-1}\mathbf{K}\right)^{-1}\left(\mathbf{u}_m + \Delta t\frac{1}{2}\mathbf{C}^{-1}(\mathbf{F}_{m+1} + \mathbf{F}_m - \mathbf{K}\mathbf{u}_m)\right)$

Δt is a time step, $\mathbf{u}_m$ is vector of temperatures in specified nodes at t_m, $\mathbf{u}_{m+1}$ is vector of temperatures in specified nodes at $t_{m+1} = t_m + \Delta t$, $\mathbf{E}$ is a unit matrix of size $n \times n$.

TABLE 1. The full-discrete governing equation obtained with FPM and several ODE solvers

After analysing the steps leading to the semi-discrete solution (see paper [2]), it can be concluded that the inversion of the $\mathbf{C}$ matrix is the most time-consuming operation, achievable in $O(n^3)$ if the Gauss elimination method is used (n is the number of nodes). However, since $\mathbf{C}$ is a sparse, symmetric, and positive-definite matrix, more advanced algorithms can be employed to reduce the complexity (e.g., $O(n^{2.2131})$ with the method proposed by Casacuberta and Kyng in [3]). Due to the multiplication of an $n \times n$ matrix with a vector of length n within each time step, the complexity of the all four methods can be roughly estimated as $O(n_t n^2)$, where n_t is the number of time steps. However, after analysing Table 1, it is clear that in practice they won't be equal. Unlike Euler methods where multiplication of an $n \times n$ matrix with an $n \times 1$ matrix appears two times, the same type of multiplication with the 4th order Runge-Kutta method appears five times, so it is expected to be 2.5 times slower.

3. NUMERICAL EXAMPLES

The first example involves 1D transient heat conduction through a homogeneous medium, $x \in [0,1]$. The thermal diffusivity is set to 1, and there are no heat sources within the domain. The initial and boundary conditions are as follows: $u(x,0) = 1, \nabla u(0,t) = 0, u(1,t) = 0$.

The analytical solution to this problem is provided by Mackowski in [4]. Its comparison with the FPM solution is conducted based on the relative error r_0 in temperature values estimated by the Lebesgue norm. Figure 1 illustrates the comparison of the analytical solution and the numerical solution obtained by FPM and the Euler Backward scheme with 20 uniformly distributed domain nodes and a time step of 10^{-3}. Table 2 presents the values of r_0 averaged per time step within the interval $t \in [0,1]$, along with the corresponding computational times, obtained with different time discretization schemes, varying number of uniformly distributed nodes, and different time steps.

As can be seen from Figure 1, this problem is stiff due to rapid changes at the left boundary. Consequently, explicit methods struggle to produce results unless a very high number of domain points is utilized in comparison to the number of nodes. On the other hand, implicit methods can provide precise results even with a small number of time steps, although accuracy improves with an increase in the number of time steps. Table 2 further supports the earlier observation that the computational time of the Euler Forward and Euler Backward methods is more or less the same and lower than that of the Runge-Kutta method.

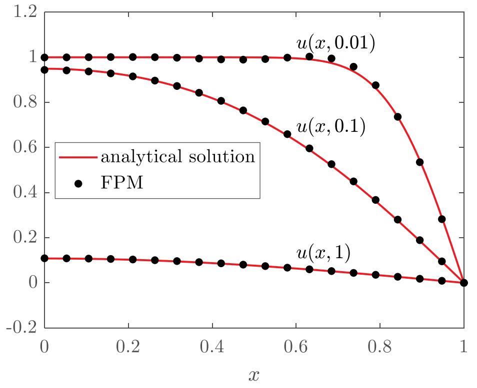

FIGURE 1. Comparison of analytical and FPM solutions for the first 1D example

n		10^1			10^2			10^3		
n_t		10^3	10^4	10^5	10^3	10^4	10^5	10^3	10^4	10^5
FE	r_0	-	-	$1.5 \cdot 10^{-2}$	-	-	-	-	-	-
	CT	-	-	0.35	-	-	-	-	-	-
RK	r_0	-	-	$1.5 \cdot 10^{-2}$	-	-	-	-	-	-
	CT	-	-	0.50	-	-	-	-	-	-
BE	r_0	$1.4 \cdot 10^{-2}$	$1.5 \cdot 10^{-2}$	$1.5 \cdot 10^{-2}$	$2.1 \cdot 10^{-3}$	$5.1 \cdot 10^{-4}$	$3.4 \cdot 10^{-4}$	$1.8 \cdot 10^{-3}$	$1.9 \cdot 10^{-4}$	$2.0 \cdot 10^{-5}$
	CT	0.06	0.09	0.36	0.09	0.45	3.58	4.99	46.82	439.30
TR	r_0	$1.6 \cdot 10^{-2}$	$1.5 \cdot 10^{-2}$	$1.5 \cdot 10^{-2}$	$1.2 \cdot 10^{-2}$	$3.9 \cdot 10^{-4}$	$3.2 \cdot 10^{-4}$	$2.7 \cdot 10^{-1}$	-	-
	CT	0.07	0.09	0.42	0.10	0.51	3.86	5.55	-	-

CT is computational time in seconds; The code was executed on a PC of the following specifications: Intel(R) Core(TM) i3-9100T CPU @ 3,10 GHz; RAM 8,00 GB; Intel(R) UHD Graphics 630.

TABLE 2. The average values of r_0 error and computational times for the first example

The second example involves 2D transient conduction across a homogeneous isotropic square-shaped domain, $x \in [0,1]$, $y \in [0,1]$. Value 1 is assigned to both density and specific heat capacity, while the thermal conductivity tensor equals the Kronecker delta function. No heat source is present. All boundaries are time variable Dirichlet, except $x = 1$ where Neumann conditions is imposed. The analytical solution is provided by Johansson et al. in [5]. Table 3 shows the r_0 relative errors at $t = 1$ obtained with different ODE solvers, varying number of uniformly distributed nodes and different time steps. Similar to the first example, explicit methods yield results only when n_t is significantly higher than n. For this category of problems, implicit methods can achieve the same computational efficiency as explicit methods while also providing accurate results for larger time steps.

n		10^2			30^2			50^2		
n_t		10^2	10^3	10^4	10^2	10^3	10^4	10^2	10^3	10^4
FE	r_0	-	-	$3.1\cdot10^{-3}$	-	-	-	-	-	-
	CT	-	-	5.44	-	-	-	-	-	-
RK	r_0	-	-	$3.2\cdot10^{-3}$	-	-	-	-	-	-
	CT	-	-	14.60	-	-	-	-	-	-
BE	r_0	$2.3\cdot10^{-2}$	$4.1\cdot10^{-3}$	$3.2\cdot10^{-3}$	$2.2\cdot10^{-2}$	$2.4\cdot10^{-3}$	$4.3\cdot10^{-4}$	$2.2\cdot10^{-2}$	$2.3\cdot10^{-3}$	$2.9\cdot10^{-4}$
	CT	0.13	0.57	4.70	0.76	5.16	51.33	4.67	32.48	308.65
TR	r_0	$3.1\cdot10^{-3}$	$3.1\cdot10^{-3}$	$3.1\cdot10^{-3}$	$4.3\cdot10^{-2}$	$2.5\cdot10^{-4}$	$2.5\cdot10^{-4}$	$8.3\cdot10^{-2}$	$8.5\cdot10^{-5}$	$8.4\cdot10^{-5}$
	CT	0.13	0.51	4.33	0.59	3.55	34.37	3.58	19.31	184.59

TABLE 3. Relative error r_0 at $t = 1$ and computational times for the second example

4. CONCLUSIONS

This research confirms the suitability of FPM for solving heat conduction problems and for incorporating various ODE solvers. The significant advantages of FPM include the symmetry and sparsity of matrices, and linearity of trial/test functions. All of these factors contribute to the computational efficiency of FPM, as evidenced by the very low computational times. With a relatively small number of points and time steps, FPM executes within a fraction of a second. Examples with a high number of nodes (i.e., 1000-2500) and a very high number of time steps (10^4-10^5) execute within 5-7 minutes on the PC used. All four ODE solvers can roughly be executed with the complexity of $O(n_t n^2)$. Indeed, for the specific problems analysed in this paper, it was demonstrated that implicit methods can execute as quickly as fast and simple Euler Forward method. On the other hand, the 4th order Runge-Kutta method appears to be three times slower. This highlights an advantage of implicit methods over explicit ones in solving the heat conduction equation, as implicit methods are capable of handling stiff problems.

REFERENCES

[1] Dong L., Yang T., Wang K., Atluri S.N. (2019). A new Fragile Points Method (FPM) in computational mechanics, based on the concepts of Point Stiffnesses and Numerical Flux Corrections, *Engineering Analysis with Boundary Elements, 107*

[2] Guan Y., Grujicic R., Wang X., Dong L., Atluri S.N. (2020). A new meshless "fragile points method" and a local variational iteration method for general transient heat conduction in anisotropic nonhomogeneous media. Part I: Theory and implementation, *Numerical Heat Transfer, Part B: Fundamentals, 78*(2)

[3] Casacuberta S., Kyng R. (2022). Faster Sparse Matrix Inversion and Rank Computation in Finite Fields, *13th Innovations in Theoretical Computer Science Conference (ITCS 2022)*, Leibniz International Proceedings in Informatics, Dagstuhl Publishing, Germany

[4] Mackowski D.W. (2011). *Conduction Heat Transfer: Notes for MECH 7210*, Alabama: Mechanical Engineering Department, Auburn University

[5] Johansson B.T., Lesnic D., Reeve T. (2011). A method of fundamental solutions for two-dimensional heat conduction, *International Journal of Computer Mathematics, 88*(8)

MODELING OF THERMAL COMFORT CONDITIONS IN A TRAIN CABIN

Reza Hamidi Jahromi, Alessandro Mauro, Simona Di Fraia, Nicola Massarotti
Department of Engineering, University of Naples “Parthenope”, Centro Direzionale, Isola C4,
80143 Naples, Italy, E-mail addresses: reza.hamidijahromi001@studenti.uniparthenope.it

Giorgio Grossi
Department of Civil and Mechanical Engineering, University of Cassino and Southern Lazio, Via
G. Di Biasio 43, Cassino, 03043, FR, Italy. E-mail address: giorgio.grossi@unicas.it

ABSTRACT

This study evaluates the thermal comfort conditions inside a train cabin by using computational fluid dynamics (CFD) simulation, focusing on the Predicted Mean Vote (PMV) index. The impact of three different velocity inlet strategies on thermal comfort has been evaluated by conducting steady-state Reynolds-Averaged Navier-Stokes (RANS) simulation. The realizable k-ε turbulence model has been selected and the calculations has been conducted using OpenFOAM software. A 3D model of a train cabin has been developed to perform these simulations. The results demonstrate that thermal comfort strongly depends on the inlet configurations, highlighting the importance of airflow inlet and outlet grilles positions. These findings offer valuable insights for optimizing train cabin air conditioning systems, in order to improve passengers’ comfort.

Key Words: *Heat Transfer, Computational Fluid Dynamics (CFD), Thermal Comfort*

1. INTRODUCTION

In recent years, due to the greater convenience and quicker operation, trains have become increasingly popular as a transport system for the society. Airflow characteristics and the distribution of thermal comfort in the train's passenger compartment have always been crucial for both crew and passengers. The geometry and air conditioning system of trains have a major impact on the airflow. Because of the long, narrow and intricate geometry, the airflow and thermal comfort in the cabin differs from one train cabin to another. Meanwhile, extended travel times can aggravate passengers' cabin conditions and, in certain situations, result in heat discomfort. Consequently, it can negatively impact passengers' experiences and possibly increase the risk to their health. To enhance the riding experience and thermal comfort, research on the thermal environment and airflow properties in train compartments can be very useful [1].

Currently, available techniques for investigating the internal environment and airflow properties in enclosed spaces mostly involve computational fluid dynamics (CFD) simulations and experimental measurements [2]. Studies of airflow characteristics, such as airflow transient characteristics, airflow patterns, and turbulence characteristics, have been extensively conducted in indoor environments. Experimental studies are frequently regarded as reliable. The train compartment's dimensions are longer and narrower than those of the indoor rooms, and it has a more intricate internal structure and a denser passenger distribution [3]. Even with the numerous improvements made to train cabin design, there is still need for improvement in the air quality and comfort. As a result, study of flow pattern is dependable to the geometry, and the outcomes can serve as helpful guidelines for designing train compartment air conditioning systems.

In this study, the authors have developed a mathematical model for studying a 3D train cabin, analyzing three different inlet strategies. The configurations are (a) Mixed inlet, (b) Lateral inlet, and

(c) Top inlet configurations. One of the thermal comfort indices (PMV- Predicted Mean Vote) has been calculated to compare the effects of airflow strategies. The PMV formulation is based on the heat balance of the human body. The PMV predicts the mean vote of a group of persons on a 7-point thermal sensation scale. The range varies from −3 to +3. Thermal sensations for each value are as follows: −3 (cold), −2 (cool), −1 (slightly cool), 0 (neutral), +1 (slightly warm), +2 (warm), and +3 (hot). The criterion defines three classes of satisfaction for the PMV range: Class A ($-0.2 < PMV < 0.2$) for highest satisfaction, Class B ($-0.5 < PMV < 0.5$) for moderate satisfaction, and Class C ($-0.7 < PMV < 0.7$) for basic thermal comfort [4].

2. METHODOLOGY

The 3D model of a full-scale train compartment based on the study of Wang et al [3] has been simulated using the open-source software OpenFOAM11. The steady-state RANS simulations with a realizable k-ε turbulence model have been carried out. Mass, momentum, and energy equations have been solved and the solutions are considered converged when all residuals are below 10^{-5}, except for the energy residuals below 10^{-6} are considered for convergence. Moreover, to calculate the PMV values, *Foam::functionObjects::comfort* class tool in Openfoam11 has been used. This tool calculates the thermal comfort quantities using related factors such as local mean velocity, temperature, external work, and metabolic rate based on DIN ISO EN 7730:2005 [4].

3. GEOMETRY AND BOUNDARY CONDITIONS

The geometry and boundary conditions of the train cabin are depicted in Figure 1. The dimensions of the cabin are L×W×H = 5.50 m × 2.83 m × 2.44 m. Moreover, simple seating areas in a 2-row by 4-column configuration have been considered. In order to reduce the computational cost and due to the symmetric condition of the geometry model, only half of the domain has been studied. The computational grid, is shown in Figure 2 and is made up of 6,766,766 million unstructured elements with refinements at all boundaries, particularly, the walls.

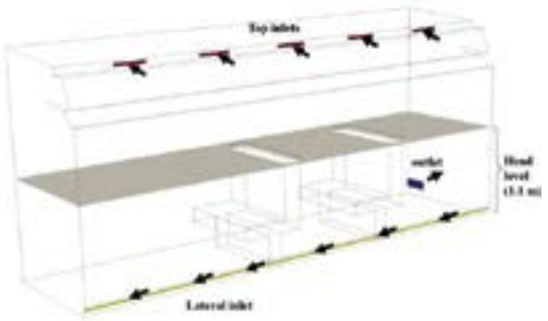

FIGURE 1. Geometry model of the train cabin and the location of head level surface

FIGURE 2. Computational domain of the train cabin

The air volumetric flow rate of the inlet in the compartment has been set to 970 m^3/h and the supply temperature has been set to 22°C. Furthermore, the outer wall temperature of the train has been set to a constant value of 36°C (i.e., summer condition). Moreover, zero-gauge pressure has been considered for the outlet, and the turbulence intensity $I = 5\%$ is specified for all inlet conditions.

3. RESULTS

In order to validate the mathematical model, the present results have been compared with the experimental (PIV) and numerical (RANS) data available for a different real case study in the work of Thysen et al [5], as shown in Figure 3. As observed, the non-dimensional x-component velocity values are in excellent agreement with the reference data in two different locations.

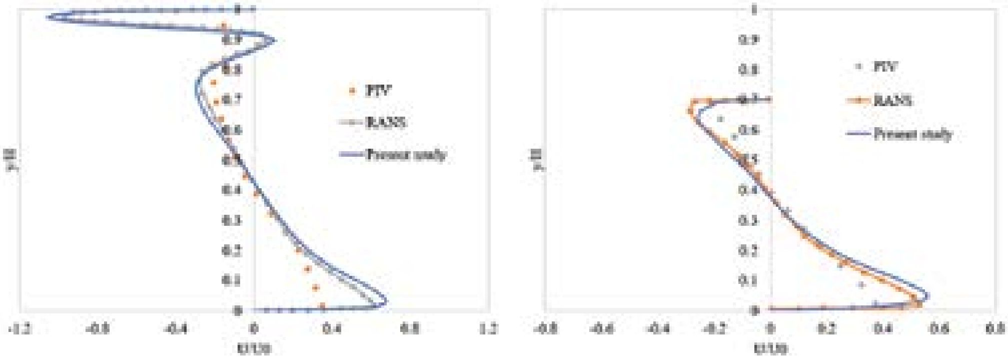

FIGURE 3. Dimensionless x-component velocity at the x/H = 1.12 and x/H=1.37, respectively [5]

After validation, the present model has been used to simulate the train cabin of Wang et al. [6]. As shown in Figure 4, the effect of different inlet strategies on the thermal comfort conditions at the head level of passengers have been presented.

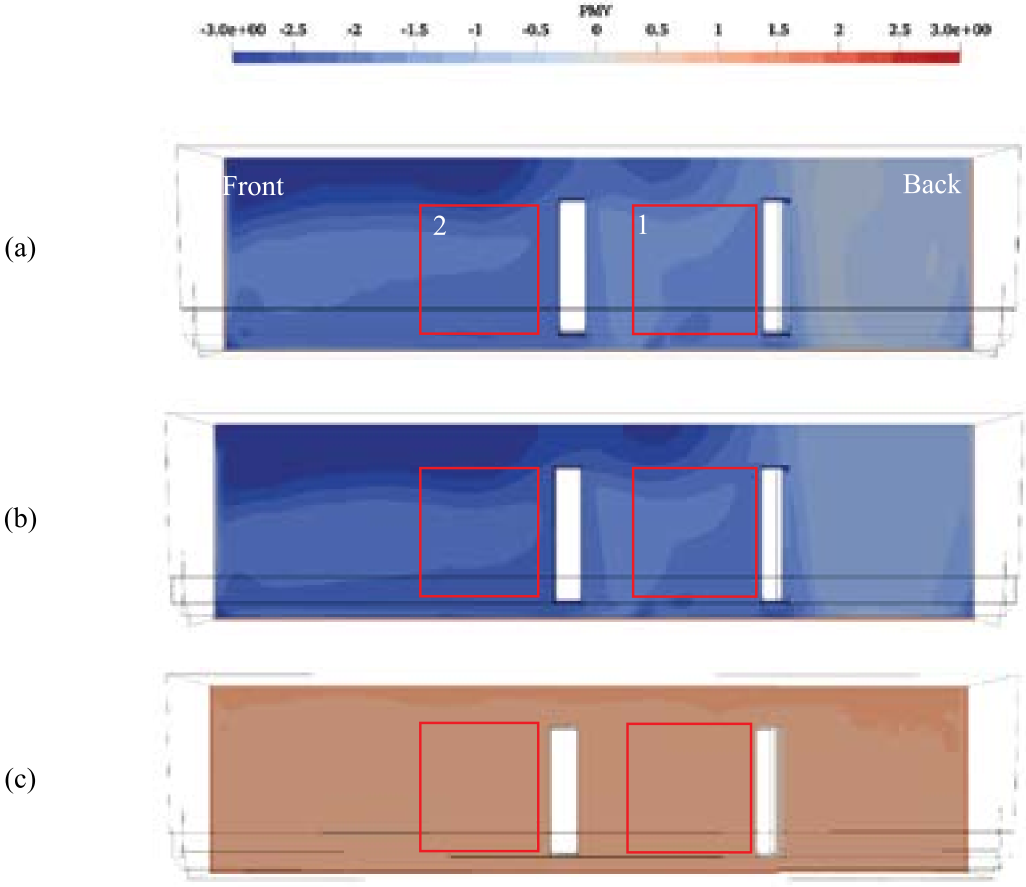

FIGURE 4. PMV values at the head level for (a) mixed inlet configuration, (b) lateral inlet configuration, and (c) top inlet configuration

The results for both the mixed and lateral inlet configurations can be considered similar. In the sitting area (red rectangular zones), the mixed inlet configuration offers larger surface areas with PMV values ranging from −1 to −1.5, which are considered as "slightly cool" feeling, than the lateral inlet configuration. The reason for this phenomenon is due to the location of the outlet, which is at the back area of the cabin (right side of the Figure 4). As it can be seen, the average PMV value in that area is −0.5, which is acceptable. However, this value decreases to less than −2 at the front area of the cabin, which is considered as "cold" and, therefore, an area of possible discomfort.

On the other hand, for the top inlet configuration, this value is in the range of +1 and +1.5, indicating a “slightly warm” condition. This might be due to the flow entering the train, which is more exposed to the heated walls than in the other two cases. Thus, the findings highlight the importance of flow strategies, as well as the locations of airflow inlets and outlets.

4. CONCLUSIONS

This study presents an analysis of PMV values inside a train cabin, using numerical approach. The three inlet flow strategies have demonstrated different impacts on the thermal environment in which the mixed inlet configuration has presented more acceptable results in comparison with the other two. The results indicate the critical role of airflow management in enhancing passenger comfort in train cabins. In future research, particle distributions will be analyzed, along with the impact of inlet and outlet locations on thermal comfort indices, taking into account real train cabins, and involving the presence of passengers, to optimize air flow configuration.

ACKNOWLEDGEMENTS

The authors gratefully acknowledge the financial support of ΩMEGA project TrenInno “Ottimizzazione di componenti e metodologie per il TRasporto fErroviarie INNOvativo”, CUP C65H23004250008, Ministero delle Imprese e del Made in Italy.

REFERENCES

[1] Wu, F., Dong, H., Yu, C., Li, H., Cui, Q. and Xu, R., 2024, February. Numerical simulation of formaldehyde distribution characteristics in the high-speed train cabin. In *Building Simulation* (Vol. 17, No. 2, pp. 285-300). Beijing: Tsinghua University Press.

[2] Massarotti, N., Mauro, A., Sainas, D., Marinetti, S. and Rossetti, A., 2019. A novel procedure for validation of flow simulations in operating theaters. *Science and Technology for the Built Environment*, 25(5), pp.629-642.

[3] Li, T., Wu, S., Yi, C., Zhang, J. and Zhang, W., 2022. Diffusion characteristics and risk assessment of respiratory pollutants in high-speed train carriages. *Journal of Wind Engineering and Industrial Aerodynamics*, *222*, p.104930.

[4] ISO 7730:2005. *Ergonomics of the thermal environment–analytical determination and interpretation of thermal comfort using calculation of the PMV and PPD indices and local thermal comfort criteria*. Geneva: International Organization for Standardization, 2005.

[5] Wang, T., Zheng, Y., Lu, Y., Shi, F., Ji, P., Qian, B., Zhang, L., Liu, D., Wang, J. and Yang, B., 2024. Reducing the contaminant dispersion and infection risks in the train cabins by adjusting the inlet turbulence intensity: A study based on turbulence simulation. *Science of the Total Environment*, *930*, p.172735.

[6] Thysen, J.H., van Hooff, T., Blocken, B. and Van Heijst, G.J.F., 2021. CFD simulations of two opposing plane wall jets in a generic empty airplane cabin: Comparison of RANS and LES. *Building and Environment*, *205*, p.108174.

Sixth International Conference on Computational Methods for Energy and Thermal Problems
THERMAECOMP2024, Sept. 9-11, 2024, Budva, Montenegro
N. Massarotti, P. Nithiarasu, and I. Vušanović (Eds.)

ON THE NUMERICAL APPROACH FOR THERMAL EFFECTS IN TUNNEL FIRES

Milan Šekularac, Esad Tombarević
Mechanical Engineering Faculty, University of Montenegro, Cetinjski put bb, 81000 Podgorica,
milans@ac.me; esadt@ac.me

ABSTRACT

In designing the longitudinal ventilation systems for traffic tunnels, the designer is faced with the necessity to account for thermal effects present during a fire scenario. The relevant ventilation operation regime with respect to sizing is the one during a fire scenario. The requirement is to provide the critical velocity for smoke control, which primarily depends on the tunnel cross section hydraulic diameter. For most road tunnels this value is ~3-3.5m/s. Various thermal effects, are present: local fire-site-induced pressure loss, combined convective-radiative heat transfer from the combustion gases to the tunnel lining walls, conduction heat transfer through tunnel's lining wall, gas acceleration due to the released fire heat, stratification, chimney effect in sloped tunnels, and the effect of deterioration of the thrust exerted by fans operating in lower density gas given the increased temperatures along the tunnel. In general, some of these effects are 3-dimensional (like stratification and fan-induced flow interaction with tunnel flow) whereas some are mostly 1-dimensional. The transient character of gas-to-walls heat transfer has to be taken into account as well. The time frame for ventilation design evaluation is approx. 15 min after fire onset, i.e. after the evacuation phase of tunnel users has finished. The designer is faced to decide on the computational approach for some of these effects, and an analysis is given by use of both 1-dimensional (1D) and (3D CFD) approach in this paper to assess the accuracy of thermal effects treatment and the resulting system sizing.

Key Words: *Heat Transfer, 1D, 3D CFD, combined heat transfer, tunnel ventilation, fire, combustion, numerical approaches.*

1. INTRODUCTION

The longitudinal ventilation system for traffic tunnels (road and rail type) consists of axial fans placed underneath the tunnel ceiling wall, Fig.1. They are normally placed in batteries, of 2 or 3 fans, with a recommended distance from the wall to the fan axis of ~1 fan hydraulic diameter, and the required spacing between batteries of fans of 100 fan diameters or more. Two approaches are possible in longitudinal distribution of batteries: equidistant placing of batteries along the tunnel, or the agglomeration of the battery placement, where fans are placed near the tunnel portals, respecting the required distance between fan batteries, [1-3].

Fig. 1. Tunnel cross section and the longitudinal ventilation layout

2. MATHEMATICAL MODEL OF THE PROBLEM

The effective exerted thrust force of a ventilation fan placed inside the tunnel can be computed using the following formula [5-8]:

$$N_e = N_s\left(1-\frac{u_t}{u_j}\right)\cdot\eta_i\cdot\eta_T \tag{1}$$

$$\eta_i = C_1C_2C_3 \approx 0.70-0.85 \tag{2}$$

$$\eta_T = \frac{\frac{T_0}{T}u_j-u_0}{u_j-u_0} \tag{3}$$

where: N_s a static thrust force is denoted, which is equal to the product of air mass flow and the exiting jet efflux velocity, the η_i and η_T denote the efficiency of momentum transfer and the thermal deterioration coefficient, respectively. The former is equal to a product of three C-coefficients which take into account: the fan distance from the wall, the jet axis angle with respect to tunnel axis and the relative distance between fan batteries. The velocities of the fan jet and the tunnel airflow velocity are denoted as u_j and u_t. To be able to compute the coefficient (3), the temperature distribution must be determined. The required velocity to direct all the smoke flow in the desired direction is called the critical velocity and is computed using formula from Wu, Bakar [4]:

$$v_{cr}^* = \frac{v_c}{\sqrt{qH}} = \begin{cases} 0.4\left(\frac{\dot{Q}^*}{0.2}\right)^{1/3}, & if\ \dot{Q}^* \le 0.2 \\ 0.4, & if\ \dot{Q}^* > 0.2 \end{cases} \tag{4}$$

$$\dot{Q}^* = \frac{\dot{Q}}{\rho_0 c_p T_0 g^{1/2} H^{5/2}} \tag{5}$$

The temperature distribution during a fire can be estimated using different approaches: semi-analytical, 1D numerical, 3D numerical. The difficulties associated with analytical approaches are related to the overall heat transfer coefficient, and the transient character of the problem.

The 3-dimensional (CFD) mathematical model [10] consists of: momentum conservation (Reynolds) equations together with the continuity equation, the equations governing the composition of the reacting mixture (mean mixture fraction and its variance), the required turbulence model for the closure of the momentum equations (here k-ε), the energy equation for fluid mixture, and the heat conduction equation for solid tunnel walls.

$$\frac{\partial(\rho\bar{v}_j)}{\partial t} + \frac{\partial(\rho\bar{v}_i\bar{v}_j)}{\partial x_i} = -\frac{\partial\bar{p}}{\partial x_j} + \mu\frac{\partial^2\bar{v}_j}{\partial x_j^2} + \frac{\partial R_{ij}}{x_i} + F_j \tag{6}$$

$$\frac{\partial\rho}{\partial t} + \frac{\partial(\rho\bar{v}_i)}{\partial x_i} = 0 \tag{7}$$

$$R_{ij} = -\overline{\rho v_i{}' v_j{}'} \tag{8}$$

$$\frac{\partial(\rho c\bar{T})}{\partial t} + \nabla\cdot\left(\rho c\vec{\bar{v}}\bar{T}\right) = \nabla\cdot(\lambda\nabla\bar{T}) + \nabla\cdot q_t + \nabla\cdot q_r + S_{chem} \tag{9}$$

$$\frac{\partial(\rho\bar{f})}{\partial t} + \nabla\cdot\left(\rho\vec{\bar{v}}\bar{f}\right) = \nabla\cdot\left(\frac{\mu_t}{\sigma_t}\nabla\bar{f}\right) + S_m + S_{user} \tag{10}$$

$$\frac{\partial(\rho\overline{f'^2})}{\partial t} + \nabla\cdot\left(\rho\vec{\bar{v}}\overline{f'^2}\right) = \nabla\cdot\left(\frac{\mu_t}{\sigma_t}\nabla\overline{f'^2}\right) + C_g\mu_t + \left(\nabla\bar{f}\right)^2 - C_d\rho\frac{\varepsilon}{k}\overline{f'^2} + S_{user} \tag{11}$$

where $R_{ij} = -\rho\overline{v_i{}'v_j{}'}$ is the Reynolds turbulence stress tensor which has to be modelled. Turbulence was modelled using standard k–ε turbulence model, and the enhanced wall function approach. All the model constants had their default values: $C_\mu = 0.09$, $C_{1\varepsilon} = 1.44$, $C_{2\varepsilon} = 1.92$, $Pr_k = 1$. The turbulent and radiative heat transfer rates are denoted by q_t, q_r, respectively.

In the 1-dimensional (1D) framework for numerical solution, a simplified version of the equations for momentum, continuity and energy conservations is computed, see [11-14].

3. RESULTS

The numerical model setup and testing has been conducted on a model-scale (laboratory) tunnel. Such tunnels have traditionally been designed and built in Laboratory conditions for the experimental research of flow and temperature properties in fire scenarios, and the results are available in the literature. The adopted test model is of a square cross section 1 x 1m, with the heat release rate of 262 kW, and the computed critical velocity for smoke control of 1.2 m/s. The heat-release rate is the scaled-down value from the object size case usually relevant for system sizing (50MW). Two cases have been computed, to estimate the important features of flow and temperature distribution in the fire zone, during the testing and verification phase of the CFD approach. These correspond to the adiabatic wall case and the prescribed wall temperature case. In later the temperature of the wall is held constant and equal to the undisturbed temperature T_0, thus, it corresponds to the initial phase of a fire event. After all the verifications, the cases are computed again in the CAD model corresponding to the real-scale size and shape (horse shoe) road traffic tunnel.

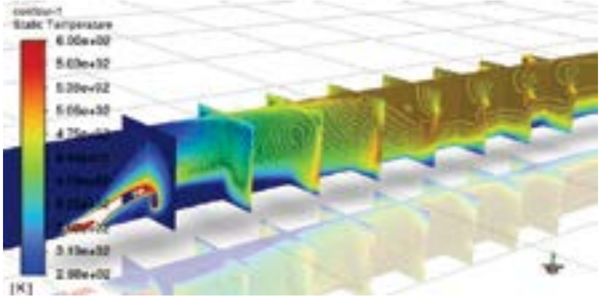

FIGURE 1. Temperature distribution in the fire zone of the tunnel.

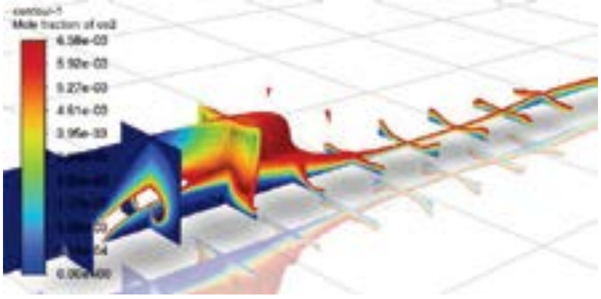

FIGURE 2. CO_2 distribution: within the range 0 – 10% of max. value shown

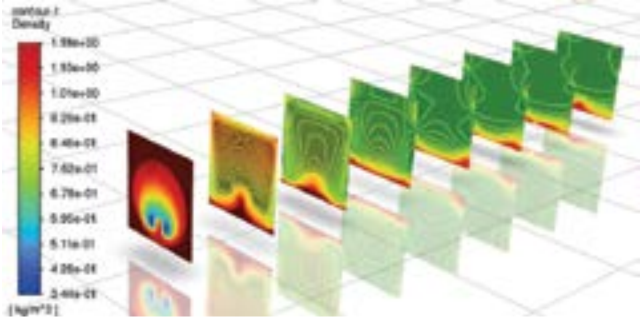

FIGURE 3. Density field

4. CONCLUSIONS

In this work a comparison of the computed distribution of averaged-temperature at a cross section, is presented, obtained by use of a 1D numerical and a 3D (CFD) approaches. Using the computed temperature fields, the effect of the selected numerical approaches, on the computation of the features relevant for the engineering task of tunnel ventilation system sizing for smoke control (eq.3), is computed. The results and the limitations of the approaches are discussed.

REFERENCES

[1] Ingason H. State of the art of tunnel fire research. *Fire safety science–proceedings of the ninth international symposium, International association for fire safety science*, 2008. pp.33-48. doi:10.3801.
[2] Ingason H. Handbook of Tunnel Fire Safety, Chapter 13: *Fire Dynamics in Tunnels*. ICE Publishing, 2012, pp.273-307. ISBN: 978-0-7277-4153-0.
[3] Barbato L, Cascetta F, Musto M, et al. Fire safety investigation for road tunnel ventilation systems – An overview. *Tunneling and Underground Space Technology*, 2014; 43: 253-265.
[4] Wu Y, and Bakar MZA. Control of smoke flow in tunnel fires using longitudinal ventilation systems - A study of the critical velocity. *Fire Safety Journal* 2000; 35(4): 363-390.
[5] CETU, 2003. Centre d'Etudes des Tunnels. Le dossier pilote des tunnels equipements, section 4.1 – Ventilation. France, ISBN 2-11-084740-9.
[6] RABT, 2006. German road and transportation research association - working group traffic routing and safety: RABT - Regulations for the equipment and operation of road tunnels. *FGSV-Verlag, Wesselinger Staße 17, 50999 Köln (Germany)*.
[7] PIARC, 2007. Committee on Road Tunnels Operation. Systems and Equipment for Fire and Smoke Control in Road Tunnels.
[8] RVS 09.02.31, 2014. Tunnel, tunnel equipment, ventilation, basic principles. *Austrian Research Association for Roads, Rail and Transport*.
[9] Vukoslavčević, P., Šekularac, M, (2022) Critical review of the common methods to determine the buoyancy-chimney effects in longitudinally-ventilated traffic tunnel fires. Advances in Mechanical Engineering 14(5) 1-13
[10] Theory guide with computational fluid dynamics solver (Fluent) – ANSYS Inc.
[11] CAMATT 2.20, 2011. *Centre d'Etudes des Tunnels*, France.
[12] Colella F, Verda V, Borcheillini R, et al. Chapter 17 in Beard A, and Carvel R: *Handbook of tunnel fire safety, 2nd edition.* ICE Publishing, 2012. ISBN: 978-0-7277- 4153-0
[13] Colella F. *Mutliscale modelling of tunnel ventilation flows and fires*. PhD thesis, Politechnico di Torino, 2010.
[14] Jang HM and Chen F. On the determination of the aerodynamic coefficients of highway tunnels. *Journal of Wind Engineering and Industrial Aerodynamics* 2002; 90: 869–896.

Sixth International Conference on Computational Methods for Energy and Thermal Problems
THERMAECOMP2024, Sept. 9-11, 2024, Budva, Montenegro
N. Massarotti, P. Nithiarasu, and I. Vušanović (Eds.)

DESIGNING A COMMERCIAL COOKING OVEN USING GAS FUELS BY ADAPTIVE COMBUSTION APPROACH

Remzi Timur*, Zafer Kahraman and Murat Hacı
R&D Center, Oztiryakiler Madeni Esya San. Ve Tic. A.S, Buyukcekmece, Istanbul, Türkiye,
*rtimur@oztiryakiler.com.tr, zkahraman@oztiryakiler.com.tr and mhaci@oztiryakiler.com.tr

Hakan Serhad Soyhan
Mechanical Engineering Department, Sakarya University, Sakarya, Türkiye
Team-San Co., Serdivan, Sakarya, Türkiye,
hsoyhan@sakarya.edu.tr

ABSTRACT

Commercial cooking ovens are used in businesses with varying capacities, either electrically or gas-fired, according to their requirements. However, the intensive use of commercial cooking ovens leads to high energy consumption for businesses. In this study, a prototype of a commercial cooking oven operated by gas (natural gas, LPG) is developed to optimize the combustion process control to achieve more efficient combustion and energy utilization through adaptive combustion conditions. Factors such as gas type, gas pressure, adaptive combustion, oxygen level, and combustion stability are continuously monitored under different operating conditions of the prototype oven to make the combustion process more efficient and low emission based on these data. Various components constituting the combustion system are uniquely designed and integrated into the oven prototype, and practical evaluations are conducted using simulation data during the design verification phase. Furthermore, after conducting tests and assessments in compliance with international standards (such as EN 203-1 and EN 203-2-2), it is aimed to obtain Research and Development (R&D) achievements in the commercial kitchen field with an innovative prototype that operates under adaptive combustion conditions. This study represents a significant advancement in energy efficiency and emission control for commercial gas-fired cooking ovens.

Key Words: *Commercial Cooking Oven, Adaptive Combustion Conditions, Simulations*

1. INTRODUCTION

According to their requirements, commercial cooking ovens are used in businesses with varying electrical or gas-fired capacities. However, the intensive use of commercial cooking ovens leads to high energy consumption for businesses. Generally, annual electricity prices are higher than natural gas. Studies have shown that the energy efficiency of commercial ovens is lower than that of domestic products. In this study, a prototype of a commercial cooking oven operated by gas (natural gas, LPG) is developed to optimize the combustion process control to achieve more efficient combustion and energy utilization through adaptive combustion conditions. Factors such as gas type, gas pressure, adaptive combustion, oxygen level, and combustion stability are continuously monitored under different operating conditions of the prototype oven to make the combustion process more efficient and low emission based on these data. Various components constituting thecombustion system are uniquely designed and integrated into the oven prototype, and practical evaluations are conducted using simulation data during the design verification phase.

In recent years, significant advancements have been made in the modeling and assessment of thermal and fluid dynamics in domestic gas ovens, as well as in the comparative evaluation of cooking energy sources. Mistry et al. [1] developed a comprehensive computational fluid dynamics (CFD) model to simulate the thermal and fluid dynamics within a domestic gas oven. Their three-dimensional, unsteady forced convection model, coupled with radiative heat transfer, provides accurate predictions of the thermal field within the stove. Experimental validation showed less than a 6% discrepancy during preheating cycles, highlighting the model's reliability and the importance of transient temperature profiles for future oven designs.

Similarly, Landi et al. [2] conducted a comparative life cycle assessment (LCA) of household electric and gas ovens according to ISO 14040/14044 standards. Their study revealed that household electric ovens have a significantly higher environmental impact compared to household gas ovens, particularly in terms of climate change, freshwater, and marine ecotoxicity. This is primarily related to the Italian electricity grid's reliance on non-renewable energy sources. The findings underscore the need to enhance the energy efficiency of electric ovens and increase the share of renewable energy in the electricity mix to mitigate environmental impacts.

Park et al. [3] investigated the effect of different hole locations in the fan case on the thermal performance inside a household gas oven range. Using CFD simulations, they demonstrated that strategic hole placement can optimize temperature uniformity and overall thermal performance. Their study identified that closing specific holes in the fan case, such as the bottom left and top right, resulted in the best thermal performance by creating effective mixing flows within the cavity. These insights are crucial for future oven design improvements to enhance thermal efficiency.

Moreover, the environmental and economic impacts of cooking energy substitution have been explored by Li et al. [4]. Their study compared gas and electricity as cooking energy sources in rural China, revealing that natural gas substitution offers substantial environmental benefits over electricity. The comprehensive assessment model used by the authors highlighted significant pollution reduction potential when transitioning from solid fuels like coal and firewood to cleaner alternatives such as natural gas and electricity. The study emphasized the importance of expanding natural gas infrastructure in rural areas to support sustainable cooking energy substitution, improving public health and environmental sustainability.

2. MAIN BODY

Furthermore, after conducting tests and evaluations in compliance with international standards (such as EN 203-1 and EN 203-2-2), it is aimed to obtain Research and Development (R&D) achievements in the commercial kitchen field with an innovative prototype that operates under adaptive combustion conditions. This study represents a significant advancement in energy efficiency and emission control for commercial gas-fired cooking ovens. The draft drawing of the gas commercial oven prototype developed by adaptive combustion conditions is given in “Figure 1”.

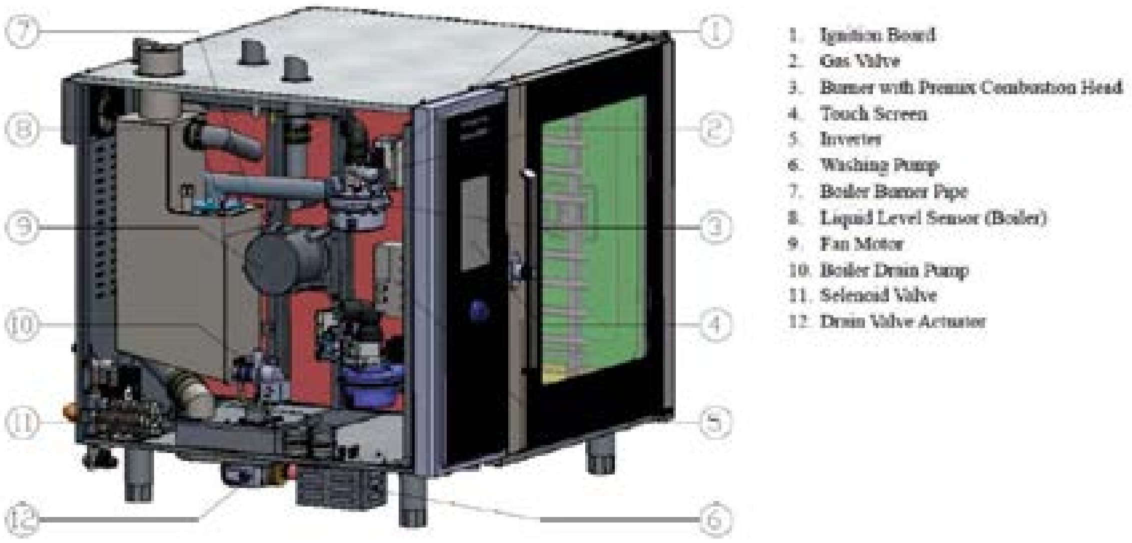

FIGURE 1. The draft drawing of the gas commercial oven prototype was developed in accordance with adaptive combustion conditions.

3. RESULTS AND DISCUSSION

This study represents an essential step towards more efficient and lower-emission operation of commercial gas cooking ovens under adaptive combustion conditions. In addition to the development of the design of the commercial oven prototype, promising results in terms of energy efficiency and emission control were obtained with design verification data. Compared to our existing commercial gas oven, it is aimed to achieve the following gains with the innovative prototype;

Energy Efficiency: The prototype oven, which uses adaptive combustion conditions, will continuously monitor and adjust factors such as gas type, gas pressure, and oxygen levels, and evaluate optimal combustion performance to improve energy efficiency compared to our standard gas oven. The adaptation of the adaptive system to changing operating conditions was assessed with simulation data.

Emission Reduction: Designs of various equipment that make up the chimney system have been developed to reduce emissions produced by commercial gas ovens.

Combustion Stability and Control: Adaptive combustion system designs for stable combustion between different gas types and pressures have been developed.

Verification and Compliance: Prototype oven designs have been developed to comply with international standards such as EN 203-1 and EN 203-2-2, and gains have been achieved in terms of the reliability and effectiveness of the prototype in commercial environments.

Design and Integration: Various combustion system components were designed and integrated specifically for the gas commercial oven prototype. By developing an adaptive combustion system with original designs, convenience has been provided in terms of prototype manufacturing and assembly applications. Simulation data in the design verification phase was critical in optimizing component integration and overall system performance.

As a result, the prototype oven, whose design with adaptive combustion conditions was developed, has shown significant progress in energy efficiency, emission control, and combustion stability. These design improvements not only contribute to the sustainability of commercial cooking operations but also provide a framework for future improvements in the design and functionality of commercial gas cooking ovens. The successful implementation and validation of this innovative prototype will pave the way for further research and development in commercial kitchens, aiming to achieve greater efficiency and lower emissions in commercial kitchens.

4. CONCLUSIONS

This study represents an essential step towards more efficient and low-emission operation of commercial gas cooking ovens under adaptive combustion conditions. The simulations performed in the prototype oven, the gains in the effectiveness of adaptive combustion conditions in optimizing the combustion process, and the continuous monitoring and control of different gas types, pressures, etc. have contributed to the energy efficiency of the developed oven prototype compared to standard gas cooking ovens. In addition, original designs of the innovative gas commercial cooking oven prototype have been developed for tests and evaluations by international standards. This study provides valuable information that can be used to design and apply future commercial gas cooking ovens.

ACKNOWLEDGMENTS

This study was prepared from the project studies numbered 3245026 within the scope of TÜBİTAK-TEYDEB 1707 coded Order-Based R&D Projects Support Program. We would like to thank TÜBİTAK-TEYDEB Transport, Defense, Energy and Textile Technologies Group (USETEG) for contributing to the project.

REFERENCES

[1] H. Mistry, S. Ganapathisubbu, S. Dey, P. Bishnoi, and J.L., Castillo, A methodology to model flow-thermals inside a domestic gas oven, *Applied Thermal Engineering*, 31, 103-111, 2011.

[2] D. Landi, A. Consolini, M. Germani, and C. Favi, Comparative life cycle assessment of electric and gas ovens in the Italian context: An environmental and technical evaluation, *Journal of Cleaner Production*, 221, 189-201, 2019.

[3] S.H. Park, Y.H. Kim, Y.S. Kim, Y.G. Park, and M.Y. Ha, Numerical study on the effect of different hole locations in the fan case on the thermal performance inside a gas oven range, *Applied Thermal Engineering*, 137, 123-133, 2018.

[4] H. Li, X. Ai, L. Wang, and R. Zhang, Substitution strategies for cooking energy: To use gas or electricity? *Journal of Environmental Management*, 303, 114135, 2022.

Sixth International Conference on Computational Methods for Energy and Thermal Problems
THERMAECOMP2024, Sept. 9-11, 2024, Budva, Montenegro
N. Massarotti, P. Nithiarasu, and I. Vušanović (Eds.)

NUMERICAL SIMULATION OF CHANGE OF "DIFFUSION – CONVECTION" MODES IN ISOTHERMAL TERNARY MIXTURES BASED ON LATTICE BOLTZMANN EQUATIONS

Vladimir Kossov
Department of Physics, Institute of Mathematics, Physics and Informatics, Abai Kazakh National Pedagogical University, 13 Dostyk Ave., 050010 Almaty, Kazakhstan, kosov_vlad_nik@list.ru

Ainur Zhumali
Faculty of Mechanics and Mathematics, Al-Farabi Kazakh National University, 71 al-Farabi Ave., 050040 Almaty, Kazakhstan, ainura.z89@gmail.com

Olga Fedorenko
Institute of Experimental and Theoretical Physics, Al-Farabi Kazakh National University, 71 al-Farabi Ave., 050040 Almaty, Kazakhstan, fedor23.04@mail.ru

ABSTRACT

The change of the "diffusion – concentration gravitational convection" regimes in an isothermal three-component gas mixture H_2 + Ar – N_2 was studied numerically. To conduct a numerical experiment, a numerical algorithm for modeling gas flows based on the D2Q9 model of lattice Boltzmann equations was developed. It has been established that in the system under study, instability of mechanical equilibrium occurs at a certain content of argon in the mixture. The distributions of argon concentrations and pressure along the length of the channel were obtained.

Key Words: *Convection, Diffusion, Instability, Gaseous Mixtures, Isoconcentration Lines, Lattice Boltzmann Method, D2Q9 Model.*

1. INTRODUCTION

The occurrence of gravitational convection in liquids and gases is determined by the medium heterogeneity caused by gradients of density, temperature and concentrations. Natural convection manifests itself in many natural processes and technological schemes [1, 2]. Among the diverse manifestations of hybrid heat and mass transfer, we should highlight the effects associated with the occurrence of convective instability [3], in which mechanical equilibrium is disturbed and increasing convective disturbances arise. The intensity of these disturbances can greatly increase when exposed to simultaneous temperature and concentration gradients.

Experimental studies of multicomponent isothermal mixing have shown that in gas mixtures, when the condition of density decreasing with height is realized, convective flows that are not typical for diffusion mixing can occur [4]. The intensity of mixing in this case depends nonlinearly on the relationships between the diffusion coefficients, pressure and a number of other thermophysical characteristics. The solution to such issues seems relevant because it clarifies the separation mechanisms in multicomponent gas mixtures.

The purpose of the work is to study numerically the change of "diffusion – concentration gravitational convection" modes in an isothermal three-component gas mixture. A ternary mixture of hydrogen, argon and nitrogen is considered at different initial compositions for a situation in which the mixture density decreases with height. Numerical studies in model situations will make it possible to recommend the mixture composition and pressure, at which the instability of the mechanical equilibrium of the system can be achieved. The obtained results of the numerical study are compared with experimental data.

2. SIMULATION METHOD

Consider the mixing process in a cylindrical channel in which a mixture of two components is mixed with a third gas. The problem statement is illustrated in Figure 1.

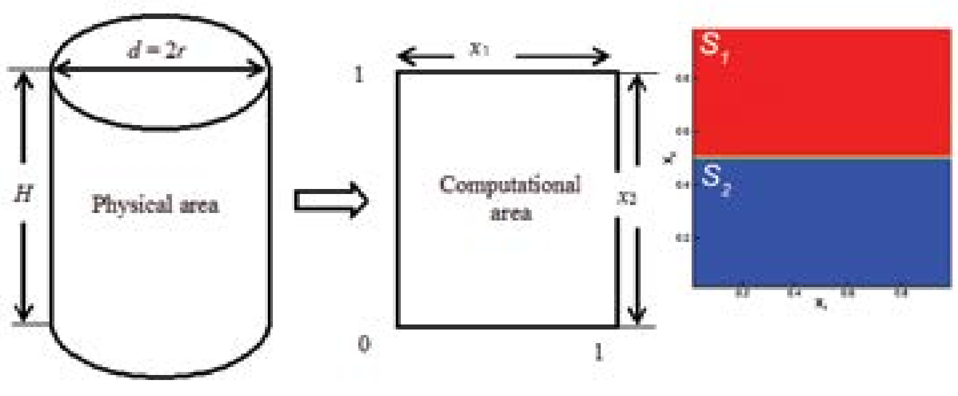

(a) (b)

FIGURE 1. Modeling of mass transfer at the boundary of regime change: a) Physical and calculated mixing areas; b) Initial conditions for placing three-component mixtures in a diffusion channel

The top of channel S_1 contains gas 1 (with the minimum molar mass M_1) and gas 3 (which has the highest molecular weight M_3) diffusing into gas 2 (with the intermediate molar mass M_2) located at the bottom of channel S_2. For the molecular weights of the components, the condition $M_3 > M_2 > M_1$ is satisfied. The change of "diffusion – convection" modes in ternary gas mixtures is described by the system of Navier-Stokes hydrodynamic equations [5]. The numerical implementation of the developed mathematical model is carried out using the D2Q9 scheme (a two-dimensional lattice with nine directions of discrete velocity) of the lattice Boltzmann equation method (LBM) [6], according to which the Boltzmann equation discretized in speed, time and space is solved. LBM has a simple structure and algorithm, which makes it easy to parallelize. The connection between the lattice Boltzmann equations and the macroscopic Navier-Stokes equations is established using the multiscale Chapman-Enskog expansion [6]. In the Bhatnagar-Gross-Krook (BGK) approximation, the lattice Boltzmann equation is written as follows:

$$f_i\left(\vec{x}+\vec{e}_i\Delta t, t+\Delta t\right) = f_i\left(\vec{x},t\right) + \Delta t\left[-\left(f_i\left(\vec{x},t\right) - f_i^{eq}\left(\vec{x},t\right)\right)/\tau_f + F_i\right], \tag{1}$$

$$h_{i,\alpha}\left(\vec{x}+\vec{e}_i\Delta t, t+\Delta t\right) = h_{i,\alpha}\left(\vec{x},t\right) + \Delta t\left[-\left(h_{i,\alpha}\left(\vec{x},t\right) - h_{i,\alpha}^{eq}\left(\vec{x},t\right)\right)/\tau_{h,\alpha} + Q_{i,\alpha}\right],$$

where f_i, $h_{i,\alpha}$ are the velocity and concentration distribution functions of the αth component, $\vec{e}_i$ is the discrete lattice velocity in the i direction, τ_f, $\tau_{h,\alpha}$ are the relaxation time, Δt is the lattice time step, $f_i^{eq}, h_{i,\alpha}^{eq}$ are the equilibrium distribution function of the velocity and concentration of the αth component, respectively. The external force F_i is approximated by means of the Guo et al. scheme [7], and the Seta scheme [8] is used to approximate the sources $Q_{i,\alpha}$. A more detailed description of the numerical method can be found in [5, 9].

Macroparameters (density, velocity, concentration) are expressed through the moments of distribution functions: $\rho = \sum_{i=0}^{8} \overline{f}_i$, $\rho\vec{u} = \sum_{i=0}^{8} \overline{f}_i \vec{e}_i + \frac{\Delta t}{2}\vec{F}$, $C_\alpha = \sum_{i=0}^{8}\left(\overline{h}_{i,\alpha} + \frac{\Delta t}{2} Q_{i,\alpha}\right)$.

The Dirichlet boundary conditions $\bar{f}_i\left(\vec{x}_w, t+\Delta t\right)=\bar{f}_{-i}\left(\vec{x}_w, t+\Delta t\right)$, $\vec{e}_i \cdot \vec{n} \succ 0$ are set for the velocity on all walls and the Neumann condition $\bar{h}_{i,\alpha}\left(\vec{x}_w, t+\Delta t\right)=\bar{h}_{-i,\alpha}\left(\vec{x}_w, t+\Delta t\right)$, $\vec{e}_i \cdot \vec{n} \succ 0$ is determined for the concentration of components on all walls.

3. RESULTS

Figure 2 at a pressure p = 1.5 MPa and T = 298.0 K shows the isoconcentration lines of argon at different mixing times of the ternary gas system 0.50 H_2 (1) + 0.50 Ar (3) – N_2 (2). At time t = 0 s, the density of the binary mixture located in the upper part of the diffusion channel is less than the density of nitrogen, which is localized in the lower part.

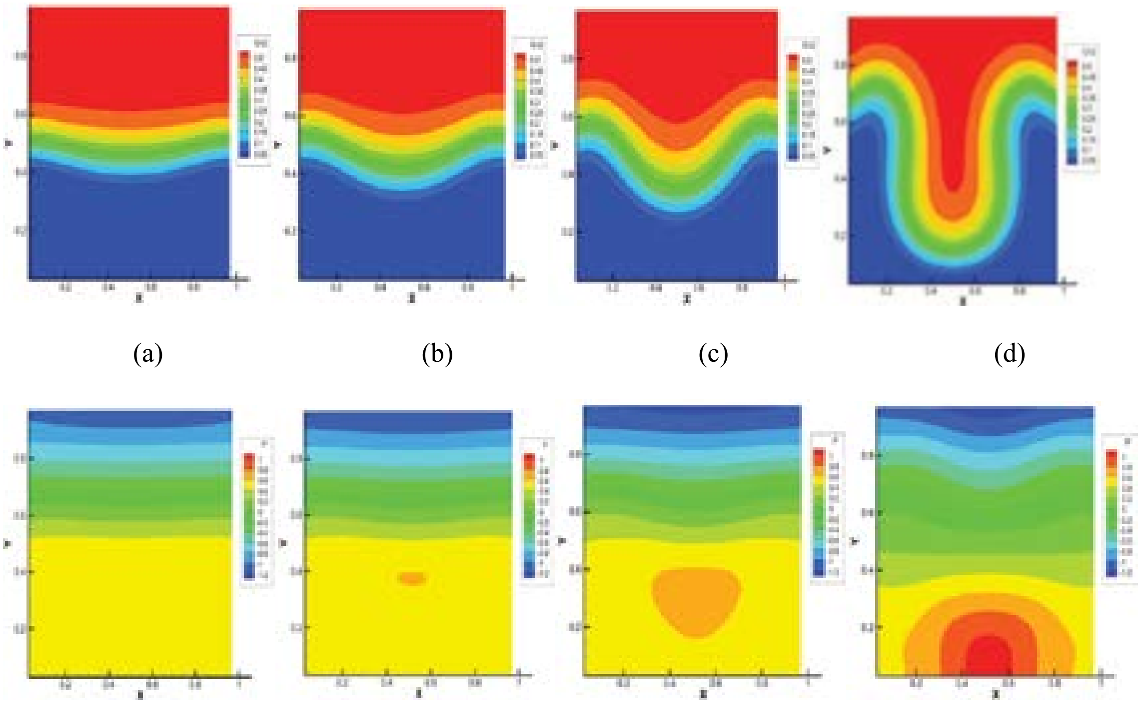

(a) (b) (c) (d)

(e) (f) (g) (h)

FIGURE 2. Calculation results for the 0.5 H_2 + 0.5 Ar – N_2 system (p = 1.5 MPa, T = 298.0 K, Ra_1 = -15.80, Ra_2 = 22.42): (a) – (d) are the isoconcentration lines of argon; (e) – (h) are the pressure distributions. The characteristic mixing times are: (a), (e) – 0.63 s; (b), (f) – 0.87 s; (c), (g) – 1.09 s; (d), (h) – 1.52 s

At the initial stage (Figure 2(a)), diffusion takes place. Then a violation of monotonicity in the distribution of isoconcentration lines, which increases over time (Figures 2(b) and 2(c)), is recorded. This distribution is not typical for diffusion. After 1.52 s of the start of mixing, a convective flow begins to form (Figure 2(d)). Subsequently (not noted in Figure 2), the evolution of convective flow is recorded. Figures 2(e) – 2(h) show the pressure distributions. It is noteworthy that the largest pressure disturbances occur at times corresponding to the formation of a convective cell (Figures 2(g) and 2(h)). Further pressure fluctuations show the presence of high and low pressure zones in the system caused by the presence of complex convective formations. The calculation results are consistent with the experimental data for the mixture under consideration [10].

4. CONCLUSIONS

Thus, the research carried out has shown that a violation of the stability of mechanical equilibrium and the occurrence of convective flows is possible in three-component gas mixtures. The emergence of convective currents is probable only in a certain range of pressures and initial concentrations in the mixture. A numerical model for describing the occurrence of convective flows, based on the method of lattice Boltzmann equations, makes it possible to trace the dynamics of the development of isoconcentration lines and determine the moments of time when convective structures are formed in the gas systems under consideration.

The Committee of Science of the Ministry of Science and Higher Education of the Republic of Kazakhstan has supported this work (the project number: AP14870237).

REFERENCES

[1] C. Wunsch and F. Raffaele, Vertical mixing, energy, and the general circulation of oceans, *Annual Review of Fluid Mechanics*, 36(1), 281–314, 2004.

[2] Y. Mao, C. Lei, and J. Patterson, Unsteady near-shore natural convection induced by surface cooling, *Journal of Fluid Mechanics*, 642, 213-233, 2010.

[3] G.Z. Gershuni and E.M. Zhukhovitskii, *Convective Stability of Incompressible Fluids*, Keter Publishing House, 1976.

[4] V. Kossov and H. Altenbach, Diffusion mechanisms of convective instability in liquid and gas mixtures, *Zeitschrift für Angewandte Mathematik und Mechanik*, 103, e202300801, 2023.

[5] V. Kossov, D. Zhakebayev, O. Fedorenko, and A. Zhumali, Distinctions of the emergence of convective flows at the “diffusion convections” boundary in isothermal ternary gas mixtures with carbon dioxide, *Fluids*, 9(2), 47, 2024.

[6] T. Krüger, H. Kusumaatmaja, A. Kuzmin, O. Shardt, G. Silva, and E.M. Viggen, *The Lattice Boltzmann Method*, Springer International Publishing, 2017.

[7] Z. Guo, C. Zheng, and B. Shi, Discrete lattice effects on the forcing term in the lattice Boltzmann method, *Physical Review E*, 65(4), 046308, 2002.

[8] T. Seta, Implicit temperature-correction-based immersed-boundary thermal lattice Boltzmann method for the simulation of natural convection, *Physical Review E*, 87(6), 063304, 2013.

[9] A.S. Zhumali, B.A. Satenova, and O.L. Karuna, Lattice Boltzmann method simulation of thermal flow dynamics in a channel, *International Journal of Mathematics and Physics*, 10, 75-81, 2019.

[10] V. Kossov, Yu. Zhavrin, and O. Fedorenko, The effect of differences in the diffusion coefficients of components on the onset of convection in isothermal multicomponent systems, *Defect and Diffusion Forum*, 367, 96-102, 2016.